Simulation of Tribological Interactions in Bonded Particle-Solid Contacts

by

Geritza van Wyk

Thesis presented in partial fulfilment
of the requirements for the Degree

MASTER OF SCIENCE IN ENGINEERING
(EXTRACTIVE METALLURGICAL ENGINEERING)

in the Faculty of Engineering
at Stellenbosch University

Supervisor

Prof G. Akdogan

Co-Supervisors

Dr D.N.J. Els

Prof S. Bradshaw

December 2012

DECLARATION

By submitting this thesis electronically, I declare that the entirety of the work contained therein is my own, original work, that I am the sole author thereof (save to the extent explicitly otherwise stated), that reproduction and publication thereof by Stellenbosch University will not infringe any third party rights and that I have not previously in its entirety or in part submitted it for obtaining any qualification.

Geritza van Wyk — Signature

5Ŝŏember 2012 — Date

ABSTRACT

In this study, tool forces from rock cutting tests were numerically simulated through a discrete element method (DEM) in association with PFC3D™. Tribological interactions such as contact, shearing, fracturing, friction and wear were presented during these cutting simulations. Particle assemblies, representing Paarl granite and Sandstone-2, were created in PFC3D™ through a material-genesis procedure. The macro-properties of these particle assemblies, namely Young's modulus, Poisson's ratio, uniaxial and triaxial compressive strength and Brazilian tensile strength, were calibrated by modelling the uniaxial and triaxial compressive strength test and the Brazilian tensile strength test. The calibration was done through adjustment of the micro-properties of the assembly, namely the stiffness and strength parameters of the particles and bonds. The influence of particle size on the calibration was also investigated. These assemblies were used in the rock cutting tests. Results suggested that DEM can reproduce the damage formation during calibration tests successfully. From the results obtained from the calibration tests, it was also concluded that particle size is not a free parameter but influences the macro-properties greatly.

Different rock cutting tools were simulated, namely point-attack (conical) picks, chisel-shaped tools and button-shaped tools. The numerical cutting tools were treated as rigid walls to simplify the simulation and the tool forces were not influenced by wear. In each simulation the cutting tools advanced at a constant velocity. The tool forces acting on the cutting tool, in three orthogonal directions, were recorded during the numerical simulations and the peak cutting forces were predicted by theoretical equations. The damage to the Paarl granite and Sandstone-2 assemblies was revealed as broken bonds, which merge into microscopic fractures. The mean peak cutting forces of sharp cutting tools obtained from numerical, theoretical and experimental models (from the literature) were compared. Finally the influence of factors, including wear on the tool and depth of cut, on the value of tool forces was also investigated.

The results from the rock cutting tests revealed that the correlation between the numerical and the experimental models as well as the theoretical and experimental models was not strong when using sharp point-attack and chisel-shaped picks. It was concluded that the influence of wear plays a substantial part in the cutting process and it has to be included during the numerical simulation for the results to be accurate and verifiable. This study also found that there is a non-linear increase in tool forces with an increase in depth of cut, since the contact area increases. At larger cutting depths, chip formation also generally increased and therefore damage to the sample as well as wear on the cutting

tool will be minimized at shallow cutting depths. Overall this study concludes that DEM are capable of simulating calibration methods and rock cutting processes with different cutting tools and producing results which are verifiable with experimental data. Therefore numerical prediction of tool forces will allow the design of efficient cutting systems and the operational parameters as well as the performance prediction of excavation machines.

OPSOMMING

In hierdie studie is die kragte wat tydens rotssny-toetse op die sny gereedskap inwerk, numeries gesimuleer met behulp van ‘n diskrete element metode (DEM) in samewerking met PFC3D™. Tribologiese interaksies soos kontak, skeer, breking, wrywing en slytasie is gedurende hiersie snytoetse voorgestel. Partikel versamelings, wat Paarl graniet en Sandsteen-2 verteenwoordig, is in PFC3D™ geskep deur middel van ‘n materiaal-skeppings prosedure. Die makro-eienskappe van die partikel versamelings, naamlik Young se modulus, Poisson se verhouding, eenassige en drie-assige druksterkte en Brasiliaanse treksterkte, is gekalibreer deur modellering van die eenassige en drie-assige druksterkte toets en die Brasiliaanse treksterkte toets. Die kalibrasie is gedoen deur aanpassing van die mikro-eienskappe, naamlik die styfheid en die sterkte parameters van die partikels en bindings. Die invloed van partikelgrootte is ook ondersoek. Daarna is hierdie versamelings in die rotssny-toetse gebruik. Resultate het daarop gedui dat DEM die kraakvorming gedurende kalibrasie toetse suksesvol kan reproduseer. Vanuit die kalibrasie is ook gevind dat die partikelgrootte nie ‘n vrye parameter is nie, maar die makro-eienskappe grotendeels beïnvloed.

Verskillende rotssny gereedskap is gesimuleer, naamlik koniese, beitel-vormige en knopie-vormige instrumente. Die numeriese sny gereedskap is gesimuleer as rigiede mure om simulasies te vereenvoudig en die gereedskap-kragte is dus nie deur slytasie beïnvloed nie. Tydens elke simulasie is die sny gereedskap vorentoe beweeg teen ‘n konstante snelheid. Die gereedskap-kragte, in drie ortogonale rigtings, is aangeteken gedurende die numeriese simulasies en die piek snykragte is ook voorspel deur teoretiese vergelykings. Die skade aan die Paarl graniet en Sandsteen-2 versamelings, is voorgestel as gebreekte bindings, wat saamsmelt tot mikroskopiese frakture. Die gemiddelde piek snykragte van skerp sny gereedskap van numeriese, teoretiese en eksperimentele modelle (uit die literatuur) is vergelyk. Ten slotte is die invloed wat faktore, onder andere die slytasie van gereedskap en die snydiepte, op die grootte van die kragte het ondersoek.

Die resultate van die rotssny-toetse het aan die lig gebring dat die korrelasie tussen die numeriese en eksperimentale modelle sowel as die teoretiese en eksperimentele modelle nie sterk is tydens die gebruik van skerp koniese en beitel-vormige instrumente nie. Die gevolgtrekking is gemaak dat die invloed van slytasie van sny gereedskap ‘n wesenlike rol speel in die snyproses en dat dit in die numeriese simulasie ingesluit moet word sodat die resultate akkuraat en virifieerbaar is. Hierdie studie het ook gevind dat daar ‘n nie-lineêre toename in die gereedskap-kragte is met ‘n toename in snydiepte aangesien die kontak-area toeneem met ‘n toename in die snydiepte. By groter snydieptes, het die

formasie van afsplinterings verhoog en dus sal skade aan die partikel versamelings en die slytasie van die gereedskap geminimeer word by vlakker snydieptes. Algeheel het die studie tot die gevolgtrekking gekom dat DEM in staat is om kalibrasie metodes en rotssny-toetse met verskillende sny gereedskap te simuleer asook om resultate te produseer wat verifieerbaar is met eksperimentele data. Numeriese voorspellings van die gereedskap-kragte sal dus toelaat om doeltreffende sny prosesse en operasionele parameters te ontwerp sowel as om die werkverrigting van uitgrawings masjiene te voorspel.

ACKNOWLEDGEMENTS

The author would like to thank the following people and companies for their contribution(s) to this study:

Prof. G. Akdogan for his guidance, advice and support throughout the study,

Dr. D.N.J. Els for his guidance, advice and insight throughout the study,

Prof. S. Bradshaw for supporting the project,

Dr. N. Sacks for her guidance and advice,

The Department of Science and Technology and National Research Foundation South Africa are thanked for their financial support.

GLOSSARY

Term	Description
Anisotropic	Unequal physical properties along different axes
Asperity	Roughness of surface or projection from a surface
BPM	Bonded particle method
Calibration	Method of checking or adjusting the accuracy of the rock parameters
Cutting depth	The thickness of the material removed during cutting
DEM	Discrete element method
Inhomogeneous	Composed of elements that are not all of the same kind or nature
PFC2D™/PFC3D™	Particle flow code in two/three dimensions, Itasca™ software
Poisson's ratio	Ratio of the contraction or transverse strain to the extension or axial strain
Rake angle	The angle between the edge of the cutting and the perpendicular of the rock surface
Shear strength	Resistance to forces that cause two adjacent parts of a body to slide relative to each other
Stiffness	A measure of the resistance to deformation offered by an elastic body
TCS	Triaxial compressive strength
Tensile strength	The maximum engineering stress, in tension, that may be sustained without fracture
Tribology	The science of interacting surfaces in relative motion
UCS	Uniaxial compressive strength
Wear flat	The blunted area of a sharp chisel tool
Yield	The volume of rock obtained per unit cutting length
Young's modulus	A measure of the stiffness of an isotropic elastic material

NOMENCLATURE

Symbol	Description	Units
A	Area	m^2
c	Width of cut	mm
d	Depth of cut	m
E_c	Young's modulus of grains	GPa
$\overline{E}_c$	Young's modulus of cement	GPa
F^d	Damping force	N
F_f	Peak force	N
F_i	Contact force vector	N
$\overline{F}_i$	Total force	N
F_n	Normal contact force	N
F_s	Shear contact force	N
F_s	Elastic shear force	N
FC	Mean cutting force	kN
FC'	Mean peak cutting force	kN
FN	Mean normal force	kN
FN'	Mean peak normal force	kN
G	Gain parameter	-
I	Moment of inertia	kg/m^2
J	Polar moment of inertia	kg/m^2
K_{Ic}	Fracture toughness	$MPa.m^{0.5}$
k	Angle of internal friction	°
k_n	Normal stiffness of grains	N/m
$\overline{k}_n$	Normal stiffness of cement	Pa/m
k_s	Shear stiffness of grains	N/m
$\overline{k}_s$	Shear stiffness of cement	Pa/m
L	Current specimen length	m

L_0	Original specimen length	m
$\overline{M}_i$	Total moment	kg/m^2
m	Radius multiplier	-
m_i	Element mass	kg
N	Number of particles	-
N_c	Number of contacts	-
n	Porosity or stress distribution factor	-
n_i	Normal unit vector	-
n_0	Old porosity	-
$O_{1,2}$	Midpoint of particle	-
Q	Seismic quality factor	-
q_u	Uniaxial compressive strength	MPa
R	Radius of Brazilian cylindrical disk	m
$\overline{R}$	Parallel-bond radius	m
$R_{1,2}$	Radius of particle	m
$R_{\min}$	Lower radius limit	m
$R_{\max}$	Upper radius limit	m
S_s	Shear strength	MPa
T	Resultant moment about the central axes	kg/m^2
t	Thickness of Brazilian cylindrical disk	m
t_i	Shear unit vector	-
U_s	Shear-displacement	m
u	Element centroid displacement	m
$\dot{u}$	Wall velocity	m/s
$\ddot{u}$	Element centroid acceleration	m/s^2
V	Volume of container	m^3
V_i	Contact velocity	m/s
V_p	Sum of particle volumes	m^3
W	Energy	J
w	Tool width	m
$\dot{x}$	Translational velocity	m/s

α	Damping coefficient or rake angle	- /(°)
ε_x	Lateral strain in x-direction	m/m
ε_y	Axial strain	m/m
ε_v	Volumetric strain	m^3/m^3
ε_z	Lateral strain in z-direction	m/m
ϕ	Angle of friction	°
$\bar{\lambda}$	Bond-radius multiplier	-
μ	Friction coefficient	-
δ	Overlap	m
$\Delta\theta$	Incremental rotation	rad
σ_c	Confining stress	Pa
$\bar{\sigma}_c$	Tensile strength of cement	Pa
σ_d	Axial deviatoric stress	Pa
$\bar{\sigma}_{\max}$	Maximum tensile stress	Pa
σ_n	Induced stress	Pa
σ_t	Brazilian tensile strength	Pa
σ_y	Axial stress	Pa
$\bar{\tau}_c$	Shear strength of cement	Pa
$\bar{\tau}_{\max}$	Maximum shear stress	Pa
ν	Poisson's Ratio of particle	-
θ	Semi-angle of conical pick	°
ω	Angular velocity	rad/s

TABLE OF CONTENTS

LIST OF TABLES

LIST OF FIGURES

CHAPTER 1:

INTRODUCTION

1.1 Background

There are many industries, for instance the oil, gas and mining industry, in which the mechanics of rock cutting as well as modelling the process have very important implications. As we drill deeper into the earth, it becomes more challenging and greater drilling problems occur. The reason for these problems is the increase in rock hardness, temperature, formation pressure and distance between the drill bit and the control unit as the depth increases. The higher temperatures and pressures, as well as harder rock, increase the wear of the bit and shorten the bit life. To overcome these problems requires a lot of time, effort and money, since experiments are costly to run and it is difficult to observe the material removal process directly.

It is therefore of great value to be able to simulate and optimize the cutting process of hard rock to reveal what happens during tool-rock interactions and to make the mineral extraction process more economic through this process. From the modelling perspective, the rock cutting analysis may seem very daunting since there is no prior knowledge of how the tool and rock will interact in underground situations and which failure mode will occur. For the model to be credible it should also be verifiable with data obtained from laboratory tests and these tests may not include the pressure factor which occurs underground during mining.

1.2 Physical and computational modelling

The rock cutting process during deep drilling takes place at elevated pressures and temperatures and through different rock layers. The rock properties needed for modelling purposes may not be economically practical. Therefore rock mechanic tests should be conducted in the lab to gather the properties data.

In this study the rock mechanics tests such as the Brazilian tensile strength test and uniaxial and triaxial compressive strength tests were used to support modelling efforts as well as model calibration. The discrete element method (DEM), in its implementation in Particle Flow Code in 3D (PFC3D™), was used to simulate the cutting process.

PFC3D™ can be briefly described as software used for modelling the movement and interaction of stress assemblies of rigid spherical particles using DEM (Su & Akcin, 2011). The basis of the simulation is spherical particles and materials are modelled as bonded or granular assemblies of particles with contact or parallel bonds between them. The dynamic behaviour is represented numerically by a time-stepping algorithm and the calculations performed alternate between the application of Newton's second law to the particles and a force-displacement law at the contacts (Particle Flow Code in 3D Manual, Version 4, 2011).

1.3 Research significance

The main focus of this project is the simulation of rock and a dynamic rock cutting process with DEM in association with PFC3D™. Many studies have already been done on rock cutting, especially soft rocks, using different models, for instance Finite element method (FEM) and Boundary element method (BEM), and simulation software, such as ANSYS, FLAC and PFC2D™. After studying the literature of the background information on DEM and PFC3D™, as well as the calibration tests, it was evident that there was no in depth information on how the modelling was accomplished. This project was therefore designed to focus on modelling the cutting process of hard rock using different shaped cutting tools and the forces exerted on these tools. Hard rock in this study is defined as very strong rock with uniaxial compressive strength ranging from 100 to 250 MPa. The study is specifically interested in hard rock since there is a greater difficulty in cutting hard rock than soft rock and the cutting process will have a greater effect on the cutting tool as well. This study will also provide information on dynamic cutting processes with blunt cutters.

1.4 Project scope

The aim of this project is to investigate and simulate an orthogonal rock cutting procedure using a numerical method, namely discrete element method (DEM). This will be developed by:

- Obtaining the rock properties, such as Young's modulus, Poisson's ratio and shear and tensile strengths through calibration with tests such as the uniaxial compression test, the triaxial compression test and the Brazilian test.
- Simulating the rock with discrete elements in PFC3D™.
- Simulating different cutting tools as being rigid and dynamic.
- Simulating the dynamic cutting processes and fracture patterns of the rock.
- Comparing the results to experimental and theoretical models.

1.5 Layout of thesis

The objectives addressed in the thesis are presented in the following manner:

Chapter 2 presents a literature review on the mathematics of the DEM model, including the grain-based and cement-based interactions, as well as the material-genesis procedure used to simulate the rock samples. The theory and mechanics of rock cutting are also discussed in this chapter.

Chapter 3 describes the different laboratory tests that are used to determine the macro-properties of the rock samples in this study. Chapter 4 covers the methods of discrete element simulation of the calibration tests described in chapter 3, as well as the rock cutting simulations with different cutting tools.

In chapter 5 the PFC3D™ material response of the calibration tests is presented and the influence of particle size on macro-properties is discussed. The PFC3D™ material response for the rock cutting tests, using different cutting tools, and the interpretation thereof is provided in chapters 6, 7 and 8. Finally, the conclusions and recommendations are presented in chapter 9.

CHAPTER 2:

LITERATURE REVIEW

Various studies have been carried out over the past years to understand the behaviour of rock during rock cutting processes in underground conditions. This literature review is focused on the implementation of DEM, with PFC3D™ software to rock cutting, as well as the formulation of the bonded particle model (BPM) and different rock cutting theories. Throughout the literature review the BPM, consisting of grains and cement, discussed by Potyondy and Cundall (2004) is considered, where the grains represent the PFC3D™ particles and the cement (matrix) represents the parallel bonds between these particles.

2.1 Discrete element method

DEM is a numerical technique that was introduced by P.A. Cundall in 1971 (Potyondy & Cundall, 2004). This method is used for problems in rock mechanics as well as the simulation of micromechanics of granular media and other discontinuous materials.

According to Sitharam (2000) DEM is capable of handling a wide range of material behaviour, interbody interaction force laws and arbitrary geometries. This method also allows finite displacements and rotations of discrete bodies and recognizes new contacts automatically as the calculation progresses (Potyondy & Cundall, 2004). Therefore the discrete element method is distinguished from the finite element methods by these capabilities also including the analysis of multiple interacting deformable continuous, discontinuous or fracturing bodies. Although the DEM is a discontinuum based numerical method, it can be applied to continuum by introducing bonds between particles. These particles can be circular discs, ellipses and polygons in two-dimensional models, as well as spheres, blocks and ellipsoids in three-dimensional models (Sitharam, 2000).

According to Bicanic (2004) the overall algorithmic framework for the DEM has remained more or less the same since the method was first introduced. Basically the method considers each body in turn and determines all the forces acting on it at any given time. Any force that is out of balance induces an acceleration, which then determines the movement of that body during the next time step. Each DEM cycle involves the application of Newton's second law of motion to the particles and a force-displacement law to the contacts.

The DEM process involves several steps to calculate the particle movement. At a given time, each particle is defined in terms of mass, radius, position, velocity and acceleration. The next step involves finding all the existing contacts between the spheres. Each contact allows the calculation of the interaction forces between spheres and then Newton's law is applied to determine the acceleration of each particle. The particle speed and position are determined by an integration algorithm at time t+dt. The time-step is chosen to be very small to ensure that the velocities and accelerations are constant over it. A force-displacement law is then used to calculate the unbalanced forces on each individual particle. (Iliescu et al., 2010)

The translational and rotational motion of the rigid particles is described by means of the standard equations of rigid body dynamics. For the i^{th} element the equations can be written as follows (Onate & Rojek, 2004):

$$m_i \ddot{u}_i = F_i \tag{1}$$

$$I_i \dot{\omega}_i = T_i \tag{2}$$

In these equations u is the element centroid displacement in a fixed coordinate frame, ω is the angular velocity, m is the element mass, I is the moment of inertia, F is the resultant force and T is the resultant moment about the central axes. The equations of motion, equation 1 and 2, are integrated in time using a central difference scheme. The time integration operator for the translational motion at the n^{th} time step is as follows (Onate & Rojek, 2004):

$$\ddot{u}_i^n = \frac{F_i^n}{m_i} \tag{3}$$

$$\dot{u}_i^{n+1/2} = \dot{u}_i^{n-1/2} + \ddot{u}_i^n \Delta t \tag{4}$$

$$u_i^{n+1} = u_i^n + \dot{u}_i^{n+1/2} \Delta t \tag{5}$$

Equations 4 and 5 can also be written for the rotational motion and the vector of incremental rotation ($\Delta\Theta$) is calculated as follows:

$$\Delta\theta = \omega_i^{n+1/2} \Delta t \tag{6}$$

The presence of a contact can be defined when $O_1O_2 \leq R_1 + R_2$ with these variables as seen in Figure 1. In this case O_1O_2 is the distance between the centres of two spheres and R_1 and R_2 are the respective radii. An overlap occurs when $\delta = R_1 + R_2 - O_1O_2$. This can be understood as the deformation of spheres and overlap should be kept very small compared to the radius of the spheres. Three positions are taken into

account between the two particles, namely when the spheres are in contact (δ=0), when they intersect (δ<0) and when they do not touch (δ>0) (Iliescu et al., 2010).

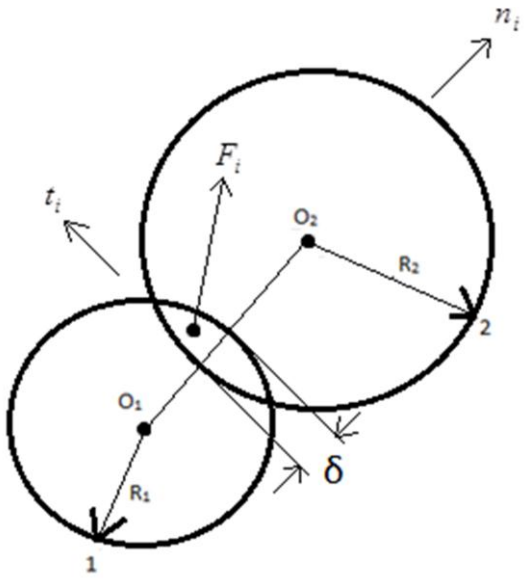

Figure 1: Interpenetration between two particles

(Adapted from Iliescu et al., 2010 and Potyondy and Cundall, 2004)

2.2 Grain-based interactions

Once the contact has been detected, the forces occurring at the contact point can be calculated. The contact force vector (F_i) has two components over this area, namely one in the contact plane (shear component) and one normal to the plane (normal component).

$$F_i = F_n n_i + F_s t_i \tag{7}$$

In this equation from Potyondy and Cundall (2004), n_i and t_i are unit vectors that define the contact plane as seen in Figure 1. The normal and shear forces between spheres are explicit functions of the overlap (δ) and the overlap speed, which is the normal or shear component of relative velocity ($\dot{\delta}$) between the spheres (Onate & Rojek, 2004). The normal force has the following definition:

$$F_n = K_n \delta \tag{8}$$

K_n is the contact normal stiffness and Potyondy and Cundall (2004) defines it as follows:

$$K_n = \frac{k_n^{(A)} k_n^{(B)}}{k_n^{(A)} + k_n^{(B)}} \tag{9}$$

In this equation $k_n^{(A)}$ and $k_n^{(B)}$ are the particle normal stiffnesses of the neighbouring particles.

On the other hand, the shear force is computed incrementally. When the contact is formed, the shear force is initialized to zero and after each subsequent relative shear-displacement increment (ΔU_s), an increment of elastic shear force is added to the initial shear force. The increment of elastic shear force is given as follows:

$$\Delta F_s = -k_s \Delta U_s \tag{10}$$

The contact shear stiffness is denoted by k_s and is given as follows, with $k_s^{(A)}$ and $k_s^{(B)}$ being the particle shear stiffnesses:

$$k_s = \frac{k_s^{(A)} k_s^{(B)}}{k_s^{(A)} + k_s^{(B)}} \tag{11}$$

The relative shear-displacement increment vector (ΔU_i^s) and contact velocity (V_i) can then be computed as follows:

$$\Delta U_i^s = V_i^s \Delta t = \left(V_i - V_i^n\right)\Delta t = \left(V_i - V_j n_j n_i\right)\Delta t \tag{12}$$

$$V_i = \left(\dot{x}_i^{(c)}\right)_B - \left(\dot{x}_i^{(c)}\right)_A = \left(\dot{x}_i^{(B)} + e_{ijk}\omega_j^{(B)}\left(x_k^{(c)} - x_k^{(B)}\right)\right) - \left(\dot{x}_i^{(A)} + e_{ijk}\omega_j^{(A)}\left(x_k^{(c)} - x_k^{(A)}\right)\right) \tag{13}$$

The translational and rotational velocities are denoted by $\dot{x}_i$ and ω_j respectively and e_{ijk} represent the permutation. If there is no overlap, the normal and shear forces are set to zero, or else slip is accommodated by computing the friction coefficient as follows, where the minimum friction coefficient is chosen when different friction coefficients were assigned to two particles:

$$\mu = \min\left(\mu^{(A)}, \mu^{(B)}\right) \tag{14}$$

$\mu^{(A)}$ and $\mu^{(B)}$ are the particle friction coefficients and the shear force is set equal to the friction coefficient multiplied by the normal force (Potyondy and Cundall, 2004).

It is concluded that the following parameters describes the grain-based portion during force-displacement: the normal and shear stiffnesses as well as the friction coefficient of the contacting particles.

2.3 Cement-based interactions

The cement-based portion can be described by five parameters, namely the normal and shear stiffnesses per unit area, the tensile and shear strengths and the bond-radius multiplier ($\bar{\lambda}$). The parallel-bond radius then becomes

$$\bar{R} = \bar{\lambda} \min\left(R^{(A)}, R^{(B)}\right) \tag{15}$$

$R^{(A)}$ and $R^{(B)}$ are the particle radii. The parallel bonds can be considered as elastic whose ends are glued on each particle. These parallel bonds are also modelled as tight linear springs with stiffness different to that of the particle, which depends on the considered material.

Parallel bonds can transmit force and moment between particles, while the grains can only transmit force. The total force and moment are denoted by $\bar{F}_i$ and $\bar{M}_i$ respectively and both consist out of a normal and shear component. When the parallel bond is formed the force and moment are initialized to zero. An increment of elastic force and moment are then added to the current values after each subsequent relative displacement- and rotation increment. These increments of elastic force and moment are given as follows:

$$\begin{aligned}
\Delta\bar{F}_n &= \bar{k}_n A \Delta\delta \\
\Delta\bar{F}_s &= -\bar{k}_s A \Delta U^s \\
\Delta\bar{M}_n &= -\bar{k}_s J \Delta\theta^n \\
\Delta\bar{M}_s &= -\bar{k}_n I \Delta\theta^s
\end{aligned} \tag{16}$$

In this equation A, I and J are the area, moment of inertia and polar moment of inertia of the parallel bond cross-section, respectively (Potyondy and Cundall, 2004). These quantities can be computed as follows:

$$\begin{aligned}
A &= \pi\bar{R}^2 \\
I &= \frac{1}{4}\pi\bar{R}^4 \\
J &= \frac{1}{2}\pi\bar{R}^4
\end{aligned} \tag{17}$$

From these equations, the maximum tensile and shear stresses acting on the parallel-bond margin can be calculated as follows:

$$\bar{\sigma}_{\max} = \frac{-\bar{F}_n}{A} + \frac{\left|\bar{M}_s\right|\bar{R}}{I}$$

$$\bar{\tau}_{\max} = \frac{\left|\bar{F}_s\right|}{A} + \frac{\left|\bar{M}_n\right|\bar{R}}{J} \tag{18}$$

There is a rupture of the bond when the normal and shear stresses exceeds the normal and shear strength. The contact between two particles is then lost, along with its force, moment and stiffnesses, and a fracture forms (Iliescu et al., 2010).

2.4 Damping of particle motion

According to Potyondy and Cundall (2004) damping is necessary in a BPM to dissipate kinetic energy since the DEM is a dynamic formulation. The local non-viscous damping is specified by a damping coefficient α. The damping force which is applied to each particle is given by the following equation:

$$F^d = -\alpha\left|F\right| sign\left(V\right) \tag{19}$$

In this equation $\left|F\right|$ is the magnitude of the unbalanced force on the particle and sign$\left(V\right)$ is the sign of the particle velocity. This equation is applied separately to each degree-of-freedom. The seismic quality factor (Q) is a measure of energy loss in rock and it is defined as 2π multiplied by the ratio of stored energy to dissipated energy in one wavelength:

$$Q = 2\pi\left(\frac{W}{\Delta W}\right) \tag{20}$$

For a single degree-of-freedom system or for oscillation in a single mode, the quality factor reduces to:

$$Q = \frac{\pi}{2\alpha} \tag{21}$$

Potyondy and Cundall (2004) used a damping coefficient of 0.7 and this was also the default value for damping coefficients in PFC3D™. Since the work of Potyondy and Cundall (2004) was used as a reference to produce a BPM, the BPM in this report was also run with a local damping coefficient of 0.7, which corresponds with a quality factor of 2.2.

2.5 Micro-properties

The following parameters influences the behaviour of the BPM, namely the grain density, grain shape, grain size distribution, grain packing and grain-cement micro-properties. The grain shape used in PFC3D™ is spherical and the diameters satisfy a uniform particle size distribution between D_{min} and D_{max}. The grain packing is a dense one and is obtained using the material-genesis procedure. The grain micro-

properties are the Young's modulus of the grains (E_c), the ratio of normal to shear stiffness of the grains (k_n / k_s) and grain friction coefficient. The cement properties are the radius multiplier ($\bar{\lambda}$) used to compute the parallel bond radii, the Young's modulus of the cement ($\bar{E}_c$), the ratio of normal to shear stiffness of the cement ($\bar{k}_n / \bar{k}_s$) and the tensile ($\bar{\sigma}_c$) and shear ($\bar{\tau}_c$) strengths of the cement (Potyondy and Cundall, 2004).

The particle and parallel-bond stiffnesses are defined as follows, where R is the particle radius:

$$k_n = 4RE_c$$

$$k_s = \frac{k_n}{(k_n / k_s)}$$

$$\bar{k}_n = \frac{\bar{E}_c}{R^{(A)} + R^{(B)}}$$

$$\bar{k}_s = \frac{\bar{k}_n}{(\bar{k}_n / \bar{k}_s)} \qquad (22)$$

The grain shape, grain packing and ratios of normal to shear stiffness of the grains and cement influence the Poisson's ratio. Increasing these ratios while keeping the grain shape and packing fixed, will increase the Poisson's ratio (Potyondy and Cundall, 2004).

2.6 Material-genesis procedure

In order to generate rock in PFC3D™, the individual particles have to be generated first and then bonded together to form a rock structure. Irregular assemblies have no noticeable pattern in the arrangement of particles and this type of assembly is generally used to represent a solid or granular material. When creating this irregular assembly, a selected space is filled with particles at a given porosity and it is ensured that the assembly is at equilibrium. After the assembly is created, the conditions within are adjusted so that a given stress is obtained within the assembly. (Particle Flow Code in 3 Dimensions Manual, Version 4)

The material-genesis procedure involves the following five steps that will also be described in more detail in Appendix A. Figure 2 shows an enlarged portion of the particle assembly after each step.

2.6.1 Creating the initial assembly

A rectangular material vessel, consisting of six frictionless planar walls, is created and filled with randomly placed particles. The diameters of these particles satisfy a uniform size distribution bounded

by a minimum and maximum radius value. According to Potyondy and Cundall (2004) the overall porosity in the vessel should be 35% for a PFC3D™ granite model to ensure that the number of particles ensures a tight initial packing. The particles are created at half their final size to ensure that there is no overlap between particles and then their radii are increased to the final values through the radius expansion method. The normal stiffnesses of the walls are specified to be just larger than the average particle normal stiffness to ensure that the particle-wall overlap is minimal. The material vessel is then allowed to rearrange under zero friction. The complete procedure is described in Appendix A1.

2.6.2 Installing the specified isotropic stress

Radius expansion is used again during the isotropic stress installation. The radii are firstly reduced uniformly to achieve the specified isotropic stress, which is the average of all the direct stresses. The specified isotropic stress is set equal to 1% of the uniaxial compressive strength (Potyondy and Cundall, 2004). This is done to reduce the magnitude of the locked-in forces which develop during the parallel-bond installation and removal from the material vessel. The direct stresses are defined as the average of the total forces acting on the opposing walls divided by the area of the corresponding specimen cross-section. This procedure is described in more detail in Appendix A2.

2.6.3 Floater-elimination procedure

The material assembly containing the randomly placed spherical particles may contain a number of floating particles, which have less than 3 contacts and are indicated in red in Figure 2. Up to 15% of the particles may be floaters (Potyondy and Cundall, 2004). Since granite is a rather dense material, it is necessary to reduce the number of floating particles so that the assembly will mimic the structure of granite. The complete procedure is given in Appendix A3.

2.6.4 Installing parallel bonds

According to Potyondy and Cundall (2004), parallel bonds are installed throughout the material vessel between all neighbouring particles. The parallel-bond properties are assigned by the last two definitions in equation 22 and the grain friction coefficient is also specified.

2.1.1 Removal from material vessel

The last step in the material-genesis procedure is to remove the specimen from the material vessel and allow it to relax. All six walls are deleted and the system is cycled until static equilibrium is achieved. During this step, the material vessel expands and generates a set of self-equilibrating locked in forces.

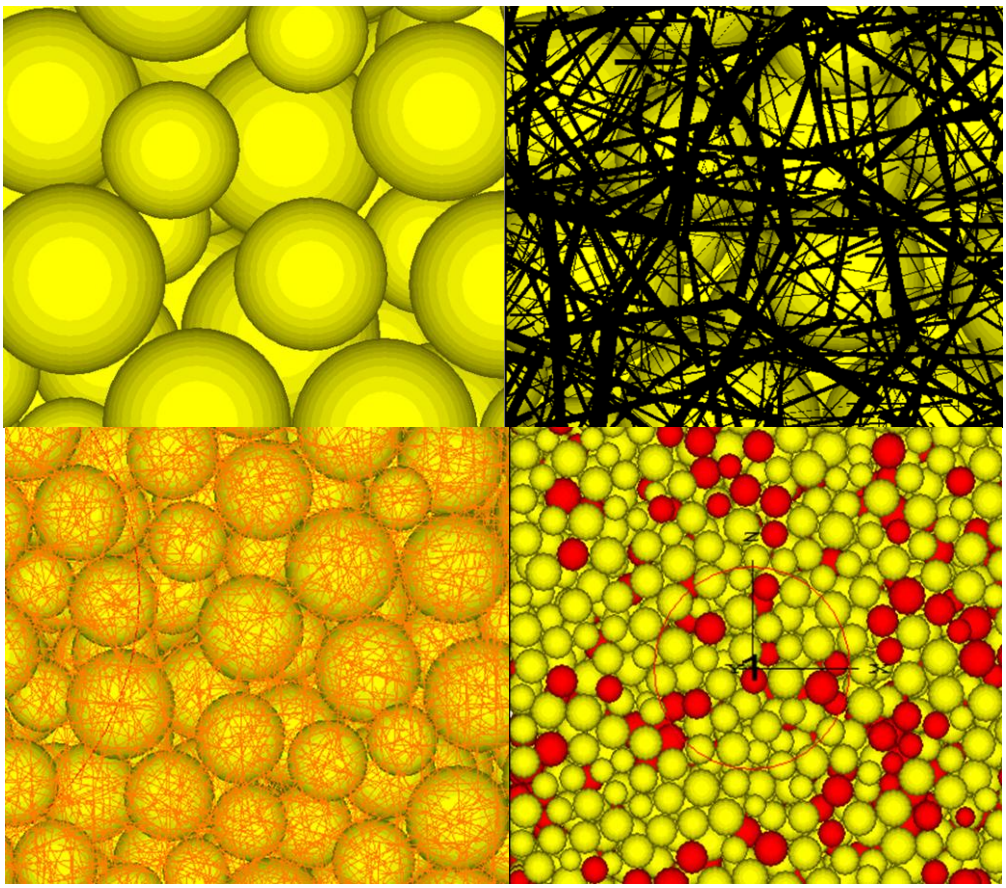

Figure 2: Material-genesis procedure

Clockwise: particles after initial generation; contact-force distribution after isotropic stress installation; floating particles before floater-elimination; parallel-bond network.

2.2 Theory and mechanics of rock cutting

2.2.1 Prediction of cutting forces

The forces acting on the cutting tool determines the rock cuttability and in turn, the cuttability of rock leads to the determination of the specific energy, installed power and advance rate of the machine. The tool forces can be divided into three orthogonal forces, namely normal, cutting and sideway forces. The normal forces are perpendicular to the direction of cutting while the cutting forces are applied parallel to the direction of cutting and the sideway forces are measured transverse to the cutting direction. From these forces, the cutting force plays the leading role in optimizing cuttability (Su & Akcin, 2011). Figure 3 displays the direction of the cutting and normal forces, as well as the other parameters used in the different theories of rock cutting.

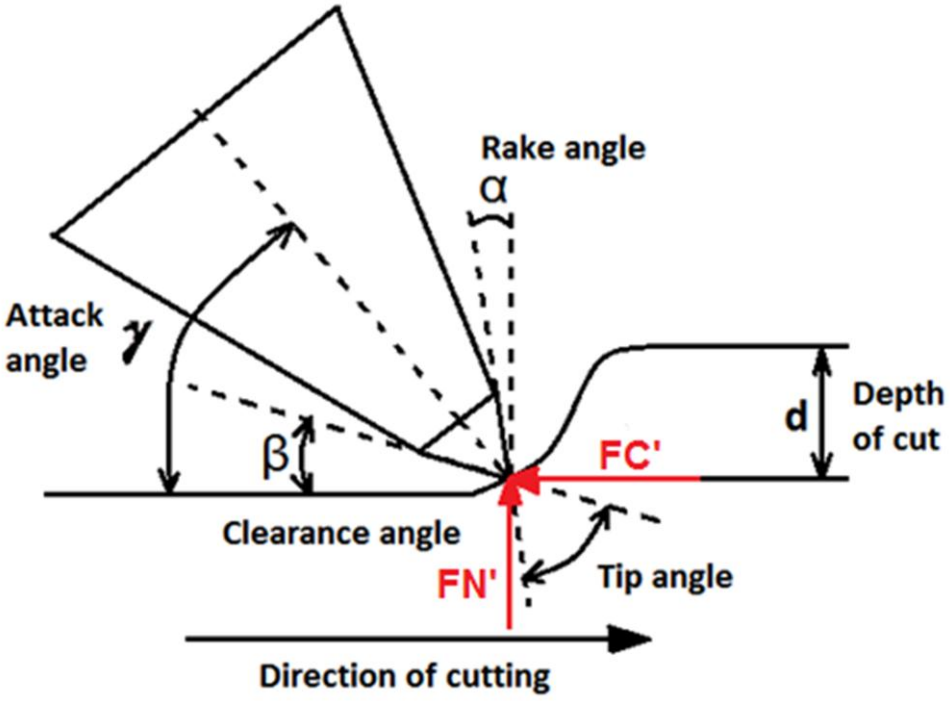

Figure 3: Cutting parameters of a point-attack pick

(Source: Adapted from Su & Akcin, 2011)

Nishimatsu (1972) observed the process of rock cutting with an orthogonal cutting tool and he assumed that failure is only due to shear and occurs along a plane. He also observed that the deeper the penetration of the tool edge, the greater the cutting force becomes. Therefore, in rock cutting, the cutting force increases with the depth of penetration of the tool edge to a maximum at the initiation of the macroscopic failure crack and decreases suddenly after this maximum value has been reached. Nishimatsu (1972) derived the following equation for the resulting cutting force FC' for chisel picks:

$$FC' = \frac{2\sigma_s dw\cos(k)\cdot\cos(\phi-\alpha)}{(n+1)(1-\sin(k-\alpha+\phi))} \tag{23}$$

In this equation n is the stress distribution factor as estimated in equation 24, σ_s is the shear strength of the specimen rock, d is the depth of the cut, w is the width of the cutting tool, k is the angle of internal friction of the rock, α is the rake angle of the cutting tool and ϕ is the angle of friction between the tool and the rock during rock cutting.

$$n = 12 - (\alpha/5) \tag{24}$$

The angle of internal friction (k) can be calculated as follows, if the shear and compressive strength of the rock are known:

$$\tan k = \frac{\sigma_c^2 - 4\sigma_s^2}{4\sigma_c\sigma_s} \tag{25}$$

Evans (1984) developed a model for rock cutting with point-attack picks. He assumed that the penetration of the conical pick attacking a buttock of rock produces radial compressive stresses in the rock. Evans' equation for the peak cutting force is as follows:

$$FC' = \frac{16\pi\sigma_t^2 d^2}{\sigma_c \cos^2\theta} \tag{26}$$

He also formulated a model for chisel picks (Bilgin et al., 2006):

$$FC' = \frac{2\sigma_t dw \sin\frac{1}{2}\left(\frac{\pi}{2}-\alpha\right)}{1-\sin\frac{1}{2}\left(\frac{\pi}{2}-\alpha\right)} \tag{27}$$

In these equations σ_t is the tensile strength of rock, d is the cutting depth, σ_c is the uniaxial compressive strength of rock, Θ is the semi-angle of the conical pick, w is the tool width and α is the rake angle.

According to Su & Akcin (2011) F.F. Roxborough and Z.C. Liu adapted Evans' theory for point attack picks and added the friction between the tool and rock in 1995. Their equation is as follows, with all the notations as stated above:

$$FC' = \frac{16\pi\sigma_c d^2 \sigma_t^2}{\left(2\sigma_t + \left((\sigma_c \cos\theta)/[(1+\tan\phi)/\tan\theta]\right)\right)^2} \tag{28}$$

Evans' equation for point-attack picks was also developed further by Goktan (2005) by taking account of asymmetrical attack by introducing the rake angle parameter and removing the uniaxial compressive strength.

$$FC' = \frac{4\pi\sigma_t d^2 \sin^2[\theta+\phi]}{\cos[\theta+\phi]} \tag{29}$$

2.2.2 Influence of cutting parameters on cutting forces

The theoretical models of rock cutting were developed by means of the geometrical shape of the tool and the direction of cutting into the rock. The basic tool geometric parameters are tool width and the rake angle, while the basic tool operational parameters are cutting depth and cutting velocity (Mak et al., 2012).

The tool width, rake angle and cutting depth used in the simulations are usually chosen to be the same as that of the experimental set-up in the laboratory. The cutting velocity on the other hand cannot be

chosen likewise. All these parameters have an influence on the simulation of the cutting forces developed during cutting.

2.2.2.1 *Influence of tool width and wear flat*

Bilgin (1977) tested the cutting of high strength rocks with picks and found that the cutting and normal forces were linearly affected by the tool width. This is true since the contact area between the rock and the tool increases as the tool becomes wider. For a given depth of cut, the specific energy also decreases with an increase in the tool width (Dagrain, 2001).

The cutting forces also increases as the wear flat of the tool increases, according to Appl et al. (1993), Bilgin et al. (2012), Hood & Alehossein (2000), Kaitkay & Lei (2005) and Loui & Karanam (2012). Cigla and Ozdemir (2012) also stated that the increasing wear flat of a tool can increase the normal force requirements by up to 2 to 3 times. The wear flat can be defined as the blunted area of a sharp chisel tool as seen in Figure 4.

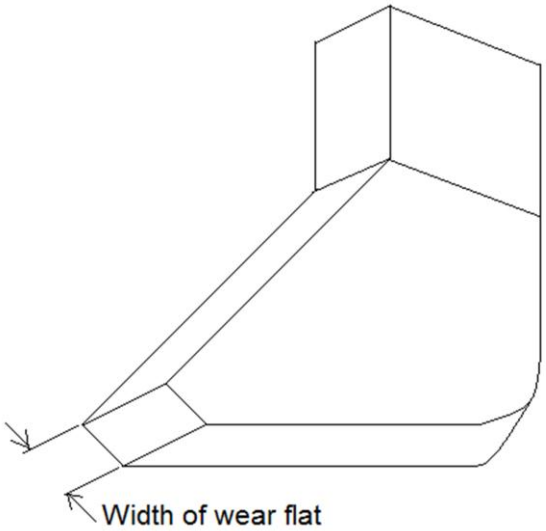

Figure 4: Blunted chisel tool with wear flat

(Source: Adapted from Bilgin & Balci, 2012)

Although the definition of a wear flat is the blunted area of a sharp chisel tool, a wear flat can also be introduced to a sharp point-attack or conical pick by cutting off the tip of the pick at a certain diameter. This was done in the current study and will be discussed further in chapter 4 and 5. An example of a point-attack pick with a wear flat of 1.5 mm in diameter can be seen in Figure 5.

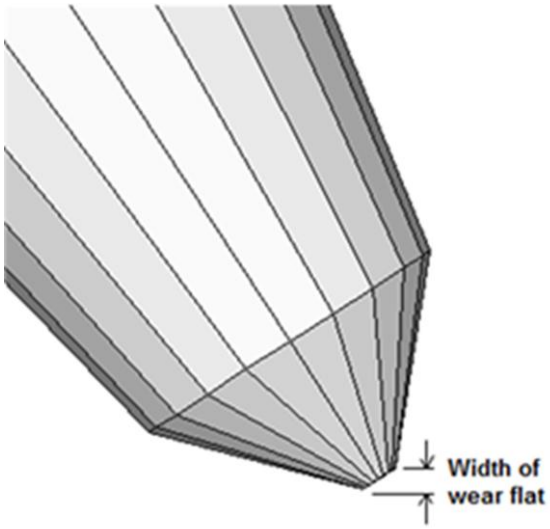

Figure 5: Blunted point-attack pick with wear flat

2.2.2.2 *Influence of rake angle*

The rake angle is the angle between the edge of the cutting tool and the perpendicular of the rock surface. This angle can be positive or negative. A positive rake angle tilts the cutting tool backwards, while a negative rake angle tilts the cutting tool towards the surface being cut.

According to Da Fontoura et al. (2012), who used PFC2D™ to simulate a cutting process, an increase in the rake angle causes more scattering of the particles of which bonds are broken. The horizontal as well as the vertical forces also increase as the negative rake angle increases. Kaitkay & Lei (2005) experimentally found that cutting forces increase with an increase in negative rake angle.

Loui & Karaman (2012) used two dimensional non-linear FEM to study the rock failure under a drag pick cutter. They came to the conclusion that chip formation takes place by shear failure during negative angle cutting, while chip formation is caused by tensile failure during the use of a higher positive rake angle. For zero rake angle cuttings the failure may then be due to a combination of shear and tension.

According to Sankar (2011) an increase in the positive rake angle causes a monotonically decrease in cutting and normal forces. This study also stated that a positive rake angle of 20° gives the most benefit to pick cutters and that picks with higher positive rake angles may not be suitable since they become susceptible to gross failure.

2.2.2.3 *Influence of cutting depth*

The cutting depth is the thickness of the material which is removed during cutting and some studies have been made on the effect of this cutting depth on the cutting forces. Tulu et al. (2009) and Tulu (2009) found that the forces generally increase with the cutting depth and that the contact area between the rock and the tool also increases with increasing depth. Kaitkay & Lei (2005), Bilgin et al.

(2006), Gertsch et al. (2007), Patten et al. (2007), Lunow and Konietzky (2009) and Da Fontoura et al (2012) also found that there is a steady linear increase in the cutting force with an increase in cutting depth. This is because more material in volume is removed with an increase in cutting depth.

Dagrain (2001) made a study of the influence of tool geometry in rock cutting with PDC cutters and gathered that there is a linear relationship between forces and the cutting depth when cutting is performed at shallow depths of cut. When the cutting depth becomes deeper, the relationship becomes non-linear. Shallow cutting also leads to a ductile failure mode, while a deeper cut causes brittle fracture propagation. This linear and non-linear relationship can be seen in Figure 6 where the cutting forces increases linearly for cutting depths of up to 6 mm beyond which there is a steeper change in the cutting forces. This data was taken out of Su & Akcin (2011) and Bilgin et al. (2006) together with a zero point, who both studied the cutting of different rock materials with the use of sharp point-attack picks. These trend lines support the study of Dagrain (2001), who studied cutting forces with respect to depth of cut.

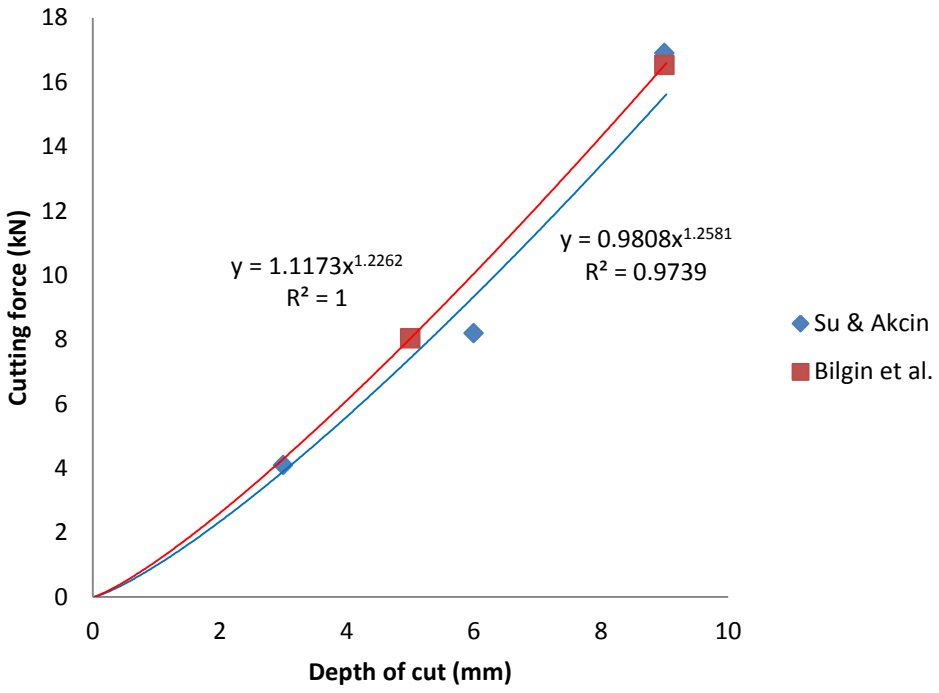

Figure 6: The relationship between cutting forces and cutting depth

(Source: Data taken from Su & Akcin, 2011 and Bilgin et al., 2006)

2.2.2.4 Influence of cutting velocity

Selecting the cutting velocity of the simulated cutting tool is a difficult task, since this velocity determines the computation time of the simulation and it furthermore influences the simulated cutting

force, as well as fracture behaviour of the rock. According to Rizo (2010) there has been no research done previously to determine an appropriate velocity in rock cutting.

Rizo (2010) explained, from a DEM perspective, that a very low cutting velocity of 4 mm/s, used in laboratory tests, would require more than a million steps of computation to advance the cutting tool by only a millimetre. In his study the appropriate cutting velocity for the simulation was estimated by conducting simulations with different cutting velocities, ranging from 0.25 to 3.0 m/s, and then observing the failure behaviour and cutting force magnitudes and comparing it to the actual values. It was found that during a slow velocity the forces can propagate, seek and destroy the weakest bonds, while during the high velocity the force propagation is reduced and bonds fail immediately. The conclusion was made that higher velocities might lead to the correct cutting force. Tan et al. (2009) also used different cutting velocities and then chosen a representative case in the simulation of the cutting process of polycrystalline SiC.

Su & Akcin (2011) simulated rock cutting with a point attack pick in PFC3D™ using a low velocity of 0.3 m/s. The reason for this low velocity was to ensure the quasi-static equilibrium state of the assembly. Marusich (2001) looked at the influence of cutting speed on cutting forces by using finite element modelling and AdvantEdge machining simulation software. He found that there is a significant reduction in cutting force as the cutting speed increases. Zhou et al. (2011) used a finite element model in ABAQUS and also found a decreasing trend in cutting force with an increase in cutting speed.

Khair & Yu (2004) simulated the failure process in continuous miner rock cutting with the dynamic finite element analysis and found that the penetration and cutting forces do not depend on the cutting speed, while the mechanical properties of the rock material affected the cutting characteristics significantly. In this study simulations at different rotation speeds and advancing rates were done and the averages of the interaction forces were compared to each other. The results of the cutting forces were very similar and also very close to the experimental cutting results.

2.3 Rock cutting simulations in perspective

As previously mentioned this study focuses on the simulation of cutting hard rock (uniaxial compressive strength ranging from 100 to 250 MPa) pertinent to oil and gas drilling conditions as well as to coal mining. In Appendix B in Table 13 a summary is made of available information of rock cutting simulations found during a literature survey. From this table it is evident that numerous simulations were previously done on softer rocks with uniaxial compressive strengths ranging from 5.6 to 160.7 MPa. From the few tests that were done on harder rock, with uniaxial compressive strengths ranging from 173.7 to 183.86 MPa, minimal or no information regarding simulation parameters or experimental forces was published and these simulations could therefore not be repeated.

To give a few examples, Bilgin (1977) did a study on the cutting of Greywacke with a strength of 183.86 MPa with a pick tool and the experimental normal forces were available, but no other study on this type of rock was found and therefore the information was inadequate to simulate cutting processes of this rock. The study of Copur (2010) with a chisel tool had enough information regarding the rock cutting parameters and experimental data, but the rock material he used had strengths ranging from 12.7 to 83.7 MPa and therefore it was not useful in this study. Su & Akcin (2011) and Bilgin et al. (2006) did a rock cutting test on Sandstone-2 with a conical pick and provided enough information on conditions and parameters.

After this literature survey it was decided to use Sandstone-2, which is found in coal-beds and oil and gas strata, during the rock cutting simulations, since a number of papers were already published on the cutting of Sandstone-2 and the information available was enough to be able to replicate these rock cutting simulations. Sandstone-2 has relatively high uniaxial strength of 174 MPa. Although this is much lower than the uniaxial strength of Paarl granite, (198.29 MPa), which was one of the rock types of interest in this study, it has the most useful information available in the literature

.

CHAPTER 3:

MEASURED MACROSCOPIC PROPERTIES

Different tests were conducted at the University of the Witwatersrand to determine the macro-properties of Paarl granite. These laboratory tests were used to calibrate the simulated granite model and are described in this chapter. The raw data received from the University of the Witwatersrand can be found in Appendix C. The same tests were conducted to calibrate Sandstone-2, which is also under consideration in this thesis.

3.1 Brazilian tensile strength test

The Brazilian tensile strength test is a common method of indirectly measuring the tensile strength of a material. The test consists of placing a cylindrical disk diametrically between the platens of a compression testing machine as seen in Figure 7. The platens supply a line load aligned with the diameter of the sample. According to Bieniawski and Hawkes (1978), the test specimens should be cylinders with diameters of approximately 54 mm and with a thickness of approximately equal to the specimen radius. They also state that failure will occur within 15 to 30 seconds of loading when the tensile load is applied continuously at a constant rate.

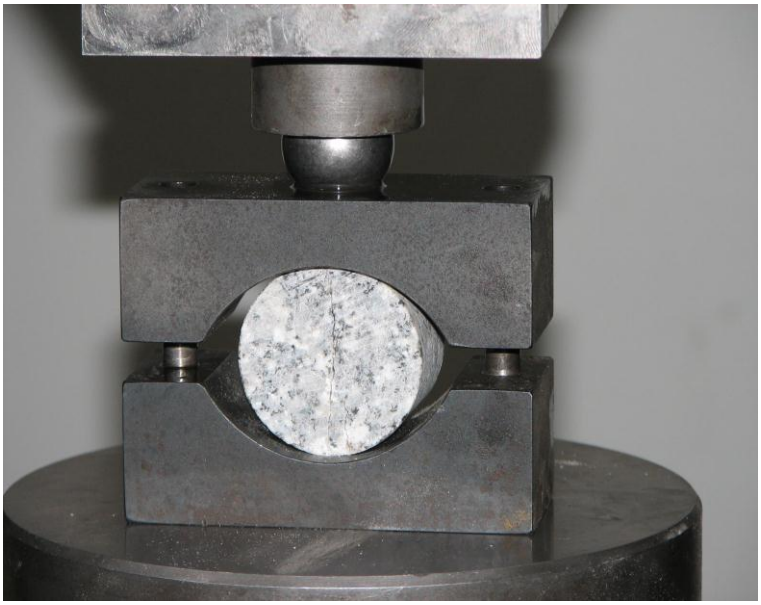

Figure 7: Indirect Brazilian tensile strength test

(Source: Private communication with Dr H. Yilmaz at the University of the Witwatersrand, Johannesburg)

This test was repeated six times, each time the University of the Witwatersrand used a sample with a diameter of 42 mm and a length of 27.9 mm. The length to diameter ratio was therefore 0.7. A loading rate of 0.4 kN/s was applied and the failure load was recorded during each test. An average failure load of 19.07 ± 2.45 kN was achieved and this was used to compute the tensile strength with the following equation from Potyondy and Cundall (2004):

$$\sigma_t = \frac{F_f}{\pi R t}, \tag{30}$$

where F_f is the peak force acting on the platens and R and t are the radius and the thickness of the cylindrical disk. The average tensile strength of Paarl granite was computed as 10.06 MPa. From Figure 7 it can be seen that the splitting plane is vertical or in the direction of compression.

3.2 Uniaxial compressive strength test

The uniaxial compression test is the most common form of direct strength testing for rock. A cylindrical specimen is used during this test, placed between two platens. These platens are made from steel and the diameter of the platens is usually equal to the diameter of the specimen or 2 mm wider and the thickness is at least 15 mm or the specimen diameter divided by 3. The platen on the upper end of the specimen is moved downwards slowly at a certain loading rate. The cylindrical specimen should have a height to diameter ratio of 2.0 - 2.5 and the diameter of the specimen should be between 1.5 and 4 inches (Hawkes & Mellor, 1970). The cylindrical granite specimen can be seen in Figure 8 with electrical resistance strain gauges.

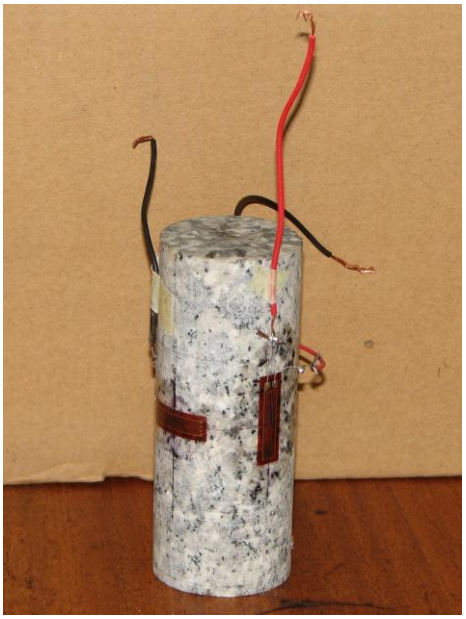

Figure 8: Uniaxial compressive strength test specimen

(Source: Private communication with Dr H. Yilmaz at the University of the Witwatersrand, Johannesburg)

The specimens used during the uniaxial tests, performed at the University of the Witwatersrand, had a diameter of 42 mm and a length to diameter ratio of 2.5. These specimens were therefore longer than the ones used during the Brazilian test. A loading rate of 1 kN/s was applied on the upper platen and the average failure load, of five tests that were performed, was 274.2 kN. The uniaxial compressive strength can then be calculated as follows:

$$q_u = \frac{F}{\pi R^2}, \tag{31}$$

where F is the failure load and R is the radius of the specimen. An average q_u of 198.29 MPa was achieved during the uniaxial compressive tests as can be seen from the stress-strain curve in Figure 9. On the left of the figure, the axial stress is plotted against the axial strain, which is in compression and on the right of the figure the lateral stress is plotted against the axial strain, which is in tension. This test was repeated five times and stress-strain curves of the other tests as well as graphs of the Young's modulus and the Poisson's ratio versus the stress curve can be seen in Appendix C.

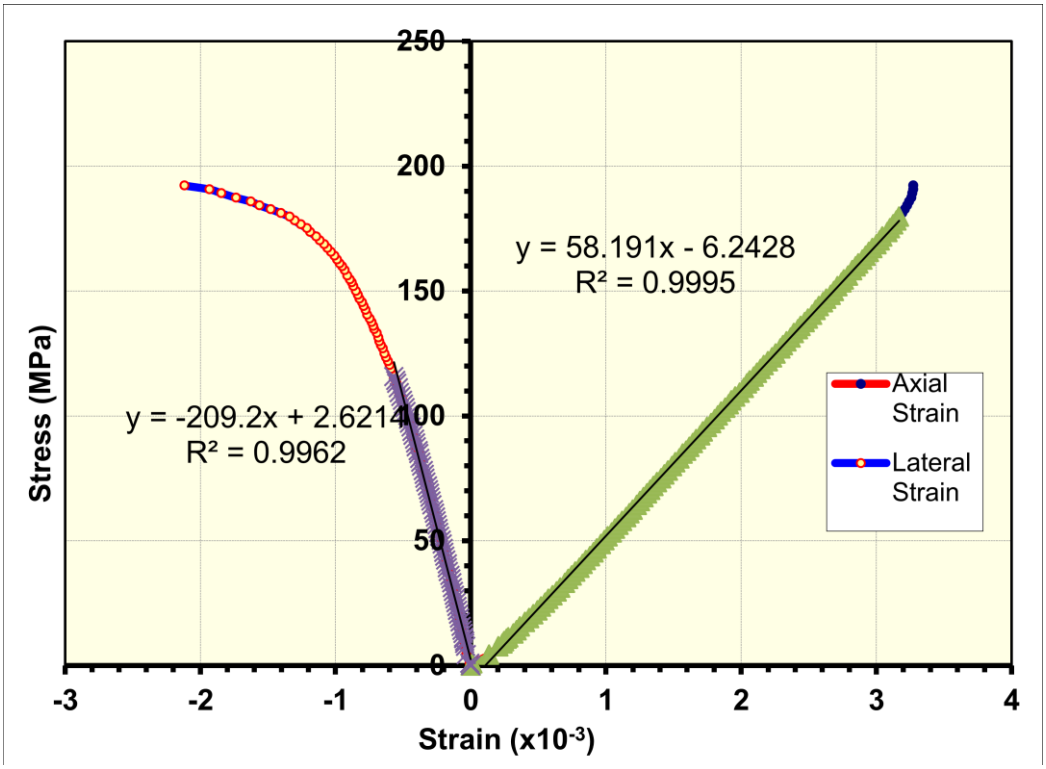

Figure 9: Stress-strain curve of uniaxial compressive strength test

(Source: Private communication with Dr H. Yilmaz at the University of the Witwatersrand, Johannesburg)

The Young's modulus and Poisson's ratio can also be computed from the stress and strain increments between the start and at a point at which one-half of the peak stress has been obtained. The Young's modulus is computed by

$$E = \frac{\Delta\sigma_y}{\Delta\varepsilon_y} \tag{32}$$

where $\Delta\sigma_y$ is the incremental axial stress and $\Delta\varepsilon_y$ is the incremental axial strain. The Poisson's ratio is computed by

$$v = -\frac{\Delta\varepsilon_x}{\Delta\varepsilon_y} = -\frac{\frac{1}{2}\left(\Delta\varepsilon_x + \Delta\varepsilon_z\right)}{\Delta\varepsilon_y} = \frac{1}{2}\left(1 - \frac{\Delta\varepsilon_v}{\Delta\varepsilon_y}\right) \tag{33}$$

In this equation the average of the two lateral strains is used to approximate the lateral strain and the volumetric strain is $\Delta\varepsilon_v = \Delta\varepsilon_x + \Delta\varepsilon_y + \Delta\varepsilon_z$. These relations are valid for constant lateral stress during the test (Potyondy and Cundall, 2004). An average Young's modulus of 58.48 GPa and an average Poisson's ratio of 0.32 were computed from the uniaxial compressive tests conducted.

3.3 Triaxial compressive strength test

According to Vogler & Kovari (1978) the apparatus for the triaxial compressive strength test consists of a triaxial cell, a loading device and a device for generating confining pressure. The specimen is placed in the triaxial cell body in order to apply the confining pressure and steel plates are placed parallel at both ends of the specimen. A suitable machine is used to apply, control and measure the axial load on the specimen. The axial load and confining pressure must be increased simultaneously and in such a way that axial stress and confining pressure is approximately equal, until the predetermined test level for the confining pressure is reached. Then the axial load on the specimen will be increased continuously at a constant stress rate and the failure will occur within 5 to 15 minutes of loading. The test specimens, before and after the test, can be seen in Figure 10.

Figure 10: Triaxial compressive strength specimen

(Source: Private communication with Dr H. Yilmaz at the University of the Witwatersrand, Johannesburg)

The test specimens used during the triaxial tests at the University of the Witwatersrand had the same dimensions as those used during the uniaxial compressive strength test. Twenty tests were performed

at a loading rate of 1-1.5 kN/s using four different confinements ranging from 2 to 15 MPa. The average failure load at the different confinements ranged from 306 to 533 MPa and therefore the average triaxial compressive strength also ranged between 221 and 385 MPa.

3.4 The tilt test

The tilt test is an easy method to determine the base friction angle of a rock specimen. For the base friction angle to be representative of the whole rock surface, the largest possible surface area should be tested and the tilting table provides a large enough sliding surface to accommodate this. The surface conditions, such as cutting grooves and polishing for instance, will have a large influence on this test. The apparatus used for the tilt test consists of a tilting table, devices to measure the angle of tilt and a device to control the tilting table, as seen in Figure 11.

Figure 11: The tilt test

(Source: Private communication with Dr H. Yilmaz at the University of the Witwatersrand, Johannesburg)

To perform the tilt test, the bottom rock specimen is placed on the horizontal table top. The bottom specimen provides the lower interface of the sliding surface. The bottom specimen is then prevented from sliding, rotating or shifting by using moulding clay or the specimen handling jig to secure the specimen. The next step is then placing the top specimen on the bottom specimen in such a way that the contact surfaces form the interfaces of the sliding surfaces. The initial angle of the tilting table top is recorded, which is close to zero, and both angle measuring devices are checked and the average angle is calculated. Afterwards the top platform of the lifting device is slowly lowered and the table top tilts. Tilting is continued until sliding just starts at the contact interface and then further lowering of the lifting device is stopped immediately. The angle of tilt is measured and recorded as well as read off from both angle measuring devices. The average base friction angle is then calculated, which is the friction angle between two flat surfaces when one surface slides over the other surface. Afterwards the tested

specimens are removed and the test area is cleaned. (Procedure for Determining the Angle of Basic Friction (Static) Using a Tilting Table Test, [S.a.]). Five tilt tests were performed and the average base friction angle was computed to be 33.2°. This friction angle is used in the simulation of rock cutting as the internal friction in the rock specimen.

3.5 Linear rock cutting tests

According to Rizo (2010) the purpose of the linear cutting test is to register the horizontal force acting on the cutting tool and to observe the failure behaviour of the rock. He concluded that a ductile failure mode at shallow depths and brittle failure mode at greater depths will be observed. In this section a few examples of linear rock cutting tests, found in the literature, will be described.

The linear cutting test, used by Bilgin et al. (2006), was carried out with a cutting rig using a S-35/80H conical pick with a gauge of 80 mm, a flange diameter of 64 mm, a shank diameter of 35 mm, a tip diameter of 22 mm and a primary tip angle of 80°. This cutting rig, as seen in Figure 12, can accommodate block rock samples up to 0.7 x 0.7 x 1 m^3. Throughout these cutting tests the following conditions were kept constant: an attack angle of 55°, skew and tilt angles of 0° and a cutting speed of 0.127 m/s. A data acquisition system was used to record the tool forces in three different directions and the sampling rate was 2000 Hz. A mechanical device was used to keep the depth of cut constant, which was changed during this study from 3 to 10 mm. The peak and mean normal and cutting forces as well as the yield were recorded in each case. A variety of rocks, with different properties, were used for cutting and each cut was replicated about 3 or 4 times.

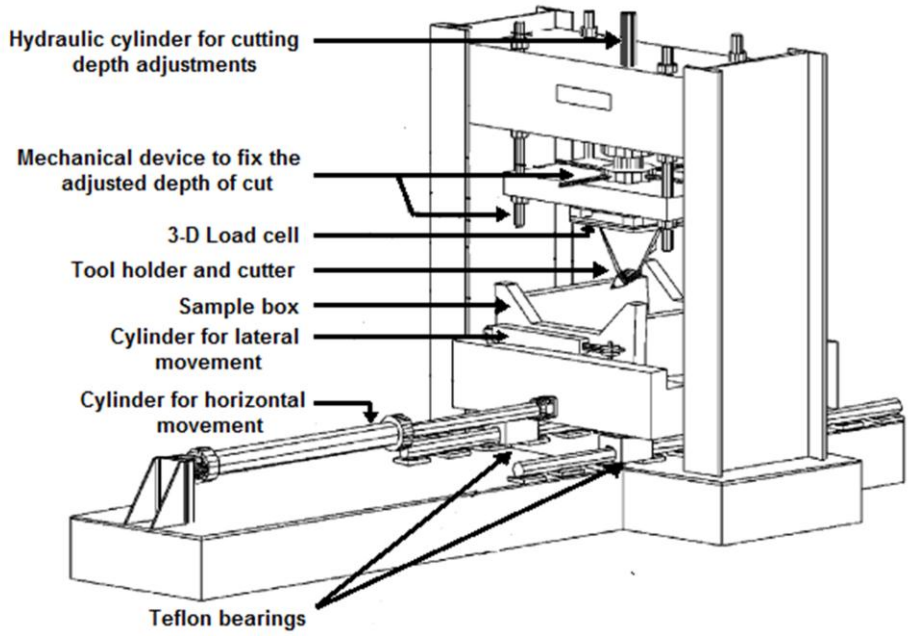

Figure 12: Schematic drawing of a linear rock cutting machine

(Adapted from Bilgin et al., 2006 and Balci & Bilgin, 2007)

Balci & Bilgin (2007) used a small-scale linear rock cutting test to measure the cuttability of different rock types. During this test a small rock sample of 20 x 10x 10 cm was fixed in a table of a shaping machine and a tungsten carbon chisel pick was used for cutting. The chisel pick had a rake angle of -5°, a clearance angle of 5°, a tool width of 12.7 mm and a cutting depth of 5 mm. A force dynamometer was used to record the cutting forces in three orthogonal directions.

A laboratory cutting test was also performed at Element Six in Johannesburg with a vertical bore machine setup as seen in Figure 13. The rock sample to be tested was Paarl granite and a chamfered button-shaped cutter was used with a rake angle of -20° and a neutral approach angle. The rock sample had an octagonal shape and was turned at 30 rpm while the cutting tool moved in a linear way. The feed rate of the cutting tool was 3 – 8 mm/rev depending on the wear scar width. A very shallow cutting depth of 250 micron was used and water was used as a coolant on the cutting tool. Forces were measured and recorded parallel to the cutting tool movement, perpendicular to the sample surface and forces acting sideways on the cutting tool. One sample could be tested a few times by flipping the sample over without having effects of neighbouring wear scars affecting the measurements.

Figure 13: Vertical bore machine

(Source: Private communication at Element Six, Johannesburg, 2011)

CHAPTER 4:

DISCRETE ELEMENT SIMULATION

A rectangular parallelepiped specimen representing Paarl granite was simulated with the material-genesis procedure described in chapter 2, using a set of micro-properties. These micro-properties have to be adapted to fit the macro-properties obtained from laboratory tests in order to prove the validity of the model. The same procedure was followed for the simulation of a Sandstone-2 specimen.

4.1 Selecting micro-properties

The difficulty in using DEM to simulate rock is that the input properties cannot generally be derived directly from the results of laboratory tests. These properties are unknown and a relation between the model properties and the measured material properties has to be found. This is done through a calibration process.

Calibration is usually performed for four tuning parameters, which are the macroscopic material properties, namely Young's modulus of the particle, Poisson's ratio, as well as tensile and shear strength for particle bonds. The microscopic parameters are all the constitutive model parameters governing the interaction between a pair of particles, namely the normal and tangential stiffness, the interface strengths in the normal and tangential directions, the Coulomb friction coefficient and the contact damping coefficient. The final micro-properties used throughout the simulations for Paarl granite can be seen in Table 1 and those for Sandstone-2 in Table 2.

Table 1: Model micro-properties for Paarl granite

Grain properties		**Cement properties**	
Density (ρ)	2630 kg/m^3		
Radius ratio (R_{max}/R_{min})	1.66	Radius multiplier ($\bar{\lambda}$)	1
Young's modulus (E_c)	63 GPa	Young's modulus ($\bar{E}_c$)	63 GPa
Ratio of normal to shear stiffness (k_n / k_s)	2.5	Ratio of normal to shear stiffness ($\bar{k}_n / \bar{k}_s$)	2.5
Friction coefficient (μ)	0.5	Tensile strength ($\bar{\sigma}_c$)	170.1 ± 40 MPa
		Shear strength ($\bar{\tau}_c$)	170.1 ± 40 MPa

Table 2: Model micro-properties for Sandstone-2

Grain properties		Cement properties	
Density (ρ)	2670 kg/m^3		
Radius ratio (R_{max}/R_{min})	1.66	Radius multiplier ($\bar{\lambda}$)	1
Young's modulus (E_c) - Sample with 0.401 mm diameter particles - Sample with 0.802 mm diameter particles	 30 GPa 33 GPa	Young's modulus ($\bar{E}_c$) - Sample with 0.401 mm diameter particles - Sample with 0.802 mm diameter particles	 30 GPa 33 GPa
Ratio of normal to shear stiffness (k_n / k_s)	2.5	Ratio of normal to shear stiffness ($\bar{k}_n / \bar{k}_s$)	2.5
Friction coefficient (μ)	0.5	Tensile strength ($\bar{\sigma}_c$) - Sample with 0.401 mm diameter particles - Sample with 0.802 mm diameter particles	 149.0 ± 40 MPa 169.5 ± 40 MPa
		Shear strength ($\bar{\tau}_c$) - Sample with 0.401 mm diameter particles - Sample with 0.802 mm diameter particles	 149.0 ± 40 MPa 169.5 ± 40 MPa

These micro-properties are chosen to match the macroscopic material properties of Paarl granite and Sandstone-2. The micro-properties used by Potyondy and Cundall (2004), to simulate Lac du Bonnet granite was consulted, since its macro-properties showed a resemblance of those collected for Paarl granite. During the calibration process these micro-properties were then altered through trial-and-error until the macro-properties matched those of Paarl granite and Sandstone-2, respectively.

According to Potyondy and Cundall (2004), the radius ratio should be greater than 1 to produce a random isotropic packing, since the packing will tend towards a crystalline packing as the ratio approaches 1. A uniform packing will exhibit anisotropic macro-properties which is not representative of granite. The radius multiplier is chosen to be 1, to produce a more dense packing. As the radius multiplier approaches 0, the material behaviour represents that of a granular material.

The grain and cement Young's moduli are chosen to match the material Young's moduli and the ratio of normal to shear stiffness of the grain and cement are chosen to match the Poisson's ratio. The only reason why the moduli and ratio of normal to shear stiffness of the grain and cement are chosen to be equal is to reduce the number of free parameters during the simulation.

The tensile and shear strength of the cement are set equal to each other so that both tensile and shear microfailures may be possible and also to reduce variables during calibration. According to Potyondy & Cundall (2004), cracking does not localize onto a single macrofracture plane under macroscopic extensile loading if microtensile failure is excluded. Since this mechanism does occur in granite, microtensile failure is also allowed to occur in the granite as well as the Sandstone-2 models. The values of the tensile and shear strengths are chosen to match the unconfined compressive strength. With an increase in the tensile and shear strength, the unconfined compressive strength also increases.

4.2 Macro-properties of PFC3D™ model

The micro-properties in Table 1 and Table 2 are used to produce Paarl granite and Sandstone-2 material respectively in PFC3D™. Since the depth of cut during the linear rock cutting test, performed at Element Six in Johannesburg, is just 0.5 mm, which is quite shallow, the average particle size was chosen to be small enough so that some whole particles would be removed during this test. Therefore the maximum particle radius was chosen to be 0.25 mm and the minimum radius was 0.15 mm, which led to an average particle of 0.4 mm in diameter. A rectangular parallelepiped specimen with dimensions of 25 x 12.5 x 25 mm^3, containing approximately 150,870 particles, was generated by a random-number generator. The specimen was made small to limit the number of particles and consequently decrease computation time. A specimen with larger particles was also simulated to look at the influence of larger particles on the rock cutting process. In this specimen the maximum particle radius was chosen to be 0.5 mm and the minimum radius was 0.3 mm, which led to an average particle diameter of 0.8 mm. This rectangular parallelepiped specimen had the same dimensions as described in the above paragraph, but the number of particles was reduced to just 18,948 because of the increase in the radii. The computation time was also decreased accordingly. A cylindrical specimen was cut out of these original rectangular parallelepiped specimens and used for the uniaxial, triaxial and Brazilian tests, from which the macro-properties were obtained.

During these tests, the specimen is loaded by frictionless walls. The top and bottom walls act as loading platens and the velocity of the cylindrical lateral wall is controlled by a servo mechanism that maintains a specified confining stress. The loading platens are treated as rigid walls. The laboratory uniaxial and Brazilian tests are unconfined and therefore their specified confining stress is set equal to a value just larger than zero, while the triaxial test was performed at a confinements of 2 MPa. The normal stiffness of the lateral wall is set equal to a fraction of 0.001 of the average particle normal stiffness to simulate a soft confinement. The normal stiffness of the loading platens is set equal to the average normal particle stiffness and the test is run under displacement control such that the platens move toward one another at a constant rate. To ensure that the test conditions remain quasi-static, the platens were loaded at very low velocities. In these tests a loading velocity of 0.05 m/s was used. During the uniaxial test the

velocity of the bottom platen is set to zero, while the triaxial and Brazilian test uses both loading platens.

According to Potyondy and Cundall (2004) the advantage of using walls around the specimen is that the alignment of boundary particles produces a uniform force transmission from the walls to the specimen. The disadvantage is that the boundary particles are not fully representative of the internal microstructure when aligned with these walls. Since the fine grains of granite doesn't allow too much deformation, the cylindrical lateral wall, with a low normal stiffness, around the specimen won't influence the test to a great extent.

The uniaxial and triaxial tests were performed using both a rectangular parallelepiped specimen with all six walls, as well as a cylindrical specimen cut out of the original specimen with a lateral cylindrical wall around it, as well as a top and bottom plate. The Brazilian test was performed with a cylinder surrounded by the six walls and just before the actual test begins, the y-walls and z-walls are moved a small distance outwards so that only the x-walls are in contact with the cylinder and they act as loading platens. These test specimens can be seen in Figure 14 and the results were compared and discussed in Chapter 5.

The setup and procedure for these three tests are very similar with the only difference in the loading platens and confinement. The simulations of these tests begin by computing the initial stress state and determining the servo gain parameters for axial and lateral motion. Cycling is performed until the requested stresses are obtained within a given tolerance and servo-control is also used to adjust the wall velocity to reduce the difference between requested and measured stresses. The servo-control acts as a switch and when set equal to one, the top and bottom walls are controlled additionally. The mathematics of the initial stress computation and servo-control can be found in Appendix A4.

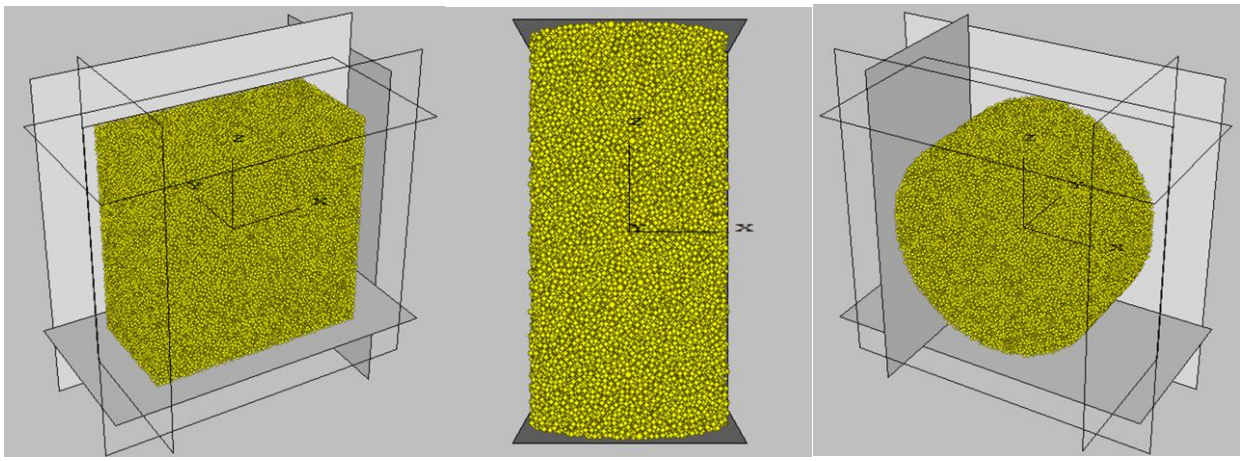

Figure 14: Test specimens for uniaxial, triaxial and Brazilian tests

From left to right: Rectangular parallelepiped specimen for uniaxial and triaxial tests; cylindrical specimen for uniaxial and triaxial tests; cylindrical specimen for Brazilian test.

After the requested stresses are obtained, the servo switch is set to 0 to release the top and bottom platens from servo-control and then the velocities of the top and bottom platens are specified to test the specimen. The servo control keeps the confining stress constant while the velocities of the top and bottom platens are ramped up in a controlled fashion. The models are monitored during the tests by recording the histories of the following variables:

- The mean confining stress (σ_c) which is equal to the radial stress.
- The axial deviatoric stress (σ_d), which is defined as $(\sigma_a - \sigma_c)$, where σ_a is the axial stress.
- The axial strain (ε_a) which is the current axial strain minus the original axial strain.
- The volumetric strain (ε_v), which is defined as $(\varepsilon_v = \varepsilon_x + \varepsilon_y + \varepsilon_z)$.
- The stress on the top plate, for the uniaxial test.
- The axial force, for the Brazilian test.

The tests are then run by accelerating the loading platens until they reach a constant velocity and load/unload steps are carried out until the specimen fails. The macro-properties of the simulated material can be analysed by the stress-strain curves obtained in PFC3D™ by monitoring the normal stress and strain in the axial direction for the uniaxial and triaxial tests. The elastic properties, namely Young's modulus and Poisson's ratio, are determined from the curves of the uniaxial test. An axial force-strain curve is obtained for the Brazilian test, from which the Brazilian tensile stress is computed.

4.3 Rock cutting simulation

4.3.1 Cutting with a point-attack pick

Su & Akcin (2011) modelled rock cutting, using PFC3D™, by positioning a perfectly sharp conical pick through the left side of the rock specimen. The rock specimen used was Sandstone-2 with a uniaxial compressive strength of 173.7 MPa. Cutting depths of 3, 6 and 9 mm were used and the pick was advanced at a low velocity of 0.3 m/s over a cutting distance of 20 mm. An attack angle of 57°, a tip angle of 80°, a clearance angle of 17°, a rake angle of -7° and a friction angle of 8.5° between the rock and the pick were used throughout the simulation of Su & Akcin (2011).

The simulation of Su & Akcin (2011) was repeated in the current study, with changes made to some parameters. Since a small rock sample of 25 x 12.5 x 25 mm^3 was calibrated, the cutting depth had to be shallow to avoid cracking throughout the sample and breaking it. A non-linear relationship between the cutting forces and cutting depth of the data found in Su & Akcin (2011) was illustrated in section 2.7 and therefore the cutting force at 0.5 mm of cutting depth was estimated through extrapolation. The simulated point-attack pick, consisted of two cylindrical walls, as can be seen in Figure 15a, with the tool parameters as described above. The dimensions of the pick were not specified in the study of Su &

Akcin (2011) and therefore the tip diameter was chosen to be just less than the width of the rock specimen. These walls were treated as rigid, as in Su & Akcin (2011), with high stiffnesses (1 x 10^9 Pa/m) to insure that there is no wear on the pick and only the rock material is damaged. At the beginning of the simulation the pick was placed at the left side of the rock sample and the top wall of the sample was deleted. Since these simulations took up to 5 days to complete, because of the large amount of computation steps, the cutting velocity in this study was increased to 5 m/s.

Another cutting test using a point-attack pick was simulated in this study, namely the test of Bilgin et al. (2006). The full-scale test was described in section 3.5 and it was numerically simulated by using the calibrated Sandstone-2 sample and a conical wall representing the tip of the pick. The tip diameter was specified as 22 mm and therefore it was almost twice as wide as the rock specimen. The cutting forces and cutting depths in Bilgin et al. (2006) also followed a non-linear relationship as illustrated in section 2.7 and a cutting depth of 0.5 mm could be used, instead of 5 mm as described earlier. Since the dimensions of the pick given in Bilgin et al. (2006) was very large compared to the simulated rock sample, the pick was simulated as a conical wall representing the tip of the real point-attack pick. The tip of the simulated point-attack can be seen in Figure 15b, also showing the parameters used for simulation. The wall was also treated as rigid and a high stiffness was given to it to ensure that only the rock sample was damaged during the simulation. The pick was placed at the left side of the rock sample and the top wall of the sample was deleted at the beginning of the simulation and it was advanced at 5 m/s. This velocity was again used to reduce the duration of simulations.

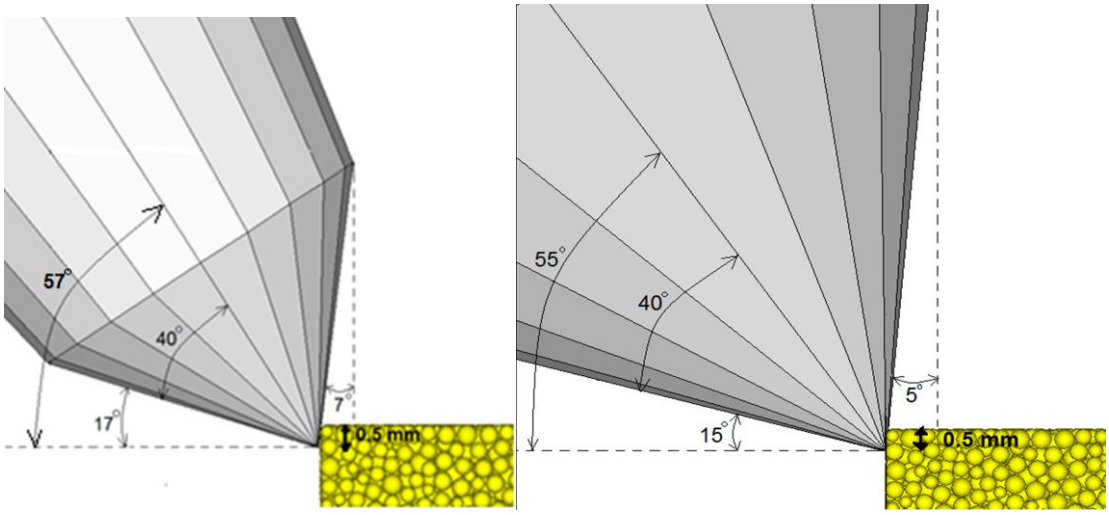

Figure 15: Numerically simulated point-attack picks
(a) Su & Akcin (2011) parameters; (b) Bilgin et al. (2006) parameters

The influence of wear on cutting forces was also considered by simulating the cutting processes, as described above, with point-attack picks which tips have been cut off at diameters ranging from 0.5 to 1.5 mm. A wear flat was therefore introduced. The blunt point-attack picks with the parameters of Su

& Akcin (2011) can be seen in Figure 16. The point-attack picks representing those of Bilgin et al. (2006) have the same tip shape and are therefore not shown here.

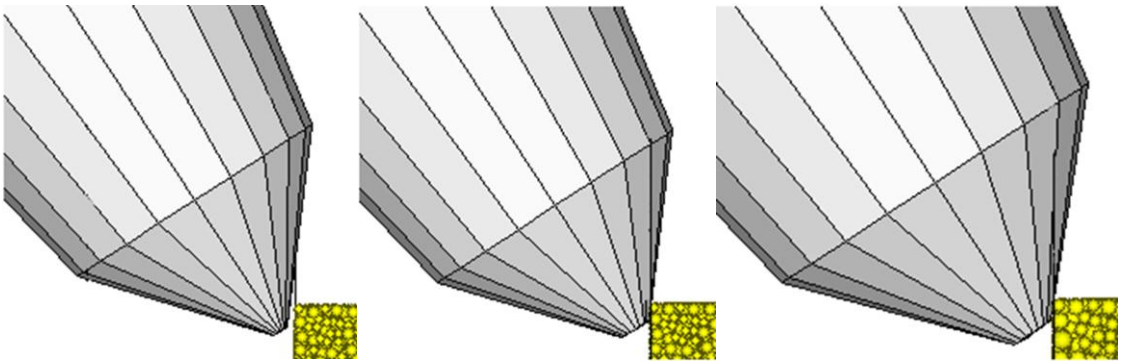

(a) (b) (c)

Figure 16: Numerically simulated point-attack picks with blunt tips

(a) 0.5 mm diameter cut off; (b) 1 mm diameter cut off; (c) 1.5 mm diameter cut off

4.3.2 Cutting with a chisel tool

Balci & Bilgin (2007) used a chisel shaped tool to perform a small-scale rock cutting test as described in section 3.5. These researchers did the unrelieved cutting test for Sandstone-2 only at 5 mm cutting depth and therefore a relationship between the cutting force and a cutting depth of 0.5 mm couldn't be made for the chisel shaped tool since only one data point was available. The simulation was therefore only done at 5 mm depth of cut although it might cause problems since the simulated rock sample is so small and cracks might develop throughout the sample causing it to break. Although the chisel tool described in section 3.5 had a tool width of 12.7 mm, the simulated chisel tool was 12.5 mm in width since the rock sample had the same width. The tool consisted of 10 walls with the rake angle and clearance angle as seen in Figure 17. The walls had high stiffnesses of 1 x 10^9 Pa/m and were treated as rigid just like in the previous cases. The chisel tool was placed at the left side of the rock sample and the top wall of the sample was deleted before the chisel tool was advanced at 5 m/s.

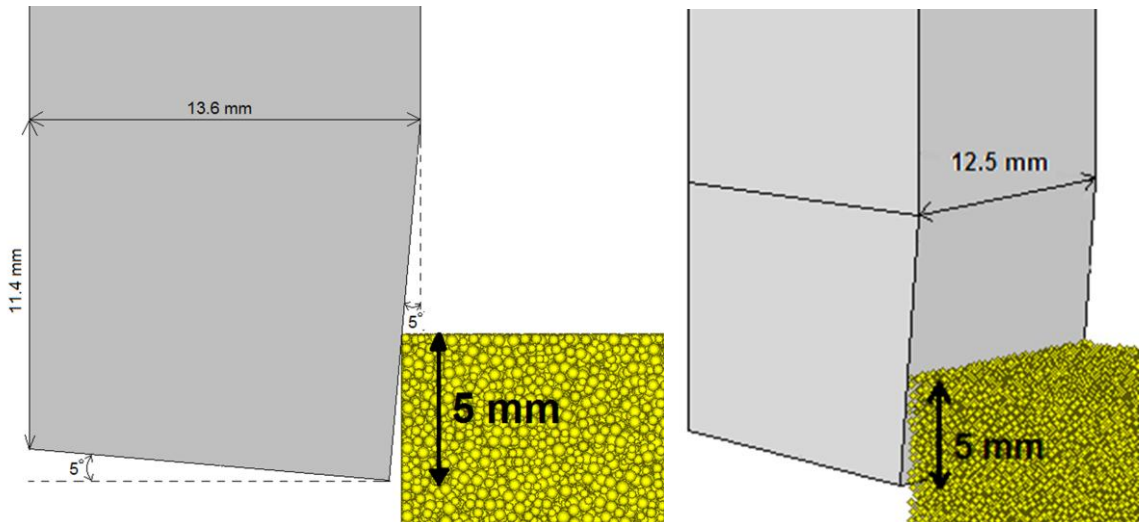

Figure 17: Numerically simulated chisel shaped pick

4.3.3 Cutting with a button-shaped cutter

The vertical bore cutting test that was done at Element Six, as described in section 3.5, was simulated during this study. The cutting tool was first modelled as a sharp button-shaped cutter and then it was modelled as a chamfered conical cutter to represent wear on the cutter. The cutting tool consisted out of three cylindrical walls, as seen in Figure 18. These walls were treated as rigid, with stiffnesses high enough to bring about breakage of the rock, without any damage to the tool itself. Since a very small rectangular shaped rock sample was simulated, the dimensions of the cutting tool were chosen in accordance. The larger part of the tool had a diameter of 8 mm and it was chamfered 0.4x45°. The chamfered tool tip was 7.2 mm in diameter. Although the cutting depth during the experimental test was only 250 µm, a cutting depth of 0.5 mm was used during the numerical simulation, since the average particle radius was 0.401 mm and particles could not be sliced in half.

In this numerical simulation two linear overlapping cuts were made, which only represented a very small piece of the real octagonal shaped block and therefore the rotation of the block was ignored during this simulation. For the first cut, the sharp cutting tool was positioned at the left side of the Paarl granite specimen with a rake angle of -20°. At the beginning of the simulation the top wall of the specimen was removed and the cutting tool was advanced at a velocity of 5 m/s over a cutting distance of 20 mm. For the second cut, the chamfered cutting tool was positioned at the left side of the rock specimen, but this time it was shifted 3 mm to the right to overlap the previous cut with *x* mm. The cutting tool was then again advanced at a velocity of 5 m/s over a cutting distance of 20 mm.

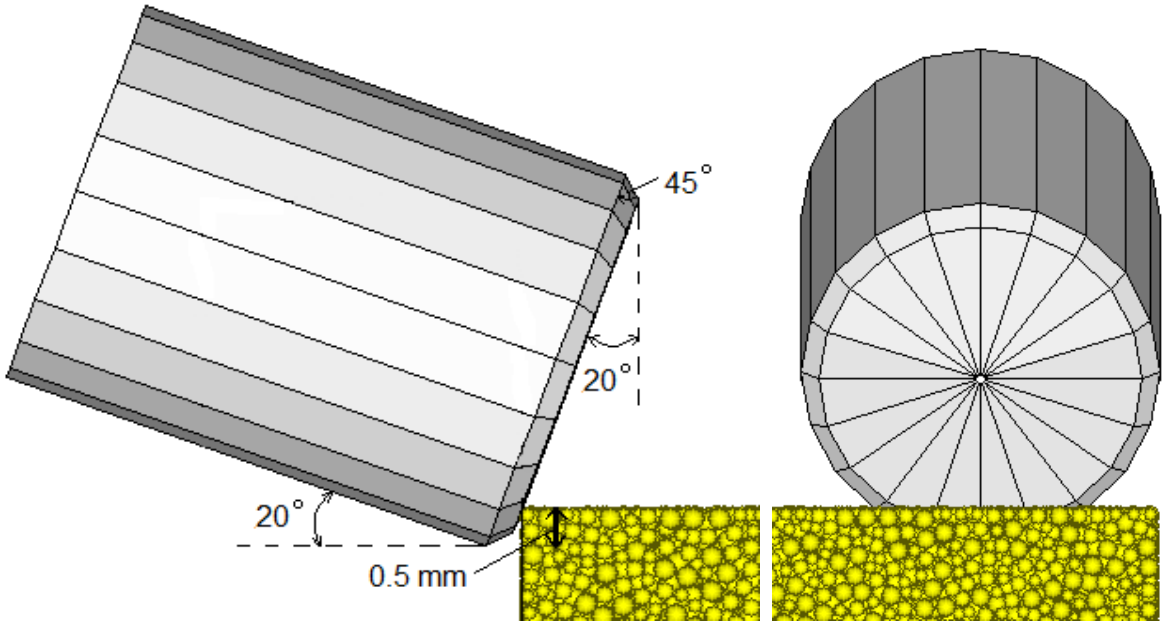

Figure 18: Numerically simulated button-shaped cutter

During all four of the linear rock cutting simulations described in this section, the six walls around the rock specimen served as the boundaries. A vacuum was also placed around the cutting tool and the rock specimen, as a whole, with a specific function to delete particles beyond this point. This was done to decrease computation time. During the rock cutting simulations the three orthogonal forces, namely the forces in the x-, y- and z-direction were measured and the histories were recorded, as well as the number of micro-cracks formed. The micro-cracks induced by shear and normal failure were also visually monitored during the simulations. The linear rock cutting tests with point-attack picks were repeated at cutting depths of 0.5, 1.5 and 3 mm, while those with chisel-shaped picks were repeated at cutting depths of 0.5 and 5 mm and the linear cutting tests with the button-shaped cutters were only done at a cutting depth of 0.5 mm.

CHAPTER 5:

PFC3D™ MATERIAL RESPONSE OF CALIBRATION TESTS

The different calibration tests were simulated as described in Chapter 4 and the results will be discussed here. It should be noted that the bond breakages during these tests were tracked as cracks, which are displayed as black or red cylinders in the figures. The thickness of these cylinders equals the gap between the initially bonded particles. The colours represent different parallel-bond failure, the black cylinders depict tension-induced parallel-bond failure and the red cylinders depict shear-induced parallel-bond failure. Therefore if the bond tensile strength was exceeded, black cylinders were used and if the bond shear strength was exceeded, red cylinders were used to represent the cracks.

After a few minutes into the uniaxial and triaxial compressive strength tests, a few cracks formed and they were distributed throughout the specimen. These cracks formed from tension-induced as well as shear-induced parallel-bond failure and can be seen in the different specimens in Figure 19. The crack-initiation stress was the onset of this early cracking throughout the specimen. More cracks were visible as the failure load was approached.

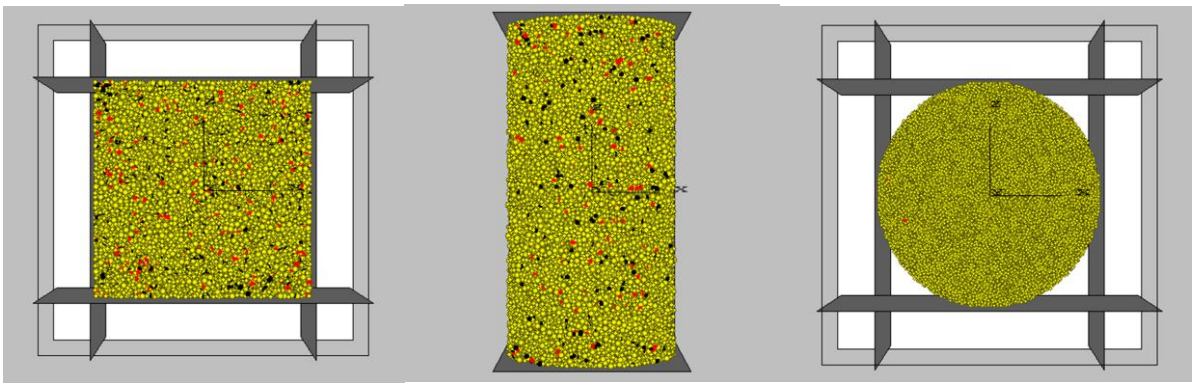

Figure 19: Crack distributions at the start of the tests

From left to right: Crack distribution in rectangular parallelepiped specimen for uniaxial and triaxial tests; cylindrical specimen for uniaxial and triaxial tests; cylindrical specimen for Brazilian test.

Figure 20 shows the crack distributions after failure has occurred for each specimen. The crack distribution in the rectangular parallelepiped specimen was similar for both the uniaxial and triaxial tests and was more concentrated near the walls with fewer cracks in the middle of the specimen. The

number of tension-induced and shear-induced parallel-bond failures is almost equal, showing that both the tensile and shear bond strength were exceeded during these tests. When looking at the crack distribution in the cylindrical specimen for the uniaxial and the triaxial tests, it can be seen that most of the cracks occur at the top and a few at the bottom of the specimen, since this is where the load is applied. It can also be observed that there is a diagonal plane of failure in the cylindrical specimen. When compared to Figure 10, showing the laboratory triaxial test specimens after failure, this type of failure plane is expected. During the Brazilian test simulation, the load was applied to the left and right walls and as seen in Figure 20, the cracks are concentrated near these walls. The failure plane is therefore horizontal, which is the direction of the applied load. When comparing this figure to Figure 7, showing the laboratory Brazilian test specimen after failure, it can be seen that the laboratory Brazilian test also induced a failure plane in the direction of applied load, which was vertical in that case.

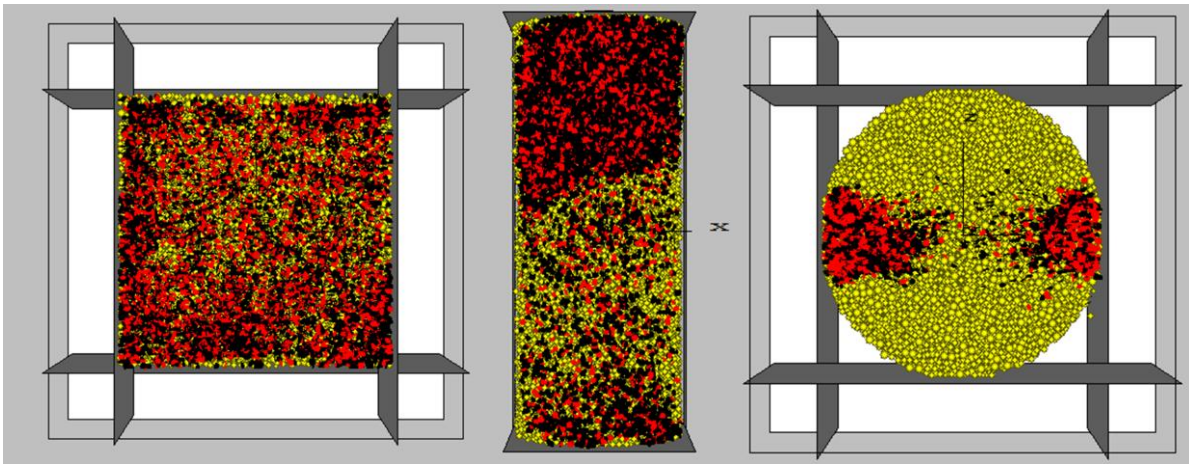

Figure 20: Crack distributions after failure

From left to right: Rectangular parallelepiped specimen for uniaxial and triaxial tests; cylindrical specimen for uniaxial and triaxial tests; cylindrical specimen for Brazilian test.

Although the shear and tensile strength of the parallel-bonds in the test specimens were set equal to each other to allow both tensile and shear microfailures, as described in section 4.1, real granite and Sandstone-2 have a lower tensile strength than compressive strength. Real granite and Sandstone-2 are brittle and will most likely fail under tension before they fail under compression. Therefore, the cracks formed by tension-induced parallel-bond failure would have been more if the tensile strength was lower in the numerical simulation.

A typical stress-strain curve, with two load/unload loops, for the uniaxial and triaxial tests are shown in Figure 21. The axial stress is plotted against the axial strain and this curve shows a large elastic region after which the material fails. This curve corresponds with the curve in Figure 9 from the triaxial compressive strength test performed in the laboratory. The uniaxial compressive strength test and triaxial compressive strength performed on Sandstone-2 will give similar stress-strain curves.

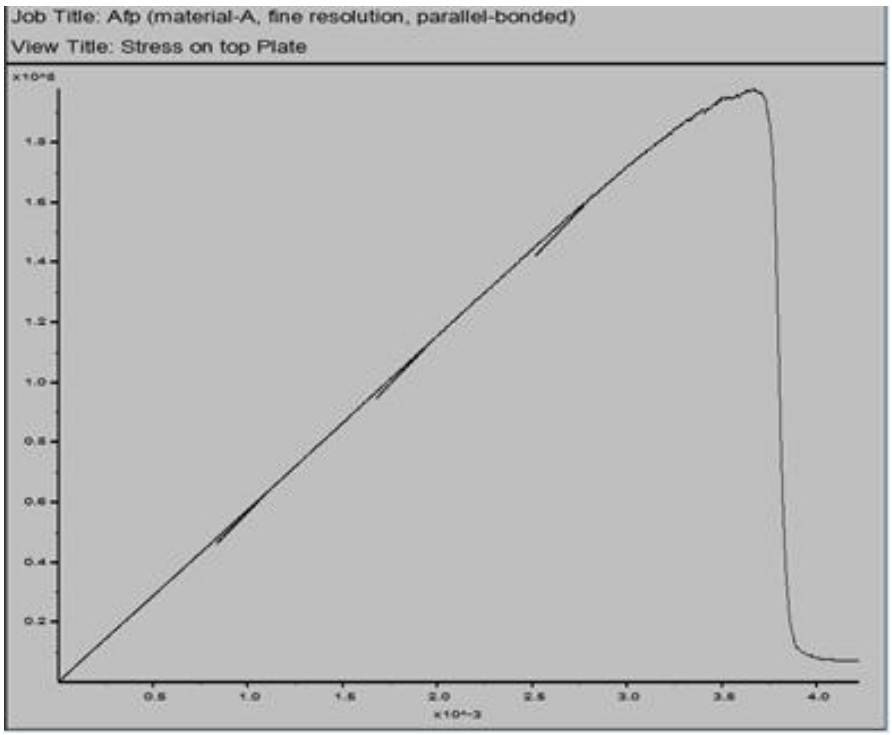

Figure 21: Typical stress-strain curve for Paarl granite

The axial force during the Brazilian test was plotted against the axial strain and the general curve is shown in Figure 22. The peak force in this curve is used to calculate the Brazilian tensile strength of the specimen.

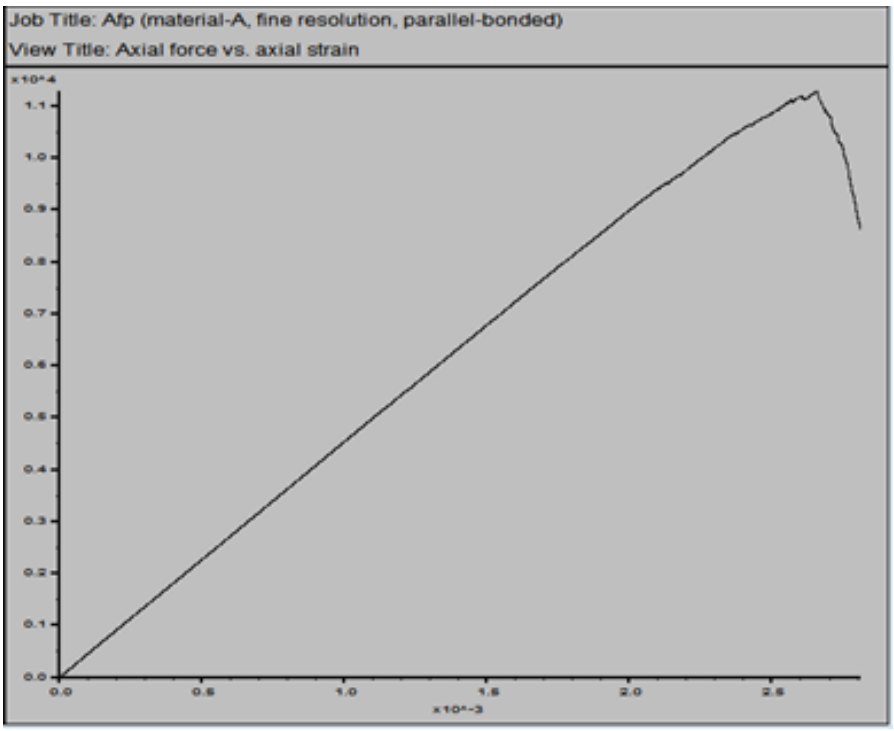

Figure 22: Force-strain curve for Brazilian Test of Paarl granite

5.1 Material response of Paarl granite

For the calibration of Paarl granite, the rectangular parallelepiped and cylindrical specimens were simulated with different values of R_{min}, while the rest of the micro-properties were kept constant. The average particle diameters ranged from 3.205 to 0.401 mm. The cylindrical specimens for the uniaxial and triaxial compressive strength tests had length to diameter ratios equal to 2.5 and the cylindrical specimen of the Brazilian test had a length to diameter ratio equal to 0.7.

Each specimen, in the different particle size ranges, was subjected to a uniaxial and triaxial compressive strength test as well as a Brazilian test. The results are displayed in Table 3. Since the amount of particles across the area of the specimen increases as the size of the particles decreases, more representative responses of the tests are extracted from specimens with smaller particles.

From Table 3 and Table 4 it is evident that the influence of particle size on the macro-properties is very significant and cannot be ignored. All the macro-properties are influenced by particle size. The unconfined compressive strength (q_u) for the cylindrical specimen increased from 70.69 to 198.1 MPa with a decrease in particle size from 3.205 to 0.401 mm. Young's modulus (E) is also clearly dependent on particle size and increased from 20.0 to 58.18 GPa for the cylindrical specimen. According to Potyondy and Cundall (2004), Poisson's ratio (ν) is only dependent on the stiffness ratios, but from these results it can be seen that Poisson's ratio is slightly influenced by the particle size decrease, especially when the largest particle size is used. The triaxial compressive strength (TCS) also increased from 86.42 to 202.9 MPa, for the cylindrical specimen, due to a decrease in the particle size. The Brazilian tensile strength is the only macro-property that decreases, from 73.37 to 52.12 MPa, when smaller particles are used. The general reason for these observations is that finer-grained rock is much stronger than coarser-grained rock.

Table 3: Effect of particle size on PFC3D™ macro-properties of a cylindrical specimen

Cylindrical Specimen					
Average particle diameter (mm)	q_u **(MPa)**	E **(GPa)**	ν	σ_t **(MPa)**	**TCS at 2 MPa confinement (MPa)**
3.205	70.69	20.00	0.14	73.37	86.42
1.200	127.9	43.08	0.18	72.59	130.6
0.798	168.7	50.56	0.23	65.77	175.6
0.401	198.1	58.18	0.25	52.12	202.9

Table 4: Effect of particle size on PFC3D™ macro-properties of a rectangular parallelepiped specimen

Rectangular parallelepiped specimen					
Average particle diameter (mm)	q_u **(MPa)**	E **(GPa)**	ν	σ_t **(MPa)**	**TCS at 2MPa confinement (MPa)**
3.205	176.6	57.65	0.25	-	181.0
1.200	184.7	63.91	0.25	-	195.0
0.798	206.4	64.52	0.27	-	211.2
0.401	219.7	61.92	0.26	-	225.2

There is also a noteworthy difference in the results obtained from rectangular parallelepiped specimens and those obtained from cylindrical specimens. The macro-properties from the rectangular parallelepiped specimens are higher than those of the cylindrical specimens. The reason for these differences may be that the packing arrangements changed when the cylinder was cut out of the rectangular parallelepiped specimen and bonds may also have broken during this process. The rectangular parallelepiped specimens are thus stronger than the cylindrical specimens. Nevertheless the focus was on the cylindrical specimens since the laboratory experiments were performed on cylindrical specimens and there was no experimental information on rectangular parallelepiped specimens. The calibration process was therefore directed on the cylindrical specimens and the rectangular parallelepiped specimens were just used for comparison purposes.

In Table 5 the macro-properties of Paarl granite, obtained from laboratory tests, and those obtained from PFC3D™ models with average particle sizes of 0.401 mm are compared. The unconfined compressive strength of the PFC3D™ cylindrical model compared well with the experimental value with a difference of only 0.3 %. The other macro-properties deviated more, with a 6.9 % difference in the Young's modulus, a 21.9 % difference in Poisson's ratio and a 5.0 % difference in triaxial compressive strength. The Brazilian tensile strength was almost 5 times larger than that of Paarl granite, which is a 400 % deviation. This shows that the Brazilian strength of the model doesn't correspond with the Brazilian strength measured in a valid Brazilian test on real Paarl granite and it is rather related to the ratio of particle size to Brazilian disk diameter, which is discussed in Appendix A6. This ratio suggests that the particles will have to be much smaller or the disk diameter has to be much wider in order to approach the real value and this would make computations even more time-consuming and the uniaxial and triaxial compressive strengths will also change. Therefore it is assumed in this study that the uniaxial and triaxial compressive strength tests are sufficient to calibrate the rock specimen, since the uniaxial compressive strength was used to define the strength of the rock.

Table 5: Macro-properties of Paarl granite and PFC3D™ model

Property	Experimental Paarl granite	PFC3D™ cylindrical model	PFC3D™ rectangular parallelepiped model
q_u (MPa)	198.29	198.1	219.7
E (GPa)	58.48	58.18	61.92
ν	0.32	0.25	0.26
σ_t (MPa)	10.06	37.33	-
TCS at 2 MPa	221.2	202.9	225.2

5.2 Material response of Sandstone-2

The calibration for Sandstone-2 was done in the same way as for Paarl granite with average particle sizes of 0.401 mm and 0.802 mm. In this case, for each particle size, the micro-properties in Table 2 were changed to fit the macro-properties of Sandstone-2. The results can be seen in Table 6. This was done to make it possible to look at the influence of larger particles during the cutting process that will be described in the next section.

Table 6: Macro-properties of Sandstone-2 and PFC3D™ model

Property	Theoretical Sandstone-2 values	Numerical PFC3D™ values for 0.401 mm particles	Numerical PFC3D™ values for 0.802 mm particles
q_u (MPa)	173.7	174.3	173.9
E (GPa)	28.0	28.42	27.7
ν	0.29	0.26	0.25
σ_t (MPa)	11.6	48.83	69.31

The numerical values of the uniaxial compressive strength, Young's modulus and Poisson's ratio compare quite well to the theoretical values found in Su & Akcin (2011). The numerical values of the Brazilian strength are again much higher than the theoretical values, which show that the Brazilian strength is rather related to the ratio of particle size to Brazilian disk diameter, which is discussed in Appendix A6.

CHAPTER 6:

PFC3D™ MATERIAL RESPONSE OF ROCK CUTTING WITH POINT-ATTACK PICKS

6.1 Overall results

Summarized herein are the most important results found throughout the study on the factors that affect the simulated forces considerably. These factors include the wear flat of the point-attack pick, the size of the particles, as well as the depth of cut. The forces determined in the numerical simulations are also compared to the forces obtained during experimental cutting tests and those calculated theoretically.

During the PFC3D™ cutting test simulations, the three orthogonal forces acting on the pick were monitored and the histories were recorded. The cutting forces were monitored by summing all the forces acting on the pick in the x-direction at each time step, while the normal forces were monitored by summing all the forces in the z-direction. Since the experimental studies only contained information about the cutting and normal forces, little attention was paid to the sideways forces. From the simulations it was evident that the average value of the sideways forces was in each case close to zero and therefore it was concluded that it didn't have a great influence on cutting.

Since 20 mm of cutting distance and 5 m/s of cutting speed were applied during the numerical study, the simulations took from one day to about 5 days to complete depending on the particle size and depth of cut among others factors. After each simulation the graph of the forces varying with increasing cutting distance was generated. The mean cutting and normal forces were obtained by taking the average of the force histories over the cutting distance where a steady state was reach, while the mean peak cutting and normal forces were gained by averaging the peak forces taken from increments of 20 data points.

In Figure 23 the variations of sideways forces during a cutting test with a sharp point-attack pick at 0.5 mm depth of cut are illustrated. It is shown that the sideways forces fluctuate around zero for the point-attack pick with parameters of Su & Akcin (2011) as well as those of Bilgin et al. (2006). Therefore the previous conclusion to ignore sideways forces is valid. This type of figure of the sideways forces was seen throughout the simulations and the rest of the graphs can be seen in Appendix D.

From this point forward the point-attack pick simulated with the parameters of Su & Akcin (2011) will be referred to as the narrow point-attack pick and the point-attack pick simulated with the parameters of Bilgin et al. (2006) will be referred to as the wide point-attack pick.

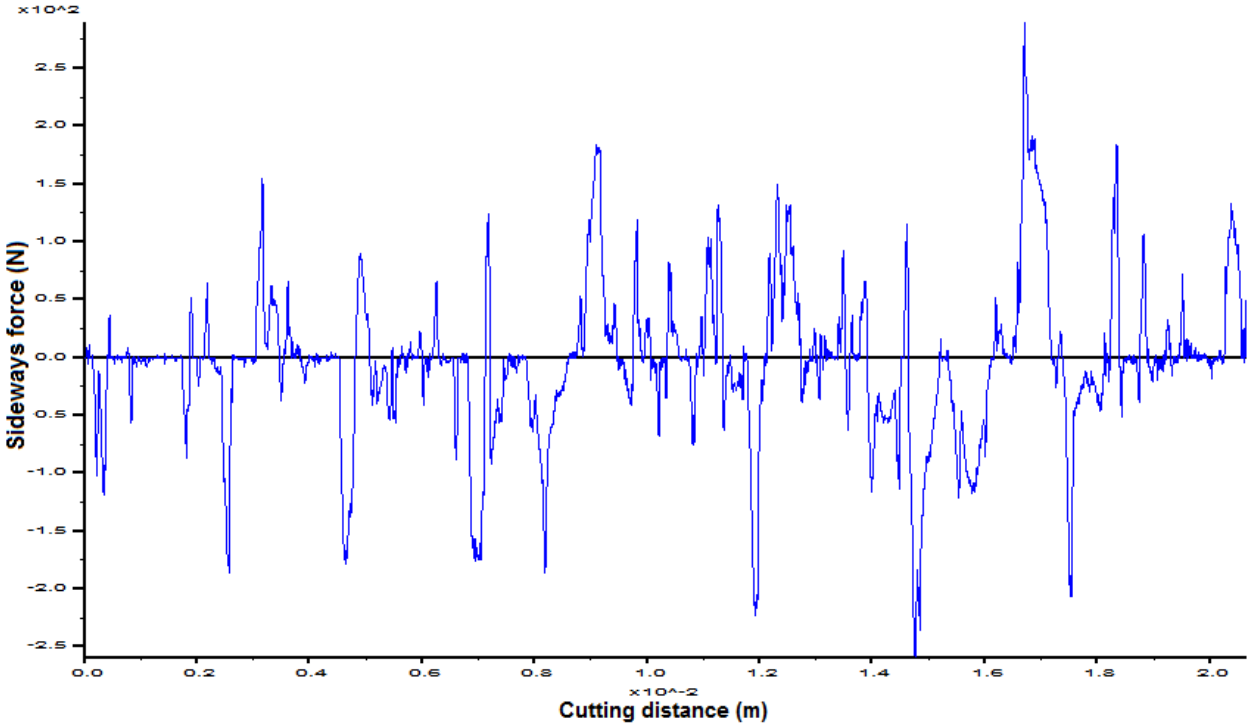

(a)

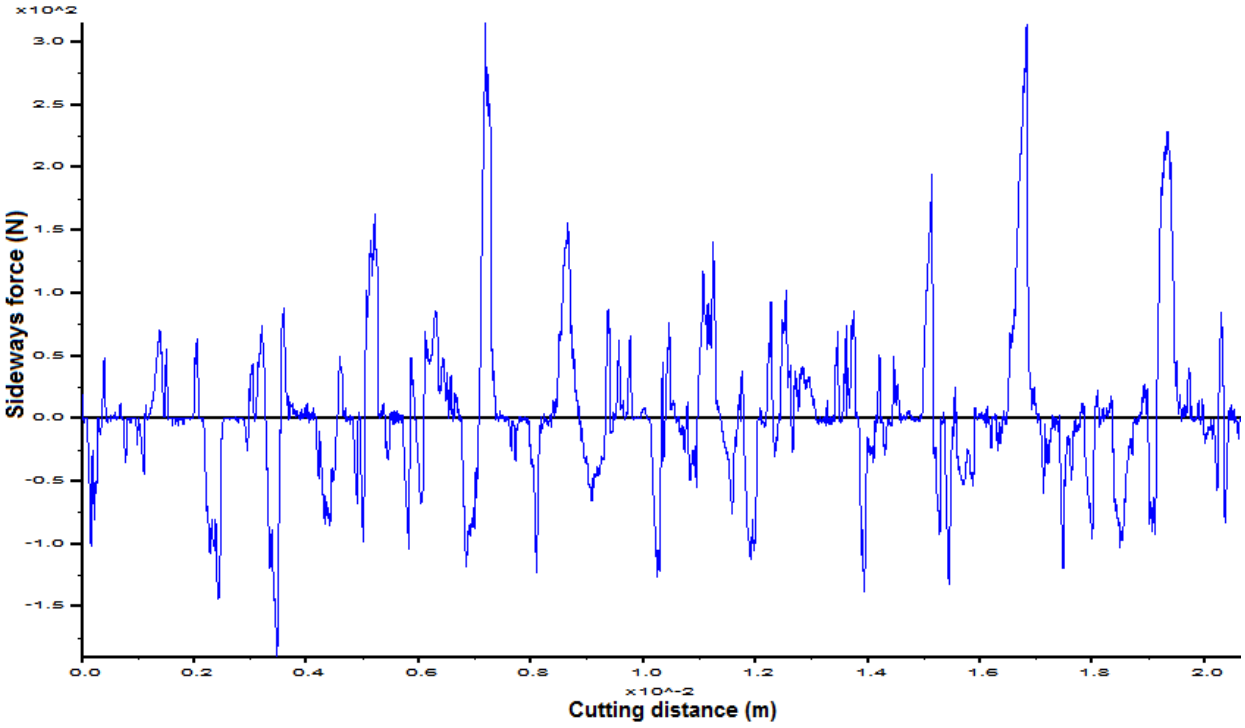

(b)

Figure 23: The variation of sideways forces versus cutting distance at 0.5 mm depth of cut
(a) Parameters of Su & Akcin (2011); (b) Parameters of Bilgin et al. (2006)

The graphs of the cutting and normal forces for the sharp narrow and wide point-attack picks at each depth of cut can be seen in Figure 24 to Figure 26. The black curves represent the cutting forces and the red curves represent the normal forces. The mean cutting and normal forces are shown with dashed lines and the values are given on the right side of the graphs.

When analysing the graphs, it can be seen that the forces fluctuate a lot, from very low values to very large values at an instant. The reason for this occurrence is that at the start of the simulation there are only a few particles in front of the pick which makes the resulting forces small. As the pick moves forwards, the particles are pushed against the wall of the pick and they build up in front of it, resulting in an increase of the forces. When the particle bonds break and the particles in front of the pick are broken off, the forces will decrease again. This process then starts all over again and it repeats itself throughout the simulation.

Figure 24 shows the cutting and normal forces for sharp point-attack picks at 0.5 mm depth of cut. At this shallow cutting depth, the forces vary from zero to more or less 320 N for a narrow point-attack pick in Figure 24a and the average cutting force is 44 N, while the average normal force is 45 N. For the wide point-attack pick in Figure 24b, the forces vary from zero to 450 N and the average cutting force is 44 N, while the average normal forces is 54 N. The cutting and normal forces are therefore very alike at a shallow depth of cut for the narrow and wide point-attack pick. As described in the previous paragraph, the particles are pushed upwards against the wall of the pick, making the forces large and when it breaks off, the forces return to zero. From the graphs below it can be seen that there are occurrences between the larger forces when the cutting and normal forces are smaller over longer distances, showing that the particles broke off quicker.

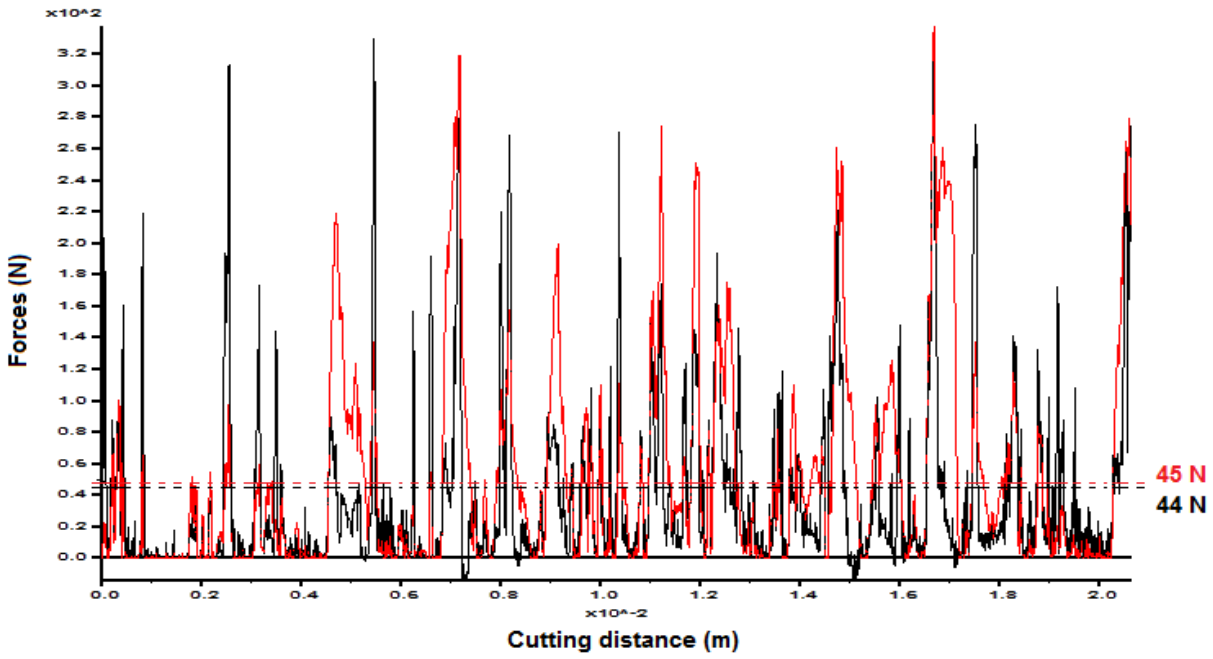

(a)

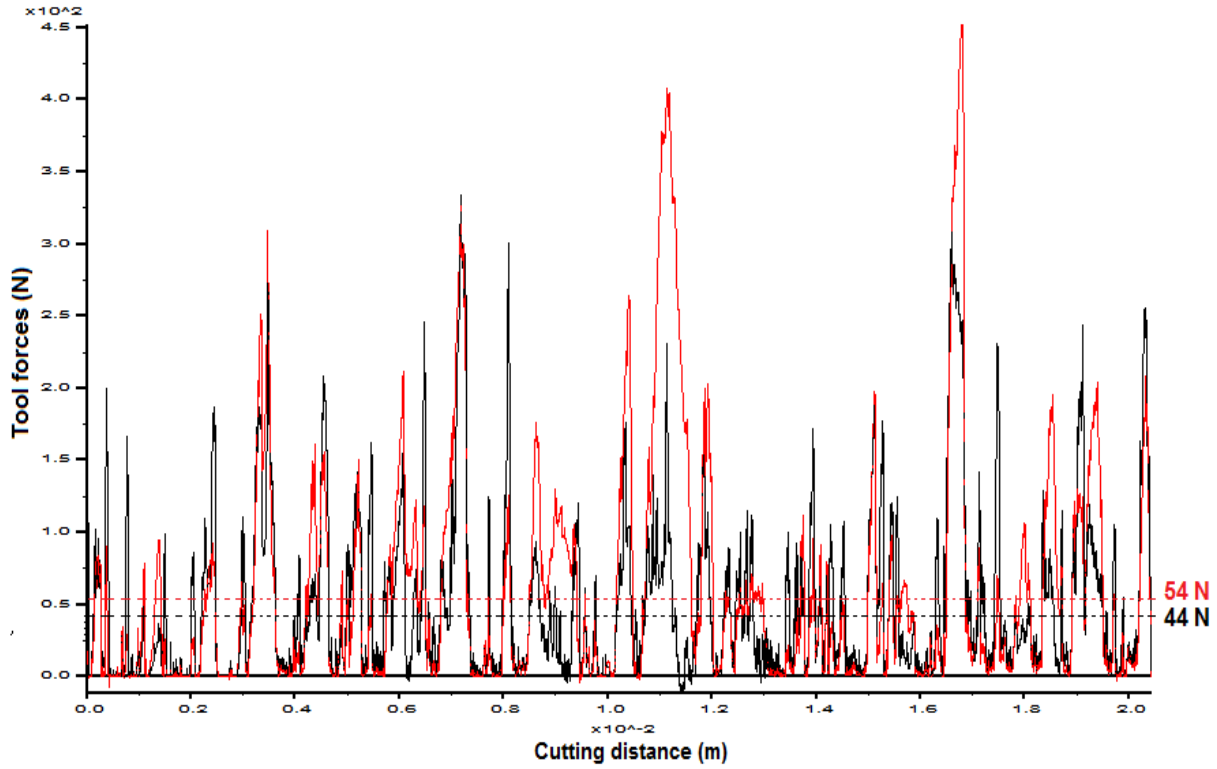

(b)

Figure 24: The variation of tool forces versus cutting distance at 0.5 mm depth of cut

(a) Narrow point-attack pick; (b) Wide point-attack pick

Figure 25 gives the cutting and normal forces for sharp point-attack picks at 1.5 mm depth of cut. There is already a great increase in value of the forces with an increase in the cutting depth. At 1.5 mm depth of cut, the forces vary between about 50 and 800 N for the narrow point-attack pick and the average cutting force is 345 N, while the average normal force is 252 N. The cutting forces are therefore almost 8 times larger when the cutting depth is tripled and the normal forces are about 6 times larger.

For the wide point-attack pick, the forces fluctuate between 150 and 1000 N and the average cutting force is 420 N while the average normal force is 389 N. For this point-attack pick the cutting forces are about 9 times larger and the normal forces are 7 times larger when the cutting depth is increased by 3 times.

At the increased depth of cut, the forces of the wide point-attack pick are larger than those of the narrow point-attack pick, since a greater area of the pick is exposed to the rock specimen. Another observation is that the cutting forces are now larger than the normal forces at 1.5 mm depth of cut, while the normal forces had larger values than the cutting forces at 0.5 mm depth of cut.

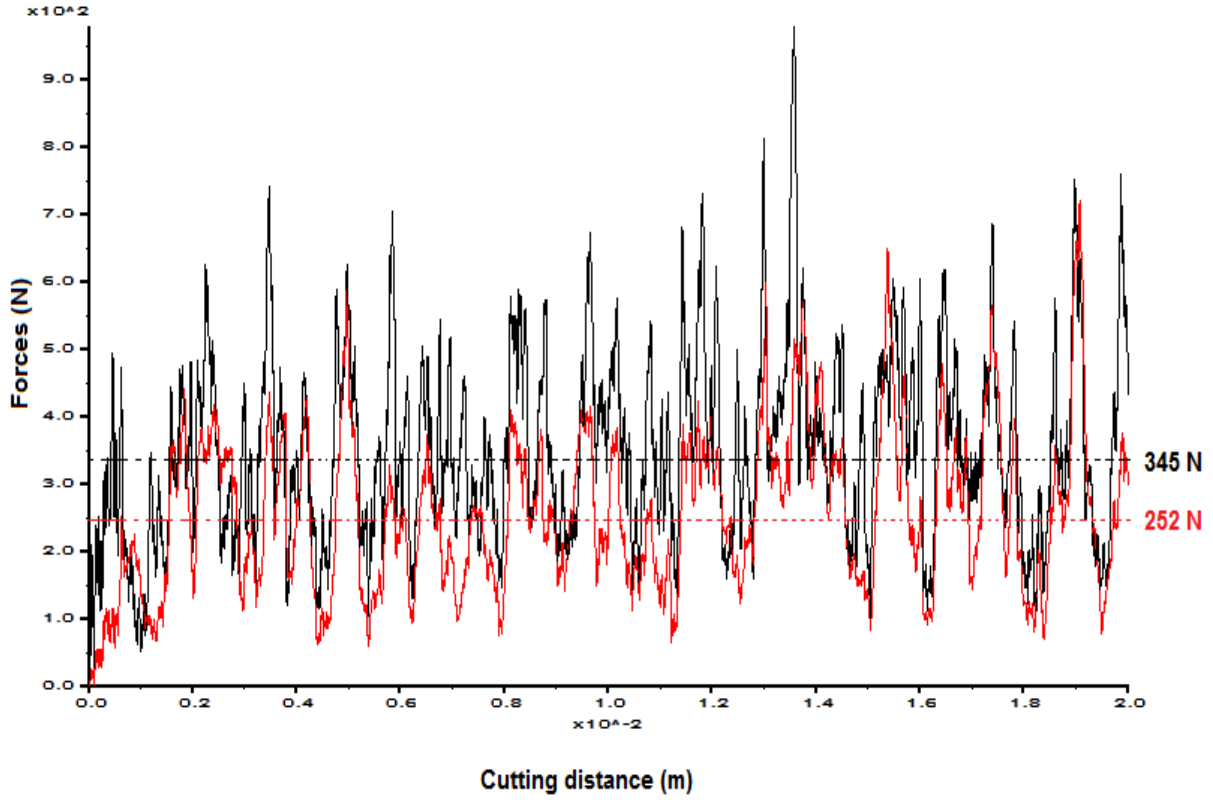

(a)

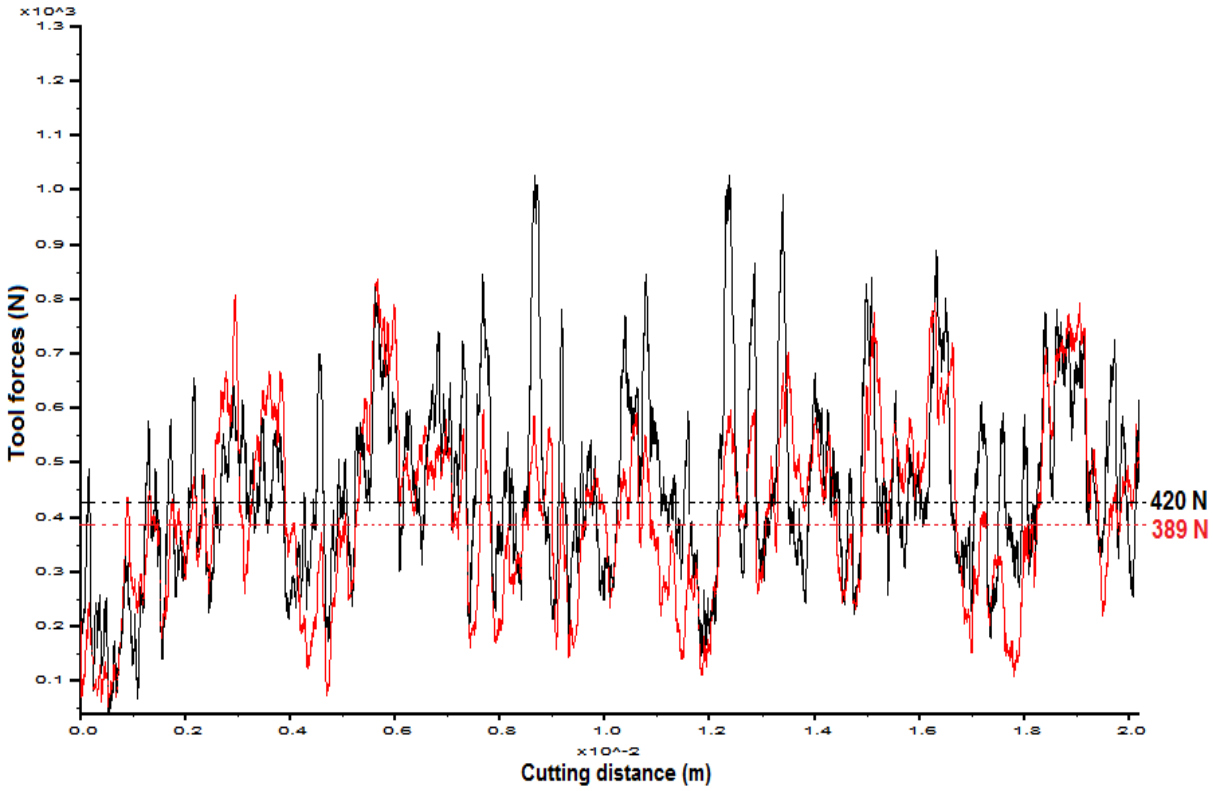

(b)

Figure 25: The variation of tool forces versus cutting distance at 1.5 mm depth of cut

(a) Narrow point-attack pick; (b) Wide point-attack pick

The cutting and normal forces for sharp point-attack picks at 3 mm depth of cut are displayed in Figure 26. During this cutting test the tool forces increase over the first 3 mm of cutting distance and then the cutting forces starts to fluctuate around an average of 1864 N and the normal forces around an average of 1253 N for the narrow point-attack pick in Figure 26a. For the wide point-attack pick, in Figure 26b, the average cutting and normal force are 2703 N and 2062 N respectively. As mentioned at 1.5 mm depth of cut, the forces of the wide point-attack pick are again larger than those of the narrow point-attack pick.

The reason for the increase in forces during the first 3 mm is that the tip of the pick now enters the rock specimen at a deeper cutting depth and there is a greater build-up of particles in front of the pick before they start to break off. From a cutting depth of 1.5 mm to a cutting depth of 3 mm the cutting and normal forces are about 5 times larger for the narrow point-attack pick and for the wide point-attack pick the cutting forces are 6 times larger while the normal forces are 5 times larger. The difference between the values of cutting and normal forces also increases more at the deeper depth of cut. The effect of the cutting depth will also be discussed in more detail in section 6.1.2.

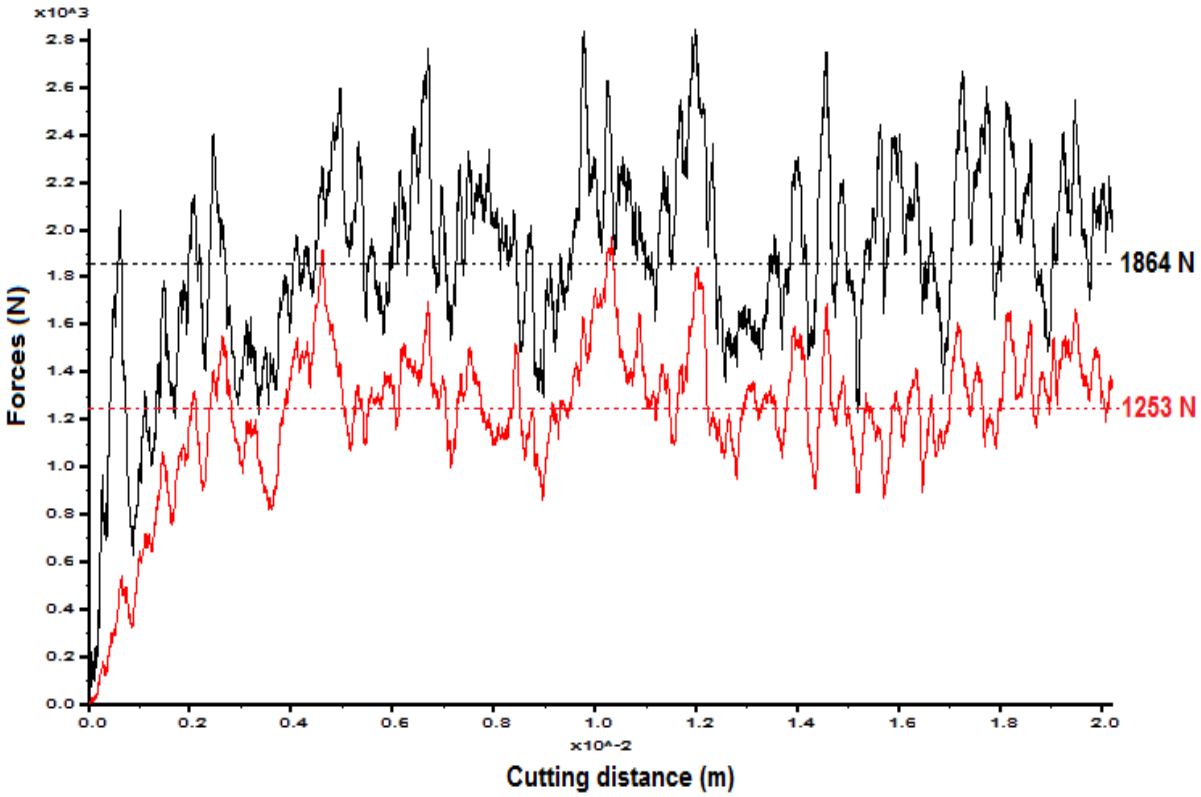

(a)

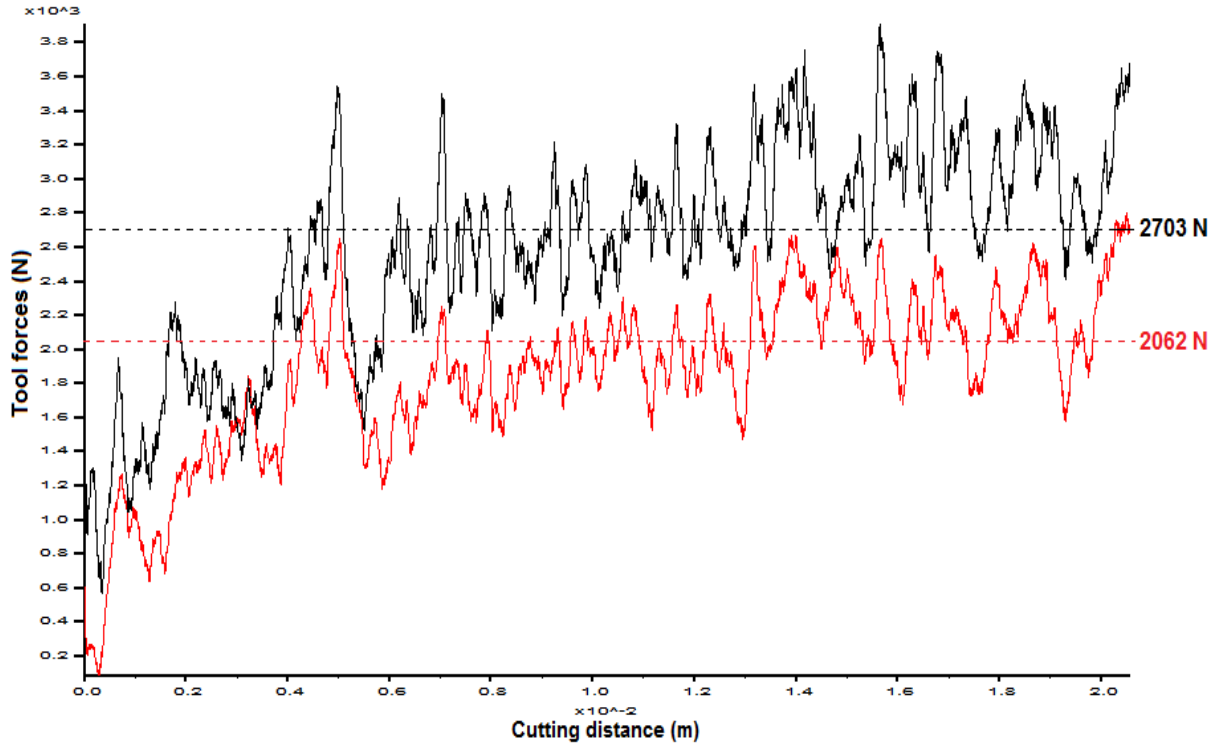

(b)

Figure 26: The variation of tool forces versus cutting distance at 3 mm depth of cut

(a) Narrow point-attack pick; (b) Wide point-attack pick

Although only the graphs for sharp point-attack picks, using the parameters of Su & Akcin (2011) and Bilgin et al. (2006), are shown here, all the other simulations will show a similar trend in the forces. When repeating the simulations, the graphs won't look exactly the same and the peak forces might be higher or lower, since the particles won't break off at the same place, but the mean forces are similar. Therefore the simulations are repeatable. The graphs of the rock cutting simulations using blunt picks are given in Appendix D.

The variation of the tool forces around an average value can also be expressed with graphs showing the standard deviation, where standard deviation is defined as the statistical measure of spread or variability. The following graphs, namely Figure 27 to Figure 29, gives the standard deviation of the forces during the simulations of cutting samples with 0.401 mm particles using a narrow point-attack pick at different depths of cut. A complete summary of the standard deviation of all the simulations with point-attack picks is given in Appendix D.

At 0.5 mm depth of cut the standard deviation is high compared to the average values, especially for the normal forces. This high standard deviation indicates that the data points of the forces are spread out over a large range of values. When looking back at the graphs of the variation of tool forces versus cutting distance in Figure 24, this large variation in forces can be seen clearly.

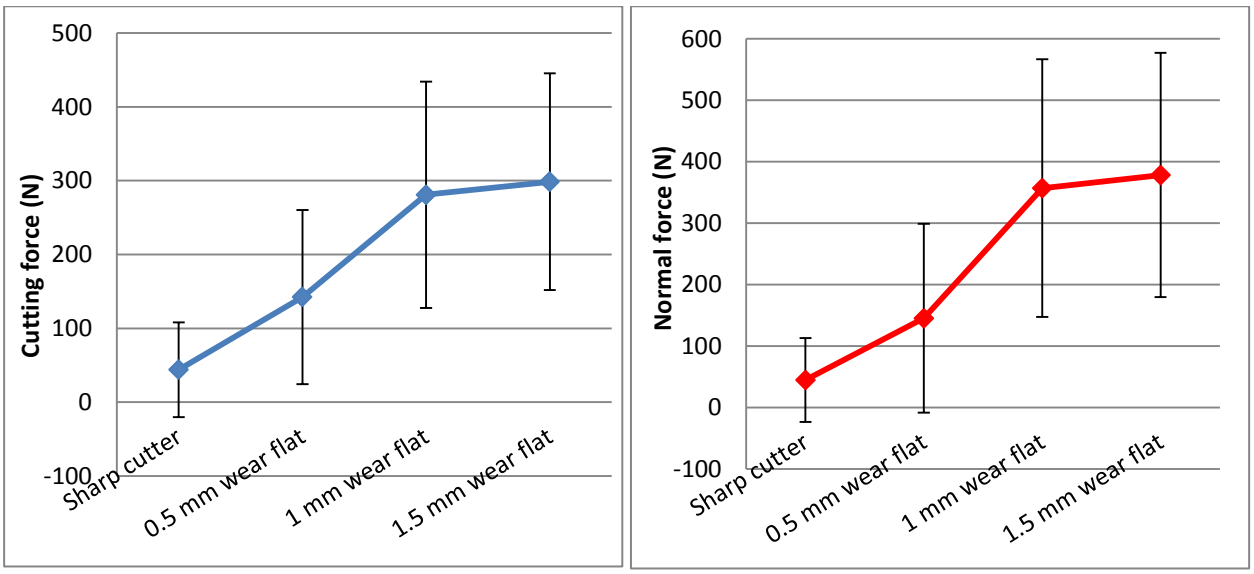

(a) (b)

Figure 27: Average force and standard deviation when cutting with a narrow point-attack pick at 0.5 mm depth of cut

(a) Cutting forces; (b) Normal forces

As the depth increases the standard deviation becomes lower in relation to the average values. The lower standard deviation indicates that the data points of the forces tend to be closer to the average value or in other words the variation in tool forces, at the deeper depths of cut, is less as can be seen in Figure 25 and Figure 26.

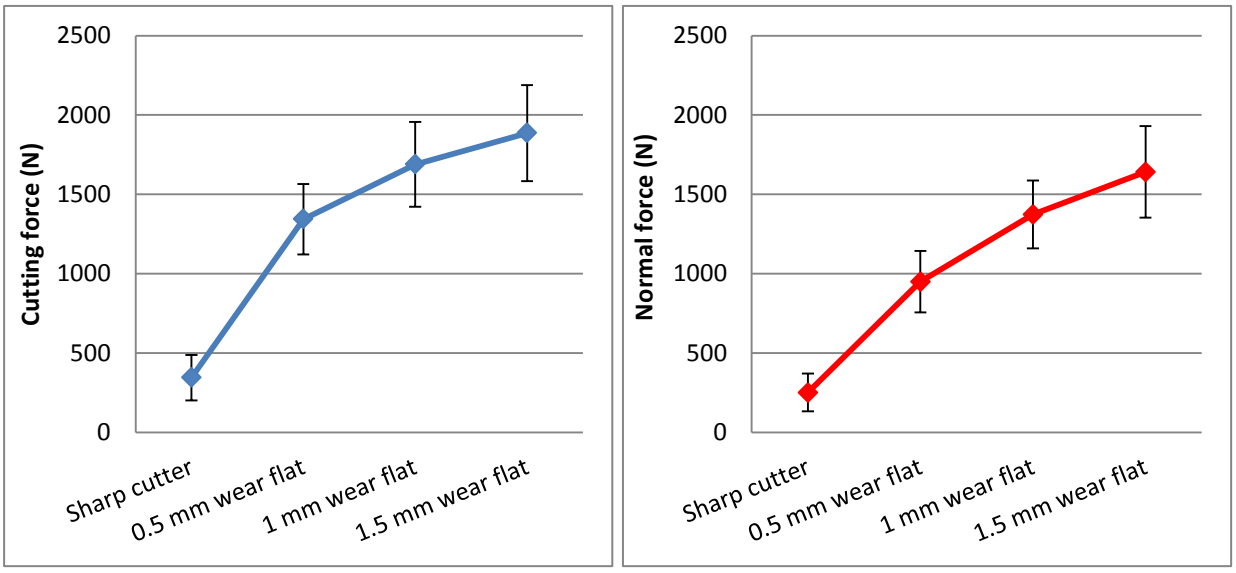

(a) (b)

Figure 28: Average force and standard deviation when cutting with a narrow point-attack pick at 1.5 mm depth of cut

(a) Cutting forces; (b) Normal forces

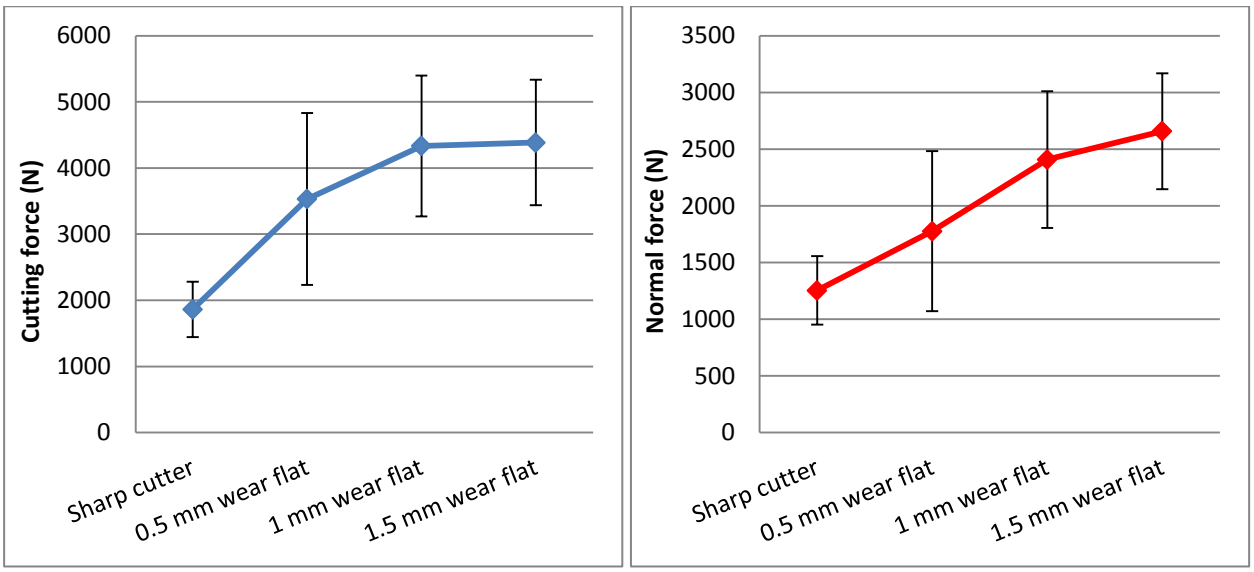

(a) (b)

Figure 29: Average force and standard deviation when cutting with a narrow point-attack pick at 3 mm depth of cut

(a) Cutting forces; (b) Normal forces

Although it is more accurate to include the standard deviation, only the average values of the forces will be used throughout the study for comparison to experimental and theoretical values and to look at the influence of certain parameters.

The Sandstone-2 specimen and the sharp narrow and wide point-attack picks at 0.5 mm depth of cut are shown in Figure 30 and Figure 31 after 20 mm of cutting distance. After the point-attack picks began to interact with the particles, micro-cracks were initiated and they propagated from the tip of the picks. These micro-cracks formed when bonds were broken in the simulation and they are also an indicator of the damage on the specimen. In Figure 30b and Figure 31b the black spots represents the micro-cracks due to tensile bond failure, while the red spots represents the micro-cracks due to shear bond failure. According to Su & Akcin (2011) it is not possible to see macro-cracks in PFC3D™. From Figure 31b it can be seen that the formation of micro-cracks is irregular and highlights the subsurface crack systems and damage accumulation during ploughing of the rock. The micro-cracks also led to chip formations which are more visible at deeper depths of cut but can also be seen in front of the tip of the picks in Figure 30a and Figure 31a.

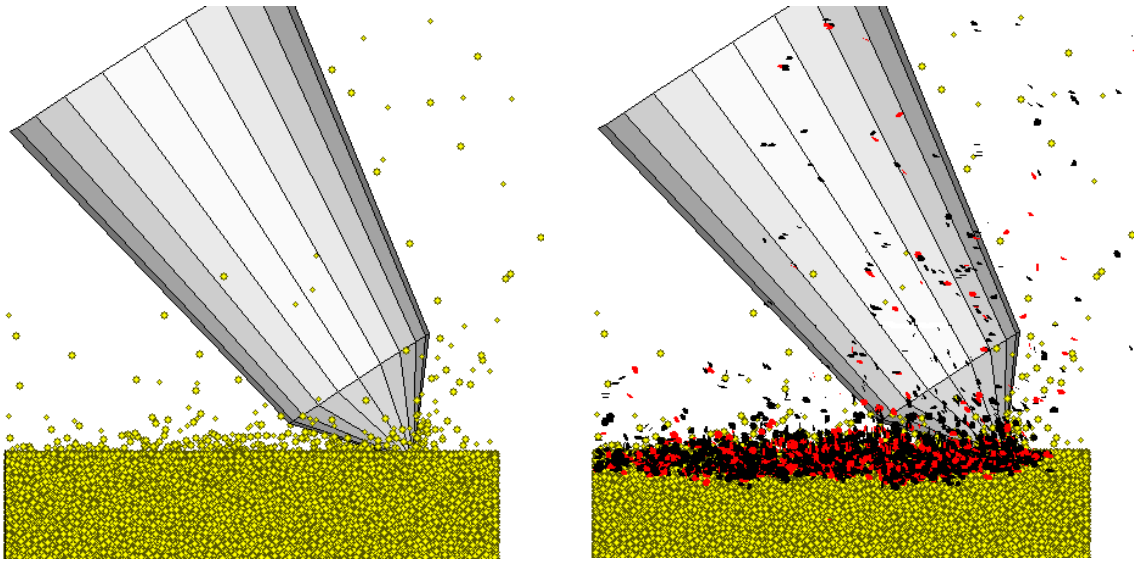

(a) (b)

Figure 30: A schematic view of the specimen and the narrow point-attack pick after the simulation

(a) The chip formation in front of the pick; (b) The micro-cracks occurring around the pick

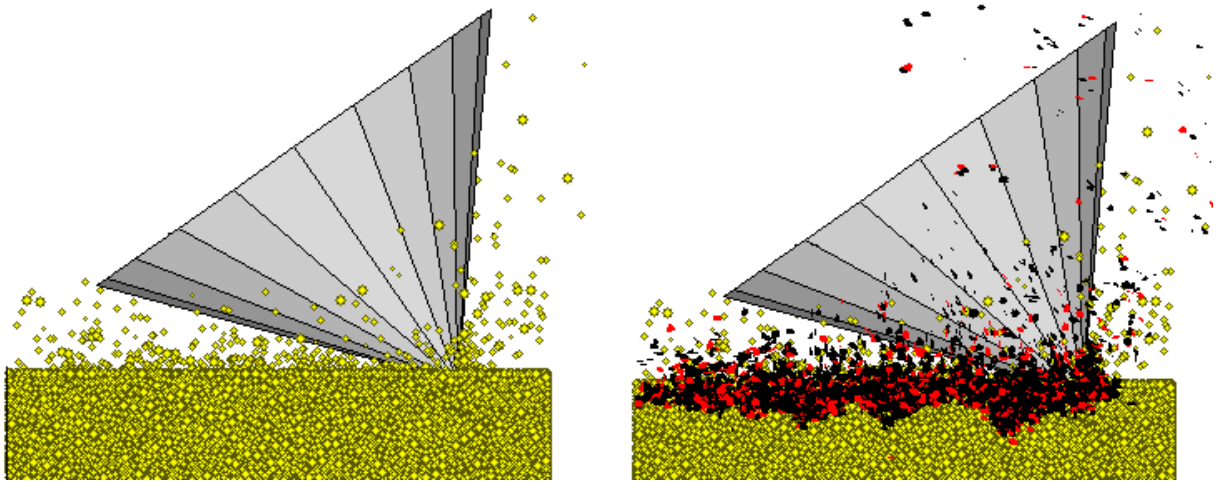

(a) (b)

Figure 31: A schematic view of the specimen and the wide point-attack pick after the simulation

(a) The chip formation in front of the pick; (b) The micro-cracks occurring around the pick

The number of micro-cracks formed per unit volume of cutting, clearly increases over the cutting distance and this is illustrated in Figure 32 and Figure 33, which was recorded during cutting tests with a sharp narrow point-attack pick at 0.5 mm and 3 mm depth of cut. The number of micro-cracks that formed is also an indication of the number of broken bonds throughout the simulation, since micro-cracks form when bonds are broken. When comparing Figure 32 to Figure 33, the increase in the number of micro-cracks becomes more linear with an increase in cutting depth. These graphs look more or less the same for each rock cutting simulation, except that there will be an increase in the number of micro-cracks with an increase in the cutting depth and bluntness of the pick. These observations are

also illustrated in Table 7 and Table 8, which gives the number of micro-cracks formed during each rock cutting simulation.

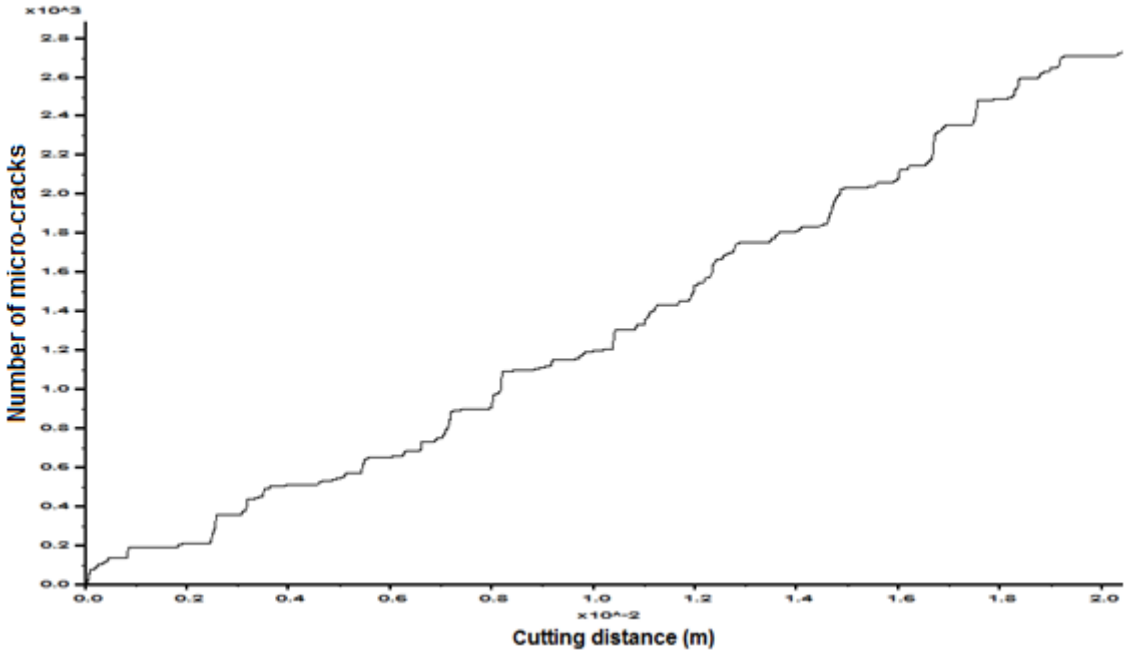

Figure 32: The variation of micro-cracks at 0.5 mm depth of cut for sharp narrow point-attack pick

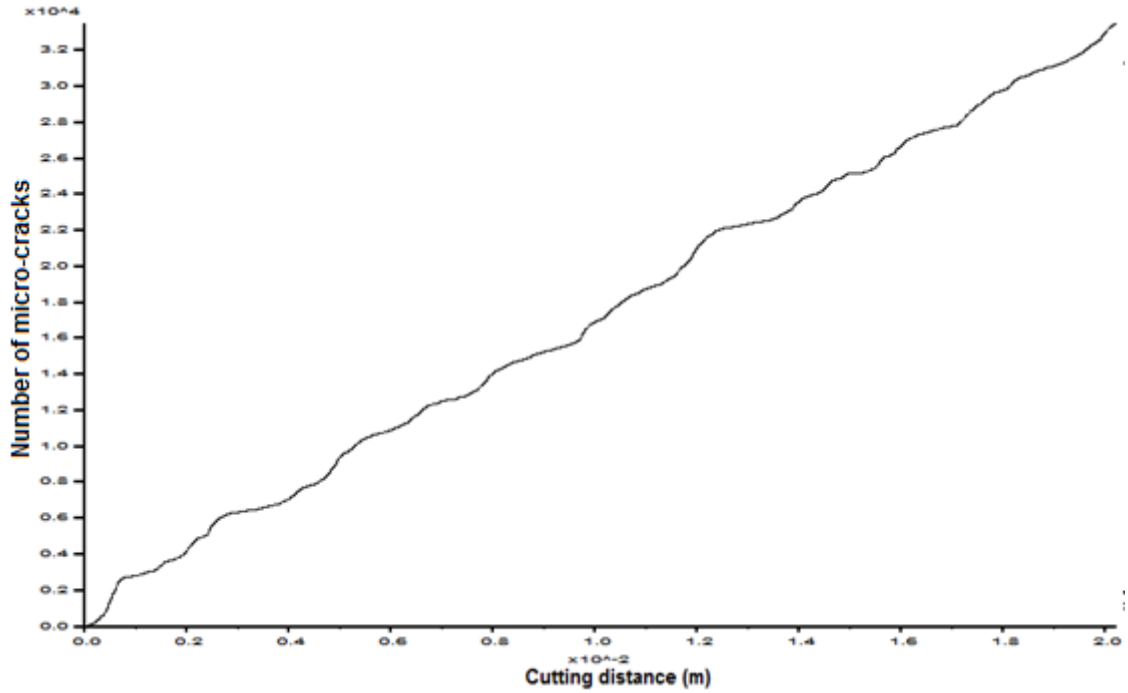

Figure 33: The variation of micro-cracks at 3 mm depth of cut for sharp narrow point-attack pick

These tables show a definite increase in the number of micro-cracks with an increase in the wear flat of the pick and with an increase in the cutting depth. The number of micro-cracks is also more when using a wide point-attack pick than a narrow point-attack pick, because of the larger exposed contact area. Interesting to note is that the number of micro-cracks formed is considerably lower when using larger

particles in the rock specimen than using smaller particles. Fewer bonds were therefore broken when larger particles were used. Another important point is the effect of cutter sharpness on the micro-crack generation as illustrated in Table 7 that at 3 mm depth of cut there is a decrease in the number of micro-cracks from using a blunt pick with 1 mm wear flat to one with 1.5 mm wear flat.

Table 7: Number of micro-cracks formed during rock cutting simulations with 0.401 mm particles

Narrow point-attack pick								
0.5 mm depth of cut		**Number of micro-cracks**	**1.5 mm depth of cut**		**Number of micro-cracks**	**3.0 mm depth of cut**		**Number of micro-cracks**
Sharp pick		2700	**Sharp pick**		10720	**Sharp pick**		33550
Blunt pick	**0.5 mm wear flat**	7573	**Blunt pick**	**0.5 mm wear flat**	24370	**Blunt pick**	**0.5 mm wear flat**	53310
	1 mm wear flat	10550		**1 mm wear flat**	29610		**1 mm wear flat**	67970
	1.5 mm wear flat	11130		**1.5 mm wear flat**	31520		**1.5 mm wear flat**	62700
Wide point-attack pick								
0.5 mm depth of cut		**Number of micro-cracks**	**1.5 mm depth of cut**		**Number of micro-cracks**	**3.0 mm depth of cut**		**Number of micro-cracks**
Sharp pick		3700	**Sharp pick**		13500	**Sharp pick**		37670
Blunt pick	**0.5 mm wear flat**	9250	**Blunt pick**	**0.5 mm wear flat**	29333	**Blunt pick**	**0.5 mm wear flat**	64166
	1 mm wear flat	12250		**1 mm wear flat**	34395		**1 mm wear flat**	75783
	1.5 mm wear flat	12500		**1.5 mm wear flat**	35333		**1.5 mm wear flat**	73750

Table 8: Number of micro-cracks formed during rock cutting simulations with 0.802 mm particles

Narrow point-attack pick								
0.5 mm depth of cut		**Number of micro-cracks**	**1.5 mm depth of cut**		**Number of micro-cracks**	**3.0 mm depth of cut**		**Number of micro-cracks**
Sharp pick		488	**Sharp pick**		2225	**Sharp pick**		5875
Blunt pick	**0.5 mm wear flat**	1466	**Blunt pick**	**0.5 mm wear flat**	4955	**Blunt pick**	**0.5 mm wear flat**	8333
	1 mm wear flat	2350		**1 mm wear flat**	5540		**1 mm wear flat**	9750
	1.5 mm wear flat	2366		**1.5 mm wear flat**	5810		**1.5 mm wear flat**	10500

Wide point-attack pick								
0.5 mm depth of cut		**Number of micro-cracks**	**1.5 mm depth of cut**		**Number of micro-cracks**	**3.0 mm depth of cut**		**Number of micro-cracks**
Sharp pick		874	**Sharp pick**		2750	**Sharp pick**		7113
Blunt pick	**0.5 mm wear flat**	2324	**Blunt pick**	**0.5 mm wear flat**	5800	**Blunt pick**	**0.5 mm wear flat**	10500
	1 mm wear flat	2633		**1 mm wear flat**	6720		**1 mm wear flat**	11750
	1.5 mm wear flat	3066		**1.5 mm wear flat**	6875		**1.5 mm wear flat**	11625

The numerical simulations of the cutting processes were also viewed from the back of the point-attack picks and the direction that the micro-cracks followed into the specimen could be observed. For the sharp narrow point-attack pick the micro-cracks follow an almost triangular shape and as the depth of cut increases, the shape becomes more oval, as seen in Figure 34. The shape of the cut for the sharp point-attack picks is triangular and since the narrow point-attack pick is positioned at a rake angle of -7°, not only the tip of the pick enters the specimen at deeper cuts, but also the rest of the pick. The number of micro-cracks therefore increases, as also shown in Table 7, and they become more spread out. For the sharp wide point-attack pick, the micro-cracks also follow a triangular shape and become oval with an increase in depth of cut as seen in Figure 35. In this case the rake angle is -5°.

When blunt point-attack picks with different wear flats were used, the shape of the cut was trapezoidal and from the back view the micro-cracks followed an oval shape in each case as seen in Figure 35. These figures can be seen in Appendix D.

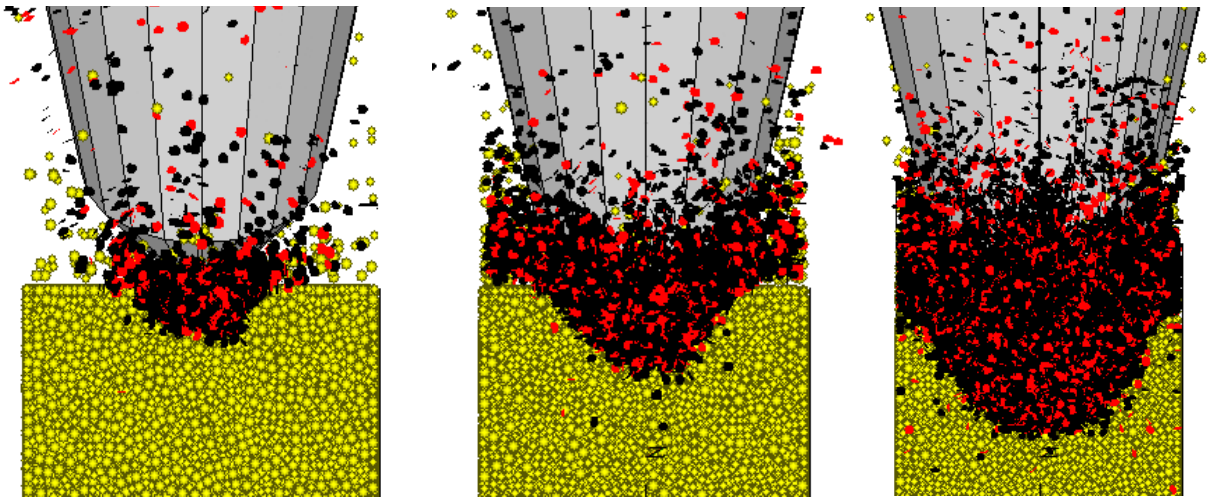

(a) (b) (c)

Figure 34: Shape of cracks in specimen with a sharp narrow point-attack pick at each cutting depth

(a) 0.5 mm depth of cut; (b) 1.5 mm depth of cut; (c) 3 mm depth of cut

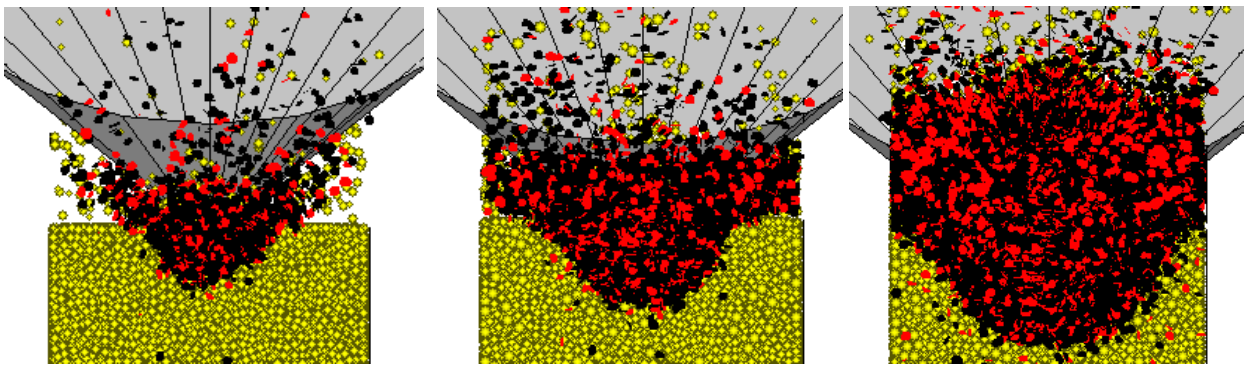

(a) (b) (c)

Figure 35: Shape of cracks in specimen with a sharp wide point-attack pick at each cutting depth

(a) 0.5 mm depth of cut; (b) 1.5 mm depth of cut; (c) 3 mm depth of cut

6.2 Comparison between numerical, theoretical and experimental values

The numerically simulated forces were also compared to experimental and theoretical data. The experimental rock cutting tests were previously performed and the experimental data, used in this study, were published in Su & Akcin (2011) and Bilgin et al. (2006). The trend lines in Figure 6 were used to calculate the experimental forces at 0.5 and 1.5 mm cutting depth. The theoretical models of Evans (1984), Roxborough (Su & Akcin, 2011) and Goktan (1995), as described in section 2.7 with equations 26, 28 and 29, were used to determine the mean peak cutting forces from the mechanical properties of Sandstone-2 in Table 6 and the cutting parameters described in section 4.3. These models are only valid for sharp point-attack picks.

The results of the numerical, theoretical and experimental data for sharp point-attack picks at different depths of cut are summarized in Table 9, using the parameters from Su & Akcin (2011) and in Table 10, using the parameters from Bilgin et al. (2006). From these tables it is evident that the numerically simulated forces are much smaller than the experimental forces. The main reason for the differences in values are the effect of wear on the pick, while the conditions of the cutting process for instance temperature and the distribution of locked-in stresses in the particle assembly possibly contributed to these differences as well. During the numerical simulations perfectly sharp point-attack picks with high stiffness, rigid walls were used and therefore there was no wear on the pick itself and only the rock material was damaged. During the experimental studies, on the other hand, there is damage to the pick and the wear increases over the cutting distance, causing the forces to increase and giving higher mean and peak forces in the process. The commercially manufactured point-attack picks used in the mining industry are also not perfectly sharp and generally have rounded tips (Su & Akcin, 2011). Therefore the influence of wear flat on the forces will be discussed in the next section.

When comparing Table 9 to the results of Su & Akcin (2011), which are given in Appendix D, it is found that the numerically simulated forces of this study are larger than those simulated by Su & Akcin (2011).

The reason is that there might have been differences in the simulation of the Sandstone-2 specimen or the dimensions of the simulated pick may have differed slightly.

Table 9: Results of the tool forces for a sharp narrow pick with Su & Akcin (2011) data

d (mm)	Forces of numerical simulation (kN)				Theoretical cutting forces (kN)			Experimental forces (kN)			
	FN	FN'	FC	FC'	FC'_{Evans}	FC'_{Rox}	FC'_{Goktan}	FN	FN'	FC	FC'
0.5	0.045	0.319	0.044	0.330	0.017	0.020	0.031	0.94	1.48	0.41	0.61
1.5	0.25	0.722	0.35	0.981	0.149	0.183	0.278	2.89	5.23	1.63	3.16
3.0	1.25	1.97	1.86	2.88	0.597	0.730	1.111	6.1	11.9	4.1	9.2

Table 10: Results of the tool forces for a sharp wide pick with Bilgin et al. (2006) data

d (mm)	Forces of numerical simulation (kN)				Theoretical cutting forces (kN)			Experimental forces (kN)	
	FN	FN'	FC	FC'	FC'_{Evans}	FC'_{Rox}	FC'_{Goktan}	FC	FC'
0.5	0.051	0.453	0.044	0.334	0.017	0.033	0.094	0.48	1.32
1.5	0.386	0.837	0.420	1.304	0.149	0.299	0.847	1.84	5.14
3.0	1.828	2.803	2.356	3.915	0.597	1.197	3.387	4.30	12.12

As can be seen from the rock cutting test data presented in Table 9 and Table 10, the forces predicted by the theoretical models are significantly lower compared with the numerical and experimental forces. Goktan's model gives the nearest values to the real data since he further developed Evans' model and included the rake angle parameters as well. An important conclusion can be drawn that these models are not reliable to predict cutting forces. Sample calculations of these theoretical forces can be seen in Appendix D.

Since the theoretical models are only valid for sharp point-attack picks, the numerical values of blunt picks could not be compared.

6.3 Influence of wear flat on forces

The point-attack picks were simulated of high strength, rigid walls to insure that there is no wear on the pick itself during simulation. To look at the influence of wear on the simulated forces, a wear flat was introduced by cutting off the tip of the point-attack pick at diameters ranging from 0.5 to 1.5 mm.

In Figure 36 the damage to the specimen can be seen when using a sharp narrow point-attack pick compared with a blunt one with a wear flat of 1.5 mm in diameter at a cutting depth of 0.5 mm. When

a sharp narrow point-attack was used, the micro-cracks did not propagate much deeper into the specimen than the depth of cut. On the other hand, when a blunt narrow pick with a wear flat of 1.5 mm in diameter was used, the micro-cracks propagated downwards into the specimen to about twice the depth of cut. It is also observed that there is more chip formations in front of the blunt pick than the sharp pick during the simulations of the cutting tests.

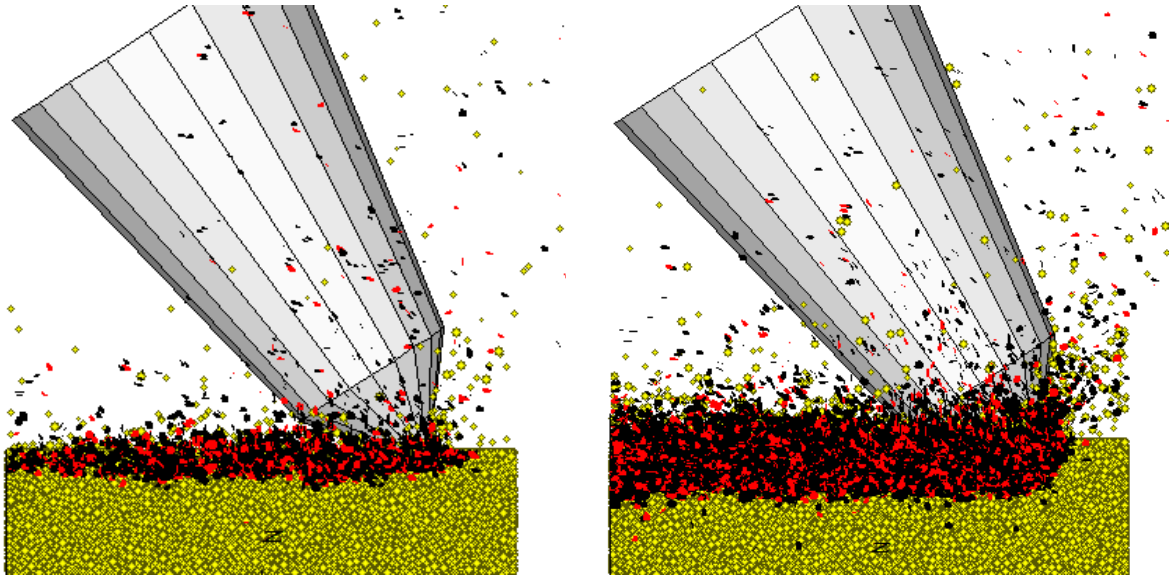

(a) (b)

Figure 36: A schematic view of the influence of wear on a narrow point-attack pick

(a) Sharp pick at 0.5 mm depth of cut; (b) Blunt pick with 1.5 mm wear flat at 0.5 mm depth of cut

In Figure 37 the damage to the specimen is shown when using a sharp wide point-attack pick and a blunt one with a wear flat of 1.5 mm in diameter at a cutting depth of 0.5 mm. The same observations can be made as for the narrow point-attack pick.

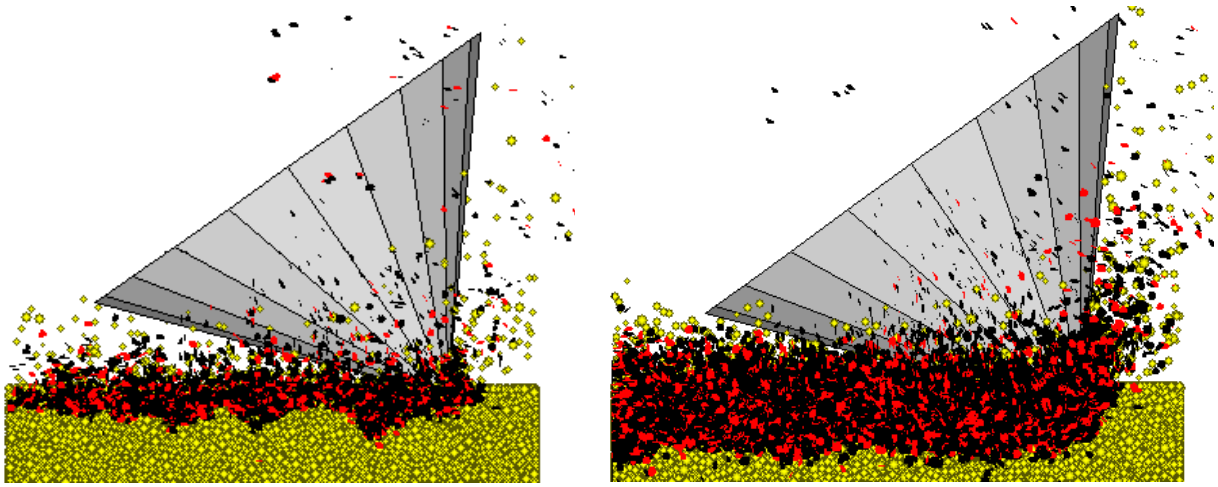

(a) (b)

Figure 37: A schematic view of the influence of wear on a wide point-attack pick

(a) Sharp pick at 0.5 mm depth of cut; (b) Blunt pick with 1.5 mm wear flat at 0.5 mm depth of cut

The forces simulated during cutting tests, using the parameters of Su & Akcin (2011), are displayed in Figure 38 and Figure 39. At all three cutting depths, in Figure 38, the non-linear behaviour of the cutting forces can be fitted reasonably well with a 2nd order polynomial as the force increases from using a sharp pick (0 mm wear flat) to a blunt pick with 1.5 mm diameter wear flat. Another observation that can be made is that the cutting forces increase very rapidly from using a sharp pick to a blunt pick with 0.5 mm wear flat and then the increase flattens as the wear flat becomes larger.

The simulated cutting forces using 0.401 mm particles are higher than the simulated cutting force using 0.802 mm particles at cutting depths of 1.5 mm and 3 mm and very similar at a cutting depth of 0.5 mm. The reason might be that the larger particles break off easier, while the smaller particles are difficult to break owing to their high strength. When the particles break off, the force becomes smaller and therefore the cutting test simulation using larger particles gives lower cutting forces. At 0.5 mm depth of cut, on the other hand, chip formations are not that prominent and the 0.401 mm particles as well as the 0.802 mm particles scatter in the same way causing the forces to be similar.

At 0.5 mm depth of cut the simulated cutting force do not reach the experimental value and the force achieved with a blunt pick with 1.5 mm diameter wear flat is the nearest to the experimental value. The reason may be that the particles cannot be sliced by the pick and they are removed entirely when a bond is broken. When looking at Figure 38b and c, the simulated cutting force reaches the experimental value faster as the depth of cut increases, but the blunt pick with 1 mm diameter wear flat still give the closest values to the experimental one when cutting a sample with 0.401 mm particles. When cutting a sample with 0.802 mm particles, the value of the numerical force doesn't reach the experimental force at 1.5 mm depth of cut, but at 3 mm depth of cut a wear flat of 1.5 mm gives a close approximation of the experimental force.

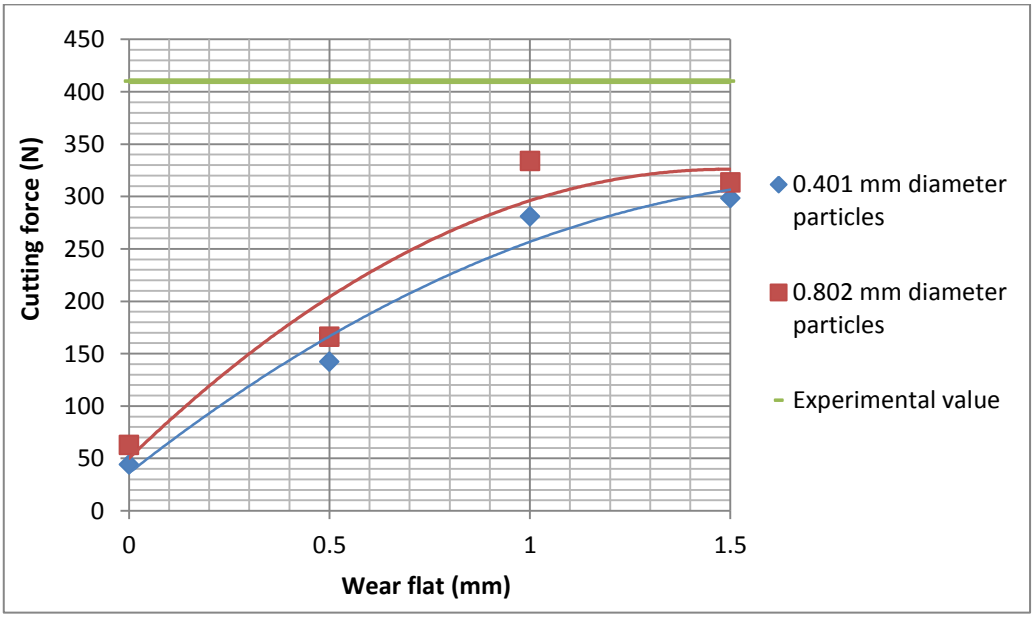

(a)

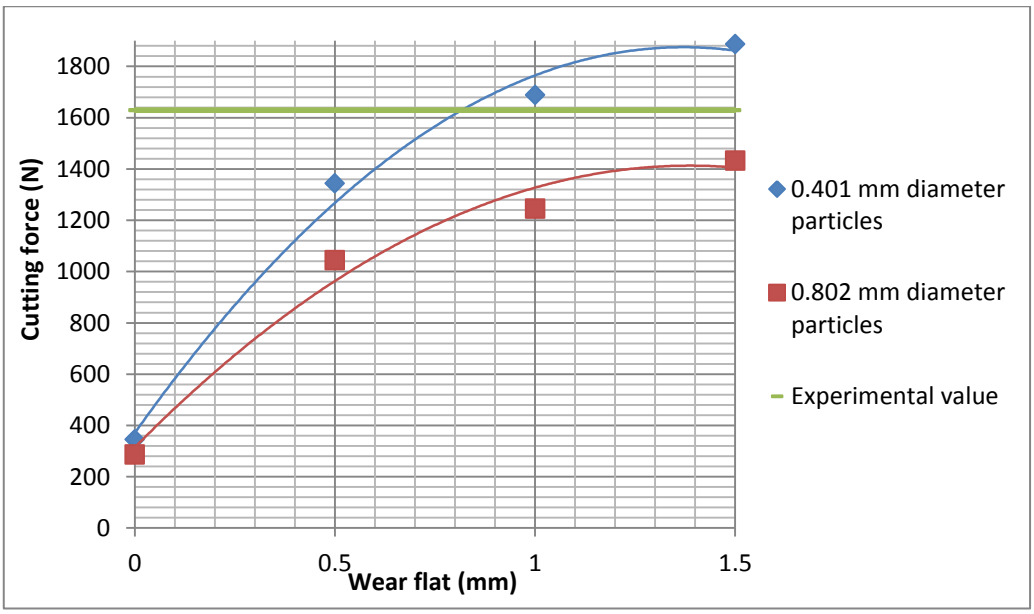

(b)

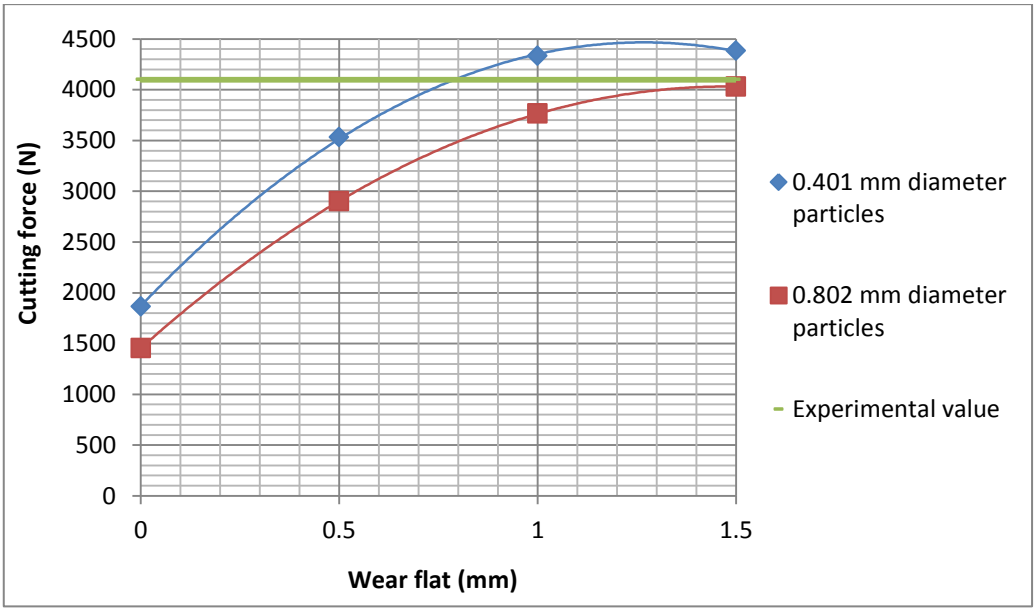

(c)

Figure 38: The influence of wear flat on cutting forces for narrow point-attack picks

0.5 mm depth of cut; (b) 1.5 mm depth of cut; (c) 3 mm depth of cut

The non-linear behaviour of the normal forces in Figure 39 below can also be fitted reasonably well with a 2nd order polynomial, except at 3 mm depth of cut it follows a linear trend. The same observations can be made about the influence of the size of the particles as in the case of the cutting forces. At each depth of cut the numerical values of the normal forces are about half the size of the experimental values. The simulated forces in the z-direction are therefore much smaller than it is during actual cutting. The reason why the numerical normal forces are so low, may be the fact that the particles cannot be broken into smaller pieces during the simulation, but the particle, as a whole, is cut off if its bond is broken. The pick is also not pushed downwards on the rock specimen as the velocity is applied

in the x-direction and that might be another reason for the low normal forces during the numerical simulation.

The numerical results of Su & Akcin (2011), in Appendix D, also showed that the normal forces were in each case lower than the cutting forces while it is in fact the other way around during the experimental cutting.

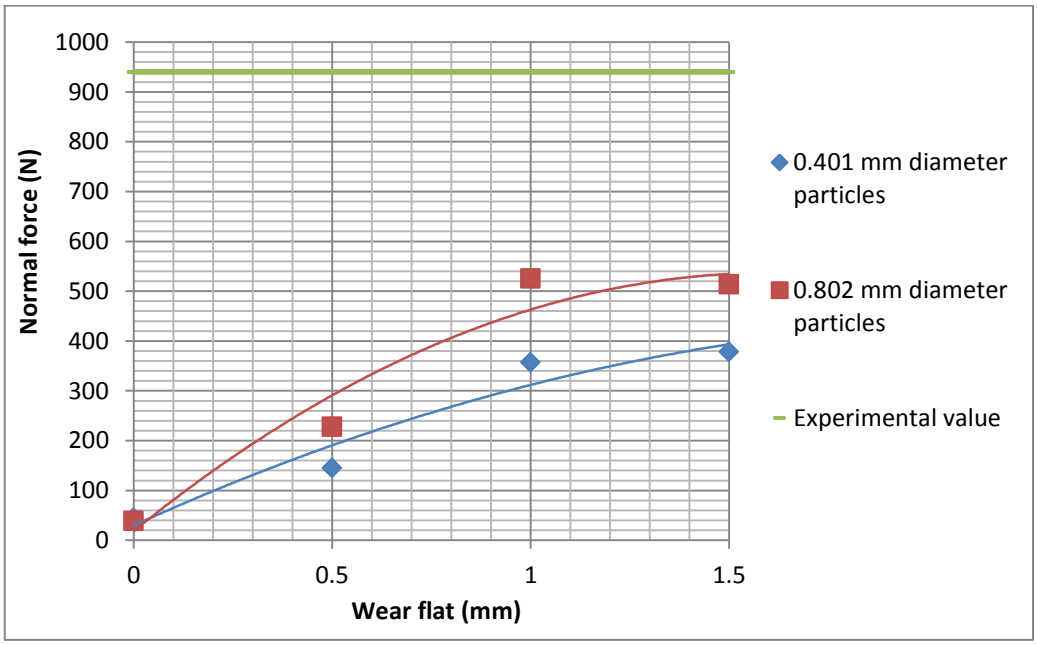

(a)

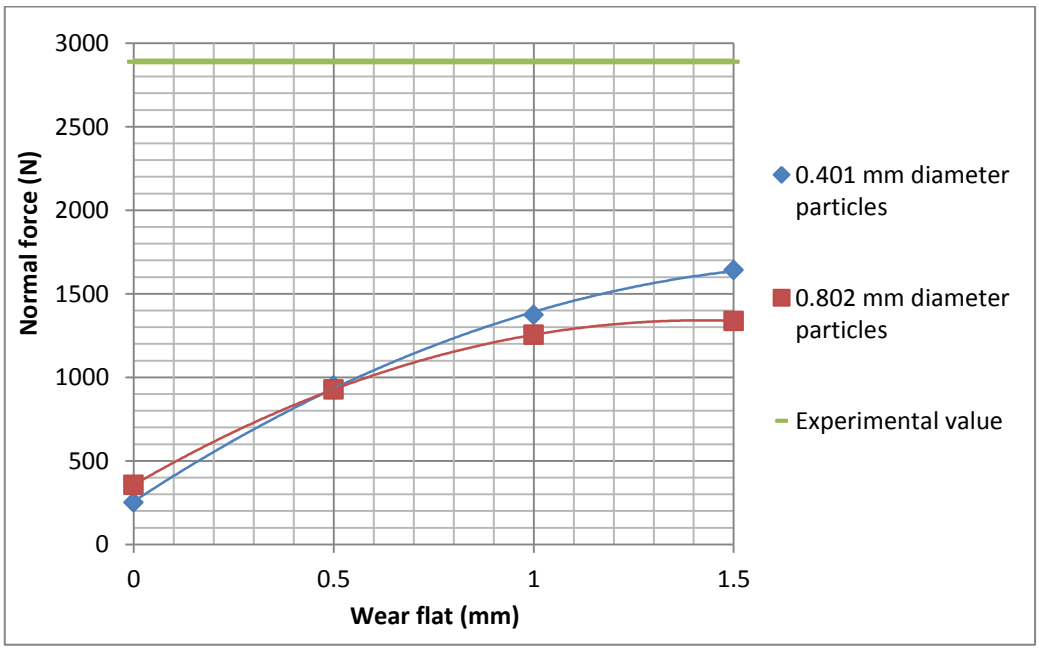

(b)

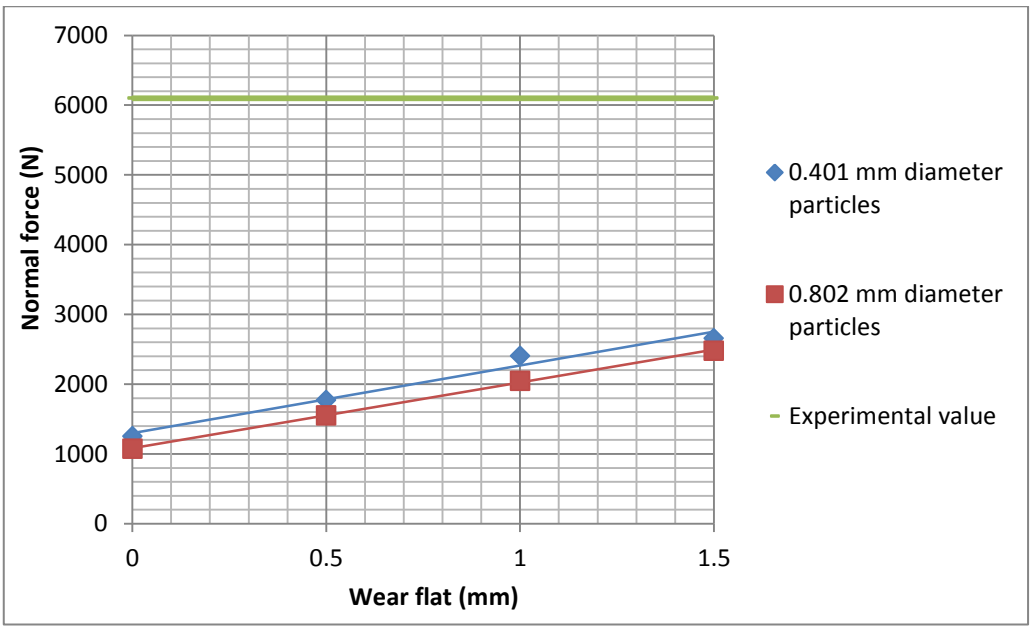

(c)

Figure 39: The influence of wear flat on normal forces for narrow point-attack picks

(a) 0.5 mm depth of cut; (b) 1.5 mm depth of cut; (c) 3 mm depth of cut

The forces simulated during cutting tests, using the parameters of Bilgin et al. (2006), are displayed in Figure 40. The experimental data of only the cutting forces were available in this case, but the numerical results of the normal forces will also be given in this section for interest.

At all three cutting depths the non-linear behaviour of the cutting forces can be fitted reasonably well with a 2nd order polynomial. The simulated cutting forces, in each simulation, were very similar for the two particle sizes used, except at 1.5 mm depth of cut there is a notable difference with the 0.401 mm particles giving higher force values. At 0.5 mm depth of cut the numerical cutting force, of a blunt pick with 1.5 mm wear flat, is still much lower than the experimental cutting force. At a cutting depth of 1.5 mm, the numerical value agrees with the experimental value of the cutting force at a wear flat of 0.5 mm cutting a sample with a particle size of 0.401 mm. At the same cutting depth, when cutting a sample with a particle size of 0.802 mm, the numerical value of the cutting forces reaches the experimental value at a wear flat of 1 mm. At a deeper depth of cut of 3 mm in Figure 40c, the experimental cutting force is reached even earlier before a wear flat of 0.5 mm.

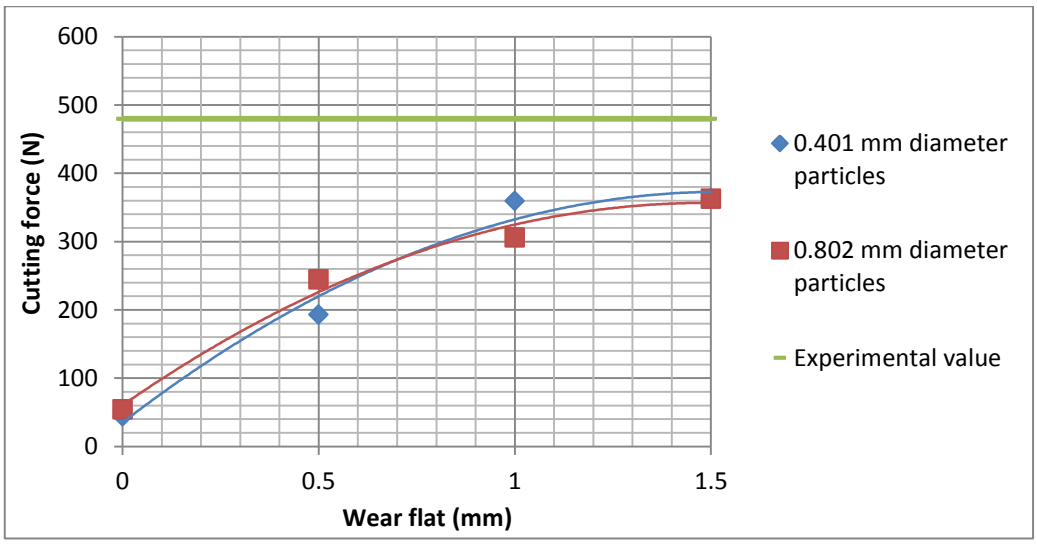

(a)

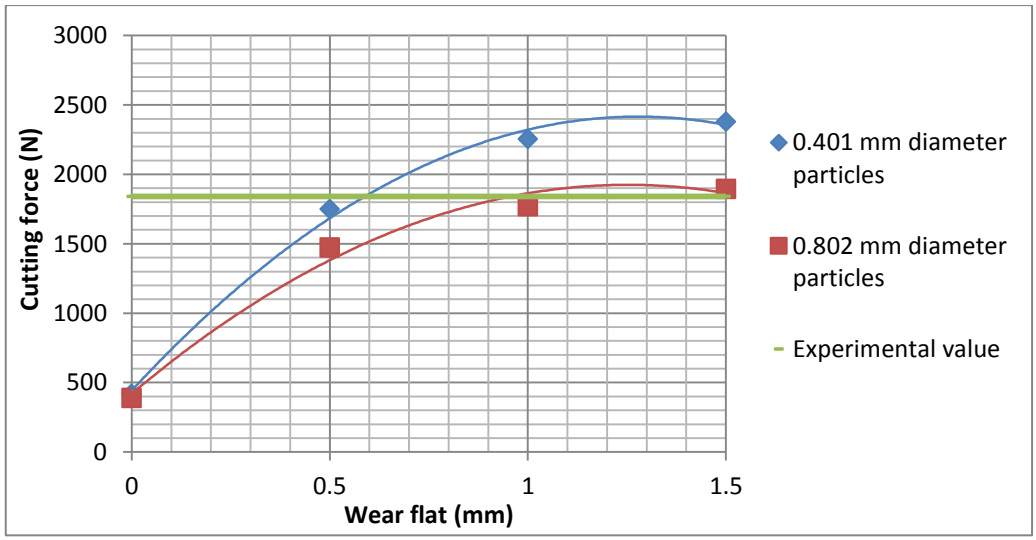

(b)

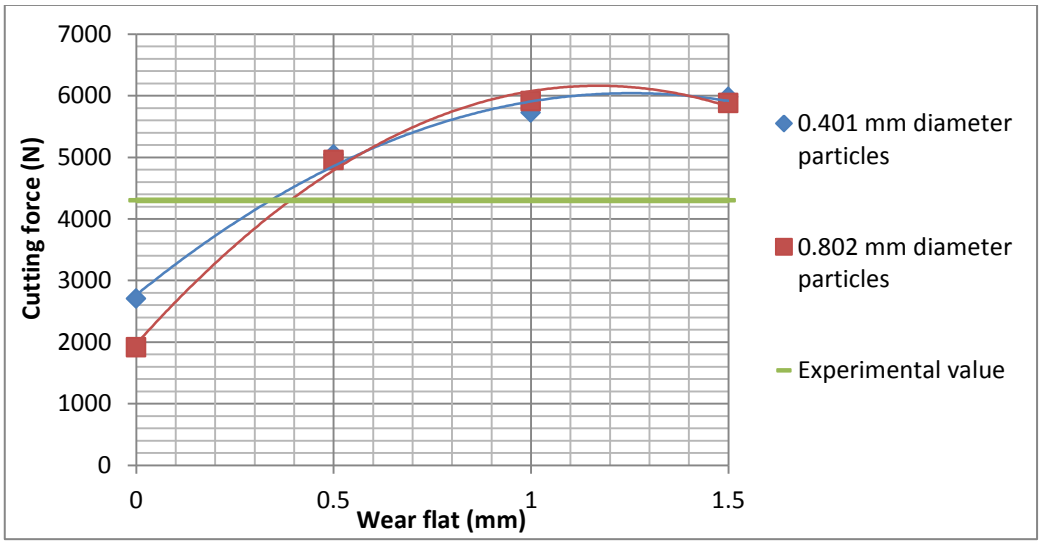

(c)

Figure 40: The influence of wear flat on cutting forces for wide point-attack picks

(a) 0.5 mm depth of cut; (b) 1.5 mm depth of cut; (c) 3 mm depth of cut

The variation of the normal forces with an increase in wear flat of the wide point-attack pick, at the different depths of cut, is shown in Figure 41. In each case the normal forces follow a 2nd order polynomial trend, except at 0.5 mm depth of cut it follows a linear trend when cutting a sample with 0.802 mm particles. The size of the particles in the rock sample only has a distinguished influence at a cutting depth of 0.5 mm using a blunt pick with 1 mm and 1.5 mm of wear flat respectively. In this case the sample with the 0.802 mm particles gave larger normal forces. At 1.5 mm and 3 mm depth of cut, the normal forces are quite similar for the two different rock samples.

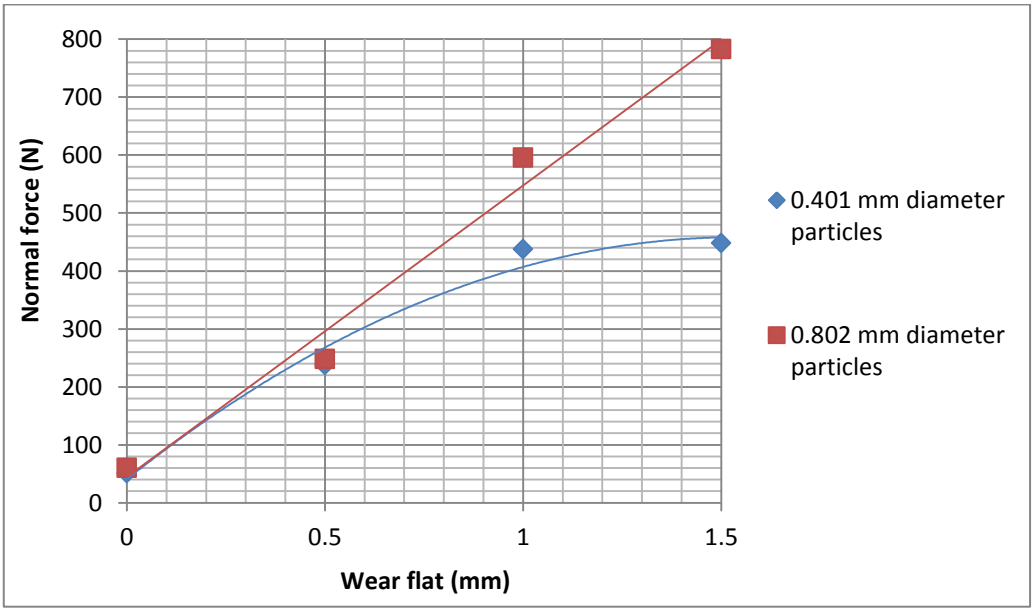

(a)

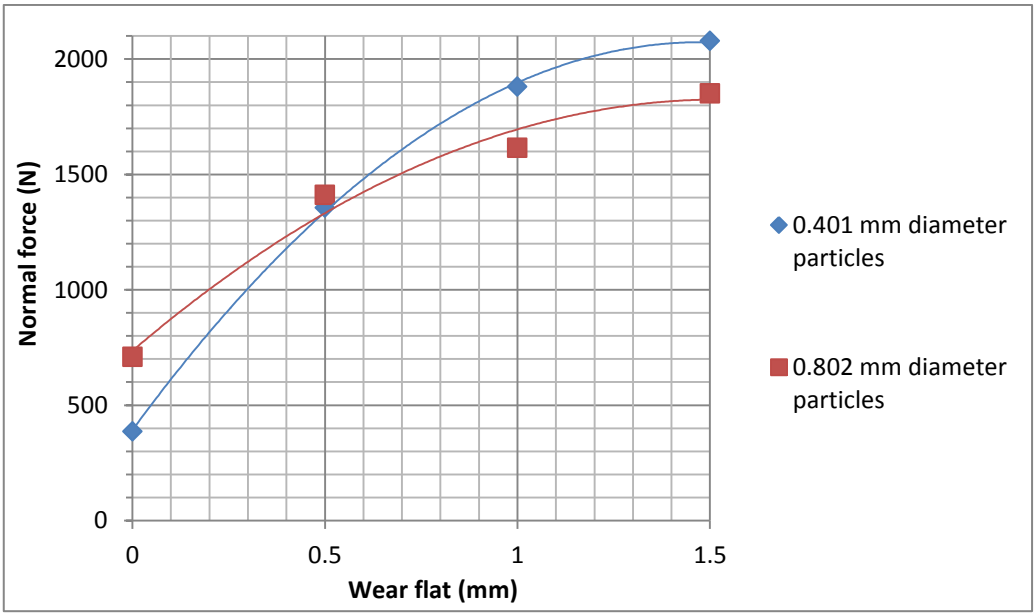

(b)

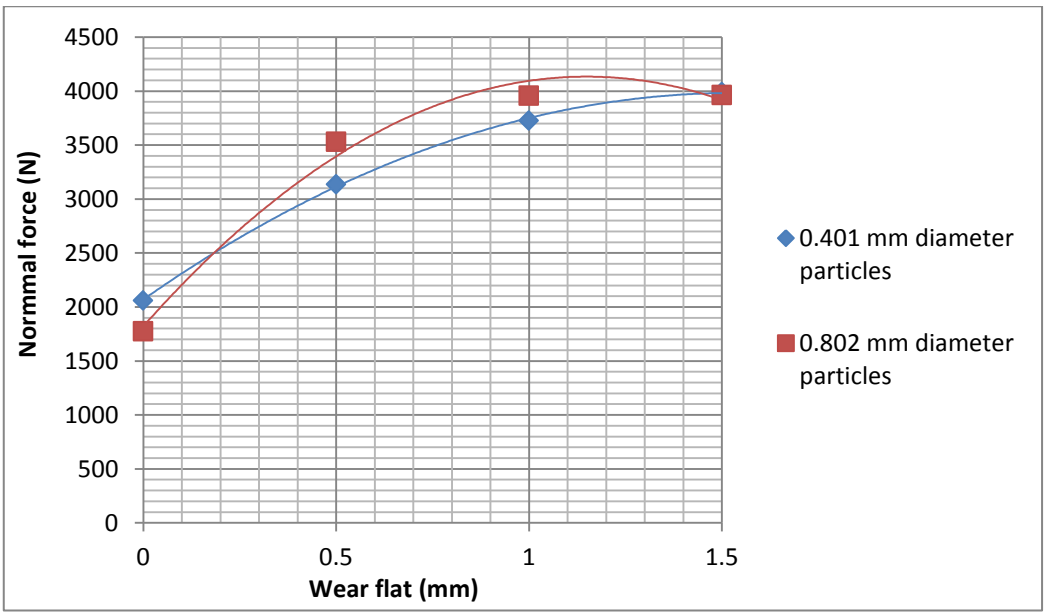

(c)

Figure 41: The influence of wear flat on normal forces for wide point-attack picks

(a) 0.5 mm depth of cut; (b) 1.5 mm depth of cut; (c) 3 mm depth of cut

After these observations it is obvious that the point-attack picks do not stay sharp throughout the cutting tests and the wear of the pick has to be considered during the numerical simulation. When using the parameters of Su & Akcin (2011) an average wear of 1 mm in diameter has to be considered, while an average wear of 0.5 mm in diameter has to be considered when using the parameters of Bilgin et al. (2006).

The influence of the particle size in the assembly is not that clear, but overall the smaller particle size of 0.401 mm gives better results. Since Sandstone-2 has a rather large uniaxial compressive strength, simulating the assembly out of smaller particles will also enhance the strength of the numerical rock.

6.4 Influence of depth of cut on forces

The influence of the depth of cut on the simulated forces is shown in Figure 42 and Figure 43 for the parameters of Su & Akcin (2011) and in Figure 44 and Figure 45 for the parameters of Bilgin et al. (2006). All the figures show the same trend, namely that the forces increase non-linearly with an increase in the depth of cut. The cutting mechanism becomes related to chipping as the depth of cut increases, which contributes to this non-linear increase in forces at deeper cuts. As discussed in section 2.7 a larger part of the point-attack pick is in contact with the specimen as the depth of cut increases and therefore the forces will also increase accordingly.

In these figures the large jump in the value of the cutting forces, at 1.5 mm and 3 mm depth of cut, from using a sharp point-attack pick to using a blunt pick with 0.5 mm diameter wear flat can be seen more clearly. As the wear flat increases from 0.5 mm to 1.5 mm, the difference in the cutting force values are

not that significant. This can be seen especially for the cutting forces at a depth of cut of 1.5 mm in Figure 42 and Figure 44, as well as for the normal forces when cutting a sample of 0.802 mm particles in Figure 45b. Consequently it can be said that a sharp point-attack pick cuts more efficiently and at a certain wear flat a further increase in the wear of the pick won't increase the cutting force anymore.

When comparing the trends of the normal forces in Figure 43 and Figure 45b to the trends of the cutting forces in Figure 42 and Figure 44, it can be seen that the cutting forces of the sharp and blunt picks are very similar at a cutting depth of 0.5 mm, in other words the first group of data points in each graph, while there is a notable difference in the values of the normal forces with the increasing wear flat at 0.5 mm depth of cut. The difference in the normal force values, with an increasing wear flat, does not become insignificant at the deeper depths of cut as in the case for the cutting forces.

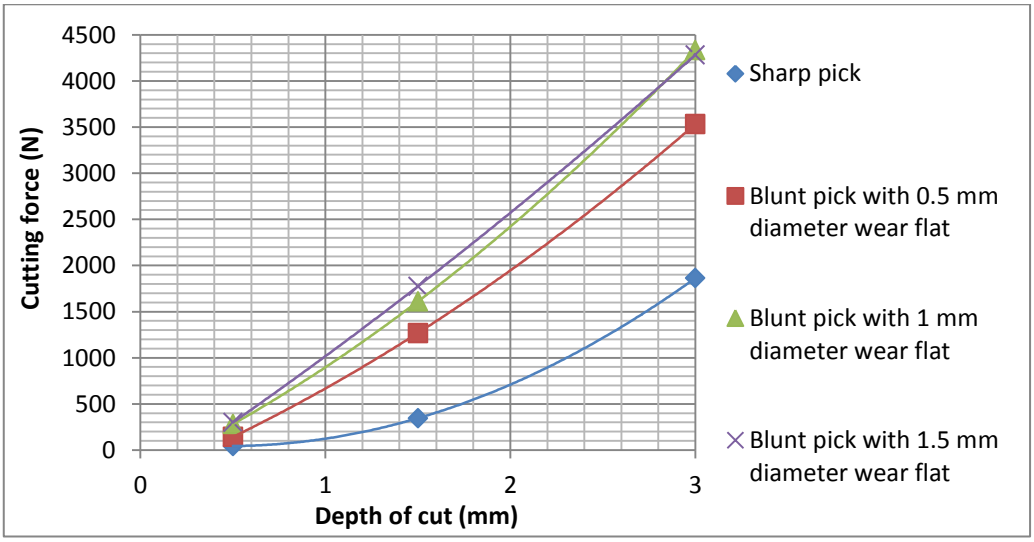

(a)

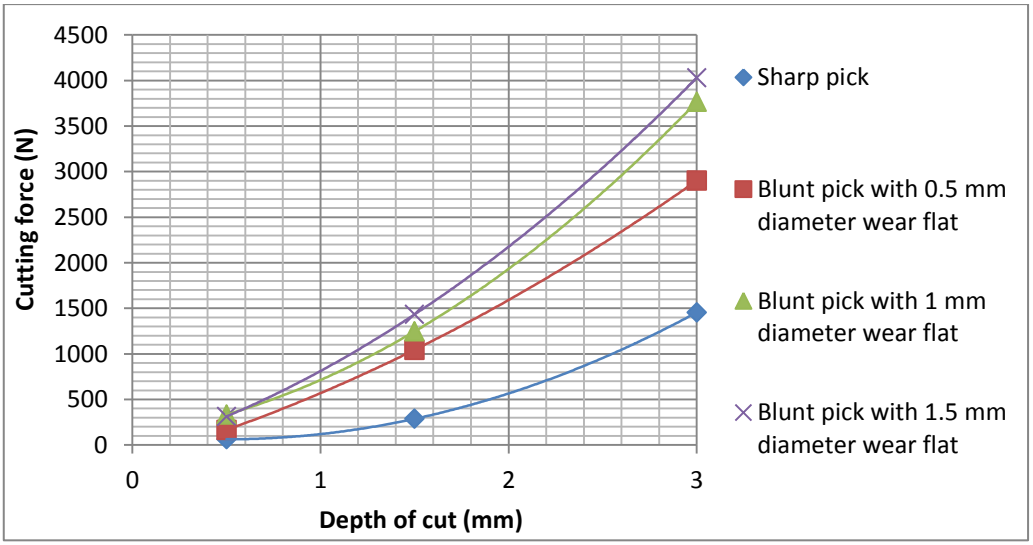

(b)

Figure 42: The influence of depth of cut on cutting forces for a narrow point-attack pick

(a) Sample with 0.401 mm particles; (b) Sample with 0.802 mm particles

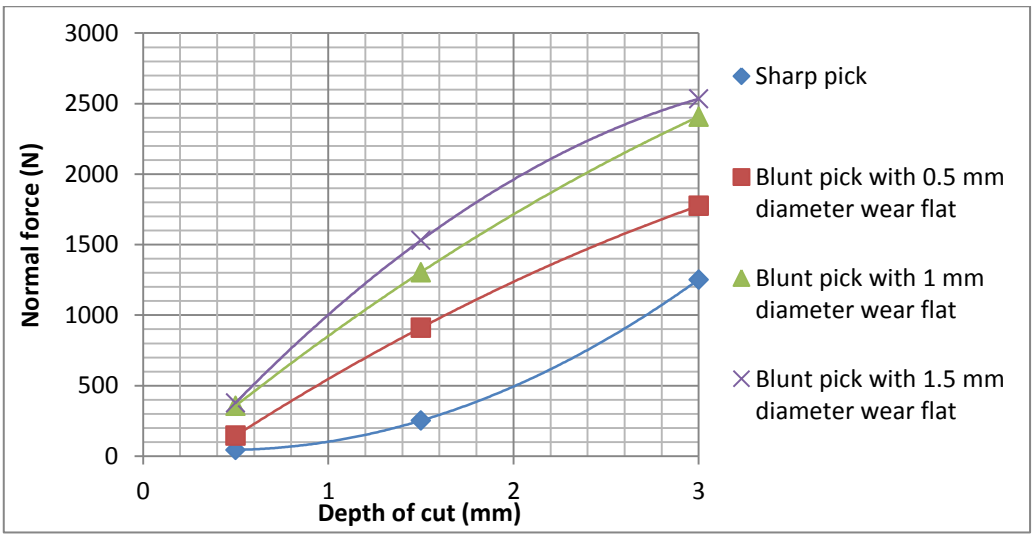

(a)

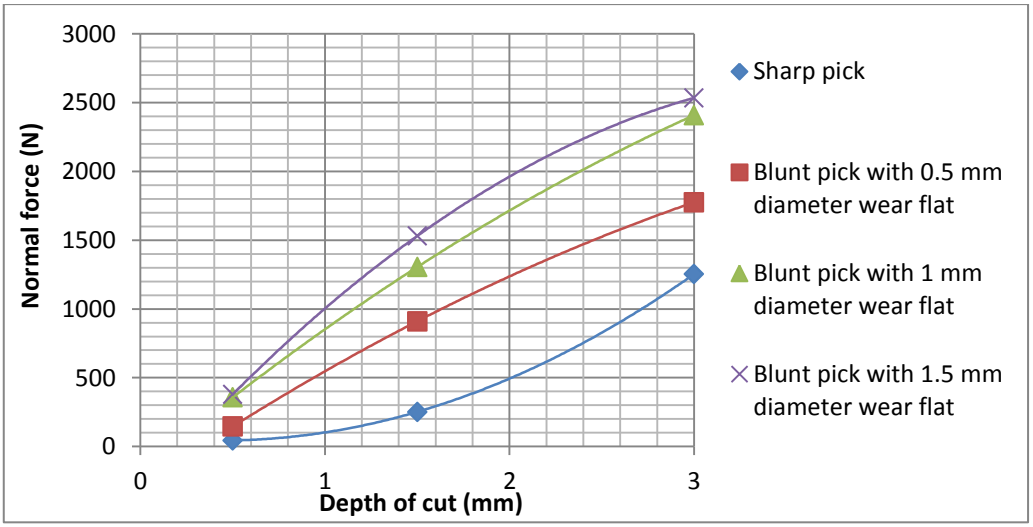

(b)

Figure 43: The influence of depth of cut on normal forces for a narrow point-attack pick
(a) Sample with 0.401 mm particles; (b) Sample with 0.802 mm particles

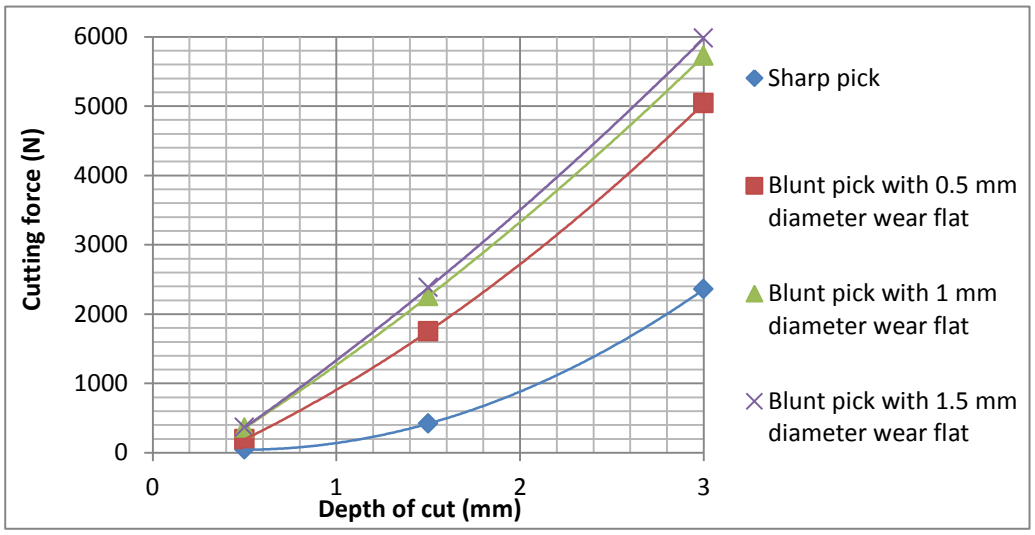

(a)

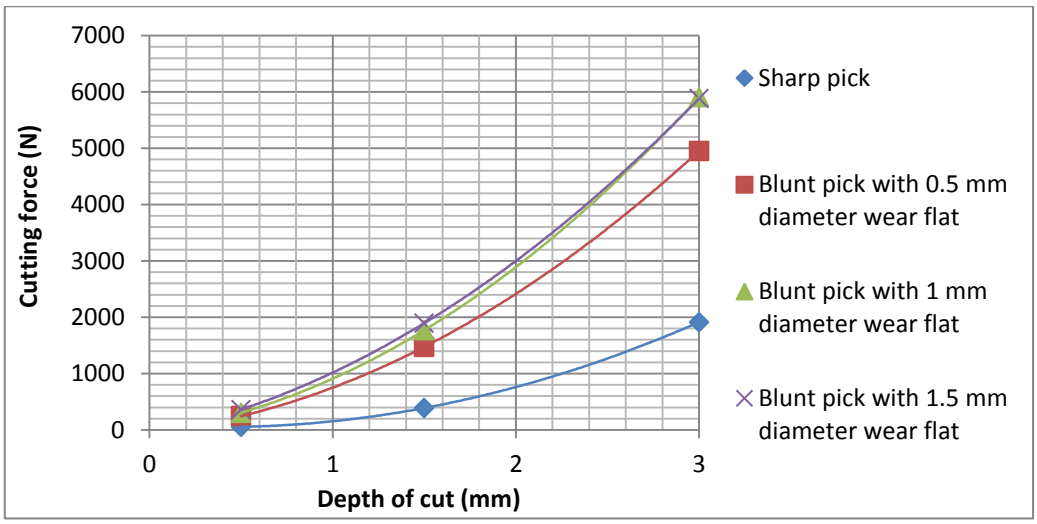

(b)

Figure 44: The influence of depth of cut on cutting forces for a wide point-attack pick

(a) Sample with 0.401 mm particles; (b) Sample with 0.802 mm particles

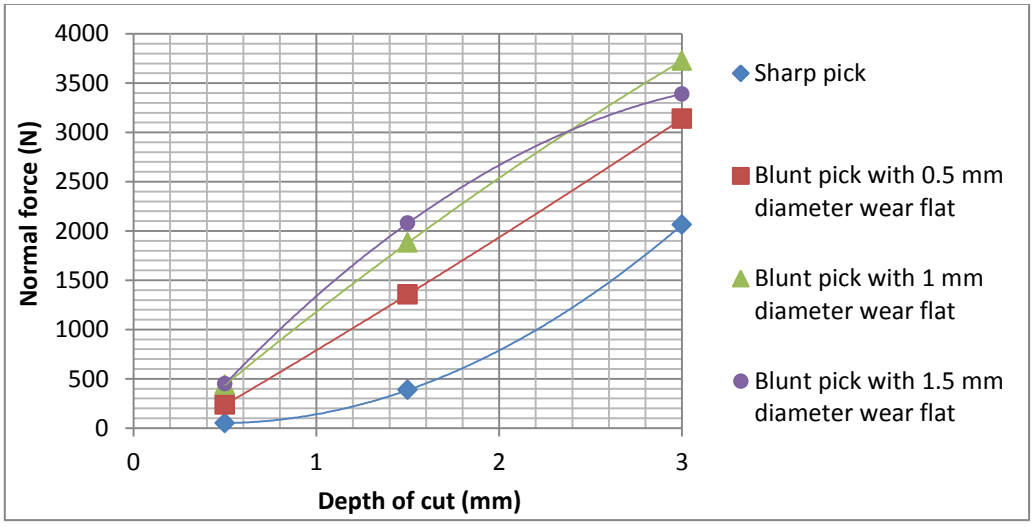

(a)

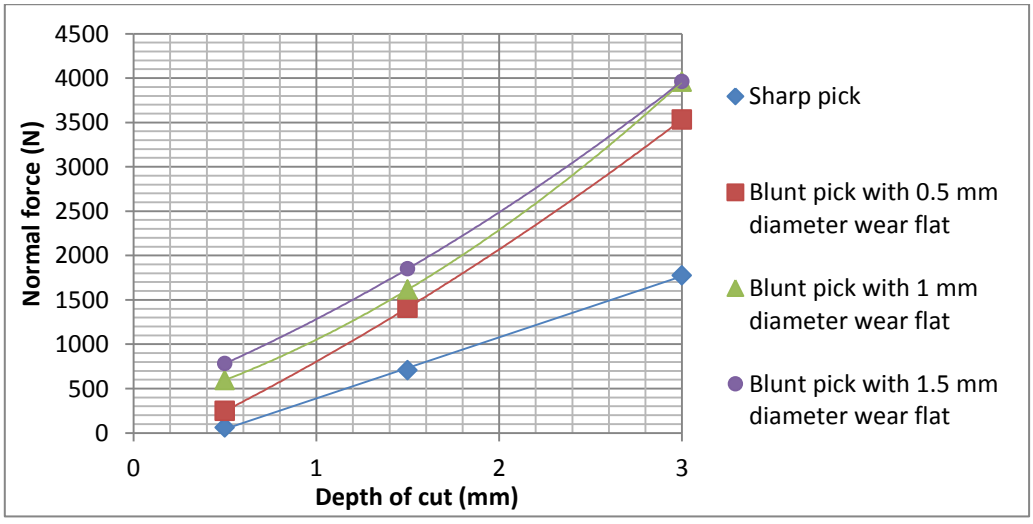

(b)

Figure 45: The influence of depth of cut on normal forces for a wide point-attack pick

(a) Sample with 0.401 mm particles; (b) Sample with 0.802 mm particles

After observing the graphs, it can be seen that the depth of cut has a definite influence on the cutting and normal forces. At the shallow depths of cut, from 0.5 mm to 1.5 mm, the increase in the forces is almost linear and as previously stated it becomes non-linear at the deeper depth of cut. Therefore it can be said that the rate at which the forces become larger, increases rapidly as the depth of cut increases. The cutting process will also become more challenging at the deeper depths of cut, since there is a greater build-up of particles in front of the pick than at shallow depths of cut.

CHAPTER 7:

PFC3D™ MATERIAL RESPONSE OF ROCK CUTTING WITH A CHISEL-SHAPED PICK

7.1 Overall results

Summarized herein are the most important results found throughout the study on the simulation of rock cutting with a chisel-shaped pick using the parameters of Balci & Bilgin (2007). The forces found by means of numerical simulation will also be compared to the forces obtained during experimental cutting tests and those calculated theoretically.

As described in section 4.3, the comparison of the numerical to the experimental cutting test with the chisel-shaped tool could only be done at 5 mm depth of cut because of a lack of information. However in this study a cutting test at 0.5 mm depth of cut was also simulated to see what would happen at a lower cutting depth.

As for the PFC3D™ cutting test simulations with point-attack picks, the three orthogonal forces acting on the chisel-shaped pick were also monitored and the histories were recorded. The cutting forces were monitored by summing all the forces acting on the pick in the x-direction at each time step, while the normal forces were monitored by summing all the forces in the z-direction. The experimental study of Balci & Bilgin (2007) contained information only about the cutting and normal forces and little attention was paid to the sideways forces. In Figure 46 the variations of the simulated sideways forces during a cutting test with a sharp chisel-shaped pick at 5 mm depth of cut are illustrated. The graphs of the sideways forces look very similar for the simulations cutting samples with 0.802 mm particles. It is shown that the sideways forces fluctuate around zero and therefore it is evident that these forces didn't have a great influence on the cutting process.

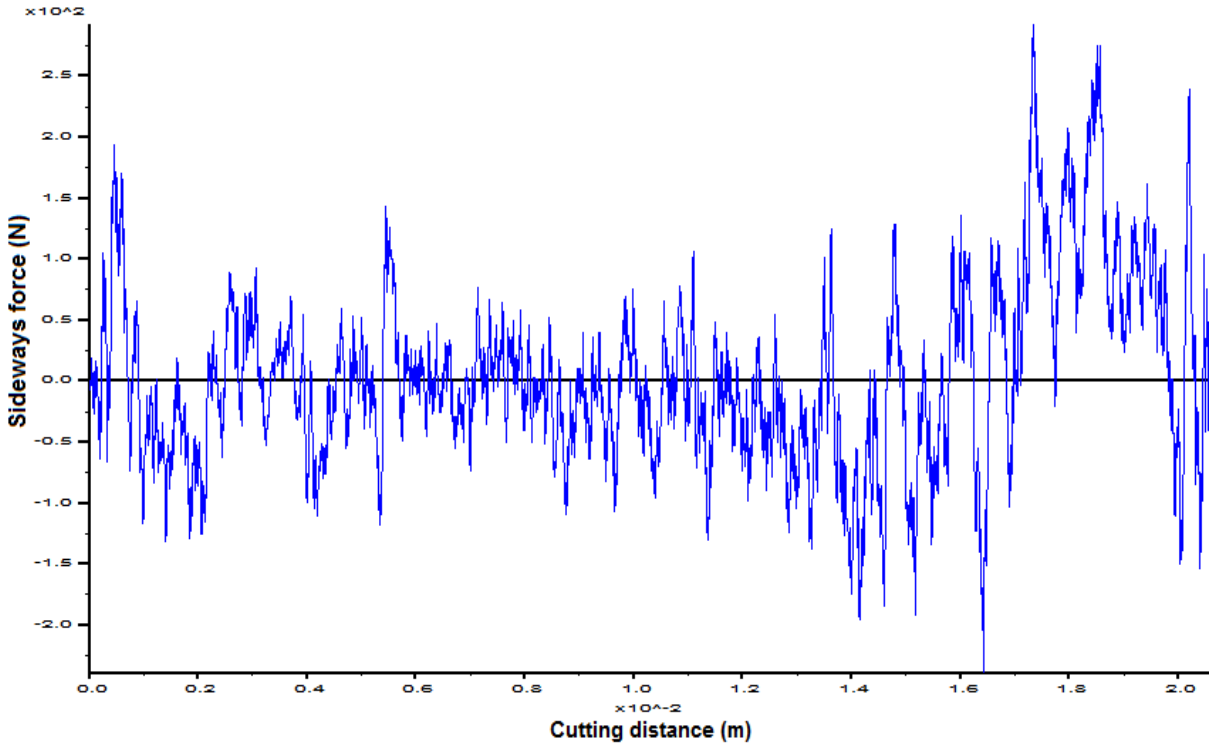

Figure 46: The variation of sideways forces versus cutting distance at 5 mm depth of cut

The graphs of the cutting and normal forces for the chisel-shaped picks at each depth of cut can be seen in Figure 47 and Figure 49. To repeat, the black curves represent the cutting forces and the red curves represent the normal forces. The mean cutting and normal forces are shown with dashed lines and the values are given on the right of the graphs.

When analysing Figure 47, it can be seen that the cutting forces continuously increase over the entire cutting distance at a cutting depth of 5 mm. The reason for this occurrence is that at the start of the simulation there are only a few particles in front of the pick which makes the resulting forces small. As the pick moves forwards, the particles are pushed against the wall of the pick and they build up in front of it, resulting in an increase of the forces. When the particles break off, the forces become smaller again. Since the rock sample has a depth of 25 mm, this cutting depth of 5 mm is quite large and the particles do not break off easily, resulting in the increase of the cutting forces over the cutting distance. When cutting a sample with 0.401 mm particles, the cutting forces reach a steady value of 4484 N between a cutting distance of 4 and 9 mm, but overall the average value is 9790 N. The same observation is made when cutting a sample with 0.802 mm particles. In this case the average value between a cutting distance of 4 and 9 mm is 2805 N and the overall average value is 8076 N. The cutting forces are therefore smaller when cutting larger particles.

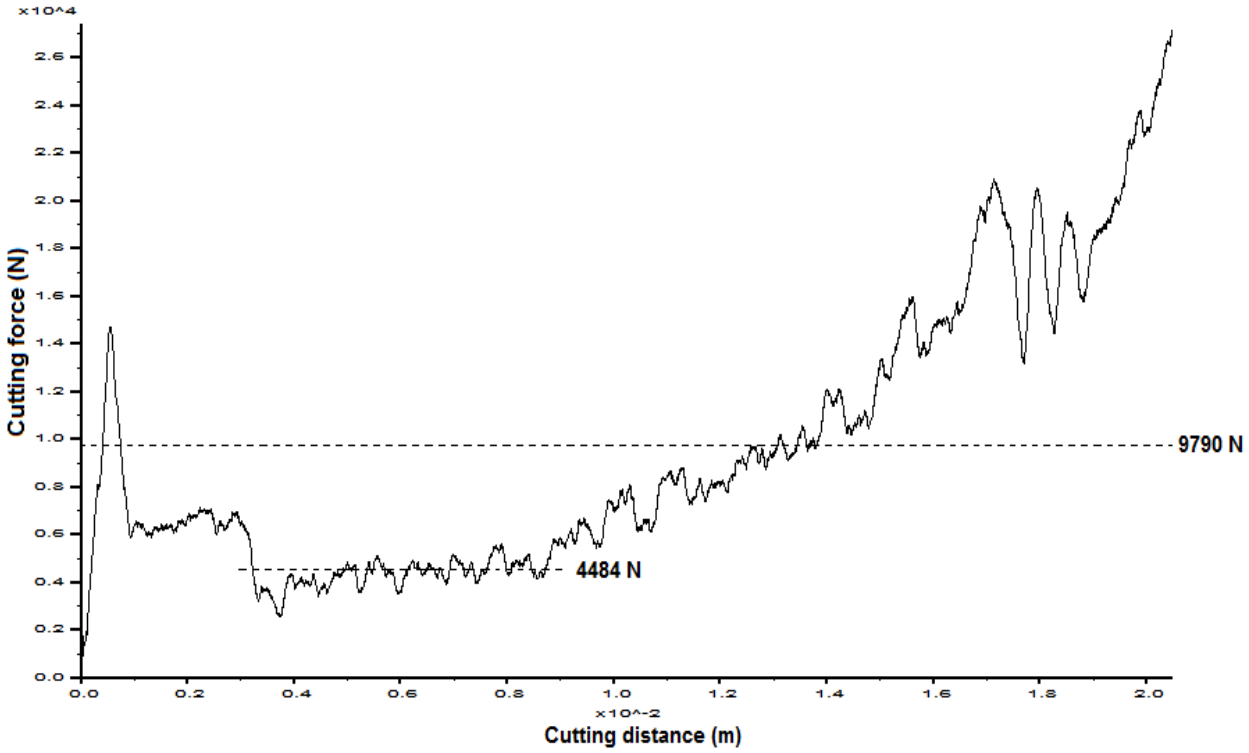

(a)

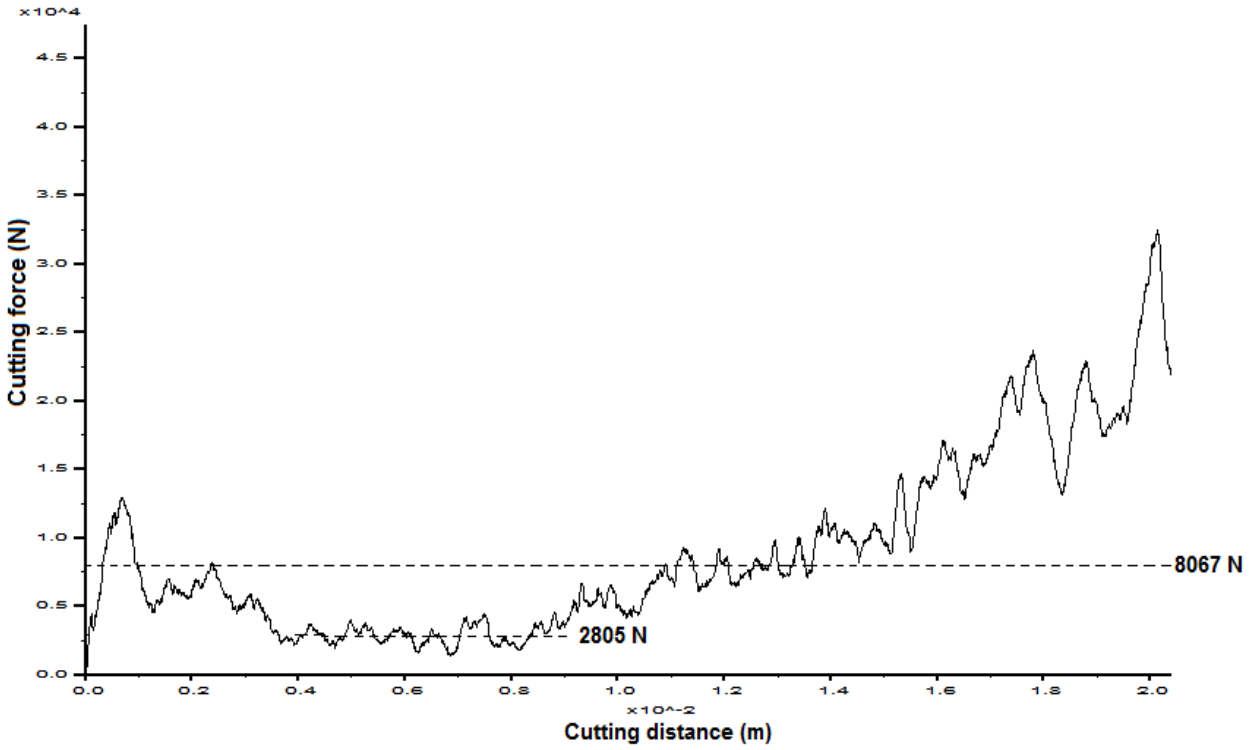

(b)

Figure 47: The variation of cutting forces versus cutting distance for a chisel-shaped pick at 5 mm depth of cut

(a) Sample with 0.401 mm particles; (b) Sample with 0.802 mm particles

When cutting a sample with 0.401 mm particles, the normal forces in Figure 48a, follow the same trend as the cutting forces in Figure 47 and it also reaches a steady value of 974 N between a cutting distance of 4 and 9 mm. The overall average value of the normal forces is 1763 N. When cutting a sample with

0.802 mm particles, the normal forces are more stable and fluctuate around an average value of 1985 N. In this case the normal forces are also larger.

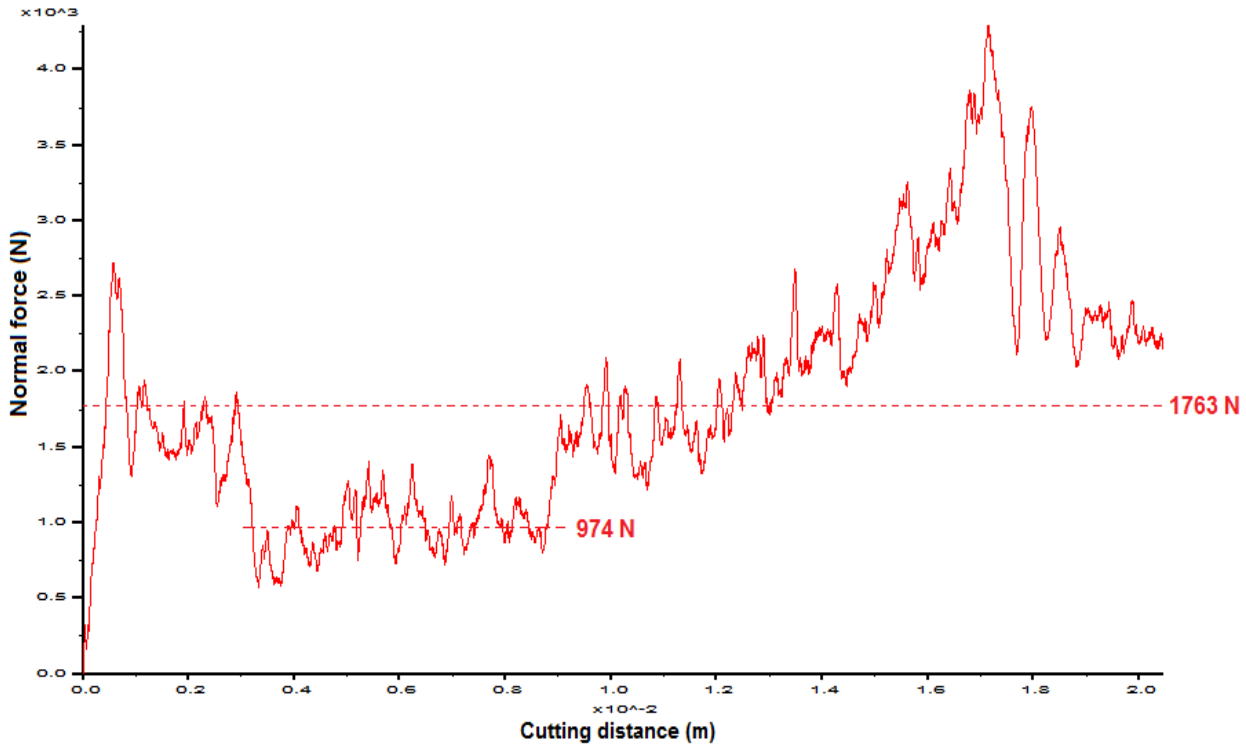

(a)

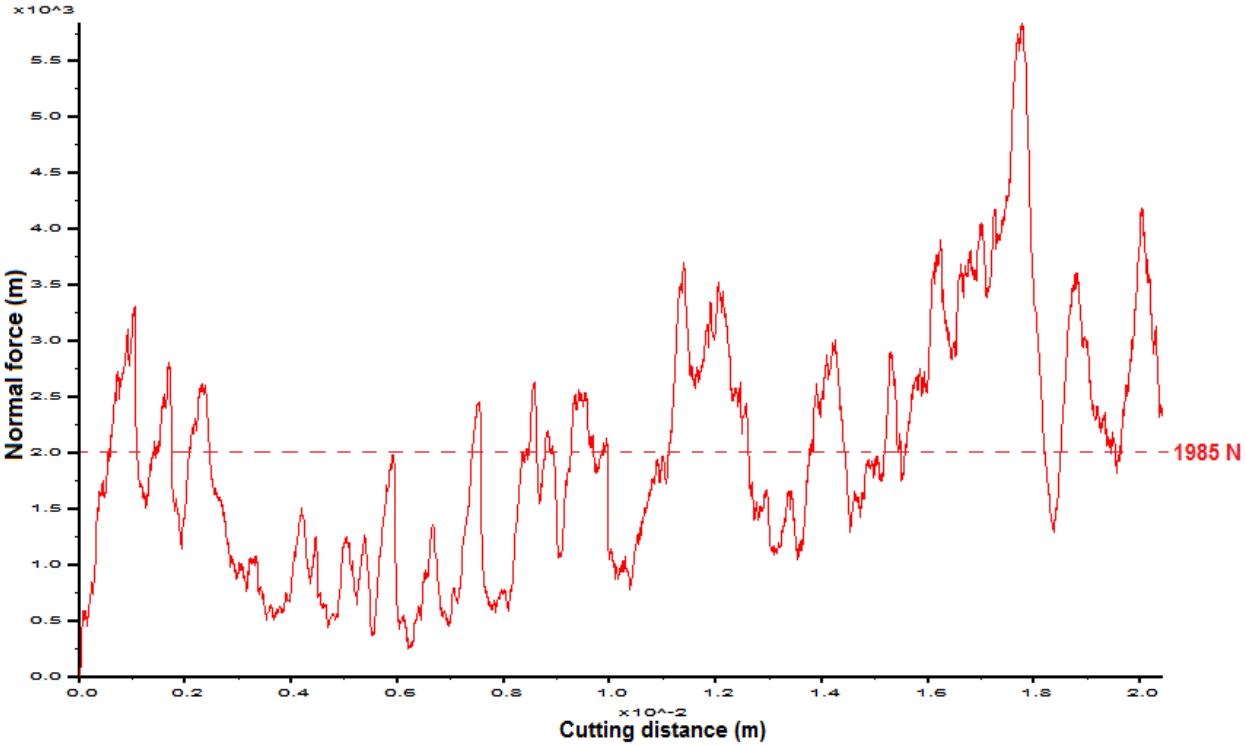

(b)

Figure 48: The variation of normal forces versus cutting distance for a chisel-shaped pick at 5 mm depth of cut

(a) Sample with 0.401 mm particles; (b) Sample with 0.802 mm particles

The simulated forces of the point-attack picks in chapter 6 increased over the first few millimetres of the cutting distance and then became stable and fluctuated around an average value. In this case, with the chisel-shaped pick at 5 mm depth of cut, the forces are stable more or less at the beginning of the simulation and then they increase over the rest of the cutting distance. The reason may be the larger cutting depth and the fact that the chisel-shaped pick is in contact with the entire width of the rock sample from the beginning to the end of the simulation.

The tool forces in Figure 49 were recorded during the cutting tests at 0.5 mm depth of cut. It can be seen that the cutting and normal forces follow the same trend as the cutting tests with point-attack picks at shallow depths of cut and they are more stable than the forces at 5 mm depth of cut. The average cutting force for cutting a sample with 0.401 mm particles is 974 N and for cutting one with 0.802 mm particles is 627 N. The average normal force is 377 N and 396 N for cutting a sample with 0.401 mm particles and one with 0.802 mm particles respectively. It can be seen again that the cutting forces are larger for a sample with smaller particles, while the normal forces are larger for a sample with larger particles. The same reasons can be given for this observation as were given in the previous chapter.

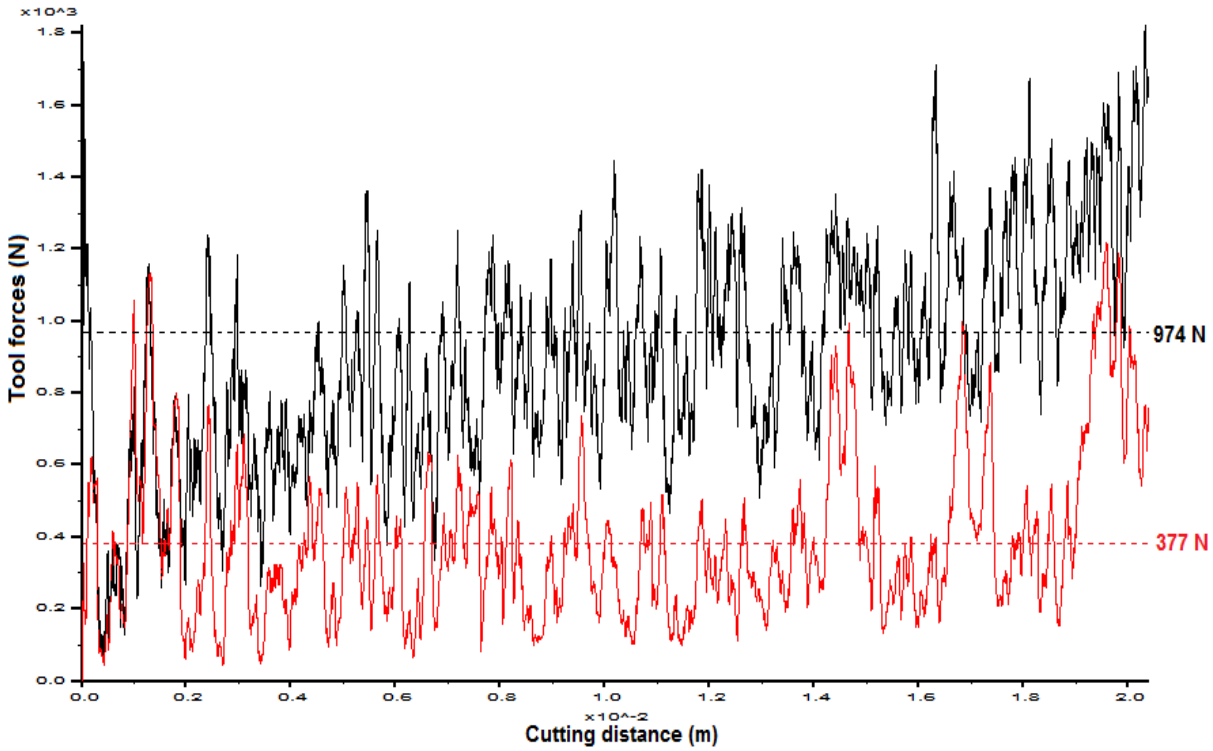

(a)

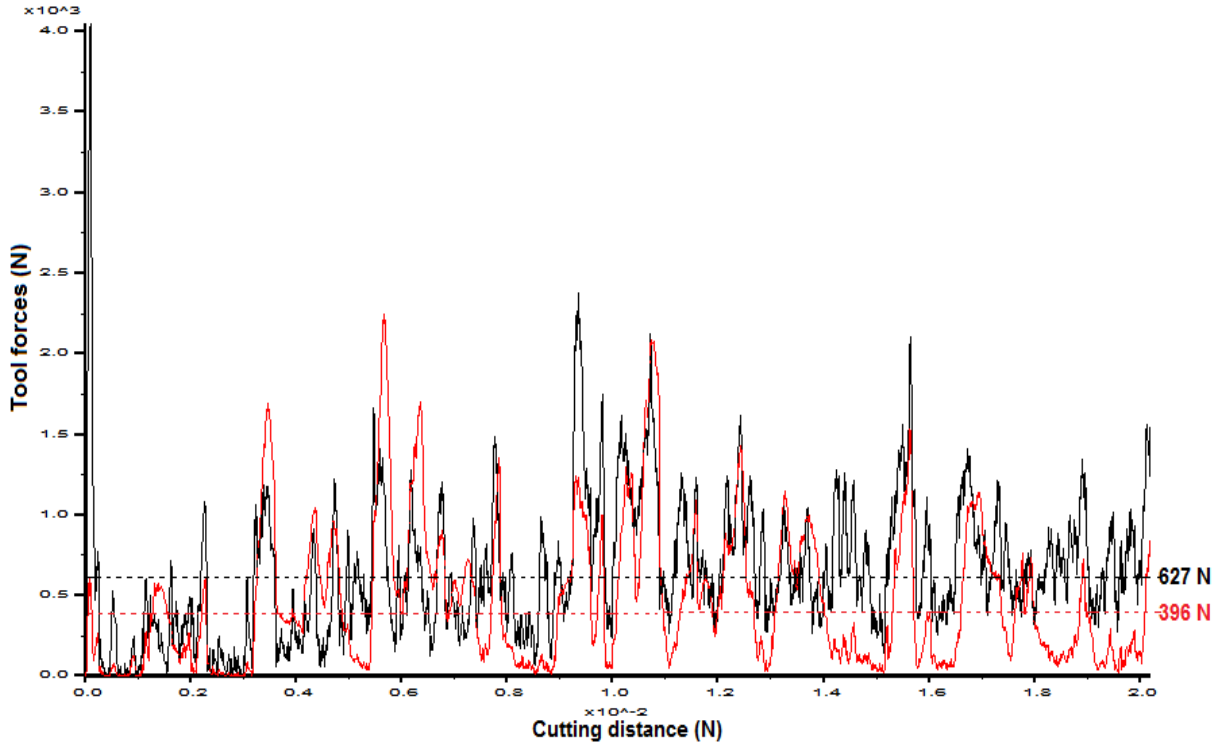

(b)

Figure 49: The variation of tool forces versus cutting distance for a chisel-shaped pick at 0.5 mm depth of cut

(a) Sample with 0.401 mm particles; (b) Sample with 0.802 mm particles

The variation of the tool forces is also expressed with the standard deviation in Figure 50. Unlike the case with point-attack picks, the standard deviation becomes higher at the deeper depth of cut. The reason is the continuous increase in the forces as seen in Figure 47 and Figure 48. The high standard deviation indicates the large spread in the force values. At 0.5 mm depth of cut the standard deviation is low which shows that the forces are closer to the average value or in other words little variation in forces.

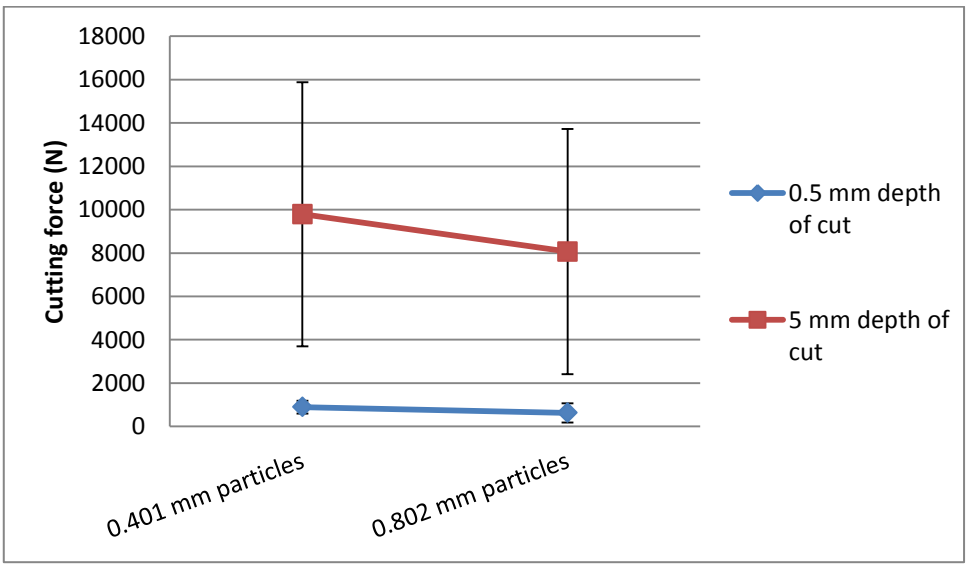

(a)

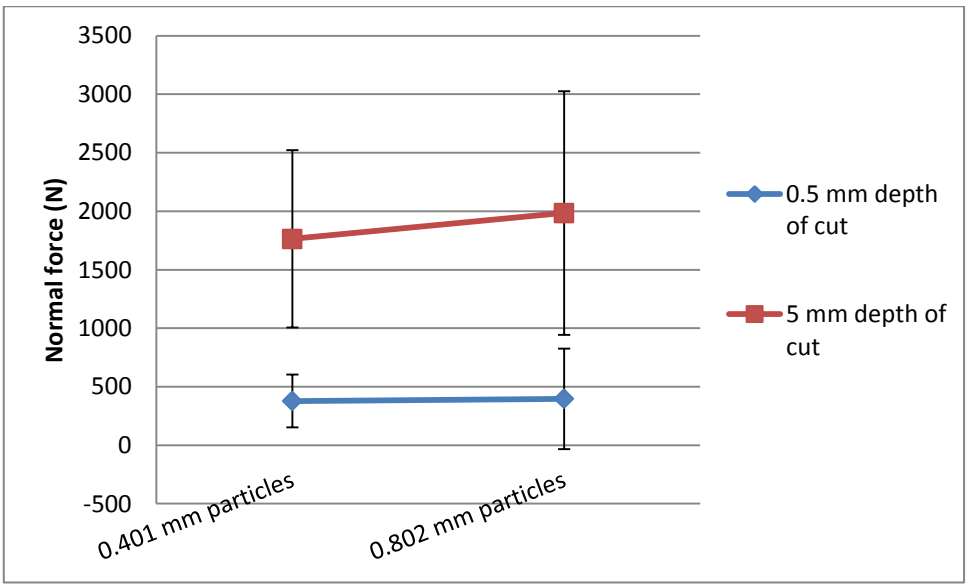

(b)

Figure 50: Average force and standard deviation of forces when cutting with a chisel-shaped pick
(a) Cutting forces; (b) Normal forces

The Sandstone-2 specimen and the sharp chisel-shaped pick at 0.5 mm and 5 mm depth of cut are shown in Figure 51 and Figure 52 after 20 mm of cutting distance. After the chisel-shaped pick began to interact with the particles, micro-cracks were initiated and they propagated from the front of the pick. These micro-cracks formed when bonds were broken in the simulation and they are also an indicator of the damage on the specimen. In Figure 51 the black spots represents the micro-cracks due to tensile bond failure, while the red spots represents the micro-cracks due to shear bond failure. Just underneath the chisel-shaped pick the rock sample cracked throughout the width of the sample during the cutting test at 5 mm depth of cut. This shows that 5 mm depth of cut is too deep for the depth of the rock sample and this simulation is not very realistic. Little damage occurred during the cutting test at 0.5 mm depth of cut, with cracks only a few millimetres beneath the cut. The micro-cracks also led to chip formations which can be seen in front of the pick at the top of the sample in Figure 52. The chip formations are greater and more compact in front of the pick at the deeper depth of cut, while more particles broke off one by one in front of the pick at the lower depth of cut.

Although the stiffness of the walls around the specimen was decreased to a fraction of 0.001 of the average particle normal stiffness to simulate a soft confinement, it can be seen in Figure 51 and Figure 52 that the wall at the right side did not deform under the force and the particles were pushed against it. This was probably the reason for the continuous increase in the forces seen in Figure 47 and Figure 48.

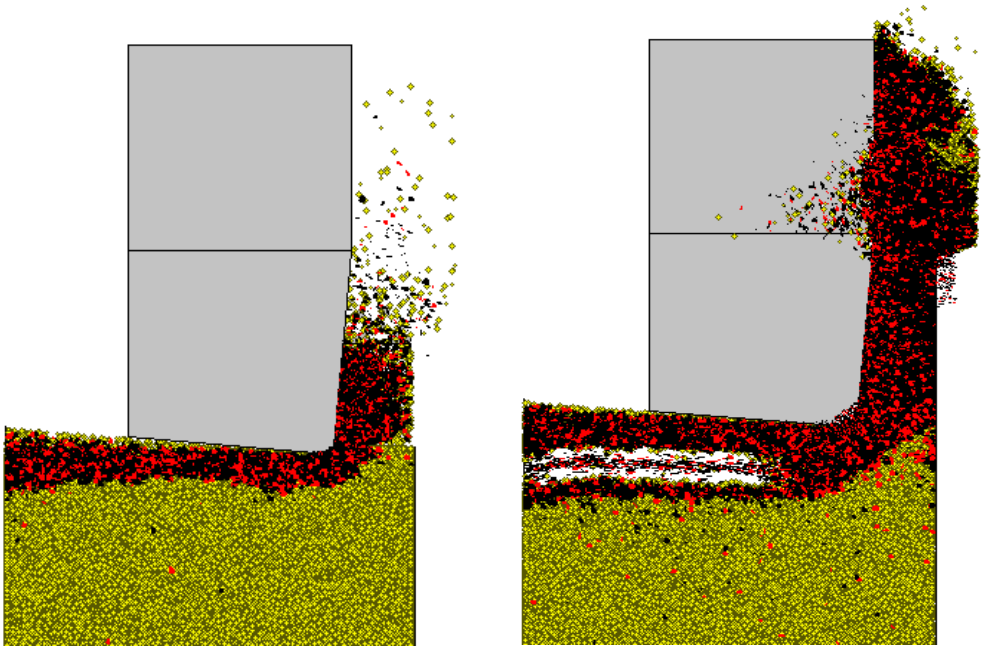

(a) (b)

Figure 51: The schematic view of the micro-cracks occurring around the chisel-shaped pick
(a) 0.5 mm depth of cut; (b) 5 mm depth of cut

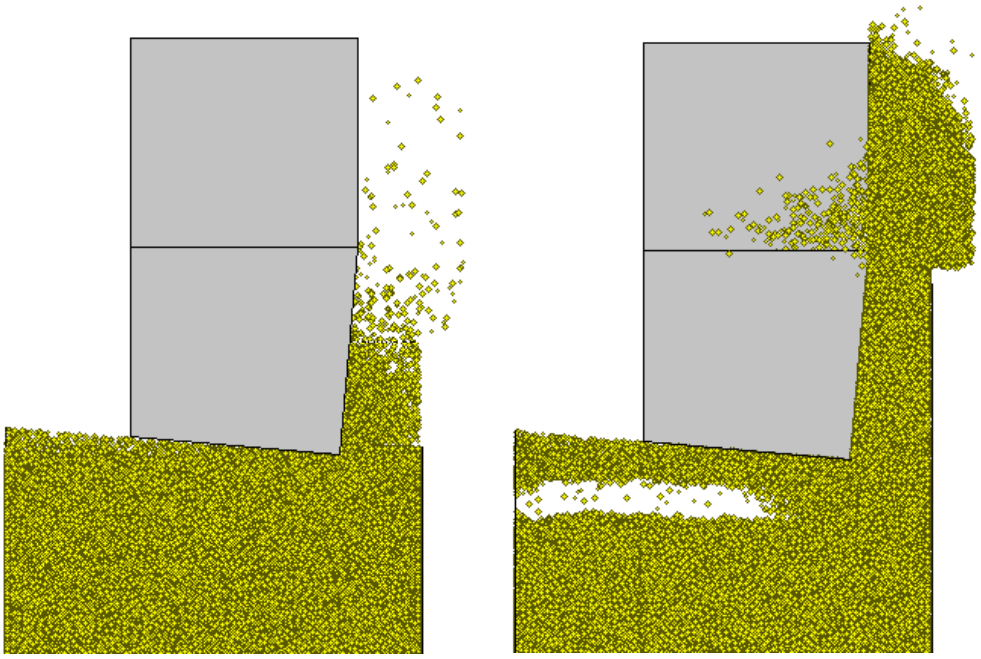

(a) (b)

Figure 52: The schematic view of the chip formation in front of the chisel-shaped pick
(a) 0.5 mm depth of cut; (b) 5 mm depth of cut

The number of micro-cracks formed, increases over the cutting distance and this is illustrated in Figure 53, which shows the micro-cracks recorded during the cutting of samples with 0.401 mm particles. At 0.5 mm and 5 mm depth of cut the number of micro-cracks increase at a fast rate over the first millimetre of cutting distance and then the rate slows down and the increase in the number of micro-

cracks becomes linear for the rest of the cutting distance. The same trends were seen when cutting samples with 0.802 mm particles.

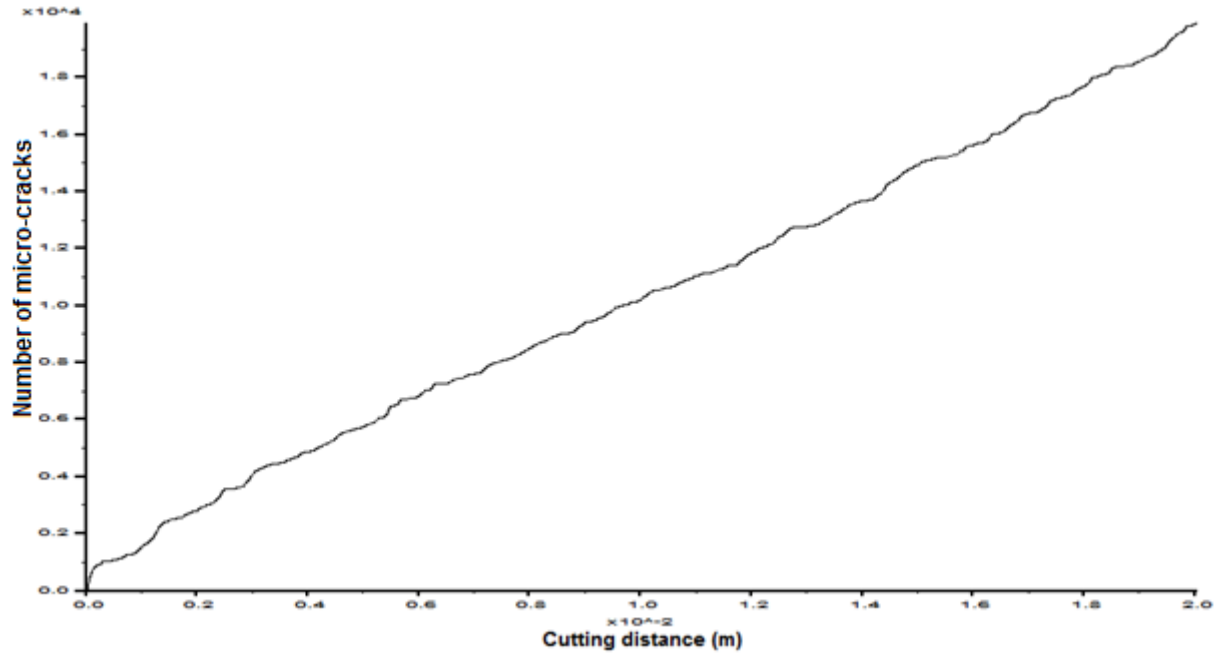

(a)

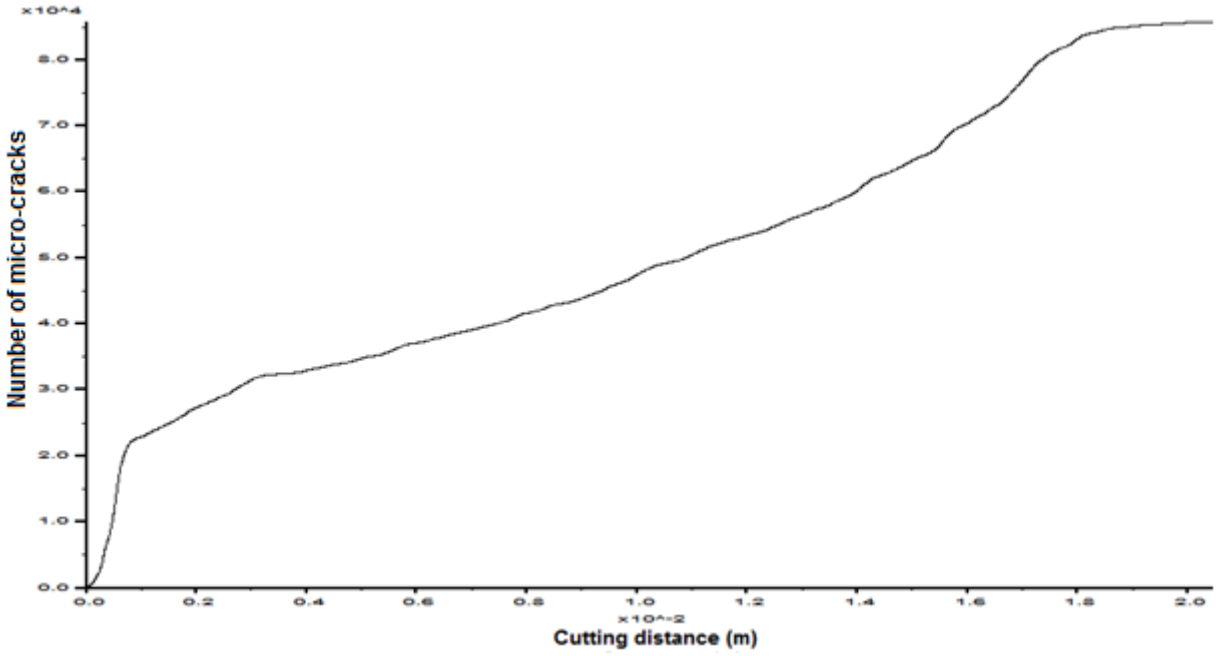

(b)

Figure 53: The number of cracks versus cutting distance for a chisel-shaped pick
(a) 0.5 mm depth of cut; (b) 5 mm depth of cut

Table 11 gives a summary of the number of micro-cracks formed during each simulation with the chisel-shaped pick. It can be seen that the number of micro-cracks was a lot less when cutting a sample with 0.802 mm particles in comparison to the sample with 0.401 mm particles. At a cutting depth of 5 mm and cutting a sample with 0.401 mm particles, the number of micro-cracks was 85820, which is a lot

more than the number of micro-cracks formed when cutting with point-attack picks at a cutting depth of 3 mm. This also shows that an increase in the cutting depth leads to an increase in micro-cracks.

Table 11: Number of micro-cracks formed during the simulations with chisel-shaped picks

0.5 mm depth of cut	Number of micro-cracks	5 mm depth of cut	Number of micro-cracks
Sample with 0.401 mm particles	20540	**Sample with 0.401 mm particles**	85820
Sample with 0.802 mm particles	2978	**Sample with 0.802 mm particles**	13560

7.2 Comparison between numerical, theoretical and experimental values

The numerically simulated forces were compared to experimental and theoretical data. The experimental rock cutting test was previously performed and the experimental data was published in Balci & Bilgin (2007). The theoretical models of Evans (1984) and Nishimatsu (1972), as described in section 2.7 with equations 23 and 27, were used to determine the mean peak cutting forces from the mechanical properties of Sandstone-2 in Table 6 and the cutting parameters described in section 4.3.

The results of the numerical, theoretical and experimental data for the chisel-shaped pick at 5 mm depth of cut are summarized in Table 12 using the parameters from Balci & Bilgin (2007). From this table it is evident that the numerically simulated cutting forces are much larger than the experimental forces and the numerically simulated normal forces are much smaller than the experimental forces.

Table 12: Results of the tool forces for a chisel-shaped pick with Balci & Bilgin (2007) data

d (mm)	Forces of numerical simulation (kN)				Theoretical cutting forces (kN)		Experimental forces (kN)			
	FN	FN'	FC	FC'	FC'_{Evans}	$FC'_{Nishimatsu}$	FN	FN'	FC	FC'
5	1.76	4.3	9.79	23.8	4.07	2.61	8.01 ± 3.44	10.65 ± 2.03	4.61 ± 0.95	11.42 ± 0.14

The reasons for this difference in values are the influence of wear on the pick as well as the conditions of the cutting process for instance temperature and the distribution of locked-in stresses in the particle assembly. The particle assembly's tensile strength was also equal to the shear strength, while the real Sandstone-2 specimen usually has a tensile strength much lower than its shear strength, as discussed in Chapter 5. A cutting distance was not specified in Balci & Bilgin (2007) and therefore 20 mm was used during the simulation since the sample was only 25 mm in length. During the simulation the forces reached a stable value between 4 and 9 mm of cutting distance. This stable value of the cutting force was 4.48 kN, which is very close to the experimental value of 4.61 kN. On the other hand, the value of

the normal force between 4 and 9 mm was 0.97 kN, which is still much smaller than the experimental value of 8.01 kN. If it was known that the cutting distance during the experimental study of Balci & Bilgin (2007) was less than 10 mm, it could be concluded that the numerical cutting forces agreed reasonably well with the experimental forces. As previously mentioned in Chapter 6, the reason for the small normal forces is the fact that the particles cannot be sliced into smaller fragments but are removed as a whole when a bond is broken, therefore the force of the whole particle is removed.

Another argument that has to be kept in mind is that a perfectly sharp chisel-shaped pick was used during the numerical simulation with high stiffness, rigid walls and therefore there could not be any wear on the pick itself, which would increase the forces. During the experimental studies, on the other hand, there is damaged to the pick and the wear increases over the cutting distance. Therefore the experimental forces should in fact be higher than the numerical forces over a longer cutting distance.

As can be seen from the rock cutting test data presented in Table 12, the forces predicted by the theoretical models are significantly lower compared to the experimental forces. Evan's model gives the nearest value to the real data, while Nishimatsu's model (1972) is only half of the value of Evan's model. An important conclusion can be drawn that these models are not reliable to predict cutting forces.

7.3 Influence of depth of cut on forces

Figure 54 visually presents the influence of the depth of cut on tool forces when cutting with a sharp chisel-shaped pick. Since only two data points were used to plot these figures, the conclusions drawn from these figures won't be realistic. Overall there is an increase in normal and cutting forces with an increase in depth of cut, since a greater area of the pick is exposed to the rock sample. The trend that this increase in forces follows, cannot be taken as linear as depicted in the graphs, because of the lack of data points, but from the previous results with point-attack picks, a non-linear increase will be expected.

Another observation that can be made from this figure is that the cutting forces are larger when cutting a sample with 0.401 mm particles, while the normal forces are larger when cutting a sample with 0.802 mm particles. It was previously discussed that the influence of the size of the particles is not evident since there is no persistent feature or trend it follows. It is therefore best to use the sample with the smaller particles to represent the Sandstone-2 sample, since smaller grains represent a stronger material.

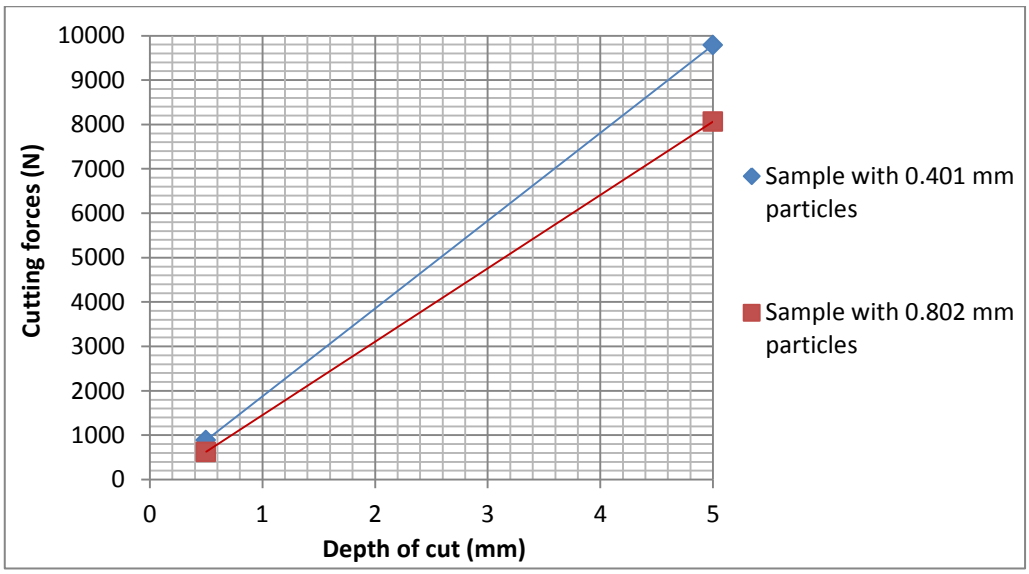

(a)

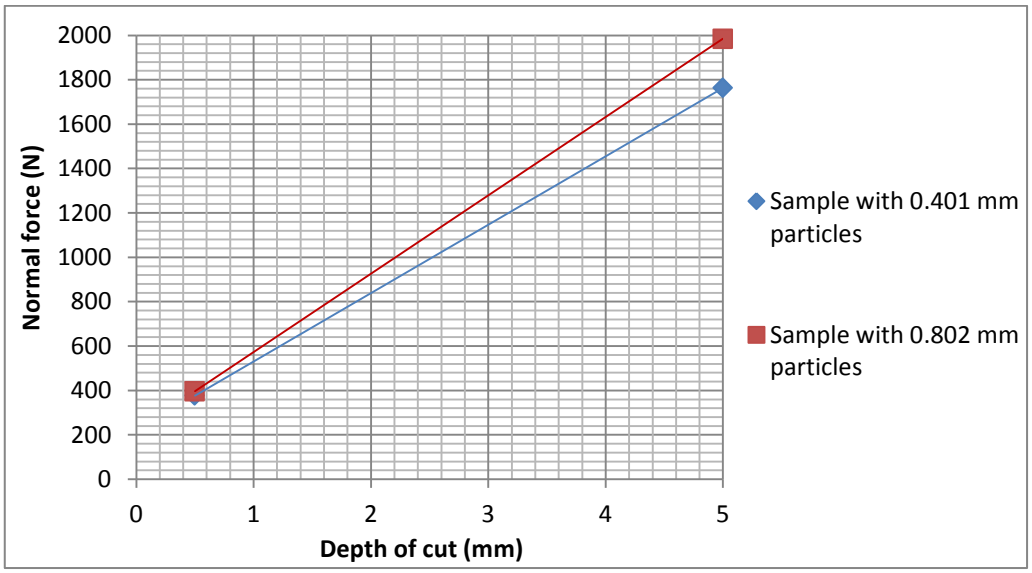

(b)

Figure 54: The influence on depth of cut of tool forces for a chisel-shaped pick

Cutting forces; (b) Normal forces

CHAPTER 8:

PFC3D™ MATERIAL RESPONSE OF ROCK CUTTING WITH A BUTTON-SHAPED CUTTER

Summarized in this chapter are the most important results found throughout the study on the simulation of rock cutting with a button-shaped cutter, using data from the vertical bore test performed at Element 6 in Johannesburg. The numerical method described in section 4.3.3 were used and during these simulations the three orthogonal forces acting on the button-shaped cutter were also monitored and the histories were recorded. As also stated previously, the cutting forces were monitored by summing all the forces acting on the cutting tool in the x-direction at each time step, while the normal forces were monitored by summing all the forces in the z-direction and the sideways forces were monitored by summing all the forces acting on the pick in the y-direction.

Since the experimental data available only gave the variation of tool forces for relieved cutting with an increasing wear flat, as seen in Figure 55, the cutting tool had to interact with an existing groove during the numerical simulation to be able to compare the results. Therefore a groove had to be simulated firstly with a sharp cutting tool and thereafter cuts could be simulated which overlapped the first groove. When looking at Figure 55, it can be seen that the normal forces played a major role in the cutting process. The sideways forces were relatively large in the vertical bore test, which is in contrast to the numerical simulations, where the sideways forces where very close to zero in the previous chapters.

Another problem with the verification of the results was that the cutting tool was simulated out of rigid walls and therefore no wear could be detected on the tool during the simulation. The only solution was to simulate a cutting tool with a chamfered area to represent the wear for the second cut. The wear flat during the vertical bore test was defined as in Figure 56. The cutting distance during the experimental vertical bore test was not specified and the cutting depth during the numerical simulation was 0.5 mm in stead of 250 µm as in the vertical bore test. The diameter of the real cutter that was used in the vertical bore test was about 20 mm, but since the width of the simulated Paarl granite sample was only 12.5 mm, the simulated cutter was chosen to be 8 mm in diameter to be able to make two overlapping cuts.

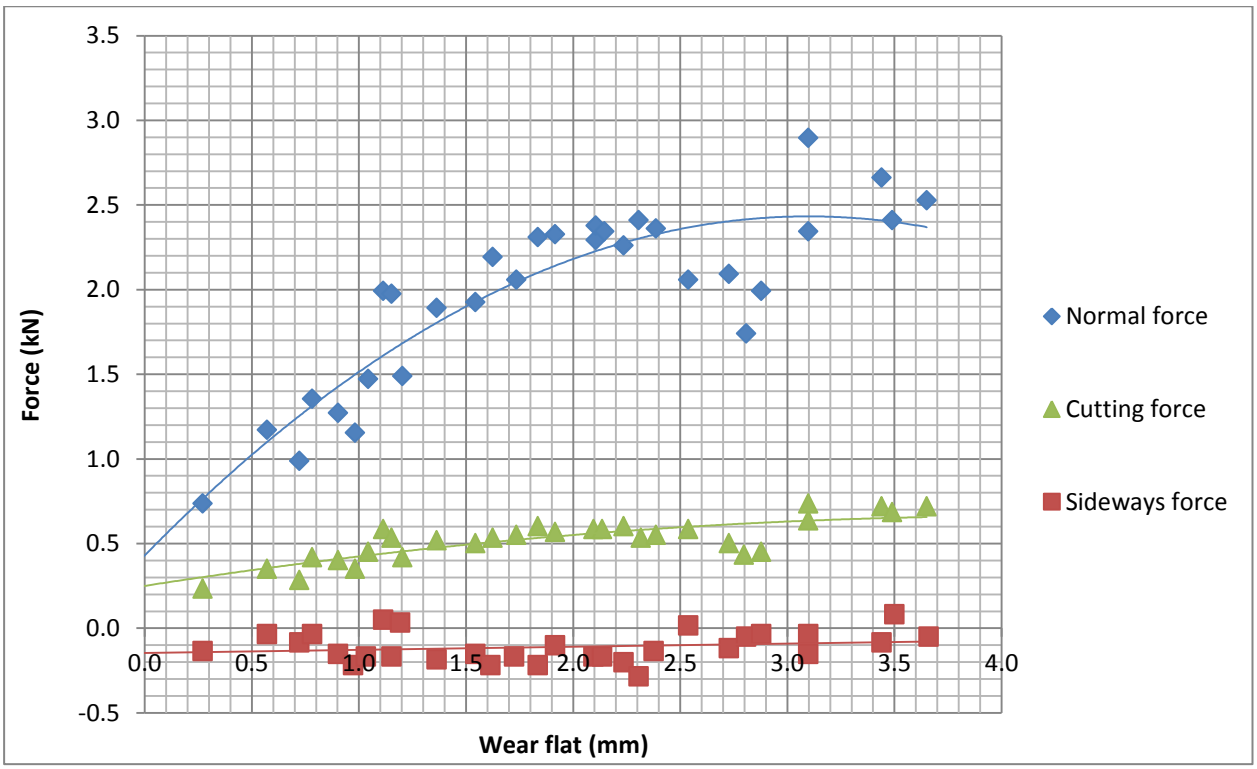

Figure 55: The variation of experimental tool forces with wear flat for a button-shaped cutter

(Source: Adapted from private communication at Element Six, Johannesburg, 2011)

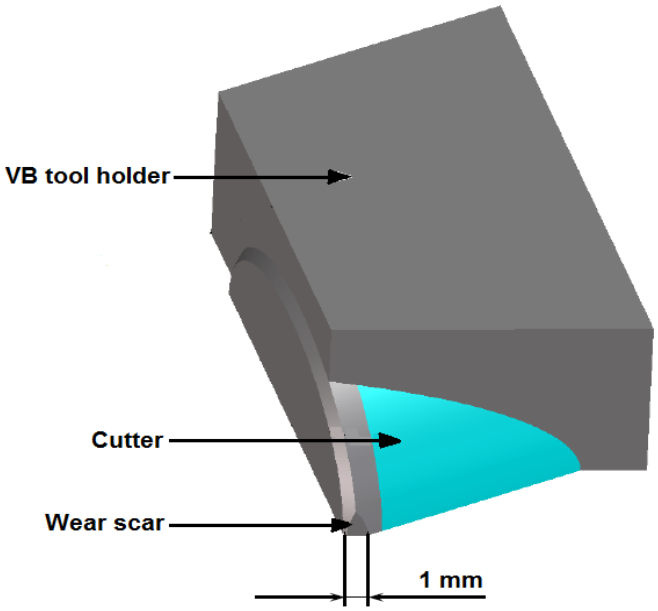

Figure 56: Wear scar on cutting tool in VB test

(Source: Adapted from private communication at Element Six, Johannesburg, 2011)

8.1 Results of the unrelieved (first) cut

The first cut was simulated with a sharp button-shaped cutter, in other words the edge of the cutter was not chamfered and therefore it had a cylindrical shape. This was done to represent a sharp cutting tool without any wear. The tool forces that were recorded during this simulation, after 20 mm of cutting

distance, are shown in Figure 57. The black curve represents the cutting force, the red curve represents the normal force and the blue curve represents the sideways force. The mean forces are shown with dashed lines and the values are given on the right of the graphs.

The average value of the normal force is 297 N, which is higher than the average value of the cutting force of 266 N. The reason why the normal force is higher is because of the large back rake angle of 20° and therefore the contact area between the particles and the cutting tool is larger in the vertical direction. The average value of the sideways force is -3 N, which is very close to zero and it shows that there is almost no interaction between the particles and the cutting tool in the y-direction.

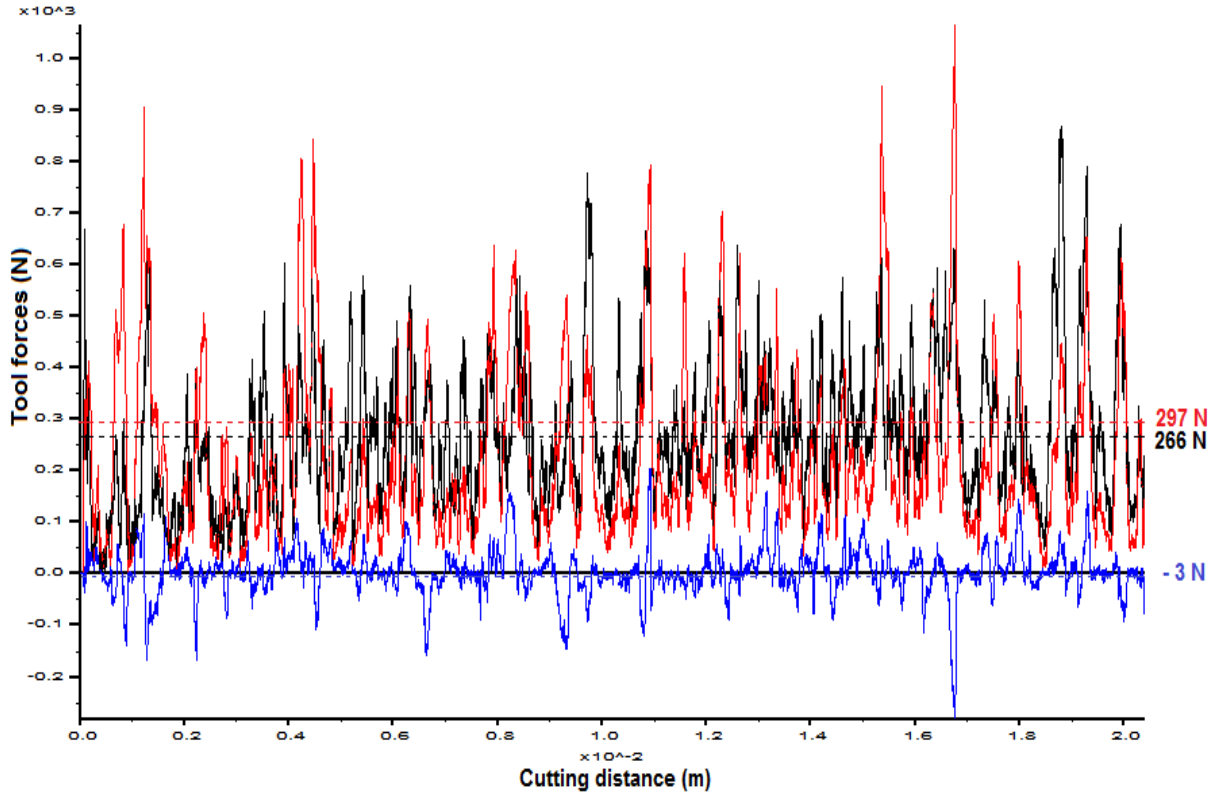

Figure 57: The variation of numerical tool forces for a sharp button-shaped cutter

When the first cut was simulated with a 0.4x45° chamfered button-shaped cutter, in other words with wear on the cutting tool, the tool forces after 20 mm of cutting distance were recorded as in Figure 58. The average values of the tool forces were twice as large for a button-shaped cutter with wear compared to a sharp one. The reason is the increase in the contact area between the simulated rock sample and the cutting tool. Therefore only a small amount of wear on the cutter already influences the cutting process to a great extent, making cutting more difficult.

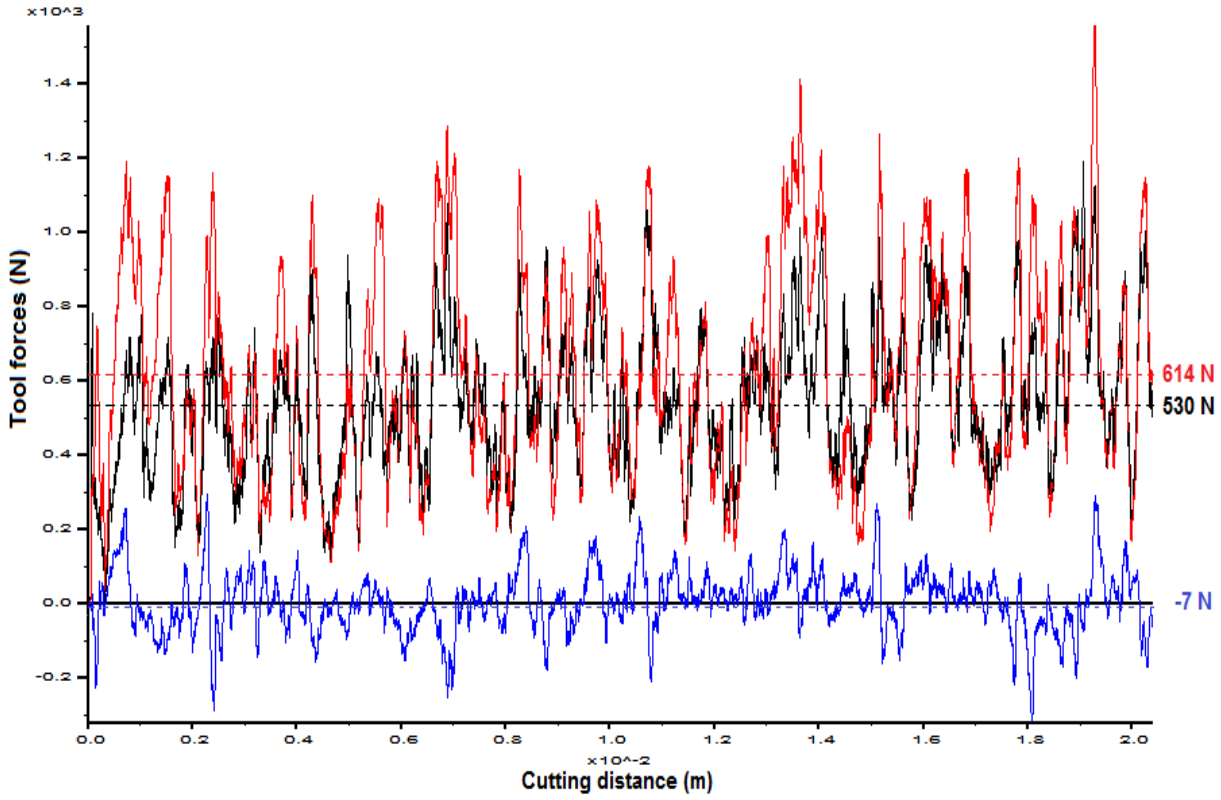

Figure 58: The variation of numerical tool forces for a chamfered button-shaped cutter in unrelieved cutting

The Paarl granite specimen and the sharp and chamfered button-shaped cutter at 0.5 mm depth of cut are shown in Figure 59 after 20 mm of cutting distance. After the button-shaped cutter began to interact with the particles, micro-cracks were initiated and they propagated from the front of the cutter. These micro-cracks formed when bonds were broken in the simulation and they are also an indicator of the damage on the specimen. The black spots represent the micro-cracks due to tensile bond failure, while the red spots represent the micro-cracks due to shear bond failure. The micro-cracks occur only a few millimetres into the specimen just beneath the cutting tool. The micro-cracks also led to chip formations which can be seen in front of and behind the cutter. The two figures look very alike for the two cutting tools, except that more micro-cracks are visible when cutting with a chamfered button-shaped cutter. This is because of the increase in the tool forces and therefore an increase in the bond breakage when cutting with a chamfered cutter.

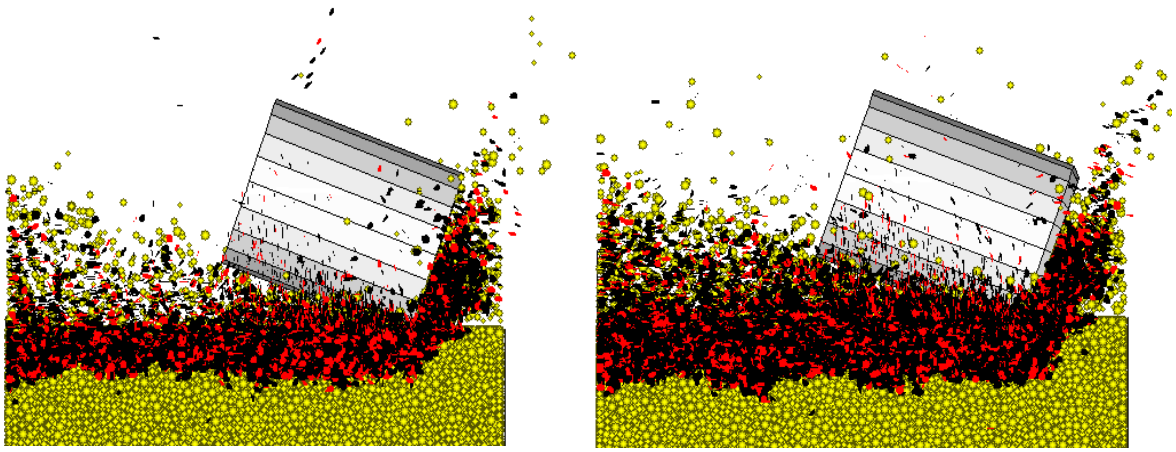

(a) (b)

Figure 59: The schematic view of the micro-cracks and chip formations occurring around the button-shaped cutter

(a) Sharp button-shaped pick; (b) Chamfered button-shaped pick

The number of micro-cracks formed increases over the cutting distance and this is illustrated in Figure 60 for a sharp button-shaped cutter. This increase is almost linear and over the cutting distance of 20 mm, 10870 micro-cracks form, which also indicates the number of bonds broken during the simulation. The same trend was found when cutting with a chamfered button-shaped cutter and in this case 17850 micro-cracks formed over a cutting distance of 20 mm.

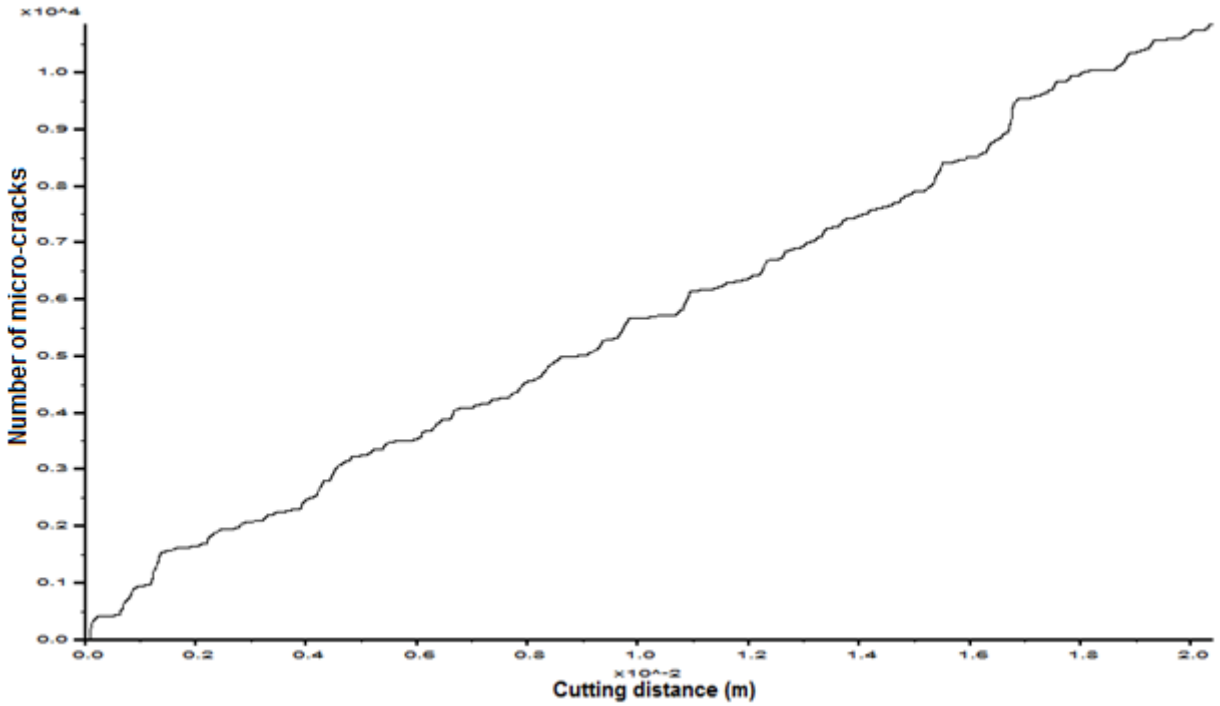

Figure 60: The number of cracks versus cutting distance for a sharp button-shaped pick

8.2 Results of the relieved (second) cut

The second cut was simulated with a 0.4x45° chamfered button-shaped cutter. The feed rate was specified as 3 – 8 mm/rev depending on the wear scar width and since the chamfered part, of only 0.4 mm, represented the wear, the centre of the pick was shifted 3 mm.

The overlap of the second cut with the first was calculated with the following method. Since the rake angle of the numerical simulation was -20°, the cut had an elliptical shape, as seen in Figure 61, and the equation for an ellipse was changed as follows, where R is the radius of the circular cutting tool:

$$\frac{x^2}{a^2}+\frac{y^2}{b^2}=1$$

$$\frac{x^2}{R^2}+\frac{y^2}{R^2\sin\theta}=1$$

$$x^2+\frac{y^2}{\sin^2\theta}=R^2$$

$$x=\pm\sqrt{R^2-\frac{y^2}{\sin^2\theta}} \tag{34}$$

The width of the cut (c) could then be calculated by substituting y with $R\sin\theta-h$ in equation 34, where h is the height of the cut:

$$x_d=\pm\sqrt{R^2-\frac{(R\sin\theta-h)^2}{\sin^2\theta}}$$

$$x_d=\pm\sqrt{\frac{R^2\sin^2\theta-R^2\sin^2\theta+2hR\sin\theta-h^2}{\sin^2\theta}}$$

$$x_d=\pm\sqrt{\frac{2hR\sin\theta-h^2}{\sin^2\theta}}$$

$$x_d=\pm\frac{\sqrt{h(2R\sin\theta-h)}}{\sin\theta} \tag{35}$$

$$c=2\cdot x_d=\frac{2}{\sin\theta}\sqrt{h(2R\sin\theta-h)} \tag{36}$$

The width of the cut was therefore 6.18 mm and the overlap of the two cuts was 3.18 mm (*c* – feed rate).

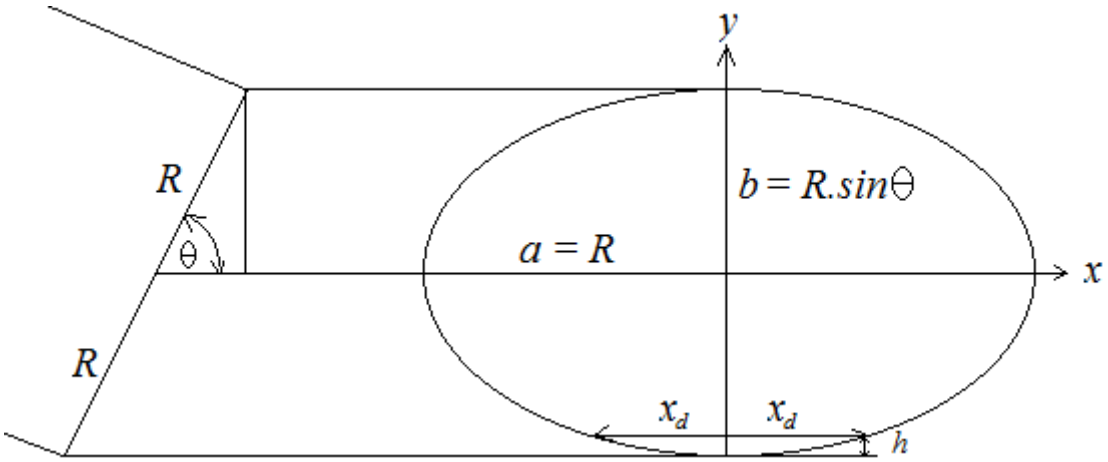

Figure 61: Height and width of cut

Using equation 36, the overlap during the real vertical bore test, at a cutting depth of 250 µm and with a 20 mm diameter cutting tool, would be 4.51 mm. This is only 1.33 mm larger than the overlap during the numerical simulation.

The tool forces that were recorded during this simulation, after 20 mm of cutting distance, are shown in Figure 62. Again, the black curve represents the cutting force, the red curve represents the normal force and the blue curve represents the sideways force. The mean forces are shown with dashed lines and the values are given on the right of the graphs.

The average value of the normal force is 333 N, which is a bit higher than the average value of the cutting force with a value of 300 N. The average value of the sideways force is 51 N, which is much larger than the sideways force in the first cut and it shows that the interaction between the particles and the cutting tool increased in the y-direction during the relieved cut.

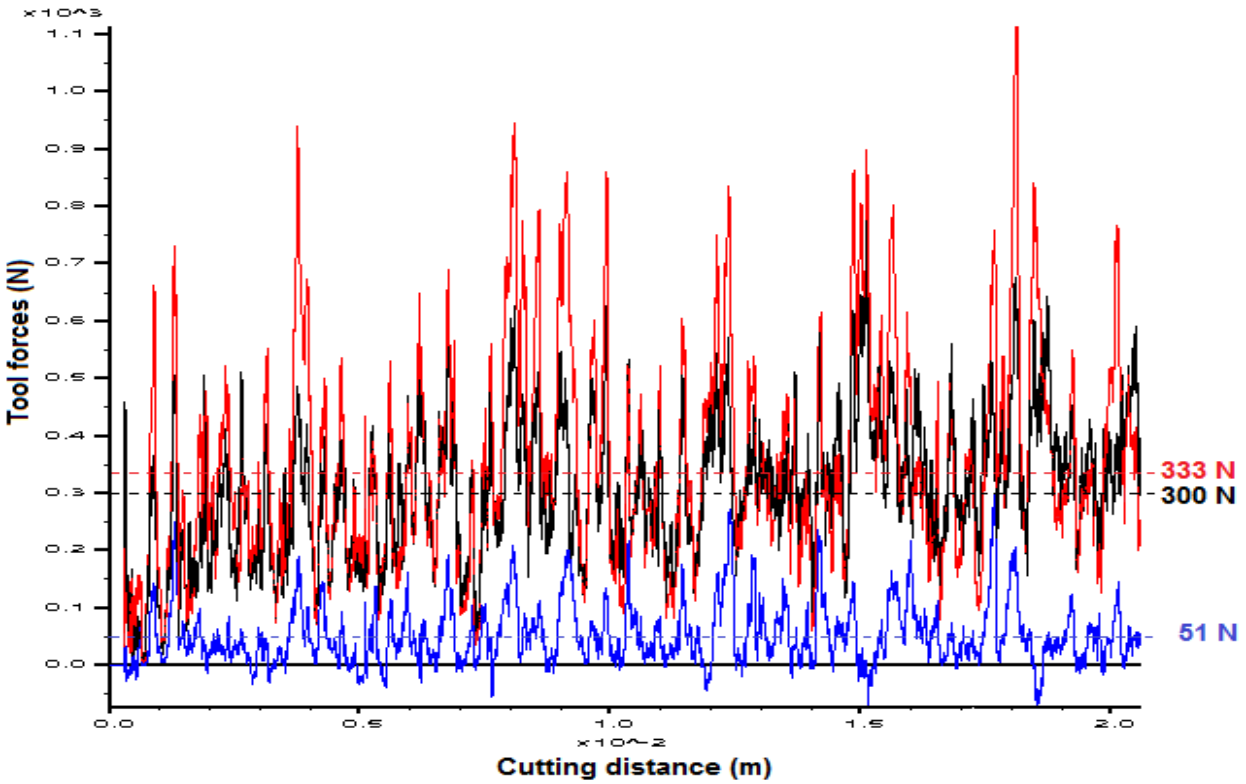

Figure 62: The variation of numerical tool forces for a chamfered button-shaped pick in relieved cutting

The difference in the average values of the tool forces during the simulations of the first and second cut, as well as the standard deviation of these forces, can be seen in Figure 63. If the first cut was conducted with a sharp button-shaped cutter, there is a minimal increase in the average values of the cutting and normal forces during the second relieved cut with a chamfered button-shaped cutter, while the increase in the sideways forces is noteworthy. Although the volume of the Paarl granite specimen which was removed during the second cut was less because of the overlap, the wear on the cutting tool played a larger role in the cutting process and produced the increase in the tool forces. The sideways force increased to a great extent since the loose particles of the first cut were not removed and interacted with the cutting tool during the second cut.

The tool forces during the second cut are much lower than the tool forces during the first cut conducted with a chamfered button-shaped cutter. The reason is the overlap during the relieved cut and therefore the contact area between the cutting tool and the Paarl granite specimen was smaller, causing the decrease in forces.

In each case, the standard deviation is proportional to the average value of the forces. The standard deviation of the tool forces is larger for the chamfered button-shaped pick during the first cut in each case, which shows that the forces varied more during this simulation.

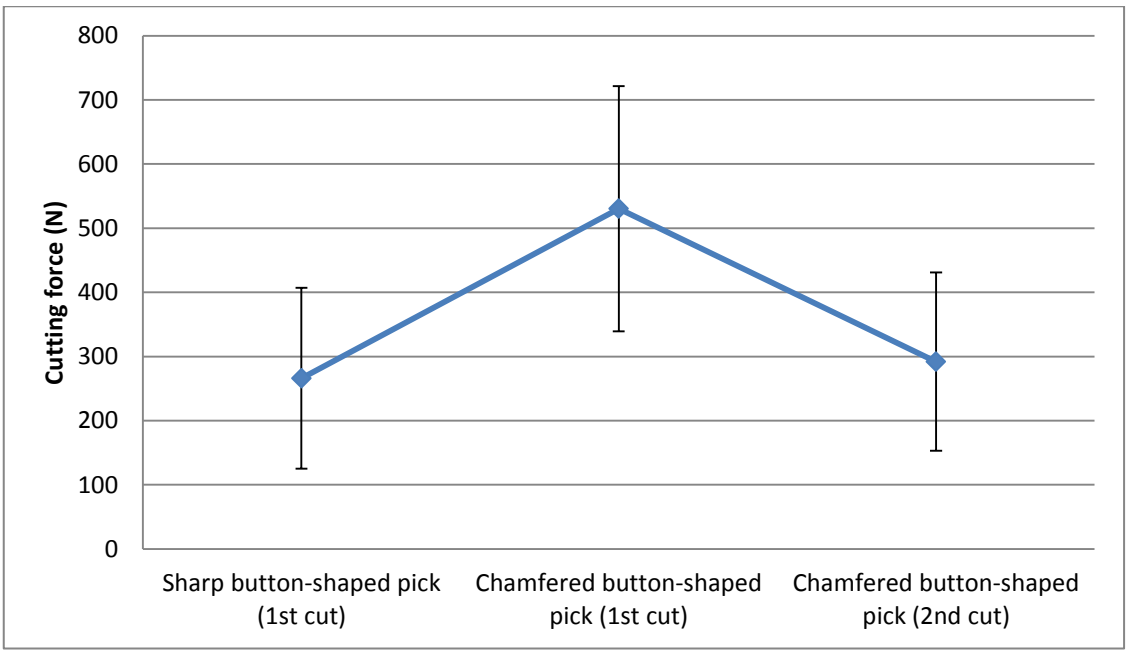

(a)

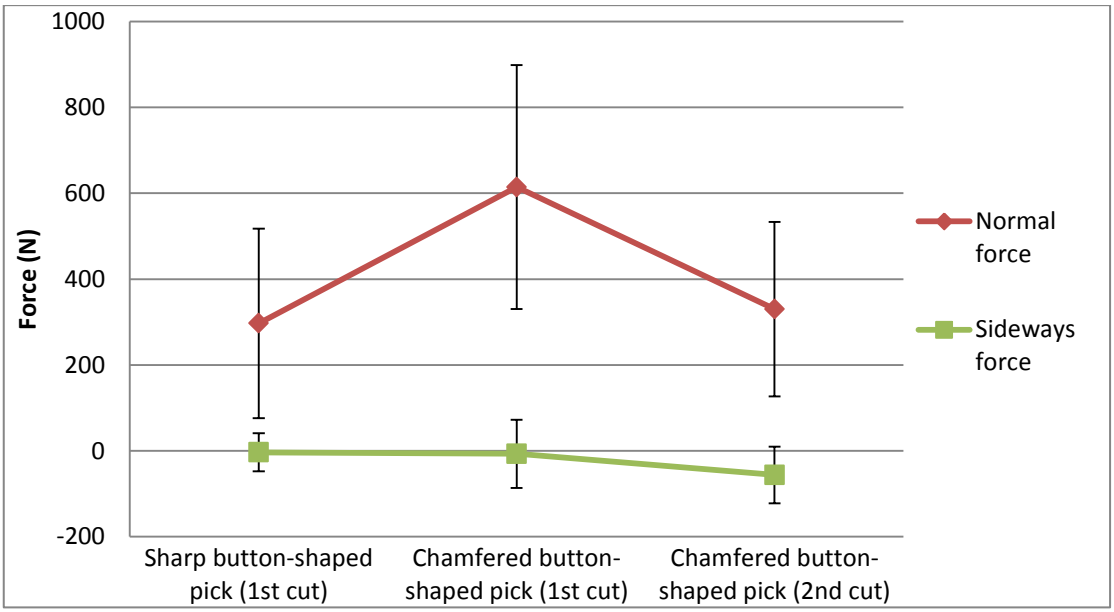

(b)

Figure 63: Average force and standard deviation of forces when cutting with a button-shaped pick

(a) Cutting force; (b) Normal and Sideways forces

Since the diameter of the cutting tool during the vertical bore test was 20 mm and the cutting distance, over which these forces were measured, was not stated, it was difficult to evaluate the tool forces recorded during the numerical simulation of the relieved cut.

When returning to Figure 55, showing the experimental forces, the average values of the cutting, normal and sideways forces at a wear flat of 0 mm are more or less 250 N, 450 N and 150 N respectively while at a wear flat of 0.4 mm they are more or less 300 N, 900 N and 150 N respectively. The

numerically simulated cutting force is equal to the experimental value at 0.4 mm wear flat, while the numerically simulated normal and sideways forces are much lower than the experimental values at 0.4 mm wear flat. The reason that can be given for the agreement between the numerically simulated and experimental cutting force at 0.4 mm wear flat, is that a velocity was specified solely in the x-direction during the numerical simulation and therefore the cutting tool was pushed only in that direction. On the other hand, during the vertical bore test the tool holder might have pushed downwards on the cutting tool and the Paarl granite specimen was also rotated which influenced the forces more in the normal and sideways directions. As also discussed previously, the reason why the numerical normal forces are so low, is the fact that the particles cannot be broken into smaller pieces during the simulation, but are removed as a whole if its bond breaks.

There is a greater agreement between the numerically simulated and experimental tool forces at 0 mm wear flat in Figure 55. Since the sharp button-shaped cutter in the real vertical bore test is a chamfered cutter, it shows that the wear flat presented as a chamfered part of the button-shaped cutter is not adequate, but has to be simulated as in Figure 56. The numerical simulation of the relieved cut in this section is therefore rather an illustration of a relieved cutting test with a sharp button-shaped cutter.

After these observations, it is evident that the overlap of cuts has to be considered during the simulation of a vertical bore test, a numerically sharp button-shaped cutter should already be chamfered and wear flat plays a significant role in the cutting process and has to be included in the simulation.

CHAPTER 9:

CONCLUSIONS AND RECOMMENDATIONS

9.1 Conclusions

In this paper three dimensional numerical modelling of rock cutting tests was conducted using DEM and BPM to represent tribological interactions such as contact, shearing, fracturing, friction and wear. Tool forces acting on the cutting tool were recorded at different cutting conditions during these simulations. Paarl granite and Sandstone-2 were simulated with DEM as cemented granular material representing the rock specimens used during the cutting tests.

Uniaxial and triaxial compressive strength tests as well as Brazilian tests were used to calibrate the macro-properties of the simulated rock specimens. The failure planes and distribution of micro-cracks during these tests were very similar to those conducted in the laboratory and the results suggested that the DEM could reproduce the damage formation during calibration tests successfully. From the results obtained from the calibration tests, it was also concluded that particle size is not a free parameter but is related to the unconfined compressive strength. As the particle size decreased the unconfined compressive strength increased. The other macro-properties, namely Young's modulus, Brazilian tensile strength and the triaxial compressive strength, were also greatly influenced by the particle size. The downside of using smaller particles was that the computations became time-consuming and restricted simulations to small volumes of rock. The calibration procedure was also very time-consuming since it was done through trial-and-error. The focus in the calibration was therefore firstly to get the unconfined compressive strength correct and more time was needed to calibrate the other macro-properties, while still maintaining a good unconfined compressive strength.

Rock cutting tests on rock samples with different particle sizes, using point-attack picks, chisel-shaped picks and button-shaped picks were conducted in this study. The three orthogonal forces were monitored during the simulations and the histories were recorded. It was concluded that the sideways forces did not have a great influence on the cutting process during the simulations with point-attack and chisel-shaped picks since the average value was close to zero during each simulation. The sideways forces played a more significant role during the relieved cutting with a button-shaped pick and had to be considered during cutting.

When cutting with point-attack and chisel-shaped picks, the cutting and normal forces increased and then fluctuated around an average value in each case. At 0.5 mm depth of cut the standard deviation of these forces were higher than at 3 mm depth of cut and therefore the fluctuations decreased with an increase in depth of cut. An exception was found when cutting with a chisel-shaped tool at 5 mm depth of cut. In this case the forces increased over the whole cutting distance and therefore standard deviation was also higher at deeper depths of cut. As the pick moved forwards, there was a build-up of particles in front of it which increased the forces and when the bonds were broken, the particles were removed, decreasing the forces in the process. The conclusion was made that this build-up is greater at deeper depths of cut, which also contributes to larger forces at increasing depths.

The number of micro-cracks was also monitored during the simulations. These micro-cracks presented the broken bonds in the sample. There was a definite increase in the number of micro-cracks with an increase in wear flat and depth of cut, while the number was considerably lower when samples with larger particles were used. At 0.5 mm depth of cut these micro-cracks resided just beneath the cutting tool and as the depth of cut increased, the micro-cracks spread wider and deeper into the sample. The conclusion was made that the damage to the sample as well as wear on the cutting tool would be less at shallow depths of cut, but the amount of work had to increase to remove an equal volume of rock.

After the simulation of the cutting tests with sharp point-attack and chisel-shaped picks, it was concluded that the correlation between the numerical and the experimental models as well as the theoretical and experimental models were not strong. The numerical tool forces of the sharp point-attack picks were significantly smaller than the experimental forces, while the cutting forces of the chisel-shaped pick were almost twice as large as the experimental forces. For the sharp point-attack picks, Goktan's equation predicted mean peak cutting forces the closest to the real values since he included the friction angle as well as the mechanical rock properties. For the chisel-shaped picks the mean peak forces predicted by Evan's model were closer.

On the other hand, commercially manufactured point-attack picks undergo wear during mining operations. Therefore a wear flat was introduced by cutting off the tip of the point-attack pick and chamfering the button-shaped pick before starting the simulations. There was a definite increase in the forces with an increase in wear flat. During the simulations with the point-attack pick a strong relationship was found between the numerical and experimental forces at a wear flat of 1 mm in diameter in the cutting tests using the parameters from Su & Akcin (2011) and at a wear flat of 0.5 mm in diameter when using the parameters from Bilgin et al. (2006). It was concluded that the influence of wear plays a substantial part in the cutting process and it has to be included during the numerical simulation for the results to be accurate and verifiable. Hence, the results of the rock cutting mechanisms were verified by the numerical models including wear flat.

This study also revealed that there is a non-linear increase in tool forces with an increase in depth of cut. At larger cutting depths, chip formation also increased. Also, simulated rock specimens containing smaller particles gave better force results.

Overall this study concluded that DEM was capable of simulating calibration methods and rock cutting processes with different cutting tools and producing results which were verifiable with experimental data. Hence the objectives of the study were achieved. Therefore numerical prediction of tool forces will allow the design of efficient cutting systems and the operational parameters as well as the performance prediction of excavation machines.

9.2 Recommendations

The following recommendations were made for future investigations:

- Since the simulated rock specimens have greater tensile strength than real rock and both tensile and shear micro-failure are possible, it is proposed that a ratio between the shear and tensile strength be found, instead of setting them equal to each other in the calibration process.
- The area around the cutting tool where the broken-off particles are removed may be improved to reduce build-up in front of the tool by studying the cutting process in the laboratory.
- To make the model of the cutting process even more realistic, it is proposed to include the impact of the rock and the wear it causes on the cutting tool as well. Wear on the cutting tool can be included by simulating the cutting tool using the same procedure as the rock sample. The micro-properties of the cutting tool will have to be available and the macro-properties will have to be calibrated.
- Including noise and vibrations of the cutting tool in the numerical simulations by introducing a damping motion of the cutting tool.
- The influence of high pressure on rock during deep drilling can be investigated by conducting cutting tests in pressure chambers.
- Water may be added as a coolant on the cutting tool, especially in the simulation of the vertical bore test, through a collaboration of a DEM simulation with a CFD simulation.

REFERENCES

[1] Akono, A.T. & Ulm, F.J. 2011. Scratch test model for the determination of fracture toughness. Engineering Fracture Mechanics. Volume 78. 334-342

[2] Akram, M.S. & Sharrock, G.B. 2010. Physical and numerical investigation of a cemented granular assembly of steel spheres. International Journal for Numerical and Analytical Methods in Geomechanics. Volume 34. 1896-1934

[3] Appl, F.C., Wilson, C.C. & Lakshman, I. 1993. Measurement of forces, temperatures and wear of PDC cutters in rock cutting. Wear. Volume 169. 9-24

[4] Balci, C. & Bilgin, N. 2007. Correlative study of linear small and full-scale rock cutting tests to select mechanized excavation machines. International Journal of Rock Mechanics & Mining Sciences. Volume 44. 468-476

[5] Bicanic, N. 2004. Chapter 11. Discrete Element Methods. Encyclopedia of Computational Mechanics. [Online]. Available: http://hasdl.kau.edu.sa/encyclopedia/1/ecm006.pdf. [2011, February 24]

[6] Bieniawski, Z.T. & Hawkes, I. 1978. Suggested Methods for Determining Tensile Strength of Rock Materials. International Journal of Rock Mechanics and Mining Sciences & Geomechanics Abstracts. Volume 15. No. 3. 99-103

[7] Bilgin, N. 1977. Investigations into the mechanical cutting characteristics of some medium and high strength rocks. Ph.D. thesis, University of Newcastle upon Tyne, United Kingdom.

[8] Bilgin, N., Demircin, M.A., Copur, H., Balci, C., Tuncdemir, H. & Akcin, N. 2006. Dominant rock properties affecting the performance of conical picks and the comparison of some experimental and theoretical results. International Journal of Rock Mechanics & Mining Sciences. Volume 43. 139-156

[9] Bilgin, N., Copur, H. & Balci, C. 2012. Effect of replacing disc cutters with chisel tools on performance of a TBM in difficult ground conditions. Tunnelling and Underground Space Technology. Volume 27. 41-51

[10] Callister, W.D. 2007. Materials Science and Engineering: An Introduction. Seventh Edition. United States of America: John Wiley & Sons.

[11] Cigla, M. & Ozdemir, L. Computer modelling for improved production of mechanical excavators. Excavation Engineering & Earth Mechanics Institute. Department of Mining Engineering Colorado school of Mines. USA.

[12] Copur, H. 2010. Linear stone cutting tests with chisel tools for identification of cutting principles and predicting performance of chainsaw machines. International Journal of Rock Mechanics & Mining Sciences. Volume 47. 104-120

[13] Da Fontoura, S.A.B., Inoue, N., Martinez, I.M.R. & Carrapatoso, C.M. 2012. Modeling of Evaporate Drilling Under High Pressure. Part I: Numerical Simulation of Rock Cutting through Distinct Element Method – PFC2D™. Progress Report. GTEP/PUC-Rio. Rio de Janeiro Brazil

[14] Dagrain, F. 2001. Influence of the Cutter Geometry in Rock Cutting with PDC cutters. Master's thesis. University of Minnesota

[15] Donze, F.V., Richefeu, V. & Magnier, S.A. 2008. Advances in Discrete Element Method Applied to Soil, Rock and Concrete Mechanics. EJGE

[16] Evans, I. 1984. A theory of the cutting force for point attack picks. International Journal of Mining and Geological Engineering. Volume 2. 63-71

[17] Fakhimi, A. & Villegas, T. 2007. Application of Dimensional Analysis in Calibration of a Discrete Element Model for Rock Deformation and Fracture. Rock Mechanics and Rock Engineering. Volume 40. 193-211

[18] Gertsch, R., Gertsch, L. & Rostami, J. 2007. Disc cutting tests in Colorado Red Granite: Implications for TBM performance prediction. International Journal of Rock Mechanics & Mining Sciences. Volume 44. 238-246

[19] Gillani, S.T.A. & Butt, N. 2009. Excavation Technology for Hard Rock – Problems and Prospects. Pakistan Journal of Engineering and Applied Sciences. Volume. 4. 24-33

[20] Goktan, R.M. and Gues, N. 2005. A semi-empirical approach to cutting force prediction for point-attack picks. The Journal of The South African Institute of Mining and Metallurgy. Volume 105. 257-264

[21] Hawkes, I. & Mellor, M. 1970. Uniaxial testing in rock mechanics laboratories. Engineering Geology. Volume 4. 177-285

[22] Holt, R.M., Kjolaas, J., Larsen, I., Li, L., Gotusso Pillitteri, A. & Sonstebo, E.F. 2005. Comparison between controlled laboratory experiments and discrete particle simulations of the mechanical behaviour of rock. Volume 42. 985-995

[23] Hood, M. & Alehossein, H. 2000. A development in rock cutting technology. International Journal of Rock Mechanics and Mining Sciences. Volume 37. 297-305

[24] Iliescu, D., Gehin, D., Iordanoff, I., Girot, F. & Gutierrez, M.E. 2010. A discrete element method for the simulation of CFRP cutting. Composites Science and Technology. Volume 70. 73-80

[25] Itasca Consulting Group. Particle Flow Code in 3 dimensions manual, version 3.1. Minneapolis, Itasca, 2006.

[26] Kaitkay, P. & Lei, S. 2005. Experimental study of rock cutting under external hydrostatic pressure. Journal of Materials Processing Technology. Volume 159. Issue 2. 206-213

[27] Khair, A.W. Research and Innovations for Continuous Miner's Cutting Head, for Efficient Cutting Process of Rock/Coal. In: 17th International Mining Congress and Exhibition of Turkey; 2001, p. 45-55.

[28] Khair, A.W. & Yu, B. Rock cutting process simulation by dynamic finite element analysis. In: Hardygora M, Paszkowska G, Sikora M, editors. Mine Planning and Equipment Selection. London: Taylor & Francis Group; 2004, p. 253-256.

[29] Kotwica, K. & Gospodarczyk, P. 2003. Hard Rock Mining with the use of new Cutting Tools. Journal of Mining Science. Volume 39. 387-393

[30] Loui, J.P. & Karanam, U.M.R. 2012. Numerical Studies on Chip Formation in Drag-Pick Cutting of Rocks. Geotechnical and Geological Engineering. Volume 30. 145-161

[31] Lunow, C. & Konietzky, H. 2009. Two-dimensional simulation of the pressing and the cutting rock destruction. 2nd International Conference on Computational Methods in Tunnelling.

[32] Mahabadi, O.K. & Grasselli, G. Numerical modelling of a Brazilian Disc test of layered rocks using the combined finite-discrete element method. In: Diederichs M, Grasselli G, editors. Proceedings of the 3rd CANUS Rock Mechanics Symposium, Toronto; 2009, p. 1-9.

[33] Mak, J., Chen, Y. & Sadek, M.A. 2012. Determining parameters of a discrete element model for soil-tool interaction. Soil & Tillage Research. Volume 118. 117-122

[34] Marusich, T.D. 2001. Effects of Friction and Cutting Speed on Cutting Force. Proceedings of ASME Congress.

[35] Nishimatsu, Y. 1972. The Mechanics of Rock Cutting. International Journal of Rock Mechanics & Mining Sciences. Volume 9. 261-270

[36] Onate, E. & Rojek, J. 2004. Combination of discrete element and finite element methods for dynamic analysis of Geomechanics problems. Computational Methods and Applications in Mechanical Engineering. Volume 193. 3087-3128

[37] Patten, J.A., Jacob, J., Bhattacharya, B., Grevstad, A., Fang, N. & Marsh, E.R. 2007. Numerical simulations and cutting experiments on single point diamond machining of semiconductors and ceramics. Semiconductor Machining at the Micro-Nano Scale. [Online]. Available: http://www.wmich.edu/mfe/mrc/pdf/Yan2new.pdf [2012, March 26]

[38] Potyondy, D.O. & Cundall, P.A. 2004. A bonded-particle model for rock. International Journal of Rock Mechanics & Mining Sciences. Volume 41. 1329-1364

[39] Private communication with Dr H. Yilmaz at the University of the Witwatersrand, Johannesburg; 2011.

[40] Rizo, J.A.M. 2010. Modelling Rock Cutting using DEM with Crushable Particles. Master's thesis. University of Pittsburgh.

[41] Rojek , J., Onate, E., Labra, C. & Kargl, H. 2011. Discrete element simulation of rock cutting. International Journal of Rock Mechanics & Mining Sciences. Volume 48. 996-1010

[42] Sankar US. Theories of Interaction of Rock Cutting tools. Project Planning. Singareni Collieries Company Ltd. [Online] Available: http://www.slideshare.net/sankarsulimella/theories-of-interaction-of-rock-cutting-tools [2011, May 6]

[43] Sitharam, T.G. 2000. Numerical simulation of particulate materials using discrete element modelling. Current Science, Volume 78, No. 7. 876-886.

[44] Shimizu, H., Koyama, T., Ishida, T., Chijimatsu, M., Fujita, T. & Nakama, S. 2010. Distinct element analysis for Class II behaviour of rocks under uniaxial compression. International Journal of Rock Mechanics & Mining Sciences. Volume 47. 323-333

[45] Su, O. & Akcin, A.N. 2011. Numerical simulation of rock cutting using the discrete element method. International Journal of Rock Mechanics & Mining Sciences. Volume 48, Issue 3. 434-442

[46] Tan, Y., Yang, D. & Sheng, Y. 2009. Discrete element method (DEM) modelling of fracture and damage in the machining process of polycrystalline (SiC). Journal of the European Ceramic Society. Volume 29. 1029-1037

[47] Tulu, I.B. 2009. Modelling PDC Cutter Rock Interaction. Master's thesis. College of Engineering and Mineral Resources at West Virginia University

[48] Tulu, I.B., Heasley, K.A., Bilgesu, I. & Sunal, O. 2008. Modelling Rock and Drill Cutter Behaviour. American Rock Mechanics Association

[49] Vogler, U.W. & Kovari, K. 1978. Suggested Methods for Determining the Strength of Rock Materials in Triaxial Compression. International Journal of Rock Mechanics and Mining Sciences & Geomechanics Abstracts. Volume 15, No.2. 47-51

[50] Wang, Y. & Tonon, F. 2009. Modelling Lac du Bonnet granite using a discrete element method. International Journal of Rock Mechanics & Mining Sciences. Volume 46. 1124-1135

[51] Yu, B. 2005. Numerical Simulation of Continuous Miner Rock Cutting Process. College of Engineering and Mineral Resources at West Virginia University

[52] Zhou, L., Huang, S.T. & Wang, D. 2011. Finite element and experimental studies of the cutting process of SiCp/Al composites with PCD tools. International Journal of Advance Manufacturing Technology. Volume 52. 619-626

APPENDIX A:

PARTICLE GENERATION AND CALIBRATION

The mathematics and procedures described in this section was taken from Potyondy & Cundall (2004) and the Particle Flow Code in 3 Dimensions Manual, Version 4.

A1. Particle-generation procedure

In order to generate rock in PFC3D™, the individual particles have to be generated first and then bonded together to form a rock structure. A procedure to generate these individual particles, within a uniform size distribution with radii in the range of [R_{min}, R_{max}] that fill a specified volume (V) at a given porosity (n), will be presented according to the method of radius expansion.

The number of particles (N) is generated in such a way that the overall porosity in the assembly is 35 % to ensure a tight initial packing. The following equation is used:

$$N = \frac{3V(1-n)}{4\pi \overline{R}^3} \text{ with } \overline{R} = \frac{R_{\min} + R_{\max}}{2} \tag{37}$$

These particles are generated at half their target sizes and placed randomly in a specified region to ensure that no overlap between neighbouring particles or particles and their region boundaries occur. The porosity of the generated assembly (n) is then computed in the algorithm as follows:

$$n = 1 - \frac{V_p}{V} \tag{38}$$

In this equation V is the volume in which the particles are contained and V_p is the total volume of the particles given by the following equation, with R being the particle radius:

$$V_p = \sum \frac{4}{3} \pi R^3 \tag{39}$$

By combining equations 38 and 39 one can write the following:

$$\sum R^3 = \frac{3V(1-n)}{4\pi} \tag{40}$$

Using equation 40 and designating the old porosity and radii by n_0 and R_0 and the new porosity and radii by n and R, the following equation is derived:

$$\frac{1-n}{1-n_0}=\frac{\sum R^3}{\sum R_0^3} \tag{41}$$

The radius multiplier (*m*) provides the number by which all the radii must be multiplied in order to change the porosity from n_0 to *n*. If the same radius multiplier is used for all the radii, then $R=mR_0$ can be substituted into equation 41 to derive the equation of the radius multiplier.

$$m=\left(\frac{1-n}{1-n_0}\right)^{1/3} \tag{42}$$

After the assembly of particles is generated, the properties of the particles are installed. These properties include normal (k_n) and shear stiffness (k_s), which is determined with the first two definitions in equation 22.

Six walls are generated as boundaries around the particles and the normal and shear stiffnesses of each wall are specified. The normal stiffness of the wall is chosen to be just larger than the average particle normal stiffness to ensure that particle-wall overlap will remain small.

A2. Isotropic stress installation procedure

The installation of the isotropic stress is an iterative procedure that is applied to all balls in an attempt to achieve the desired isotropic stress state. This isotropic stress (σ_0) of a particle is defined as the average of the direct stresses. These stresses are measured by dividing the total force acting on opposing walls by the area of the corresponding specimen cross-section.

$$\sigma_0=\frac{\bar{\sigma}_{kk}}{3} \tag{43}$$

The average stress (σ_{ij}) acting throughout a volume of a material can be written as follows:

$$\bar{\sigma}_{ij}=\frac{1}{V}\sum_{N_p}\bar{\sigma}_{ij}^{(p)}V^{(p)} \tag{44}$$

In this equation $\bar{\sigma}_{ij}^{(p)}$ is the average stress in a particle (*p*), which has the following equation:

$$\bar{\sigma}_{ij}^{(p)}=\frac{1}{V^{(p)}}\int_{V^{(p)}}\left[\left(x_i\sigma_{kj}^{(p)}\right)_{,k}-x_i\sigma_{kj,k}^{(p)}\right]dV^{(p)} \tag{45}$$

The identity $S_{ij}=\delta_{ik}S_{kj}=x_{i,k}S_{kj}=\left(x_iS_{kj}\right)_{,k}-x_iS_{kj,k}$ holds for any tensor S_{ij} and was applied in the previous equation. The Gauss divergence theorem is applied to the first term of equation 45 and the second term disappears because of the absence of body forces. This equation is then written as a surface integral.

$$\bar{\sigma}_{ij}^{(p)} = \frac{1}{V^{(p)}} \int_{S^{(p)}} x_i t_j^{(p)} dS^{(p)} \tag{46}$$

$S^{(p)}$ is the particle surface and $t_j^{(p)}$ is the traction vector. This integral can be replaced by a sum over the contacts by neglecting the moment carried by each parallel bond and replacing it with point forces acting at discrete contact locations.

$$\bar{\sigma}_{ij}^{(p)} = -\frac{1}{V^{(p)}} \sum_{N_c} x_i^{(c)} F_j^{(c)} \tag{47}$$

In this equation $x_i^{(c)}$ is the location and $F_j^{(c)}$ is the force acting at the contact. The negative sign in the equation is introduced to ensure that compressive/tensile forces produce negative/positive stresses. The contact location can be expressed as follows:

$$x_i^{(c)} = x_i^{(p)} + \left| x_i^{(c)} - x_i^{(p)} \right| n_i^{(c,p)} \tag{48}$$

The location of the particle centroid is denoted by $x_i^{(p)}$ and the unit-normal vector directed from the particle centroid to the contact location is denoted by $n_i^{(c,p)}$. By substituting equation 48 into 44 and noting that the sum of the forces acting on the contact is zero, the average stress for the particle in equilibrium can be written as follows:

$$\bar{\sigma}_{ij}^{(p)} = -\frac{1}{V^{(p)}} \sum_{N_c} \left| x_i^{(c)} - x_i^{(p)} \right| n_i^{(c,p)} F_j^{(c)} \tag{49}$$

An expression is then obtained for the average stress in a volume by combining equations 49 and 44.

$$\bar{\sigma}_{ij} = -\frac{1}{V} \sum_{N_p} \sum_{N_c} \tilde{R}^{(c,p)} n_i^{(c,p)} F_j^{(c)} \quad \text{where } \tilde{R}^{(c,p)} = \left| x_i^{(c)} - x_i^{(p)} \right| \tag{50}$$

The isotropic stress can then be estimated, where $F^{n(c)}$ the normal component of the force is acting at the contact.

$$\sigma_0 = \frac{\bar{\sigma}_{kk}}{3} - \frac{1}{3V} \sum_{N_p} \sum_{N_c} \tilde{R}^{(c,p)} F^{n(c)} \tag{51}$$

The radii of all the particles are scaled with the factor α and therefore the change in the radius is

$$\Delta R^{(p)} = \alpha R^{(p)} \tag{52}$$

When it is assumed that all the particles stay fixed, then the change in the normal component of the force acting at each contact can be written as follows:

$$\Delta F^{n(c)} = \alpha K^{n(c)} \phi^{(c)}$$

$$\phi^{(c)} = \begin{cases} R^A + R^B \\ R^{(p)} \end{cases} \tag{53}$$

In these equations $K^{n(c)}$ is the normal stiffness and $\phi^{(c)}$ are the particle radii at the contact. This is substituted into equation 51 and then rearranged as follows to obtain an expression for α:

$$\Delta\sigma_0 = -\frac{\alpha}{3V}\sum_{N_p}\sum_{N_c}\tilde{R}^{(c,p)} K^{n(c)} \phi^{(c)} \tag{54}$$

$$\alpha = -\frac{3V\Delta\sigma_0}{\sum_{N_p}\sum_{N_c}\tilde{R}^{(c,p)} K^{n(c)} \phi^{(c)}} \tag{55}$$

Equation 55 provides the change in radii that will produce a given change in isotropic stress. Unfortunately some particles rearrange when the radii change and therefore equation 55 is applied several times until the measured isotropic stress is within some tolerance of the target isotropic stress. When constructing granite, the target isotropic stress is set equal to approximately 1% of the uniaxial compressive strength to reduce the magnitude of the locked-in forces that develop after the parallel bonds are added and the specimen is removed from the material vessel and allowed to relax.

A3. Floater-elimination procedure

Floaters are particles that have less than three contacts and typically 10% to 15% of particles in an assembly are floaters. In a solid material such as rock, each floater is equivalent to a void in the material. The effect of voids can be minimized by adjusting micro-properties to obtain correct ensemble properties, but unfortunately the voids still introduce a pattern of inhomogeneity. The effect of inhomogeneity can be eliminated at its source through the floater-elimination procedure.

The algorithm starts with a stable compacted assembly with no bonds and the average stress level is low compared to the final stress level of the material. Firstly the current mean contact normal force for the assembly is acquired ($\overline{F}_a$). All the particles are scanned to identify the floaters. All the particles except the floaters are fixed and given zero velocities. The floaters are then expanded by a large amount (M_r) to ensure contact with all of their immediate neighbours. The assembly is cycled to equilibrium and the floaters are then contracted by an amount according to the following formula:

$$\Delta R = \frac{-2\left(\overline{F}_p - H\overline{F}_a f_m\right)}{k_n} \tag{56}$$

This amount is calculated to reduce the mean contact normal force below a target force $\left(F^{target} = \overline{F}_a f_m\right)$ where f_m is the target fraction of $\overline{F}_a$. This is done through the following definition:

$$R \leftarrow R - F_r\left(\overline{F}_p - H\overline{F}_a f_m\right)/k_n \tag{57}$$

If the mean contact normal force for a floater is below the target force, then the floater is inactive and is not contracted further. This step is repeated up to 100 times until all floaters become inactive and the complete procedure is repeated up to 10 times until all floaters have been removed.

Definition 57 will now be derived. The expression for the mean normal force on a single particle is given as follows:

$$\overline{F}_p = \frac{1}{N_c}\sum_{N_c} F^{n(c)} \tag{58}$$

In this equation $F^{n(c)}$ is the normal component of the force acting at a contact. Assuming that the particles remain fixed during the radius change of ΔR, the normal force at each contact is changed by the following amount:

$$\Delta F^n = \frac{1}{2}k_n \Delta R \tag{59}$$

The new mean normal force then becomes:

$$\overline{F}_p^{'} = \frac{1}{N_c}\sum_{N_c}\left(F^{n(c)} + \Delta F^n\right) \tag{60}$$

For the new mean normal force to be below the target normal force, $\overline{F}_p^{'}$ is set equal to HF^{target}, where H is the hysteresis factor with a value of 0.9, which prevents noise caused when particles satisfy the force criterion by only a small margin.

$$HF^{target} = \frac{1}{N_c}\sum_{N_c}\left(F^{n(c)} + \Delta F^n\right) = \frac{k_n \Delta R}{2} + \frac{1}{N_c}\sum_{N_c} F^{n(c)} \tag{61}$$

From this equation, equation 55 was derived which is identical to equation 57, where the factor 2 is replaced by F_r. F_r can be set to 1.5 to give smoother convergence since the radii of neighbouring particles may be adjusted simultaneously. A value of less than 2 also provides some damping which in return prevents excessive oscillation and instability.

A4. Calibration tests

During the uniaxial, triaxial and Brazilian tests, the stress state in the assembly has to be controlled and monitored to be able to obtain the macro-properties. These procedures are described below.

A4.1 Computing and controlling the stress state

The specimen is loaded by specifying the velocities of the top and bottom walls. The radial and axial stresses are computed by taking the average wall forces divided by the appropriate areas, using the current dimensions.

$$\sigma = \frac{F}{A} \tag{62}$$

The contact area for the radial and axial gain can be written respectively as follows:

$$A_{radial} = 2\pi \cdot r \cdot h \quad \text{and} \quad A_{axial} = \pi \cdot r^2 \tag{63}$$

The general relation for strain is as follows:

$$\varepsilon = \frac{L - L_0}{\frac{1}{2}(L_0 + L)} \tag{64}$$

In this equation L is the current radius or specimen length and L_0 is the original radius or specimen length.

The confining stress is kept constant throughout the loading process by adjusting the radial wall velocity using a numerical servo-mechanism. This mechanism is called once per cycle and it also uses a numerical servo-control to adjust the wall velocity in such a way that the difference between the computed and requested radial and axial stresses is minimal. The servo-control in the lateral direction has a switch and if it is turned on, the servo-control operates additionally on the top and bottom walls. The equation for the wall velocity is:

$$\dot{u}^{(w)} = G\left(\sigma^{measured} - \sigma^{required}\right) = G\Delta\sigma \tag{65}$$

In the above equation G is the gain parameter that is estimated by using the following reasoning. The maximum increment in wall force arising from wall movement in one time step is computed as follows:

$$\Delta F^{(w)} = k_n^{(w)} N_c \dot{u}^{(w)} \Delta t \tag{66}$$

N_c is the number of contacts and $k_n^{(w)}$ is the average stiffness of these contacts. Therefore the change in the mean wall stress is:

$$\Delta\sigma^{(w)} = \frac{k_n^{(w)} N_c \dot{u}^{(w)} \Delta t}{A} \tag{67}$$

The absolute value of the change in wall stress must be less than the absolute value of the difference between the measured and required stresses to ensure stability. A relaxation factor is used and the stability requirement is then written as follows:

$$\left|\Delta\sigma^{(w)}\right| < \alpha\left|\Delta\sigma\right| \tag{68}$$

Equation 65 and 67 is substituted into equation 68 to give the following expression:

$$\frac{k_n^{(w)} N_c G\left|\Delta\sigma\right|\Delta t}{A} < \alpha\left|\Delta\sigma\right| \tag{69}$$

Then the gain for the relevant walls can be determined.

$$G = \frac{\alpha A}{k_n^{(w)} N_c \Delta t} \tag{70}$$

A servo switch is then set to 1 and the requested stresses are obtained within a given tolerance.

A4.2 Elastic Properties

The Young's modulus can be determined as follows:

$$E = \frac{\Delta\sigma_a}{\Delta\in_a} = \frac{\Delta\sigma_d}{\Delta\in_a} \tag{71}$$

The Poisson's ratio has the following equation:

$$\nu = -\frac{\Delta\in_r}{\Delta\in_a} = \frac{1}{2}\left(1 - \frac{\Delta\in_v}{\Delta\in_a}\right) \tag{72}$$

A5. Reproduction of fracture mechanics and bond-breakage

The micro-cracks and prolonged cracks seen in real rock samples can be reproduced by BPM's through the patterns of bond-breakage. Since micro-cracks can only form between bonded particles, the number and location of micro-cracks are limited by the number and location of bonds in the specimen. Each micro-crack is represented as a cylinder lying between the two parent particles, from which the

micro-crack originated. The geometry of the micro-cracks can be described by the thickness (t), radius (R), unit-normal and centroid location. The thickness is represented by the gap between the particles and the radius is given by the intersection of the cylinder bisection plane. The unit-normal is directed along the line between the centres of the two particles and the centroid lies along this line and bisects the gap between the two particles. (Particle Flow Code in 3D Manual. Version 4. 2011)

A formal equivalence between the mechanisms and parameters of the BPM and the concepts and equations of linear elastic fracture mechanics (LEFM) was taken from Potyondy and Cundall (2004) and will be established in the following paragraphs.

The induced stress (σ_n), which acts on the crack plane near the crack tip for a crack of half-width (a) an infinitely wide plate of isotropic linear elastic material exposed to a remote tensile stress, is calculated as follows:

$$\sigma_n = \sigma_f \sqrt{\frac{a}{2r}} \tag{73}$$

In this equation *r* is the distance from the tip and *r << a*. The force (F_n) acting over a line segment of *2R* at a distance of *r= (2m-1)R* is given by:

$$F_n = \int_{r-R}^{r+R} \sigma_n t dr = \sigma_f t \sqrt{\frac{a}{2}} \int_{r-R}^{r+R} r^{-1/2} dr = 2\sigma_f t \sqrt{aR}\left(\sqrt{m} - \sqrt{m-1}\right), \tag{74}$$

where *m* is a positive integer representing the disk sequence number. The maximum contact force at *m=1* can then be calculated.

$$F_n^{\max} = 2tK_I \sqrt{\frac{R}{\pi}} \tag{75}$$

In this equation it should be noted that the mode-I stress intensity factor for the system is defined as $K_I - \sigma_f \sqrt{\pi a}$. The true tensile strength of the BPM, in which no force concentrations exist, for a cubically packed parallel-bonded material, is denoted by $\sigma_t^{'} = \overline{\lambda}\,\overline{\sigma}_c$

Since a non-zero bending moment ($\overline{M}^s$) develops at the crack tip and increases the maximum tensile stress acting on the bond periphery, a parallel-bonded material is weaker than a contact-bonded material for the same true tensile strength. The mode-I fracture toughness is then defined as

$$K_{Ic} = \beta \sigma_t^{'} \sqrt{\pi \alpha R}\,, \tag{76}$$

where $\alpha \geq 1$ is a non-dimensional factor that increases with packing irregularity, strength heterogeneity and bond ductility and $\beta < 1$ is a non-dimensional factor that accounts for the weakening effect of the bending moment.

A6. Relation of Brazilian tensile strength to fracture toughness

The following discussion is taken out of Potyondy and Cundall (2004). At peak load, one of the wedge-shaped regions of cracks, below the platens, initiates a single macro facture that travels across the specimen parallel with the direction of loading. To idealize the conditions at peak load, the wedge-shaped damage regions are replaced by edge cracks of length a, as seen in Figure 64. If the two cracks are not interacting (D-2a > a) then the mode-I stress-intensity factor at each crack tip is

$$K_I \propto \sigma\sqrt{a} \tag{77}$$

where σ is the tensile stress acting across the uncracked ligament.

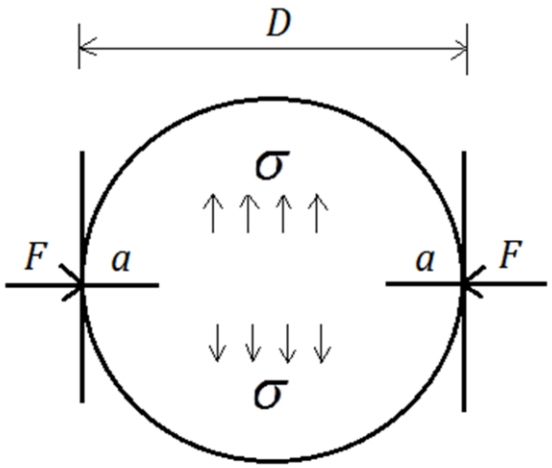

Figure 64: Idealized conditions at peak load of Brazilian test
(Adapted from Potyondy and Cundall, 2004)

At the peak load, $K_I = K_{Ic}$, $\sigma = \sigma_t$ and $a \cong 0.2D$, which can be substituted into equation 77 to give:

$$\sigma_t \propto \frac{K_{Ic}}{\sqrt{D}} \tag{78}$$

This equation suggests that the Brazilian strength should increase as the specimen size decreases. It can also be stated, from the analysis leading to equation 76, that:

$$K_{Ic} \propto \bar{\sigma}_c\sqrt{R} \tag{79}$$

where $\overline{\sigma}_c = \overline{\tau}_c$ is the mean parallel-bond strength and R is the mean particle radius. Combining equations 78 and 79 gives:

$$\sigma_t \propto \overline{\sigma}_c \sqrt{\frac{R}{D}} \tag{80}$$

Therefore it can be seen that the Brazilian strength is affected by the ratio of particle size to disk diameter. If all other micro-properties are kept fixed, the same Brazilian strength will be measured for all specimens with the same particle size to disk diameter ratio.

From equation 80 it can be derived that if the particle radius stays the same, an increase in the disk diameter will decrease the Brazilian strength. Therefore if larger specimens could be simulated in the calibration used in this study, the Brazilian strength would have been closer to the real value.

APPENDIX B:

SUMMARY OF NUMERICAL AND EXPERIMENTAL ROCK CUTTING DATA

In this Appendix a summary was made of the information found regarding the simulation and experimental parameters and the experimental data available from previous rock cutting investigations.

Table 13: Summary of information regarding rock cutting simulations

Author	Material used and Strength of material	Type of cutting tool	Simulation parameters	Experimental parameters	Experimental data
Su & Akcin (2011)	Sandstone-2: 173.7 MPa	Point attack pick	Attack angle = 57° Tip angle = 80° Clearance angle = 17° Rake angle = -7° Angle of friction = 8.5° Velocity = 0.3 m/s Cutting depth = 3 mm Cutting distance = 20 mm	None	Table comparing numerical, theoretical and experimental mean normal force, mean cutting force, mean peak normal force and mean peak cutting force.
Bilgin et al. (2012)	Granite: 180.3 MPa	Chisel tool	None	Rake angle = -10° Clearance angle = 6° Tool width = 25.4 mm	Table with experimental mean cutting force, peak cutting force, mean normal force and peak normal force.

				Velocity = N/A Cutting depth = 2.5 mm Cutting distance = 0.3 – 100 m Wear flat = 0 – 3.5 mm	
Gillani & Butt (2009)	Peridotite: 160.7 MPa Granite: 220.0 MPa	Chisel tool	None	Rake angle = -5° Clearance angle = 5° Tool width = 12 mm Velocity = 0.15 m/s Cutting depth = 5 mm Cutting distance = N/A	Table with mean peak cutting force, mean cutting force, mean peak normal force and mean normal force.
Rojek et al. (2010)	Sandstone: 127 MPa	Rotating road header pick	None	Velocity = 1.4 m/s Cutting depth = 10 mm Cutting distance = 800 mm	Graph of cutting force, normal force and side force against cutting distance; Bar graph comparing numerical results to experimental results.
Balci & Bilgin (2007)	Sandstone-2: 174 MPa	Chisel pick	None	Rake angle = -5° Clearance angle = 5° Tool width = 12.7 mm Velocity = N/A Cutting depth = 5 mm	Table of yield, mean cutting force, maximum cutting force, mean normal force and maximum normal force.
Bilgin et al. (2006)	Sandstone-2:174 MPa	Conical pick	None	Gauge = 80 mm Flange diameter = 64 mm Shank diameter = 35 mm Tip diameter = 22 mm Tip angle = 80° Attack angle = 55° Velocity = 0.127 m/s Cutting depth = 3 – 10 mm	Table comparing experimental to theoretical mean and peak cutting forces at 5 mm and 9 mm depth of cut.
Kaitkay & Lei (2005)	Carthage marble	Chisel tool	None	Rake angle = -15°, -25° Width of cut = 9.52 mm	Graph of main, thrust and side forces against time.

				Feed = 0.4, 0.8 mm/r Cutting speed = 1 m/s Cutting distance = 4.5 mm	
Akono & Ulm (2011)	Cement paste	Chisel tool	None	Rake angle = 15° Tool width = 10 mm Velocity = N/A Cutting depth = 0.5 mm Cutting distance = 35 mm	Graph of vertical and normal forces against scratch path.
Bilgin (1977)	Greywacke: 183.86 MPa	Pick tool	None	Rake angle = (-5°) – (-10°) Side clearance angle = 5° Back clearance angle = 10° Tool width = 10 mm Velocity = 0.15 m/s Cutting depth = 1.5 mm	Tables comparing experimental normal forces to predicted values.
Copur (2010)	Beige marble: 83.7 MPa, White marble: 35.8 MPa, Travertine(P): 12.7 MPa, Travertine(B): 36.7 MPa	Chisel tool	None	Sideways angles = 0°, 15°, 30°, 45° Tip angle = 90° Tool width = 12.7 mm Depth of cut = 1, 2, 3, 4 mm	Table of average normal force and average cutting force for different tools ; Graphs of normal and cutting force against depth of cut and sideways angle.
Holt et al. (2005)	Glass bead sample: 5.6-7.6 MPa	Chisel tool	Tool width = 1 mm Cutting depth = 1 mm Cutting distance = 55 mm	Tool width = 1.1 mm Velocity = 0.1 mm/s Cutting depth = 0.9 – 1.0 mm Cutting distance = 55 mm	Graph of total force of cutter against scratch length for experimental setup and numerical setup.

APPENDIX C:

RAW ROCK MECHANICS TESTS DATA

The data from the mechanical tests that were conducted at the University of the Witwatersrand, will be displayed in this Appendix. Each test was performed several times and the average value was then used to represent the macroproperty.

C1. Brazilian tensile strength test

The Brazilian tensile strength test was performed six times and the average value was 10.06 MPa, as calculated from Table 14.

Table 14: Brazilian tensile strength (UTS) test results

Specimen	Rock	Diameter	Length	L/D	Mass	Density	Failure	UTS
1	Granite	42.0	27.9	0.7	99.5	2574	22.00	**11.95**
2	Granite	42.0	27.9	0.7	100.3	2595	16.98	**9.22**
3	Granite	42.0	27.9	0.7	100.1	2590	19.62	**10.66**
4	Granite	42.0	27.9	0.7	99.5	2574	16.33	**8.87**
5	Granite	42.0	27.9	0.7	99.8	2582	17.69	**9.61**
6	Granite	42.0	33.0	0.8	118.5	2591	21.80	**10.01**

C2. Uniaxial compressive strength test

The uniaxial compressive strength test was conducted five times and from these tests the average uniaxial compressive strength, Young's modulus and Poisson's ratio were calculated as 198.23 MPa, 58.48 GPa and 0.32 respectively. The data recorded in each test can be seen in Table 15. In this table D is the diameter of the specimen and L is the length of the specimen.

Table 15: Uniaxial compressive strength (UCS) test results

Specimen Ref No		D (mm)	L (mm)	L/D	Mass (g)	ρ (kg/m^3)	Failure Load (kN)	E (GPa)	ν	UCS (MPa)
Rock Type	Wits No									
Granite	GRAN 1	42.0	106.0	2.5	382.0	2601	264.0	59.2	0.35	**190.55**
Granite	GRAN 2	42.0	106.0	2.5	386.0	2628	284.0	56.9	0.29	**204.99**
Granite	GRAN 3	42.0	105.8	2.5	382.0	2606	274.0	59.4	0.34	**197.77**
Granite	GRAN 4	41.8	102.4	2.4	368.4	2622	271.0	-	-	**197.48**
Granite	GRAN 5	42.0	105.0	2.5	378.8	2604	278.0	-	-	**200.66**

The curves presenting the data from the first test can be seen in Figure 65 and Figure 66. In Figure 65 the curve on the left is the axial stress and on the right is the lateral stress. From Figure 66 it can be seen that the elastic or Young's modulus and the Poisson's ratio increases with an increase in stress during the test. The overall value for the Young's modulus and for the Poisson's ratio for each test was determined by using equations 32 and 33 for stress and strain increments between the start and at a point at which one-half of the peak stress has been obtained.

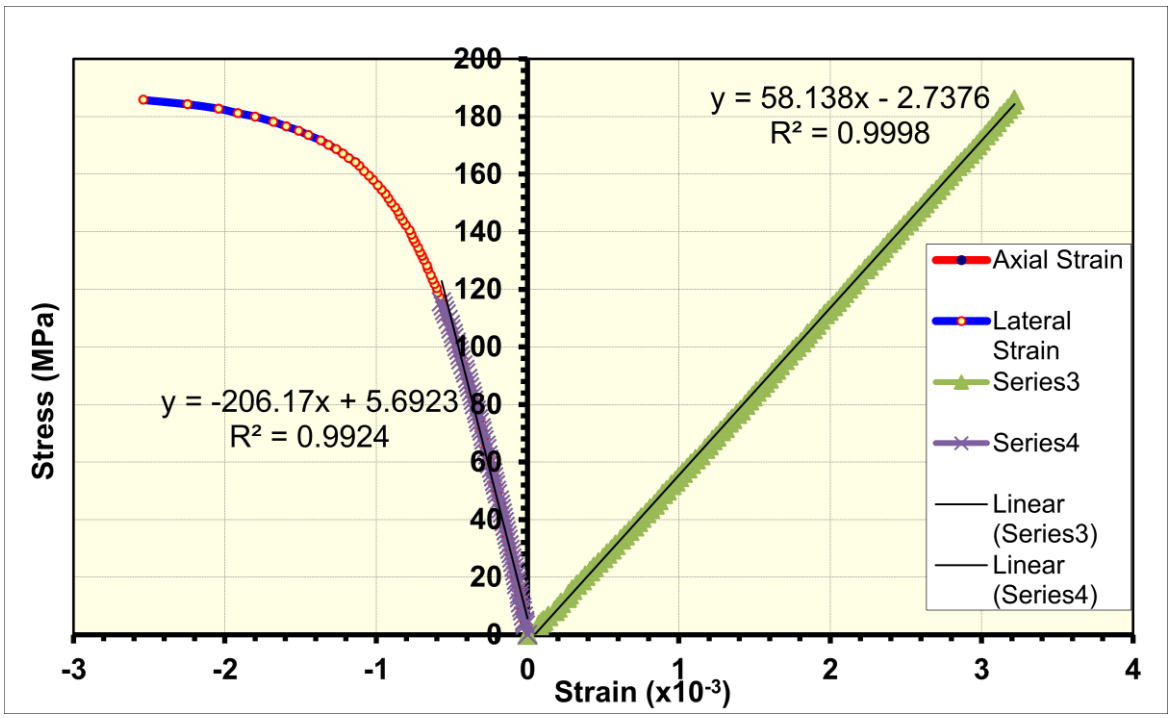

Figure 65: Stress-strain curve of specimen reference No. GRAN 1

(Source: Private communication with Dr H. Yilmaz at the University of the Witwatersrand, Johannesburg)

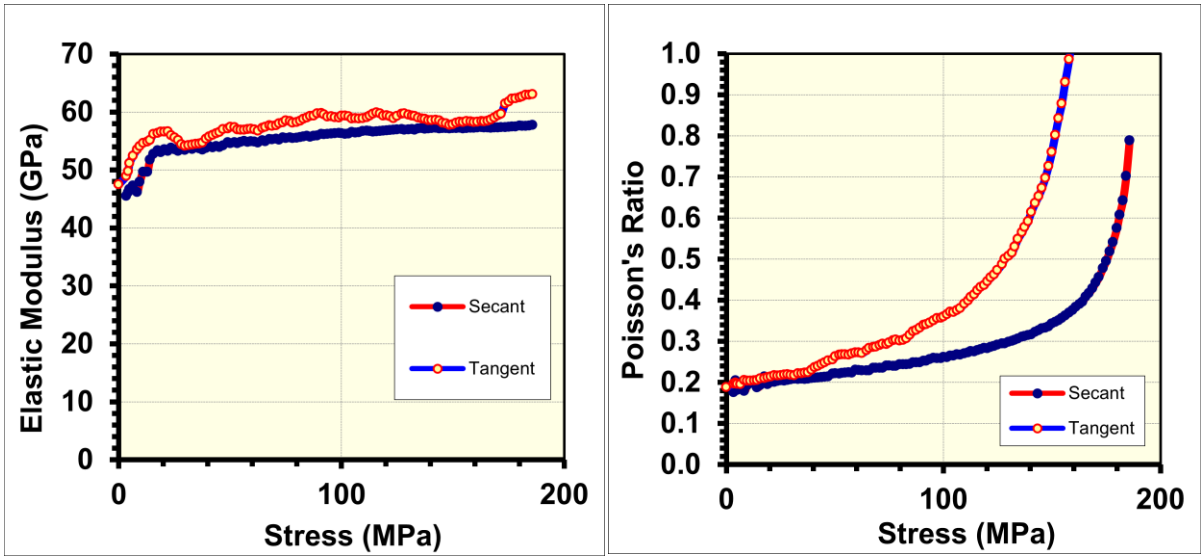

Figure 66: Elastic modulus and Poisson's ratio versus stress of specimen reference No. GRAN 1
(Source: Private communication with Dr H. Yilmaz at the University of the Witwatersrand, Johannesburg)

The curves presenting the data from the second test can be seen in Figure 67 and Figure 68. The same observations can be made as in the previous test except that the range of the elastic modulus was greater than in the previous case. The uniaxial compressive strength was also the highest during this test and the Young's modulus was the lowest.

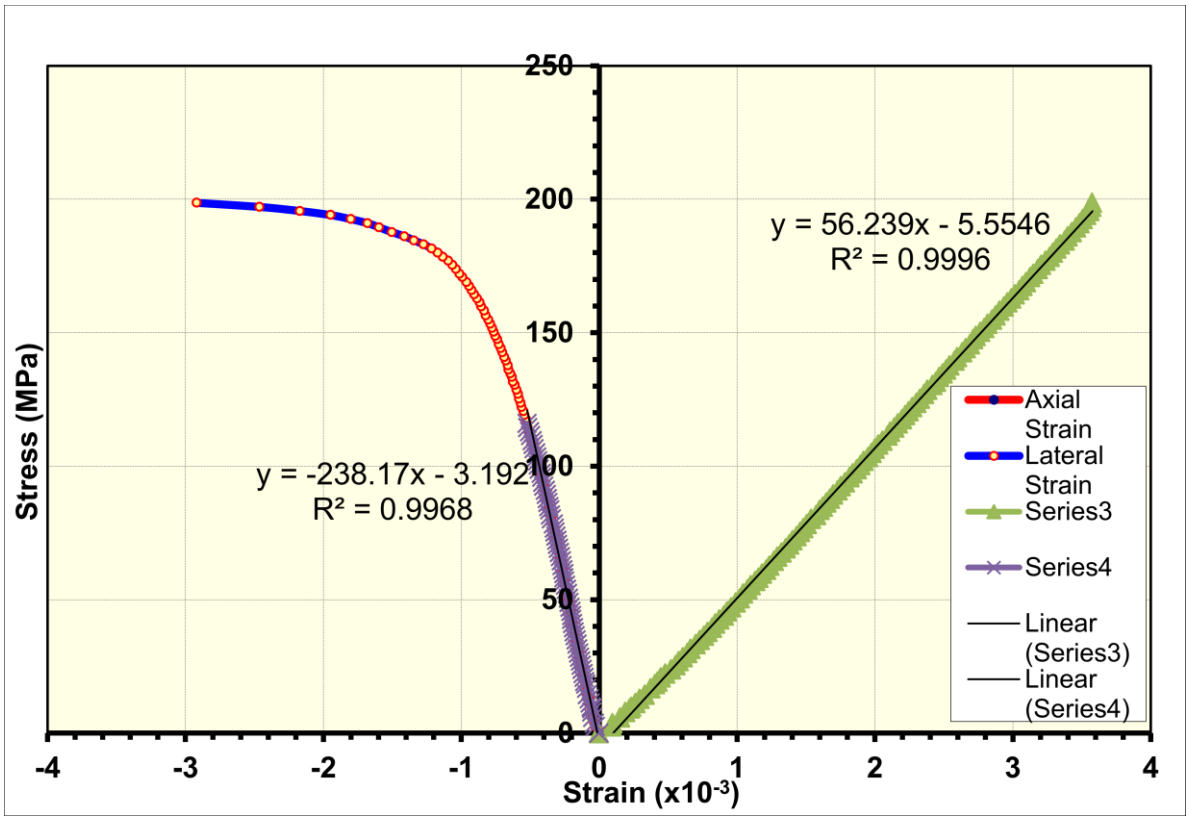

Figure 67: Stress-strain curve of specimen reference No. GRAN 2
(Source: Private communication with Dr H. Yilmaz at the University of the Witwatersrand, Johannesburg)

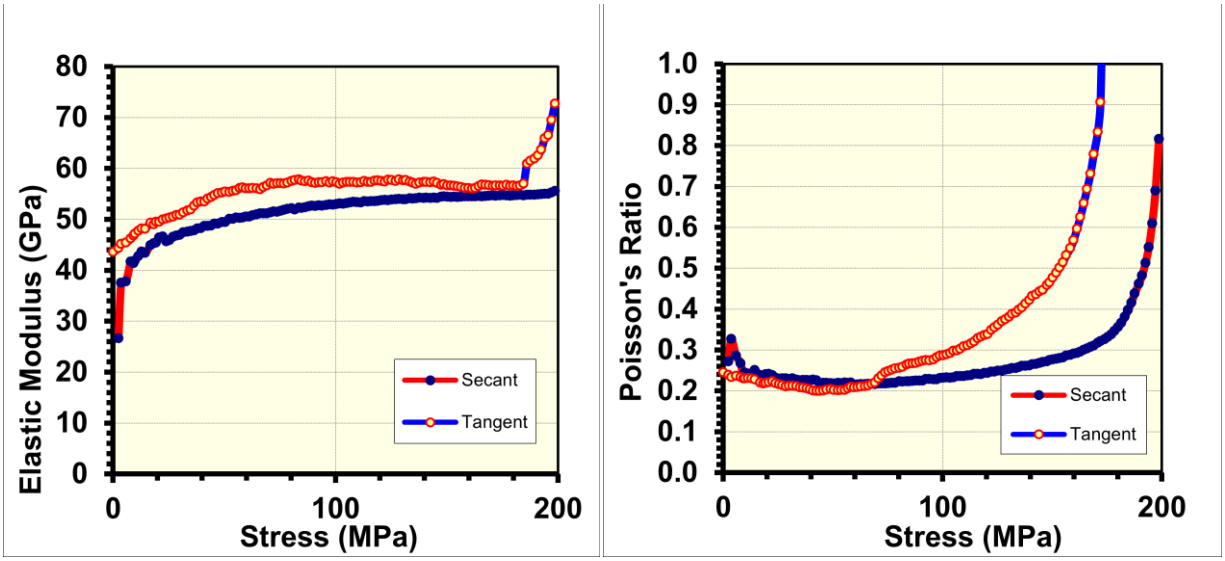

Figure 68: Elastic modulus and Poisson's ratio versus stress of specimen reference No. GRAN 2
(Source: Private communication with Dr H. Yilmaz at the University of the Witwatersrand, Johannesburg)

The curves presenting the data from the third test can be seen in Figure 69 and Figure 70. The curves still look the same as in the previous two tests but the peak value of the elastic modulus is in this case almost twice the value from the other tests.

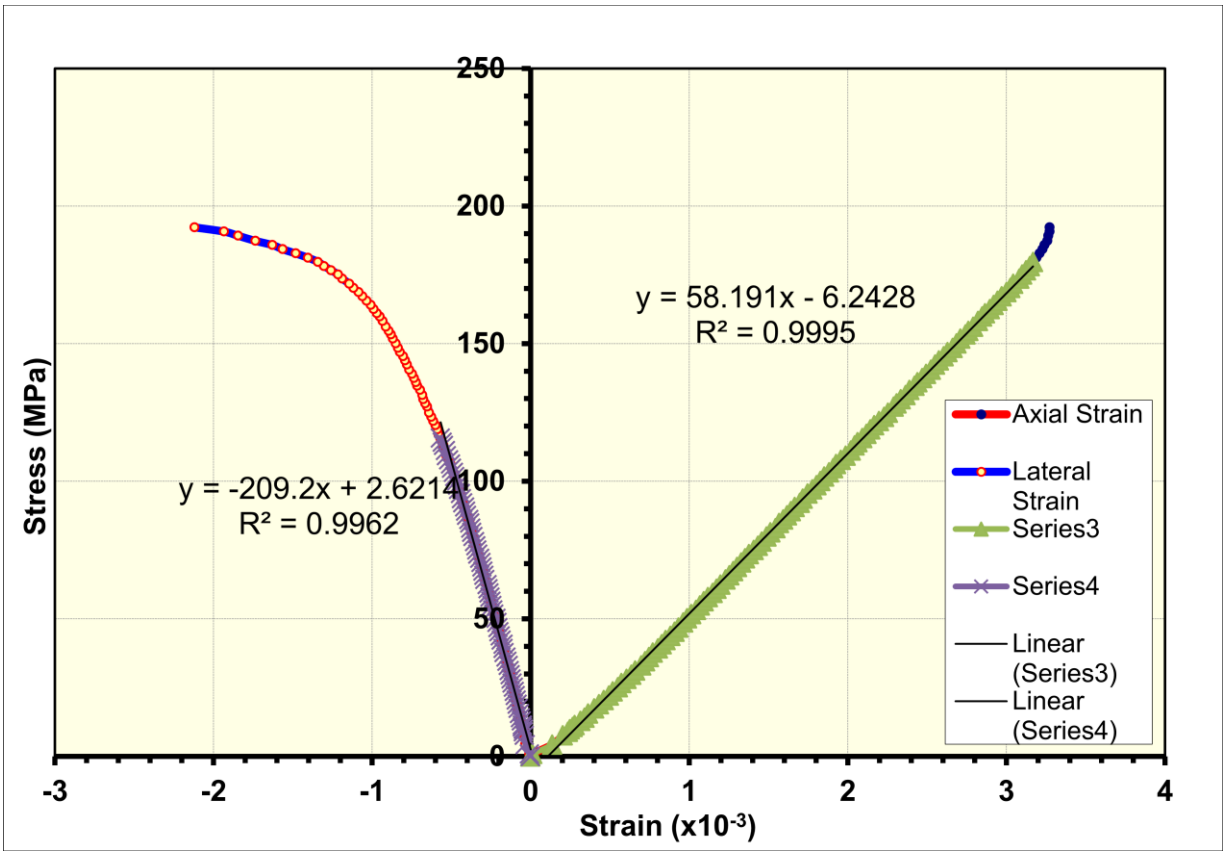

Figure 69: Stress-strain curve of specimen reference No. GRAN 3
(Source: Private communication with Dr H. Yilmaz at the University of the Witwatersrand, Johannesburg)

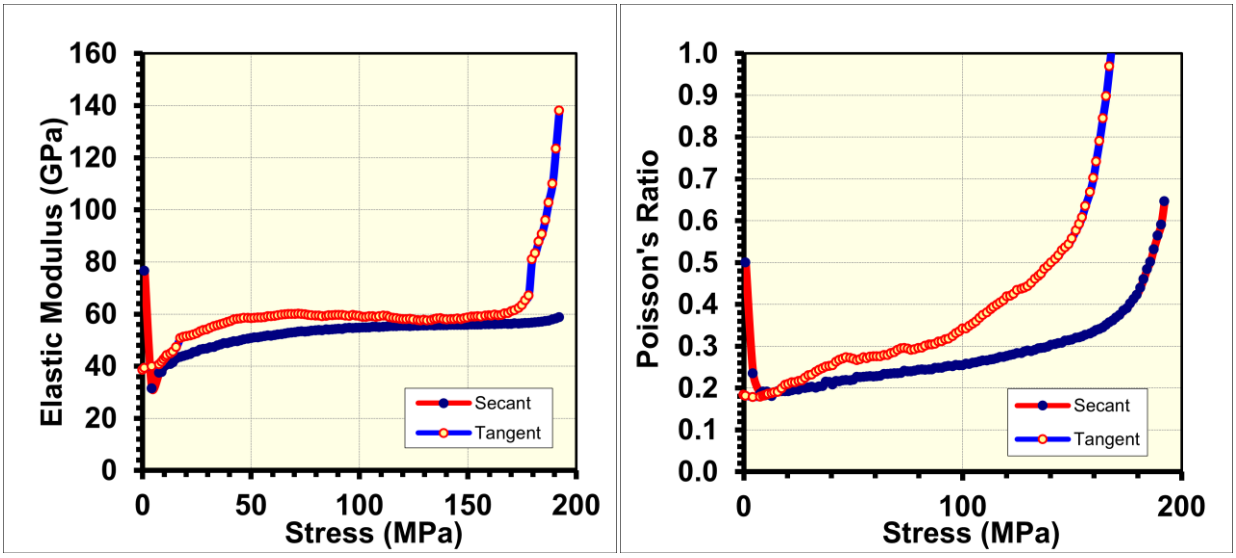

Figure 70: Elastic modulus and Poisson's ratio of specimen reference No. GRAN 3

(Source: Private communication with Dr H. Yilmaz at the University of the Witwatersrand, Johannesburg)

C3. Triaxial compressive strength test

The triaxial compressive strength test was performed twenty times with confinements ranging from 2 to 15 MPa. Therefore, for each confinement, five tests were performed. The results of these tests are shown in Table 16, where D is the diameter of the specimen and L is the length of the specimen. The average compressive strength for a confinement of 2, 6, 10 and 15 MPa was 221.2, 286.6, 331.6 and 385.0 MPa respectively. The strength increased with an increase in the confinement.

Table 16: Triaxial compressive strength test results

Specimen Ref No	Rock Type	D (mm)	L (mm)	L/D	Mass (g)	ρ (kg/m^3)	Failure Load (kN)	Strength (MPa)	Confine-ment (MPa)
1	Granite	42.0	106.0	2.5	386.0	2628	298.0	**215.1**	2
2	Granite	42.0	103.6	2.5	372.0	2592	378.0	**272.8**	6
3	Granite	42.0	105.5	2.5	380.0	2600	427.0	**308.2**	10
4	Granite	42.0	103.7	2.5	374.0	2603	539.0	**389.0**	15
5	Granite	42.0	106.0	2.5	384.0	2615	315.0	**227.4**	2
6	Granite	42.0	106.0	2.5	384.0	2615	397.0	**286.6**	6
7	Granite	42.0	105.8	2.5	388.0	2647	448.0	**323.4**	10
8	Granite	42.0	105.6	2.5	380.0	2597	548.0	**395.5**	15
9	Granite	42.0	106.0	2.5	384.0	2615	304.0	**219.4**	2
10	Granite	42.0	105.3	2.5	380.0	2605	403.0	**290.9**	6
11	Granite	42.0	106.0	2.5	384.0	2615	480.0	**346.5**	10
12	Granite	42.0	105.8	2.5	382.0	2606	533.0	**384.7**	15
13	Granite	42.0	106.0	2.5	384.0	2615	310.0	**223.8**	2

14	Granite	42.0	105.7	2.5	382.0	2609	406.0	**293.0**	6
15	Granite	42.0	106.0	2.5	384.0	2615	473.0	**341.4**	10
16	Granite	42.0	105.8	2.5	384.0	2620	541.0	**390.5**	15
17	Granite	42.0	106.0	2.5	384.0	2615	305.0	**220.1**	2
18	Granite	42.0	105.9	2.5	384.0	2617	401.0	**289.4**	6
19	Granite	42.0	105.5	2.5	382.0	2613	469.0	**338.5**	10
20	Granite	42.0	106.0	2.5	382.0	2601	506.0	**365.2**	15

C4. Base friction angle test or tilt test

The tilt test was executed five times and the results are summarised in Table 17. From these results the average base friction angle was calculated as 33.2°.

Table 17: Tilt test results

Specimen Ref No		Diameter (mm)	Length (mm)	L/D	Mass (g)	Density (kg/m^3)	Base Friction Angle (°)
Sample no	Rock Type						
1	Granite	42.0	49.7	1.2	178.8	2597	**32.1**
2	Granite	42.0	49.4	1.2	178.6	2610	**34.1**
3	Granite	42.0	49.5	1.2	178.6	2604	**32.6**
4	Granite	42.0	49.8	1.2	180.4	2615	**32.6**
5	Granite	42.0	49.2	1.2	178.5	2619	**35.0**

C5. Hook and Brown parameters

The calculation of the Hook and Brown parameters from the triaxial compressive strength test data is shown in Table 18 and by using the following equations:

$$\sigma_{ci} = \sqrt{\frac{\sum y}{n} - \frac{\sum x}{n}\left[\frac{\sum xy - \frac{\left(\sum x \sum y\right)}{n}}{\sum x^2 - \frac{\left(\sum x\right)^2}{n}}\right]} \tag{81}$$

$$m_i = \frac{1}{\sigma_{ci}}\left[\frac{\sum xy - \frac{\left(\sum x \sum y\right)}{n}}{\sum x^2 - \frac{\left(\sum x\right)^2}{n}}\right] \tag{82}$$

where σ_{ci} is the uniaxial compressive strength of the intact rock material and m_i is the material constant for the intact rock. The uniaxial compressive strength of the intact rock was calculated as 189.58 MPa and the material constant for the intact rock as 35.75.

Table 18: Calculation of the Hook and Brown parameters

σ_1 (MPa)	σ_3 (MPa) x	$(\sigma_1 - \sigma_3)^2$ y	xy	x²	y²
215.1	**2.0**	45408.9	90817.9	4.0	2061972607.8
272.8	**6.0**	71202.0	427212.1	36.0	5069726049.3
308.2	**10.0**	88926.1	889261.1	100.0	7907852855.6
389.0	**15.0**	139910.0	2098649.6	225.0	19574800702.9
227.4	**2.0**	50789.0	101578.0	4.0	2579525023.1
286.6	**6.0**	78708.9	472253.4	36.0	6195091982.1
323.4	**10.0**	98196.0	981960.1	100.0	9642456146.7
395.5	**15.0**	144811.9	2172177.9	225.0	20970475102.9
219.4	**2.0**	47273.4	94546.8	4.0	2234775679.5
290.9	**6.0**	81157.7	486945.9	36.0	6586564692.4
346.5	**10.0**	113205.2	1132051.6	100.0	12815407499.8
384.7	**15.0**	136688.9	2050334.1	225.0	18683865495.0
223.8	**2.0**	49175.4	98350.8	4.0	2418219017.7
293.0	**6.0**	82396.1	494376.6	36.0	6789116173.5
341.4	**10.0**	109830.7	1098307.3	100.0	12062790056.8
390.5	**15.0**	140992.0	2114879.8	225.0	19878740720.4
220.1	**2.0**	47587.8	95175.6	4.0	2264599205.8
289.4	**6.0**	80337.2	482023.4	36.0	6454071578.5
338.5	**10.0**	107925.4	1079254.2	100.0	11647895237.9
365.2	**15.0**	122658.5	1839877.0	225.0	15045099707.9

n	$\sum x$	$\sum y$	$\sum xy$	$\sum x^2$	$\sum y^2$
20.0	**165.0**	**1837181.1**	**18300033.2**	**1825.0**	**190883045535.7**

C6. Mohr-Coulomb parameters

The Mohr-Coulomb parameters were calculated from the data in Table 16 and Figure 71 and are displayed in Table 19. Here β is the strengthening parameter, c_o is the cohesion and ϕ is the internal friction angle.

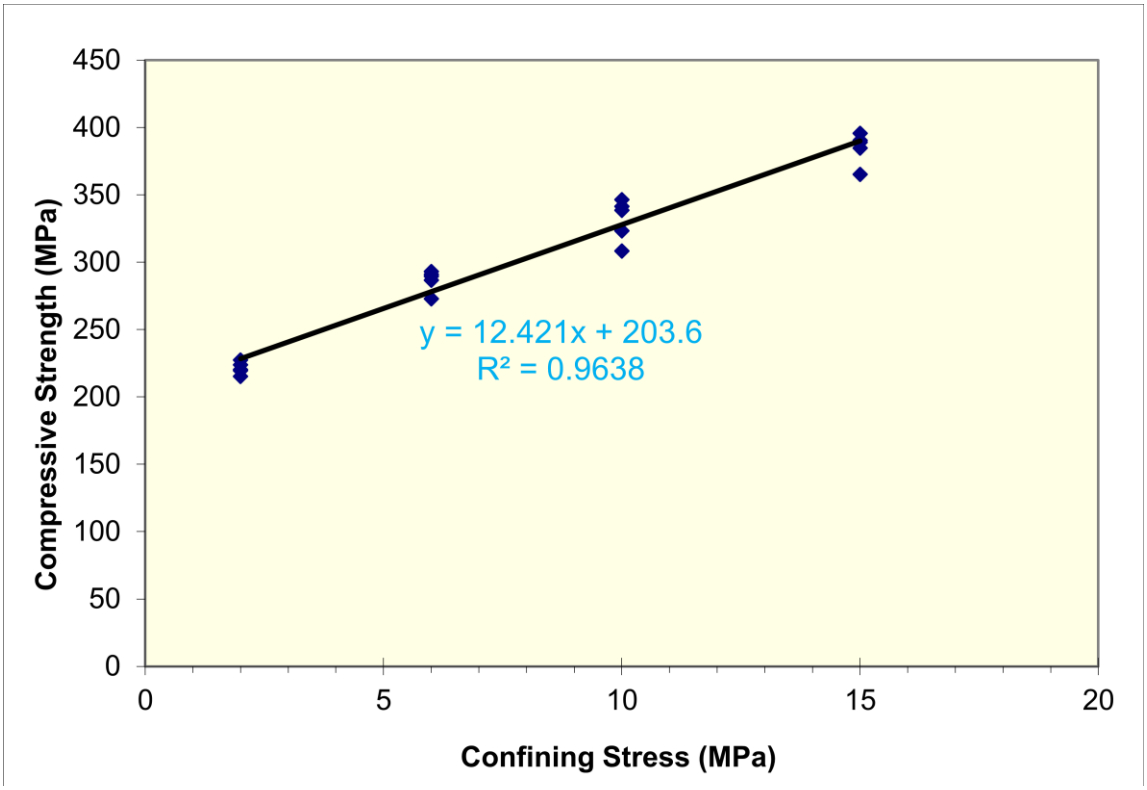

Figure 71: Mohr-Coulomb parameters analysis

(Source: Private communication with Dr H. Yilmaz at the University of the Witwatersrand, Johannesburg)

Table 19: Mohr-Coulomb parameters

UCS (MPa)	β	C_o (MPa)	ϕ (°)	R^2
203.60	12.42	28.9	58.3	0.9638

APPENDIX D:

RESULTS OF ROCK CUTTING SIMULATIONS

D1. Numerical, theoretical and experimental data from literature

Table 20 and Table 21 give the numerical, theoretical and experimental data from Su & Akcin (2011) and Bilgin et al. (2006) that was used in this study.

Table 20: Results of tool forces from numerical, theoretical and experimental data, Su & Akcin (2011)

Rock type	d (mm)	Cutting forces of numerical simulations (kN)				Theoretical cutting forces (kN)			Experimental cutting forces (kN)			
		FN	FC	FN'	FC'	FC'_{Evans}	$FC'_{Rox\&Liu}$	FC'_{Goktan}	FN	FC	FN'	FC'
Sand-stone-2	3	0.48	0.58	1.07	1.57	0.60	0.87	1.11	6.1	4.1	11.9	9.2
	6	2.05	2.48	3.48	5.47	2.39	3.50	4.44	10.8	8.2	23.9	23.3
	9	3.46	5.41	5.70	10.33	5.37	7.87	10.00	19.3	16.9	42.8	48.7

Table 21: Comparison of experimental and theoretical cutting forces for unrelieved cutting mode, Bilgin et al. (2006)

Rock name	Depth of cut = 5 mm					Depth of cut = 9 mm				
	Experimental cutting forces		Theoretical cutting force			Experimental cutting forces		Theoretical cutting force		
	Mean (kgf)	Peak (kgf)	Evans (kgf)	Goktan (kgf)	Roxborough (kgf)	Mean (kgf)	Peak (kgf)	Evans (kgf)	Goktan (kgf)	Roxborough (kgf)
Sand-stone-2	820	2325	166	941	282	1686	4810	662	3763	913

D2. Sample calculations of theoretical cutting forces

Equations 26, 28 and 29 in section 2.7 were used to determine the mean peak cutting forces for point-attack picks from the mechanical properties of Sandstone-2 in Table 6 and the cutting parameters

described in section 4. Since the calculations for each depth of cut are performed in the same way, the sample calculations will only be shown for a depth of cut of 0.5 mm.

The mean peak cutting force was calculated as follows using the model of Evan's, Roxborough and Goktan, respectively, where all the angles are in degrees:

$$FC'_{Evan's} = \frac{16\pi\sigma_t^2 d^2}{\sigma_c \cos^2\theta} = \frac{16\cdot\pi\cdot 11.6^2\cdot 0.5^2}{173.7\cdot\cos^2(40)} = 16.59N \approx 0.017kN$$

$$FC'_{Rox} = \frac{16\pi\sigma_c d^2\sigma_t^2}{\left(2\sigma_t + \left((\sigma_c\cos\theta)/\left[(1+\tan\phi)/\tan\theta\right]\right)\right)^2} = \frac{16\cdot\pi\cdot 173.7\cdot 0.5^2\cdot 11.6^2}{\left(2(11.6) + \left((173.7\cdot\cos(40))/\left[(1+\tan(8.5))/\tan(40)\right]\right)\right)^2} = 20.28N = 0.02kN$$

$$FC'_{Gok\tan} = \frac{4\pi\sigma_t d^2\sin^2\left[\theta+\phi\right]}{\cos\left[\theta+\phi\right]} = \frac{4\cdot\pi\cdot 11.6^2\cdot 0.5^2\sin^2\left[40+8.5\right]}{\cos\left[40+8.5\right]} = 30.85N = 0.031kN$$

Equations 23 and 27 in section 2.7 were used to determine the mean peak cutting forces for chisel-shaped picks from the mechanical properties of Sandstone-2 in Table 6 and the cutting parameters described in section 4. Again the sample calculations will only be shown for one depth of cut, namely a depth of cut of 5 mm.

The mean peak cutting force was calculated as follows using the model of Evan's and Nishimatsu respectively:

$$FC'_{Evan's} = \frac{2\sigma_t dw\sin\frac{1}{2}\left(\frac{\pi}{2}-\alpha\right)}{1-\sin\frac{1}{2}\left(\frac{\pi}{2}-\alpha\right)} = \frac{2\cdot 11.6\cdot 5\cdot 12.5\cdot\sin\frac{1}{2}\left(\frac{\pi}{2}-(-5)\right)}{1-\sin\frac{1}{2}\left(\frac{\pi}{2}-(-5)\right)} = 4069N = 4.07kN$$

$$FC'_{Nishimatsu} = \frac{2\sigma_s dw\cos(k)\cdot\cos(\phi-\alpha)}{(n+1)(1-\sin(k-\alpha+\phi))} = \frac{2\cdot 22.4\cdot 5\cdot 12.5\cdot\cos(61.08)\cdot\cos(8.5-(-5))}{(13+1)(1-\sin(61.08-(-5)+8.5))} = 2964.96N = 2.96kN$$

The angle of internal friction (k) was calculated as follows:

$$\tan k = \frac{\sigma_c^2 - 4\sigma_s^2}{4\sigma_c\sigma_s} = \frac{173.7^2 - 4\cdot 22.4^2}{4\cdot 173.7\cdot 22.4} = 1.809 \Rightarrow k = 61.08$$

D3. Results of rock cutting at 0.5 mm depth of cut for Su & Akcin (2011)

The simulated tool forces for the narrow point-attack picks with different wear flats at 0.5 mm depth of cut are shown in Figure 72 to Figure 75. The values of the normal and cutting forces are very similar at this shallow depth of cut and the sideways forces fluctuate around zero.

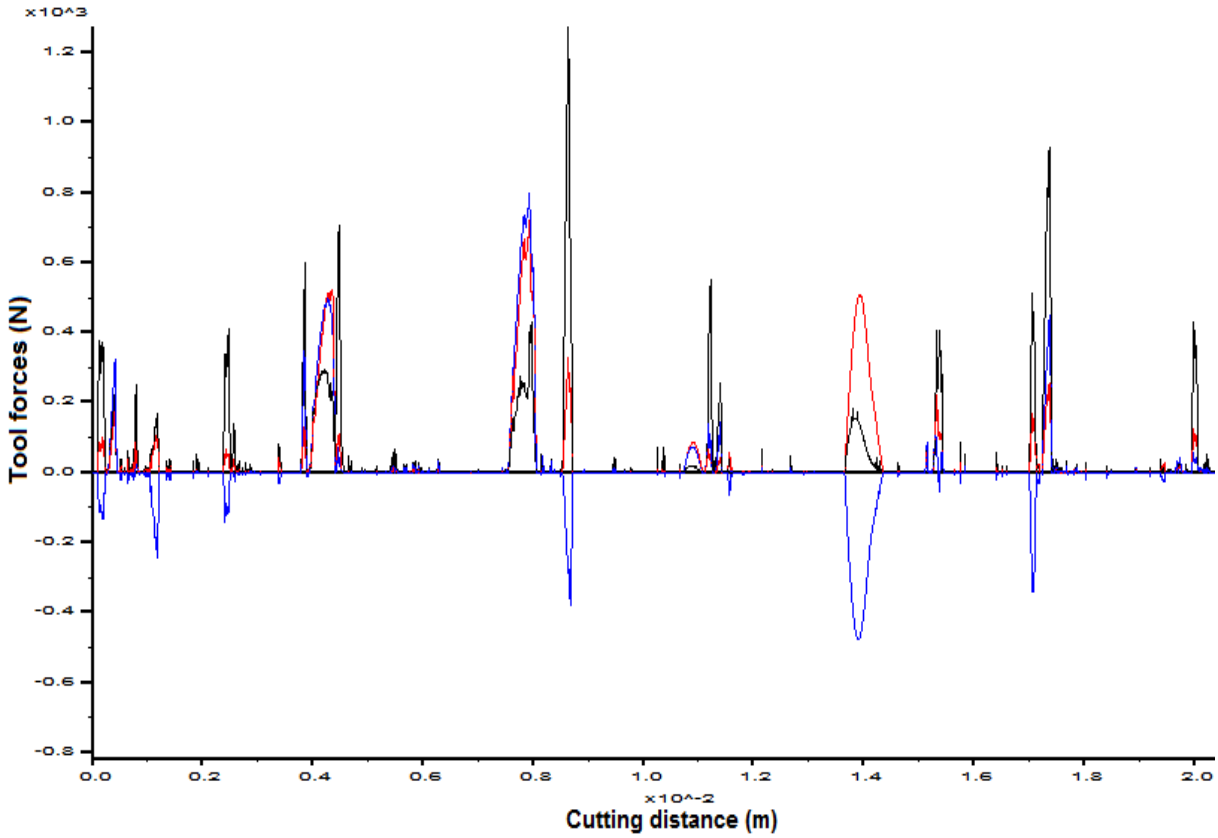

Figure 72: The variation of tool forces versus cutting distance for a sharp narrow point-attack pick cutting 0.802 mm particles at 0.5 mm depth of cut

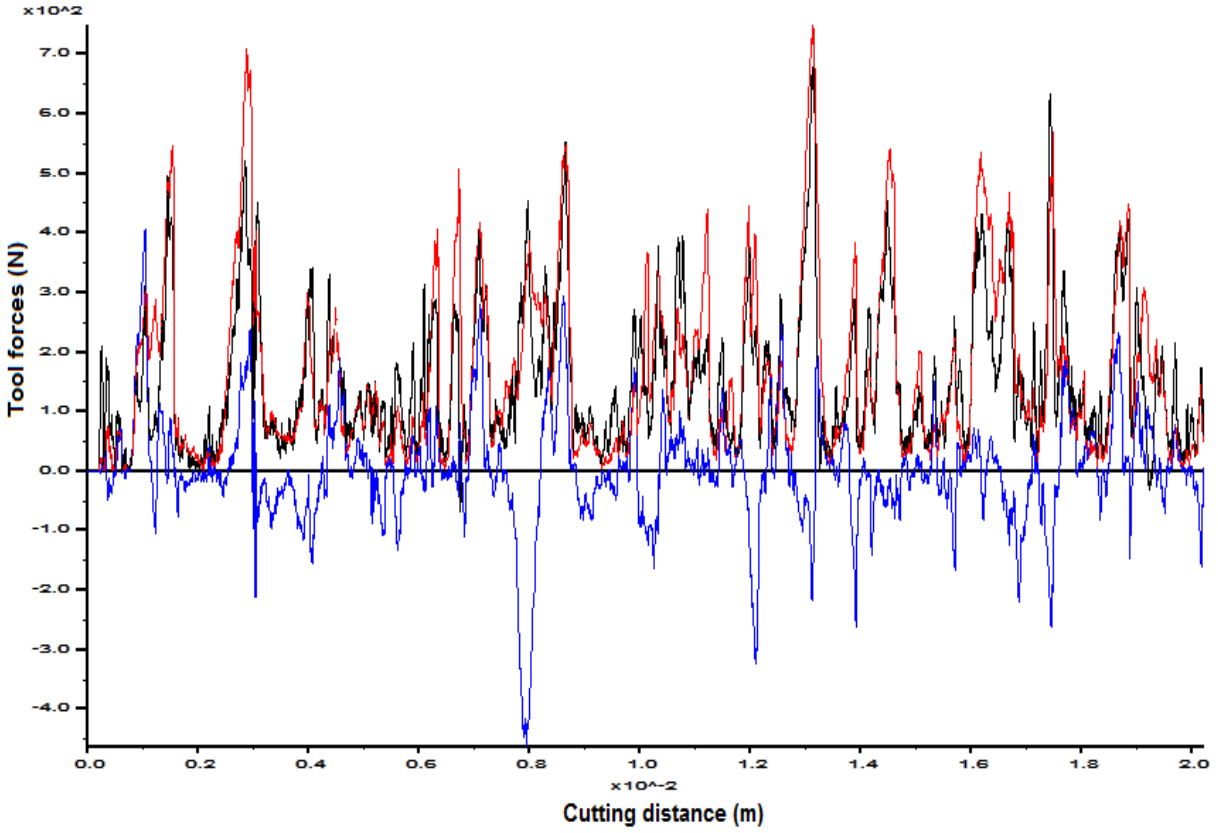

(a)

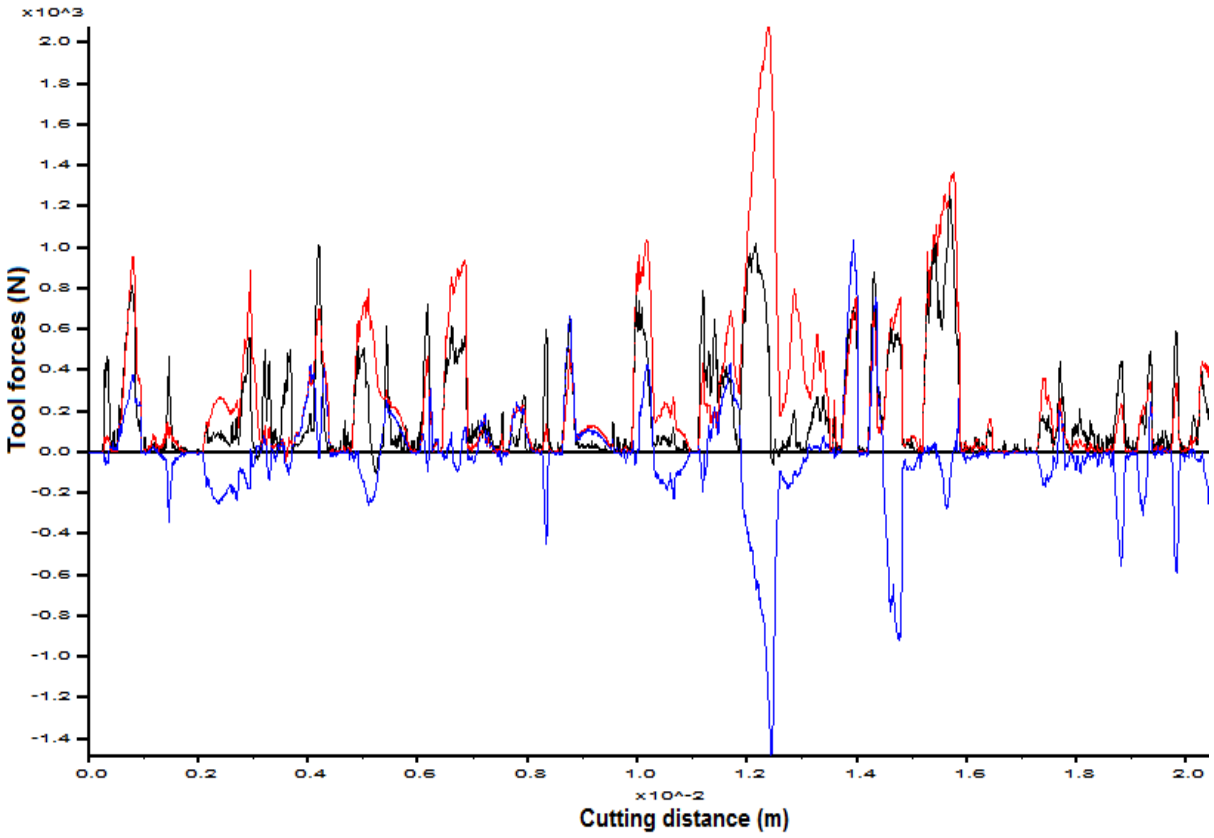

(b)

Figure 73: The variation of tool forces versus cutting distance for a blunt narrow point-attack pick with 0.5 mm wear flat at 0.5 mm depth of cut

(a) 0.401 mm particles; (b) 0.802 mm particles

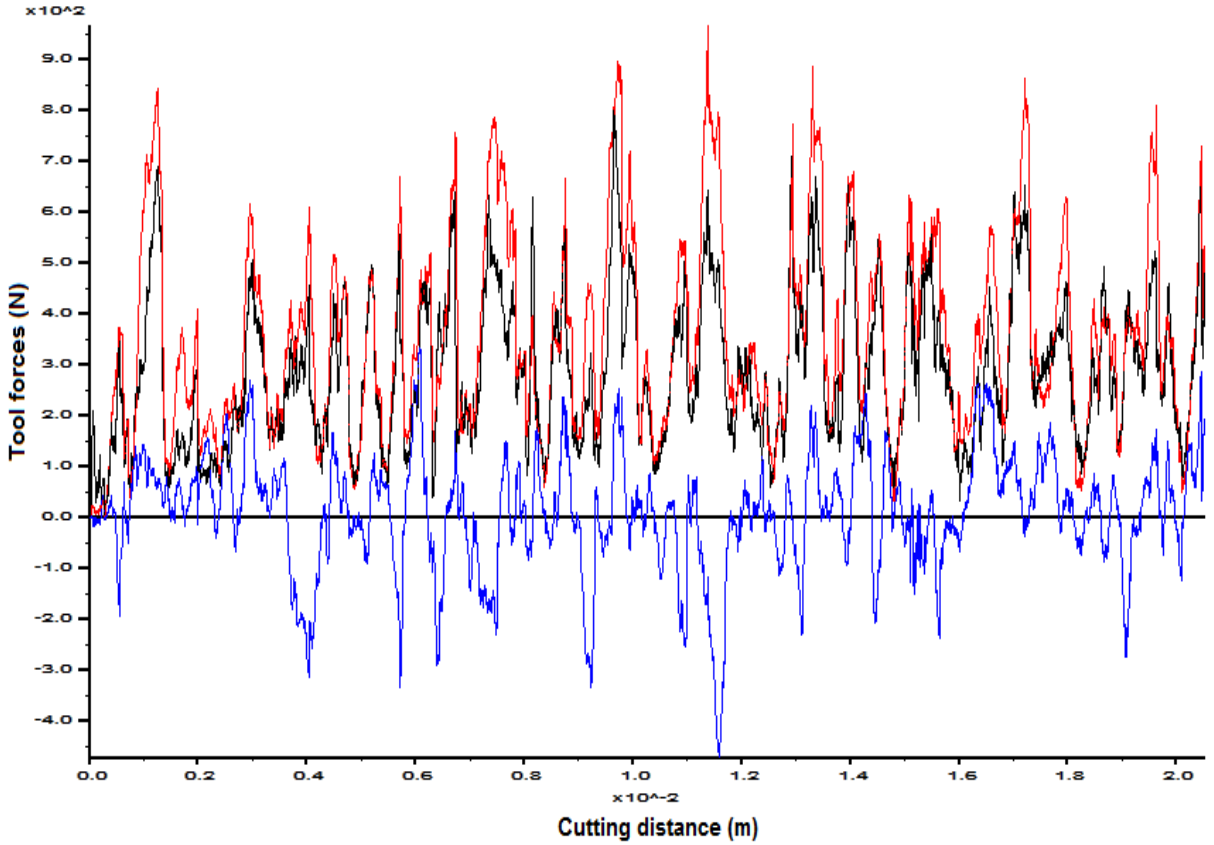

(a)

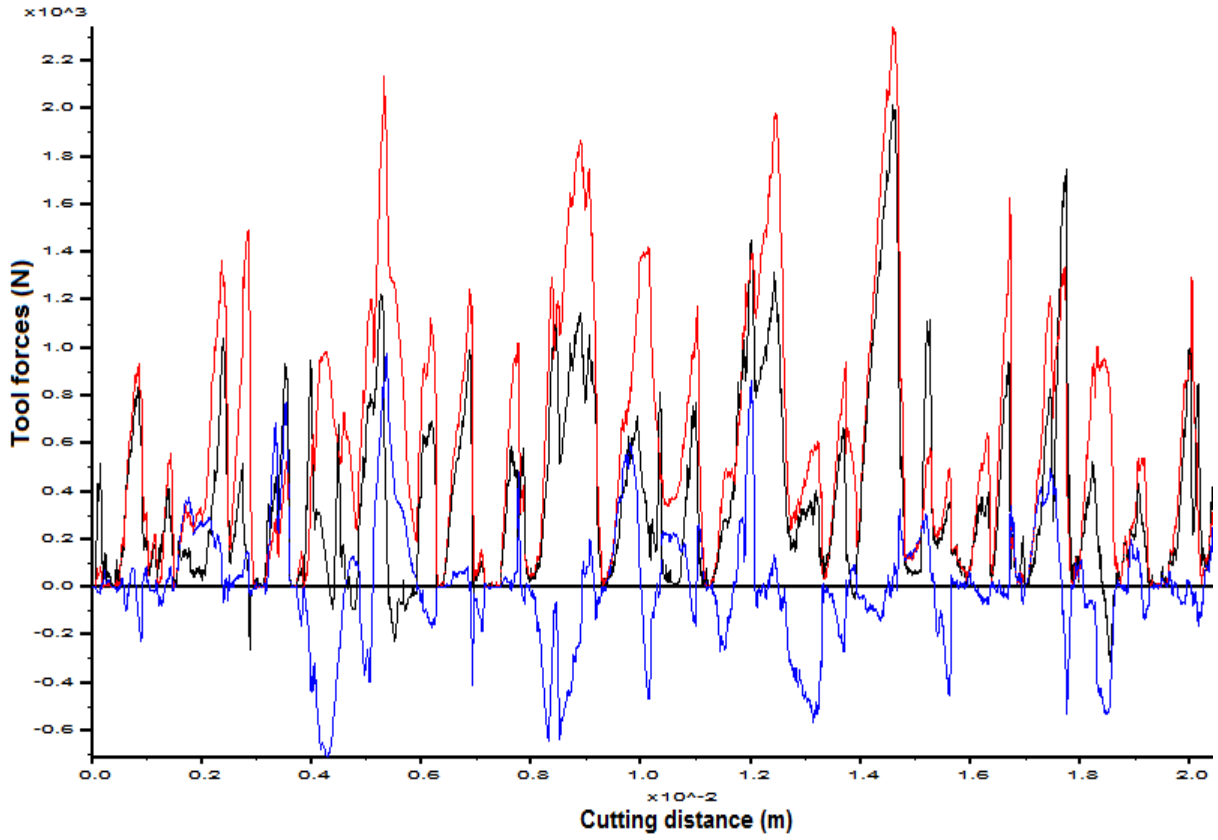

(b)

Figure 74: The variation of tool forces versus cutting distance for a blunt narrow point-attack pick with 1 mm wear flat at 0.5 mm depth of cut

(a) 0.401 mm particles; (b) 0.802 mm particles

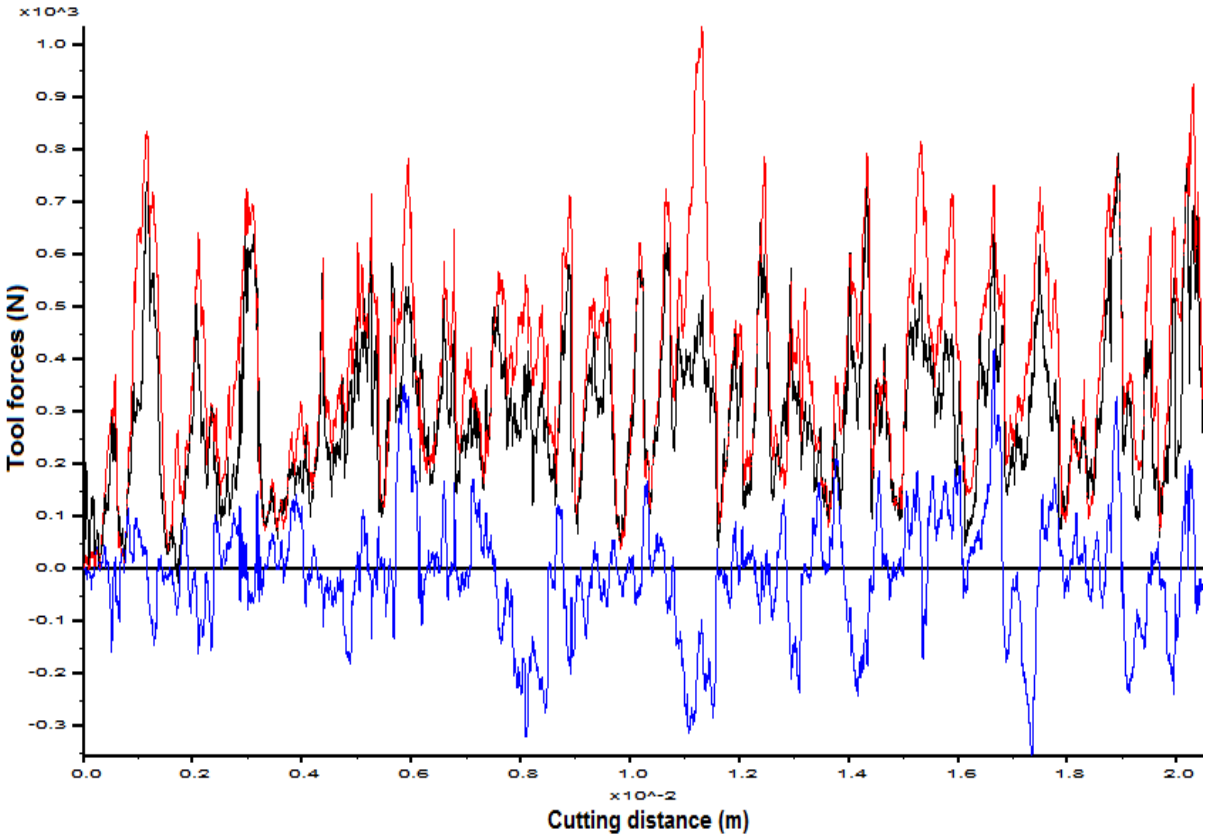

(a)

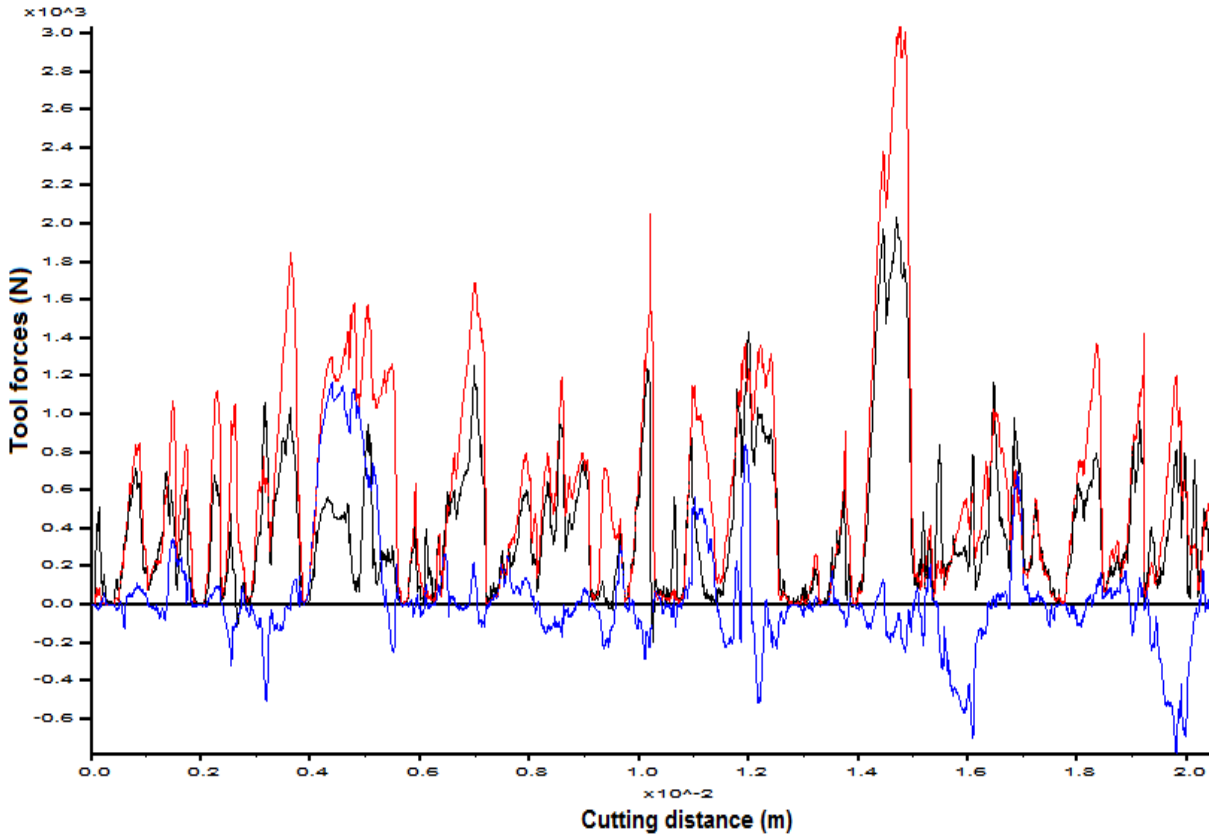

(b)

Figure 75: The variation of tool forces versus cutting distance for a blunt narrow point-attack pick with 1.5 mm wear flat at 0.5 mm depth of cut

(a) 0.401 mm particles; (b) 0.802 mm particles

Figure 76 shows the shape that the micro-cracks form after 20 mm cutting distance when cutting with blunt point-attack picks with different wear flats. The shape is almost triangular when using a pick with a small wear flat of 0.5 mm and it becomes more oval with an increase in the wear flat, since the micro-cracks spread out more.

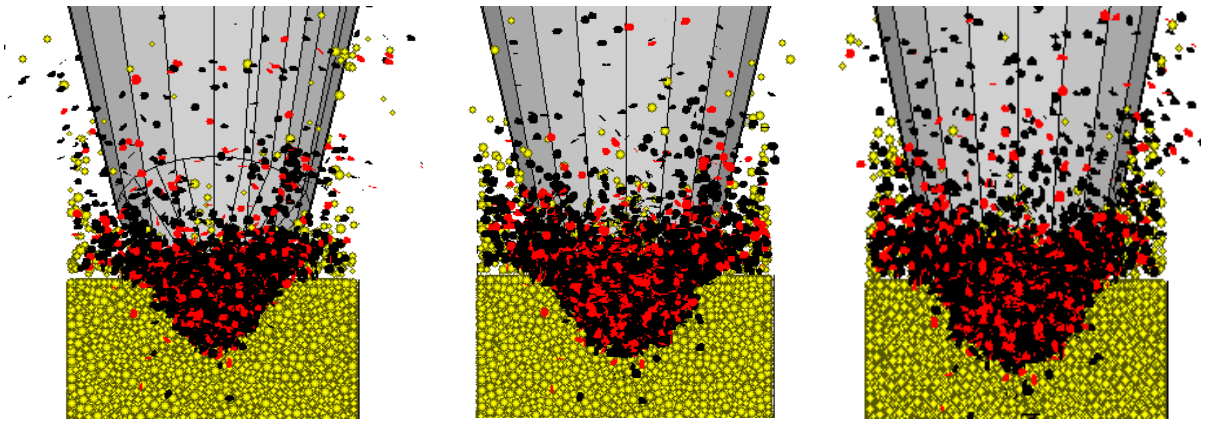

(a) (b) (c)

Figure 76: Shape of cracks in specimen when cutting with blunt narrow point-attack picks at 0.5 mm depth of cut

(a) 0.5 mm wear flat; (b) 1 mm wear flat; (c) 1.5 mm wear flat

D4. Results of rock cutting at 1.5 mm depth of cut for Su & Akcin (2011)

The simulated tool forces for the narrow point-attack picks with different wear flats at 1.5 mm depth of cut are shown in Figure 77 to Figure 80. The normal and cutting forces increase over a certain distance and then it fluctuates around an average value. For the cutting of the samples with 0.401 mm particles, there is a greater difference in the normal and cutting forces than the cutting of samples with 0.802 mm particles. The sideways forces still fluctuate around zero.

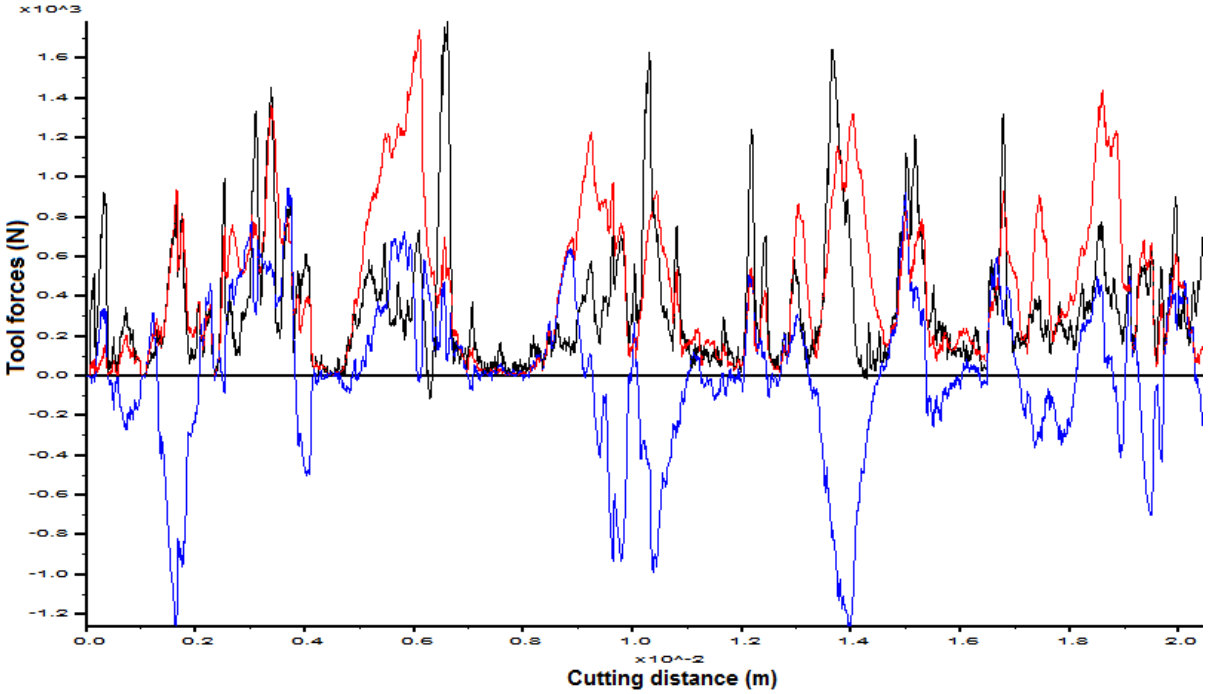

Figure 77: The variation of tool forces versus cutting distance for a sharp narrow point-attack pick cutting 0.802 mm particles at 1.5 mm depth of cut

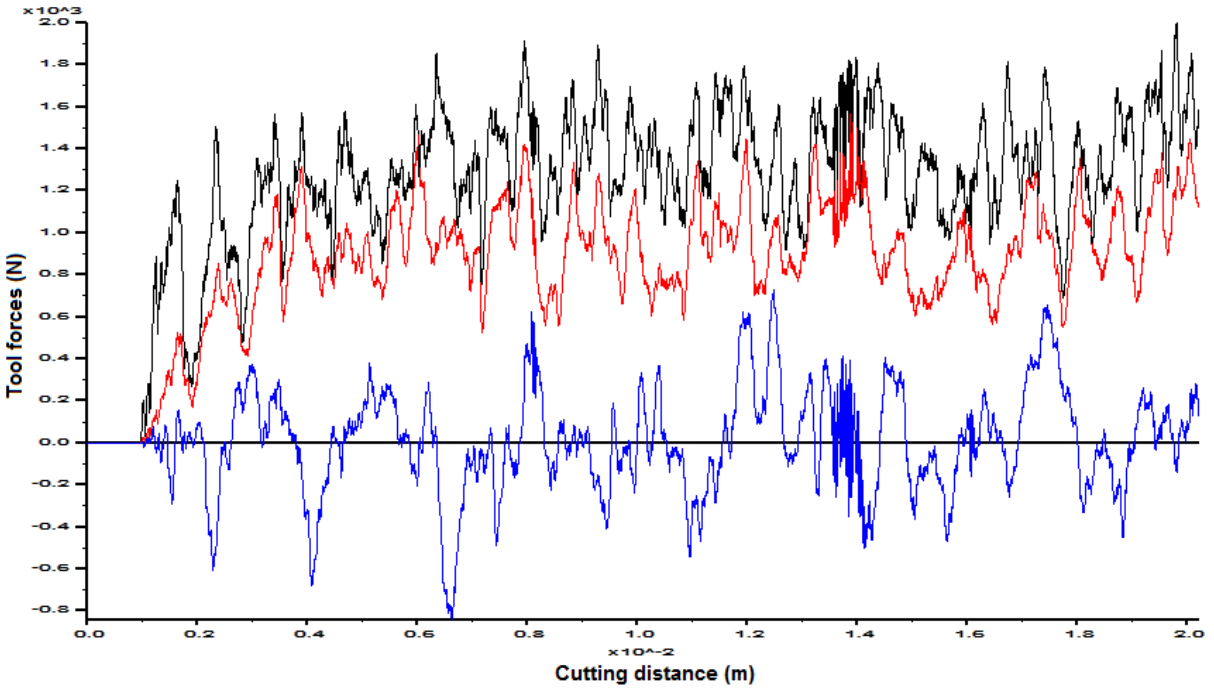

(a)

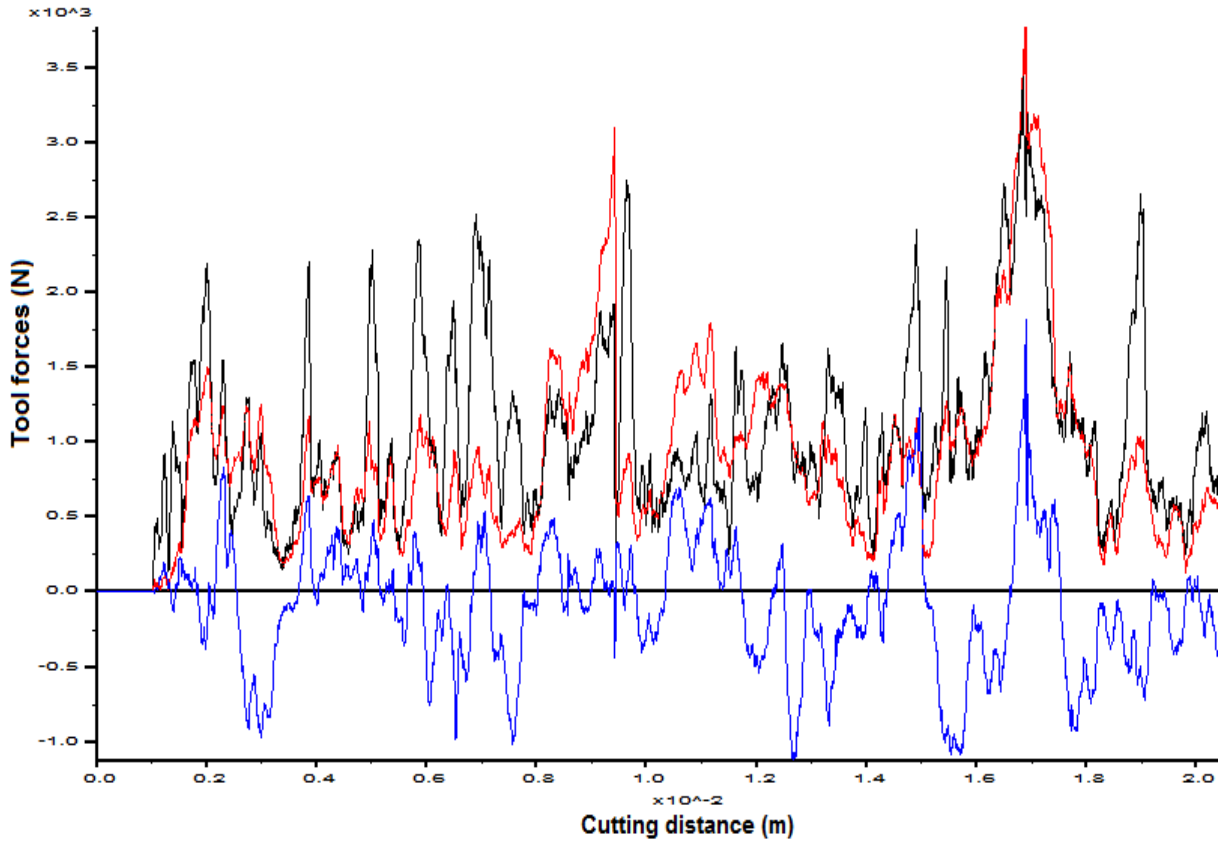

(b)

Figure 78: The variation of tool forces versus cutting distance for a blunt narrow point-attack pick with 0.5 mm wear flat at 1.5 mm depth of cut

(a) 0.401 mm particles; (b) 0.802 mm particles

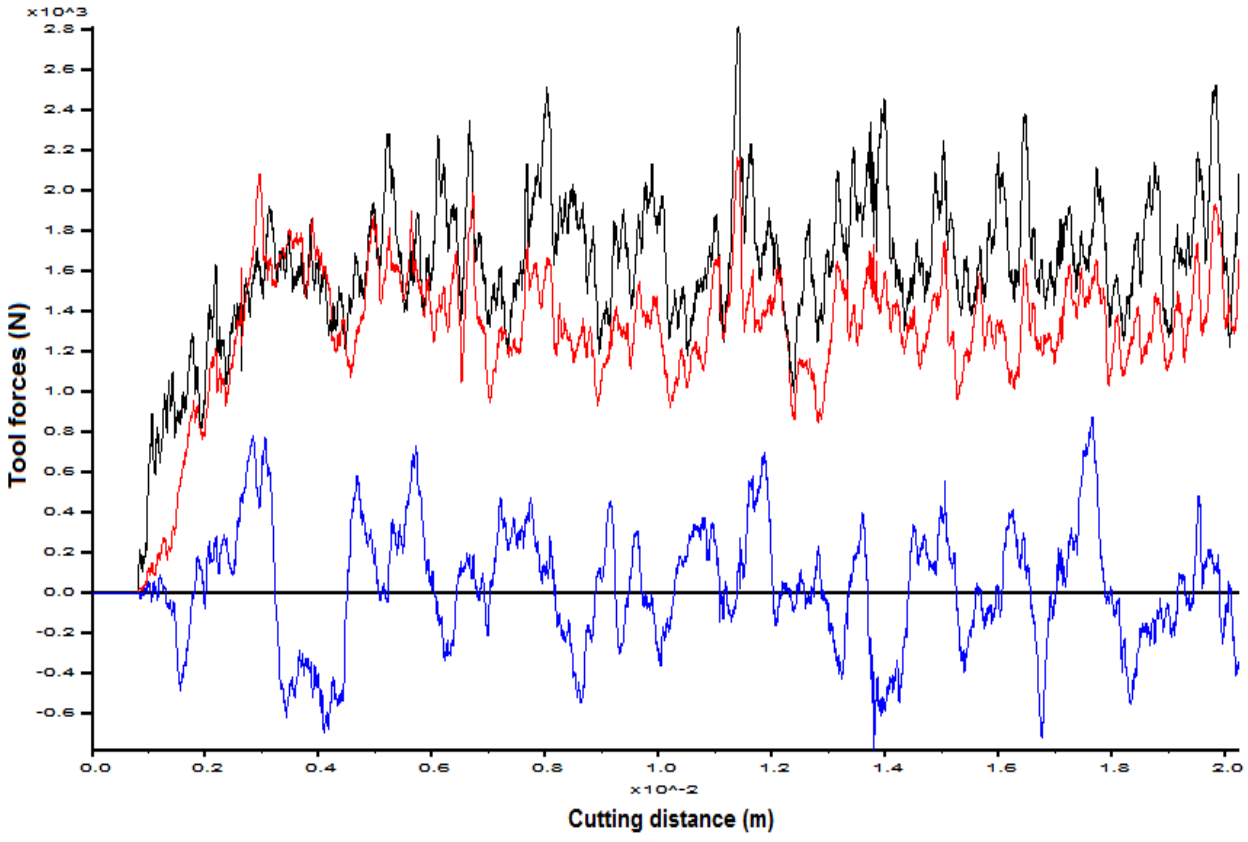

(a)

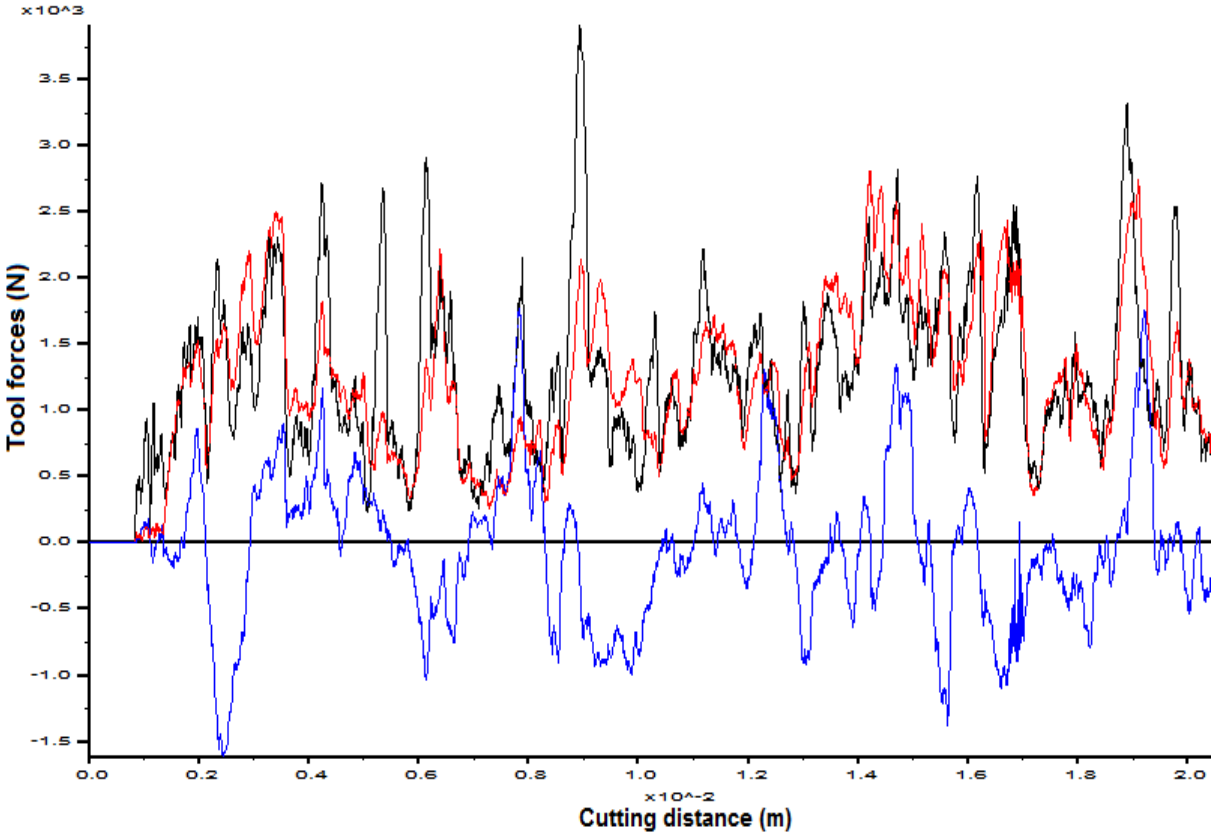

(b)

Figure 79: The variation of tool forces versus cutting distance for a blunt narrow point-attack pick with 1 mm wear flat at 1.5 mm depth of cut

(a) 0.401 mm particles; (b) 0.802 mm particles

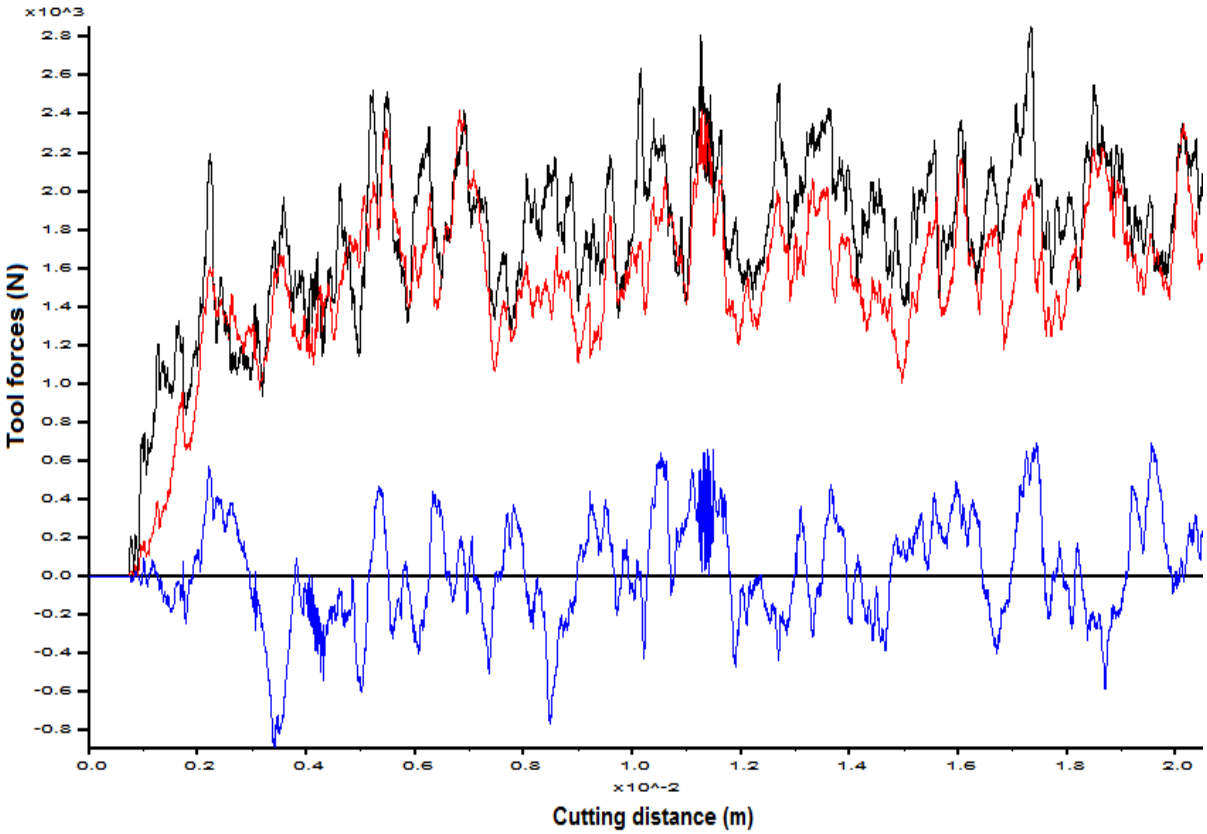

(a)

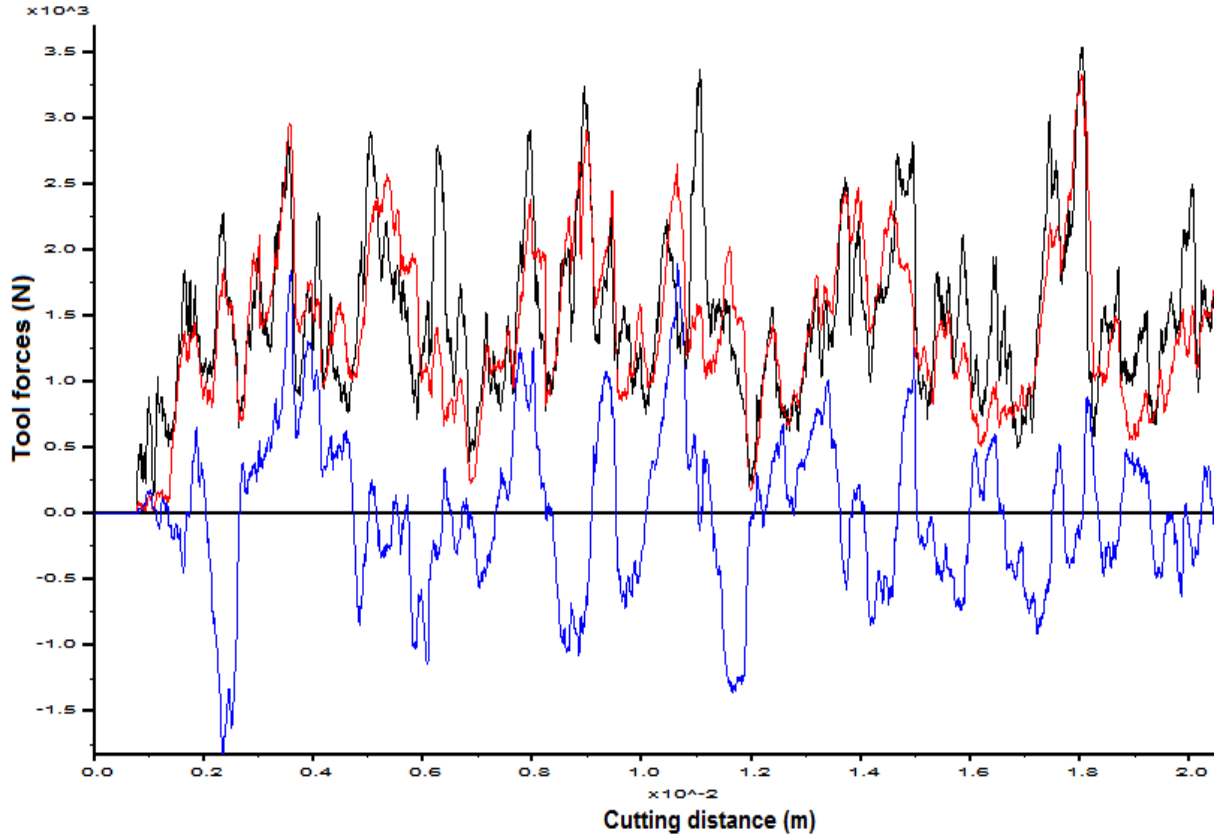

(b)

Figure 80: The variation of tool forces versus cutting distance for a blunt narrow point-attack pick with 1.5 mm wear flat at 1.5 mm depth of cut

(a) 0.401 mm particles; (b) 0.802 mm particles

Figure 81 shows the shape that the micro-cracks form after 20 mm cutting distance when cutting with blunt point-attack picks with different wear flats. The shape is oval for each wear flat at 1.5 mm depth of cut, since the micro-cracks become more at deeper depths of cut.

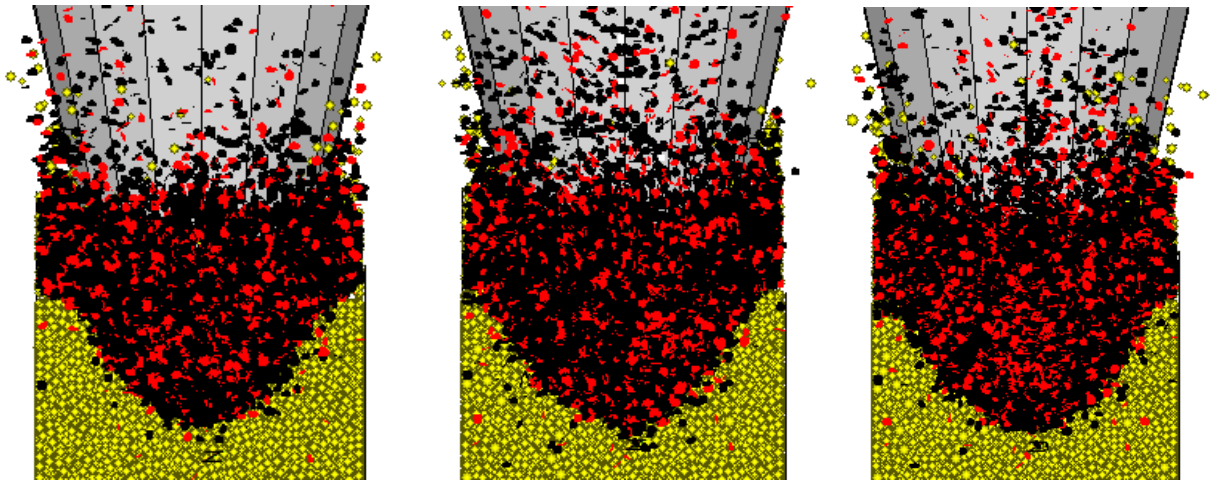

(a) (b) (c)

Figure 81: Shape of cracks in specimen when cutting with blunt narrow point-attack picks at 1.5 mm depth of cut

(a) 0.5 mm wear flat; (b) 1 mm wear flat; (c) 1.5 mm wear flat

D5. Results of rock cutting at 3 mm depth of cut for Su & Akcin (2011)

The simulated tool forces for the narrow point-attack picks with different wear flats at 3 mm depth of cut are shown in Figure 82 to Figure 85. The normal and cutting forces increase over a certain distance and then it fluctuates around an average value. At this depth of cut there is also a greater difference in the normal and cutting forces when cutting samples with 0.802 mm particles. The sideways forces still fluctuate around zero, except for the blunt point-attack pick with 0.5 mm and 1.5 mm wear flat cutting a sample with 0.401 mm particles.

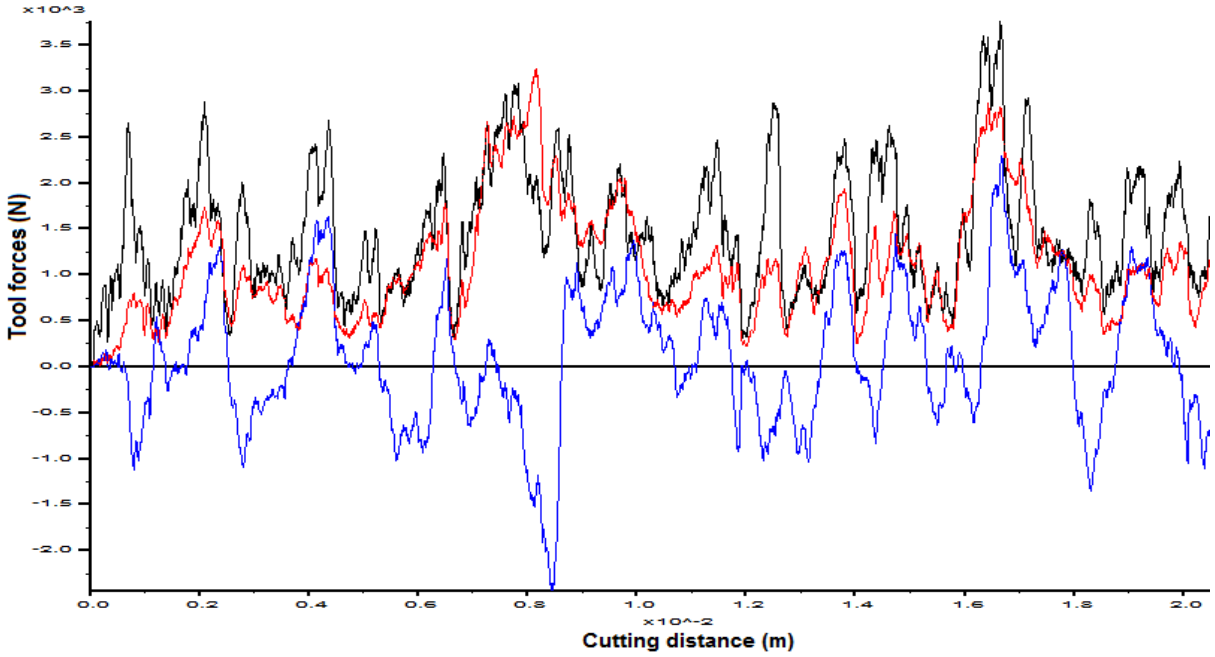

Figure 82: The variation of tool forces versus cutting distance for a sharp narrow point-attack pick cutting 0.802 mm particles at 3 mm depth of cut

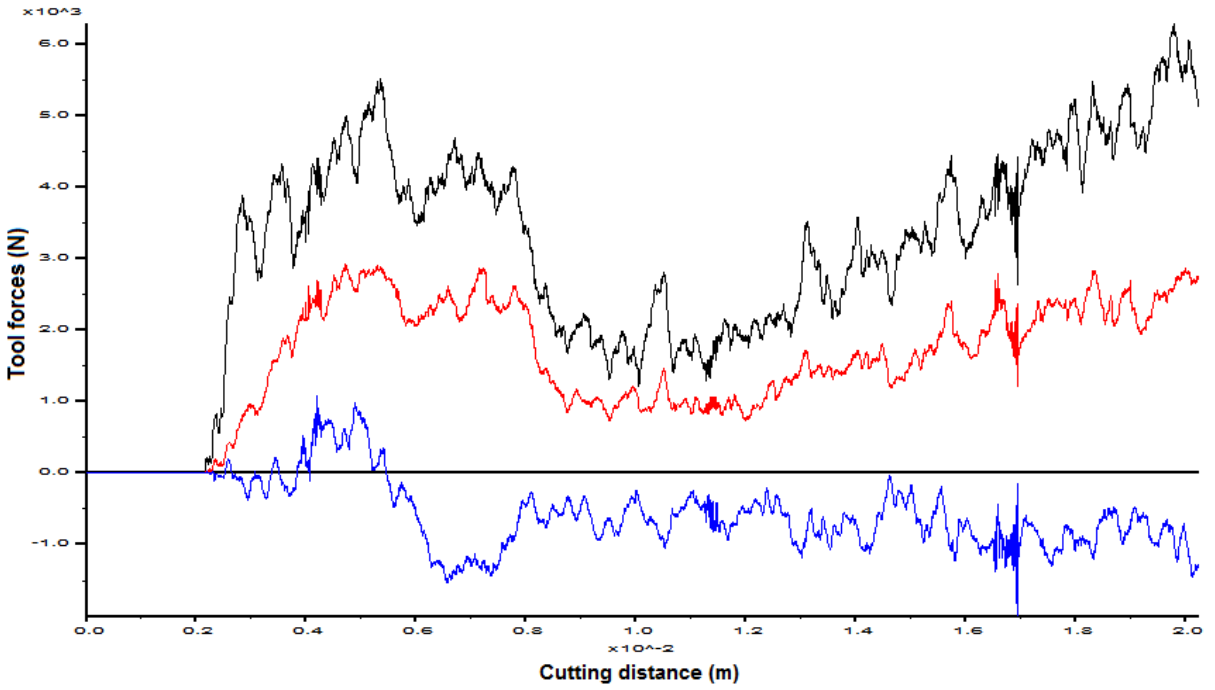

(a)

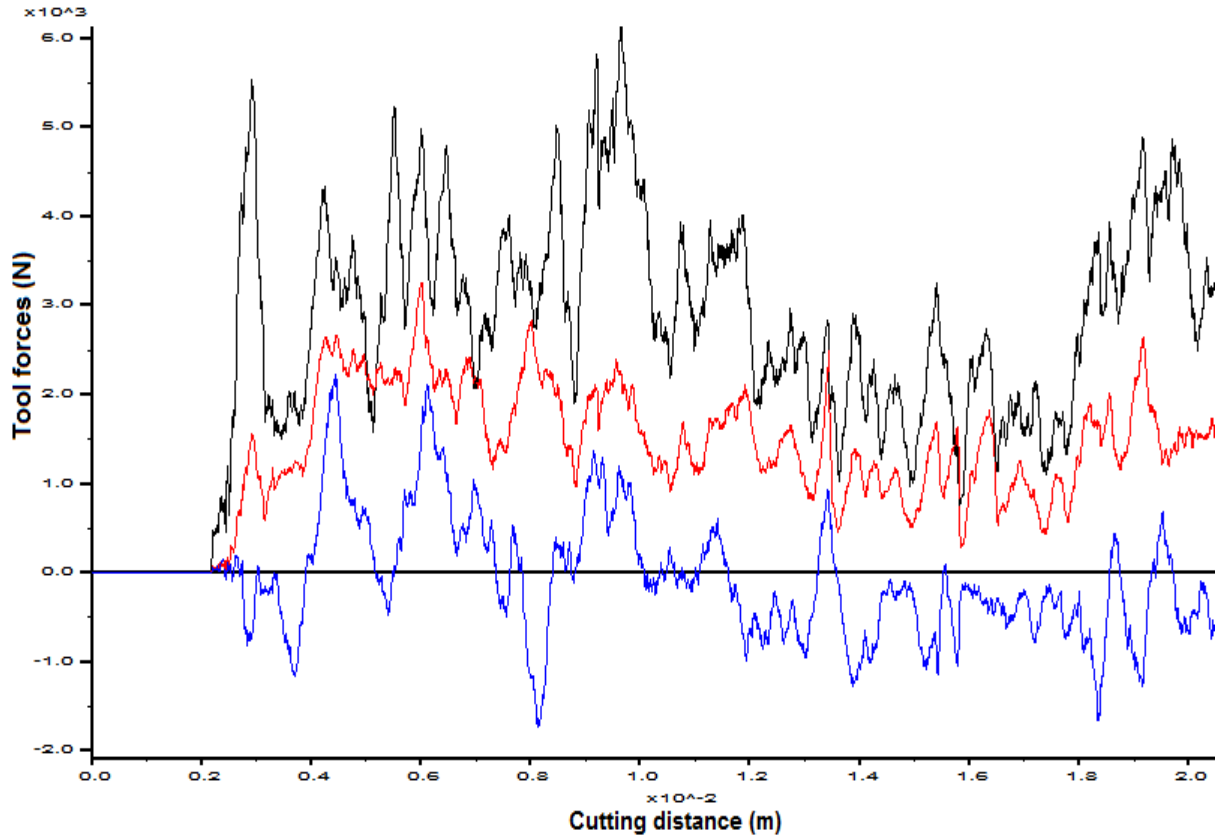

(b)

Figure 83: The variation of tool forces versus cutting distance for a blunt narrow point-attack pick with 0.5 mm wear flat at 3 mm depth of cut with

(a) 0.401 mm particles; (b) 0.802 mm particles

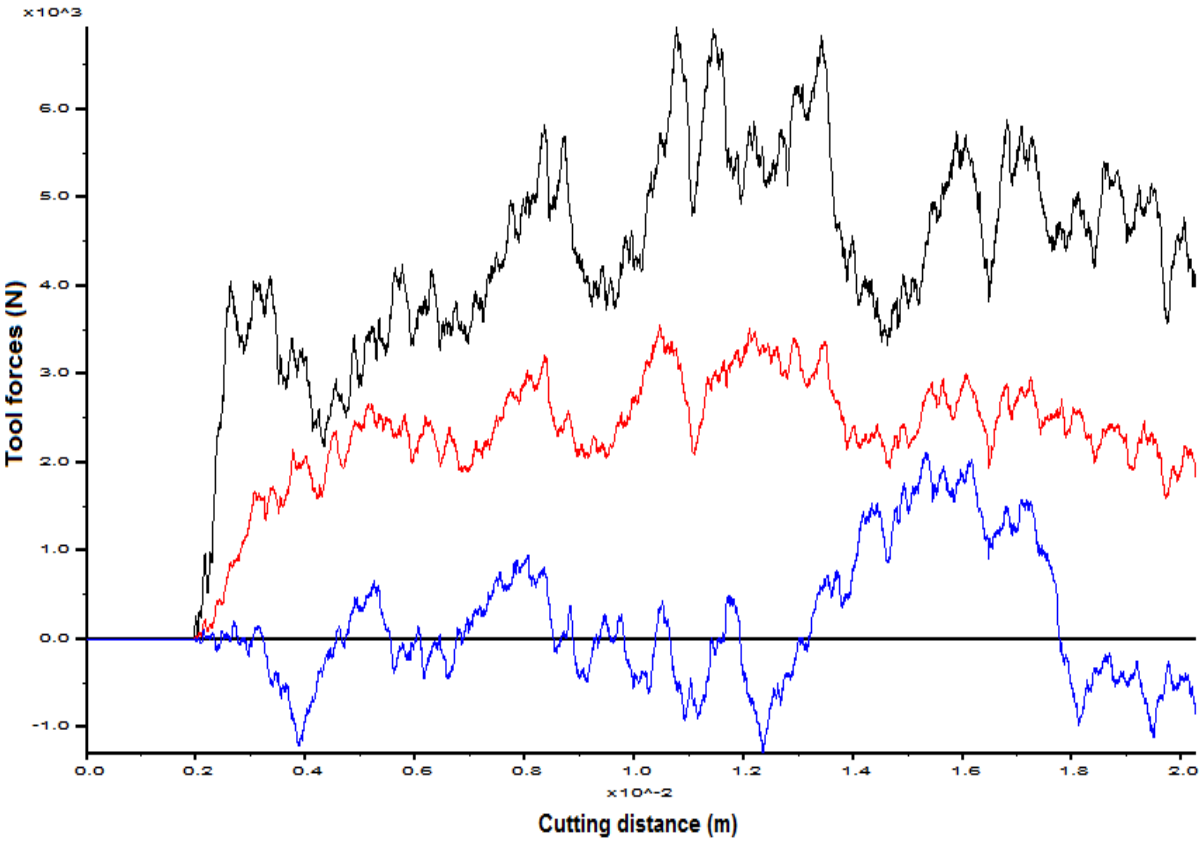

(a)

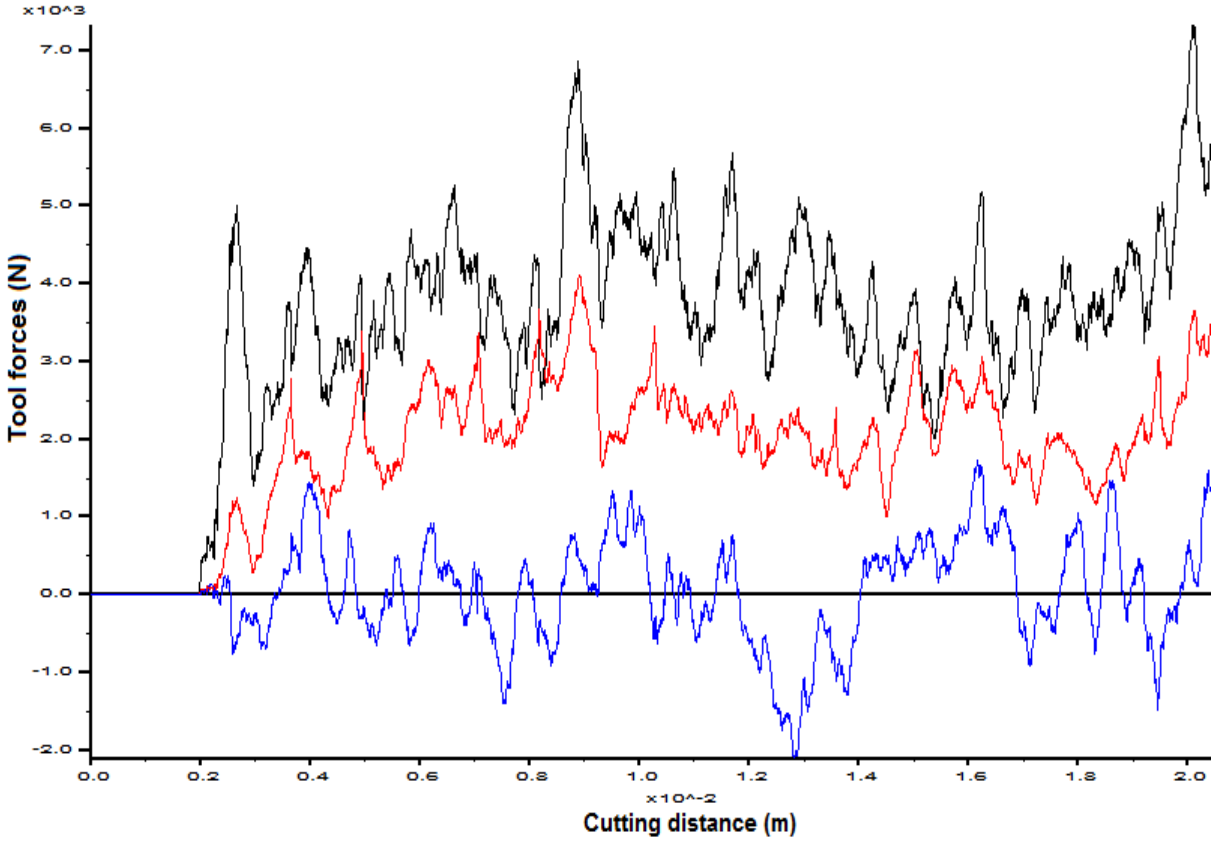

(b)

Figure 84: The variation of tool forces versus cutting distance for a blunt narrow point-attack pick with 1 mm wear flat at 3 mm depth of cut

(a) 0.401 mm particles; (b) 0.802 mm particles

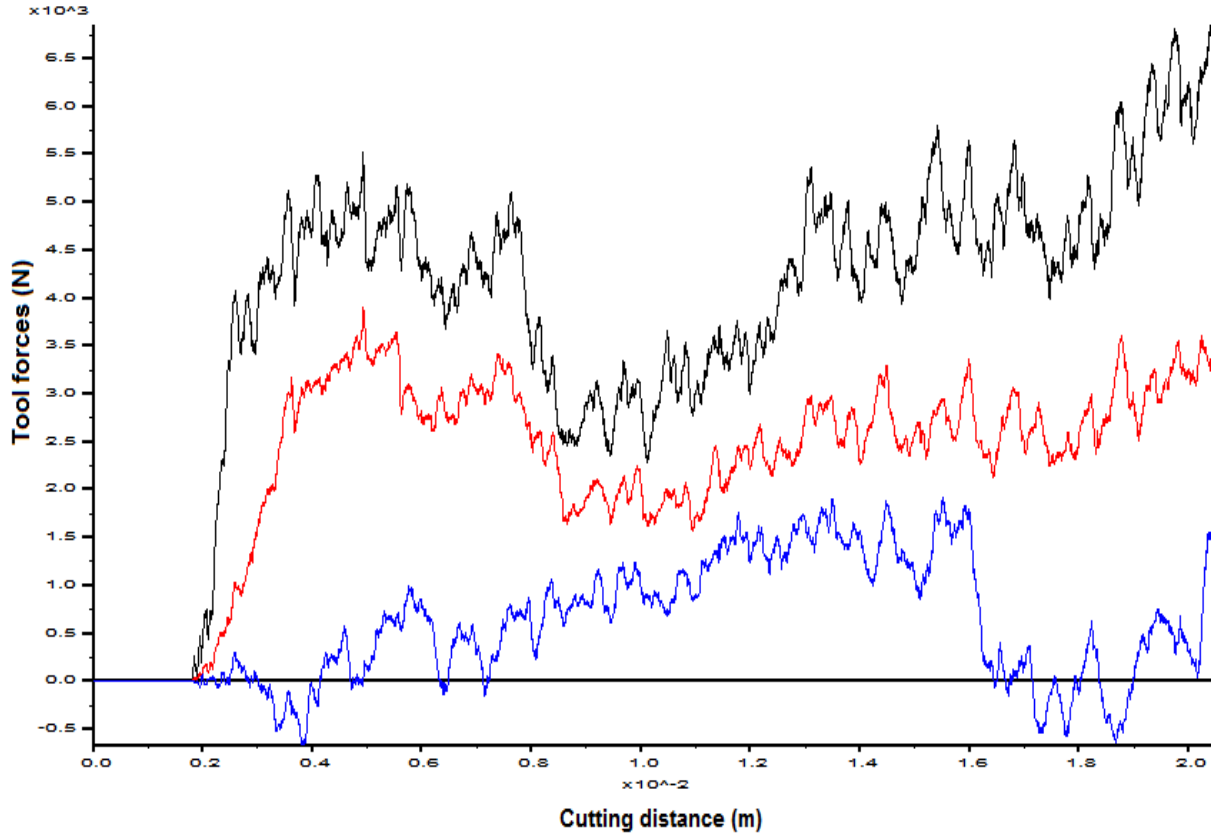

(a)

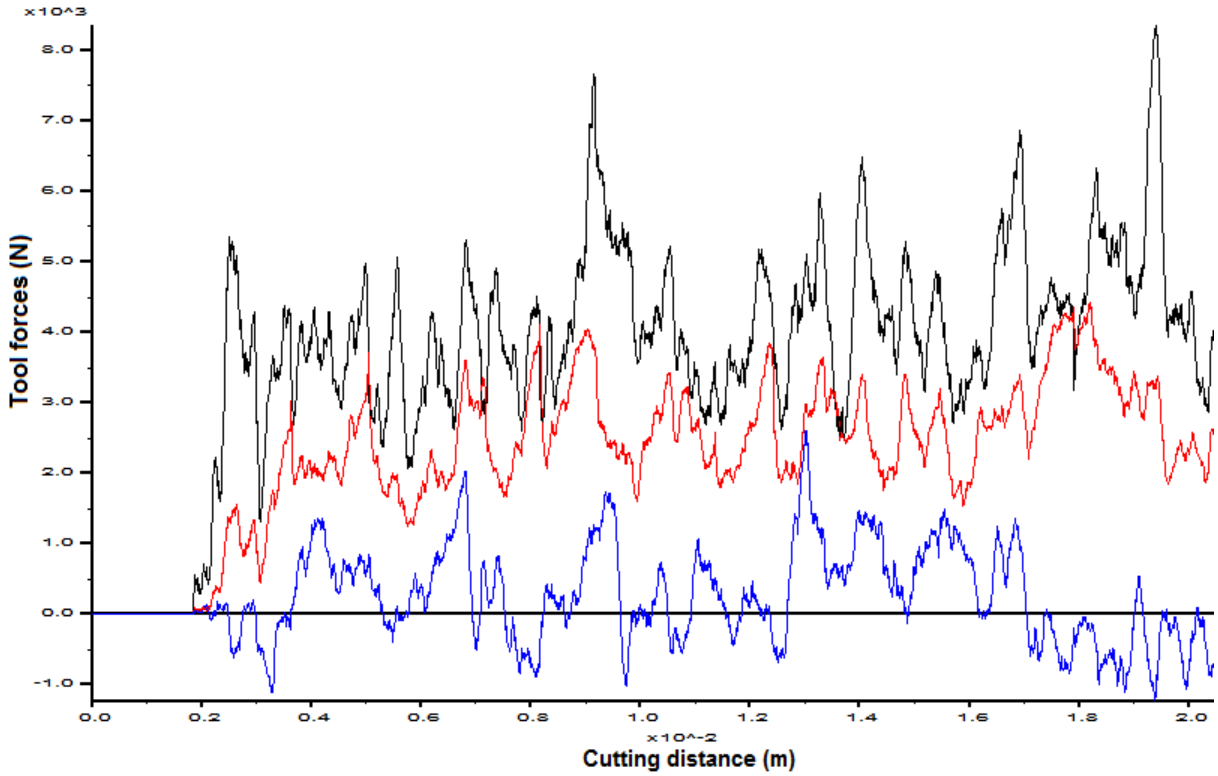

(b)

Figure 85: The variation of tool forces versus cutting distance for a blunt narrow point-attack pick with 1.5 mm wear flat at 3 mm depth of cut

(a) 0.401 mm particles; (b) 0.802 mm particles

Figure 86 shows the shape that the micro-cracks form after 20 mm cutting distance when cutting with blunt point-attack picks with different wear flats. The shape is oval for each wear flat at 3 mm depth of cut and it becomes flatter with an increase in wear flat. The micro-cracks spread throughout the width of specimen.

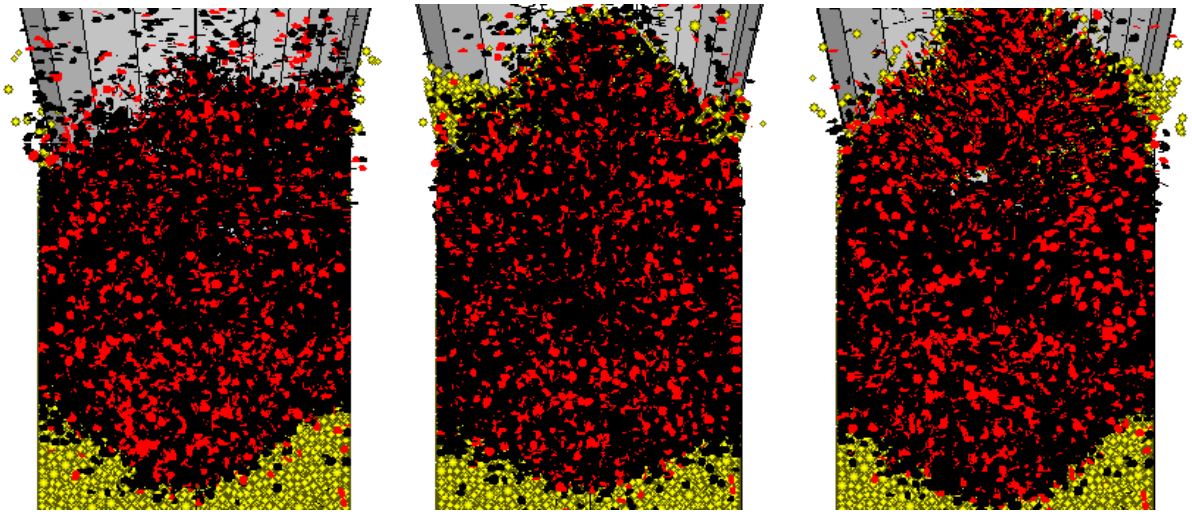

(a) (b) (c)

Figure 86: Shape of cracks in specimen when cutting with blunt narrow point-attack picks at 3 mm depth of cut

(a) 0.5 mm wear flat; (b) 1 mm wear flat; (c) 1.5 mm wear flat

D6. Results of rock cutting at 0.5 mm depth of cut for Bilgin et al. (2006)

The simulated tool forces for the wide point-attack picks with different wear flats at 0.5 mm depth of cut are shown in Figure 87 to Figure 90. The values of the normal and cutting forces are very similar at this shallow depth of cut for the sample with 0.802 mm particles, while the normal and cutting forces increase over a certain distance and then it fluctuates around a similar average value for the sample with 0.401 mm particles. The sideways forces fluctuate around zero.

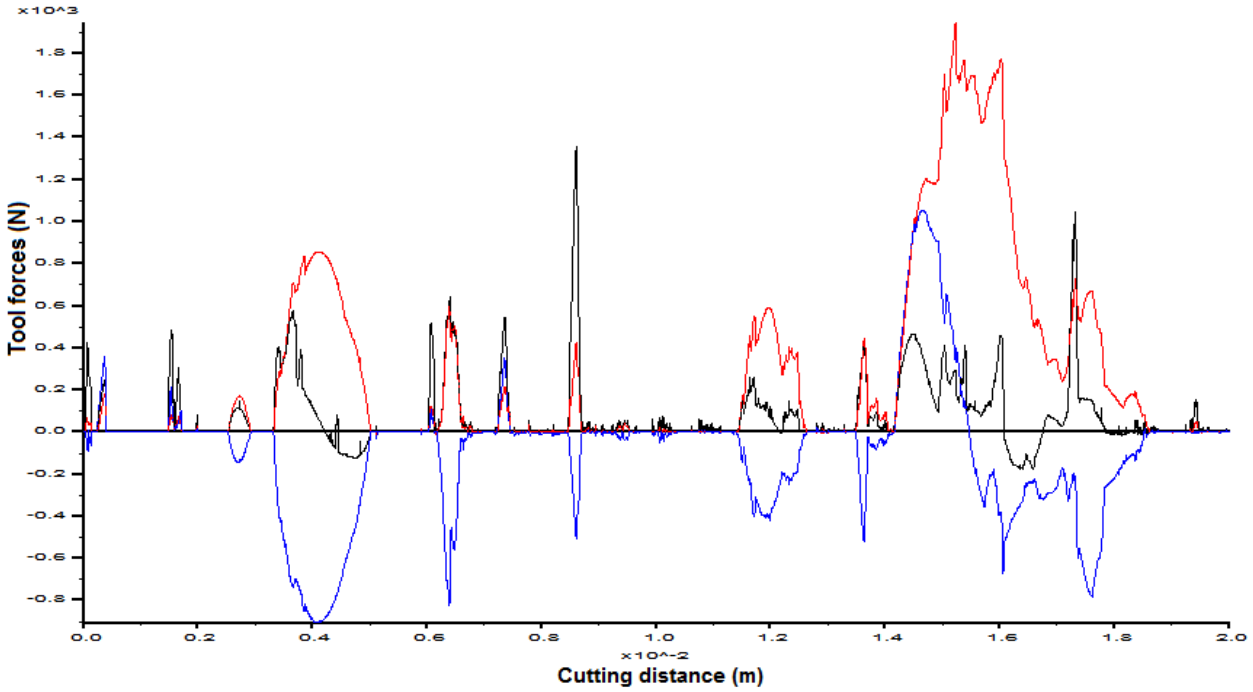

Figure 87: The variation of tool forces versus cutting distance for a wide point-attack pick cutting 0.802 mm particles at 0.5 mm depth of cut

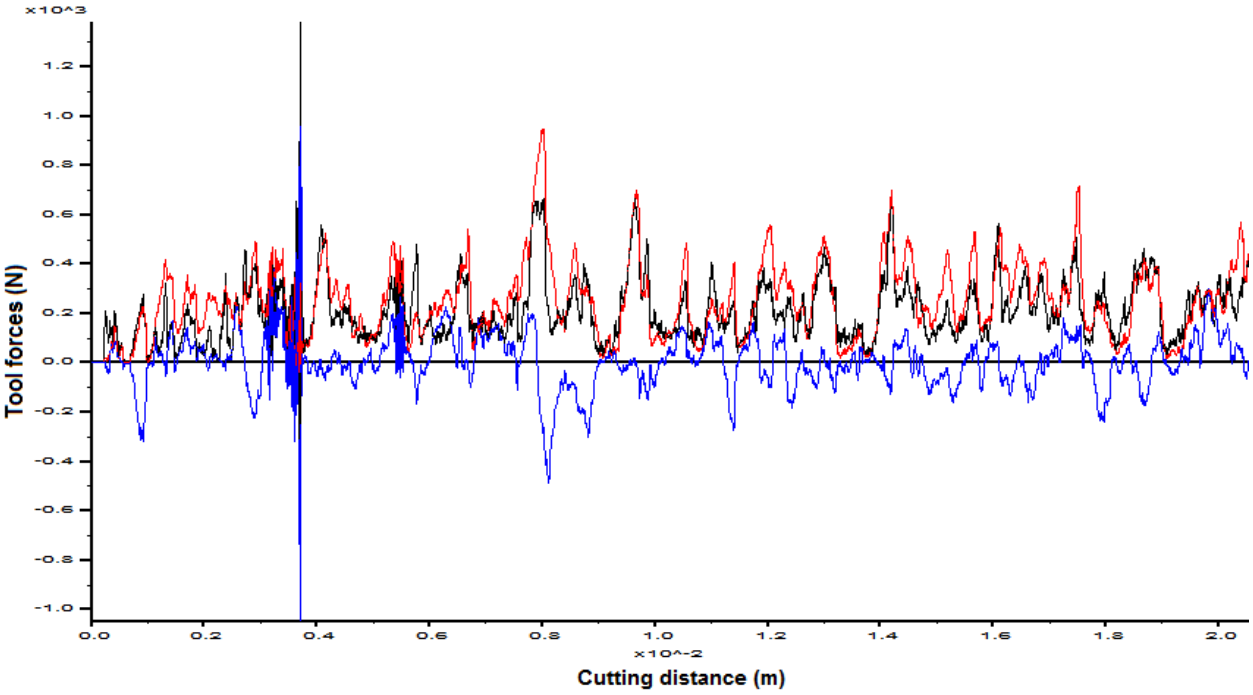

(a)

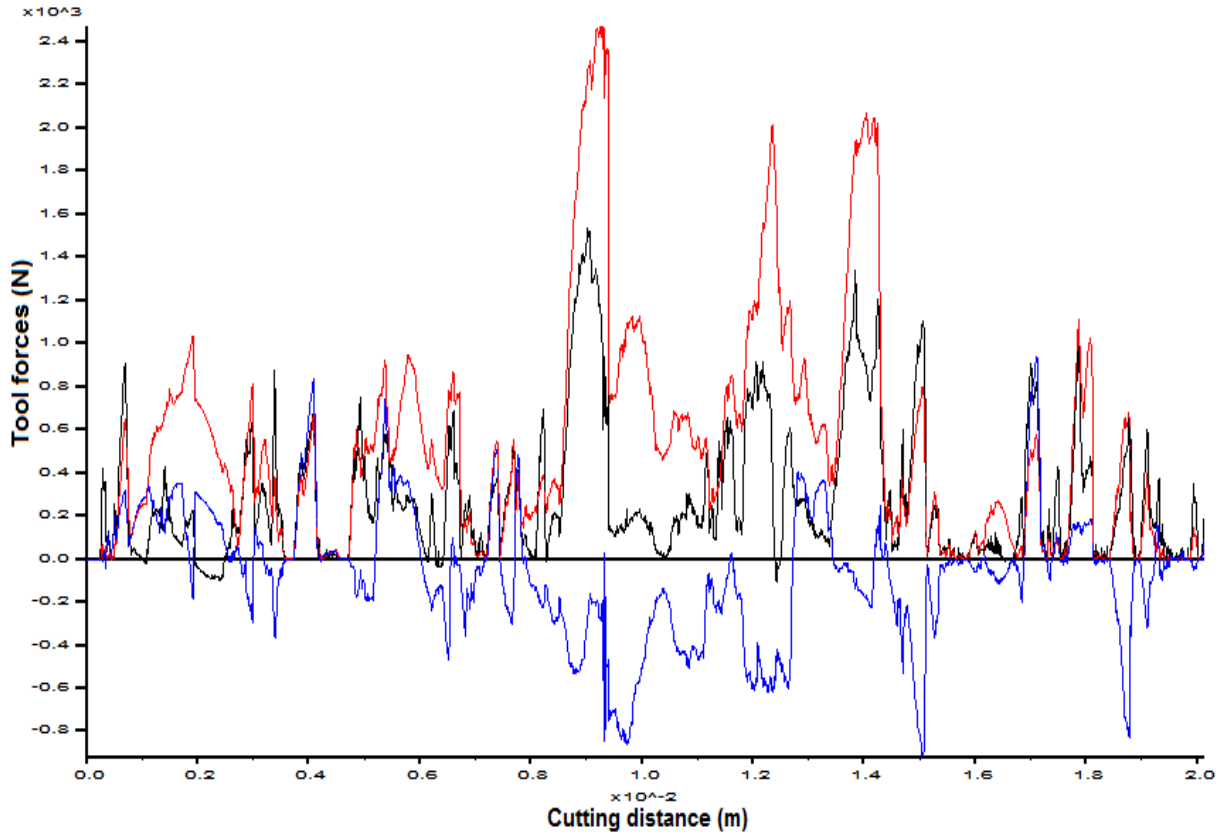

(b)

Figure 88: The variation of tool forces versus cutting distance for a blunt wide point-attack pick with 0.5 mm wear flat at 0.5 mm depth of cut

(a) 0.401 mm particles; (b) 0.802 mm particles

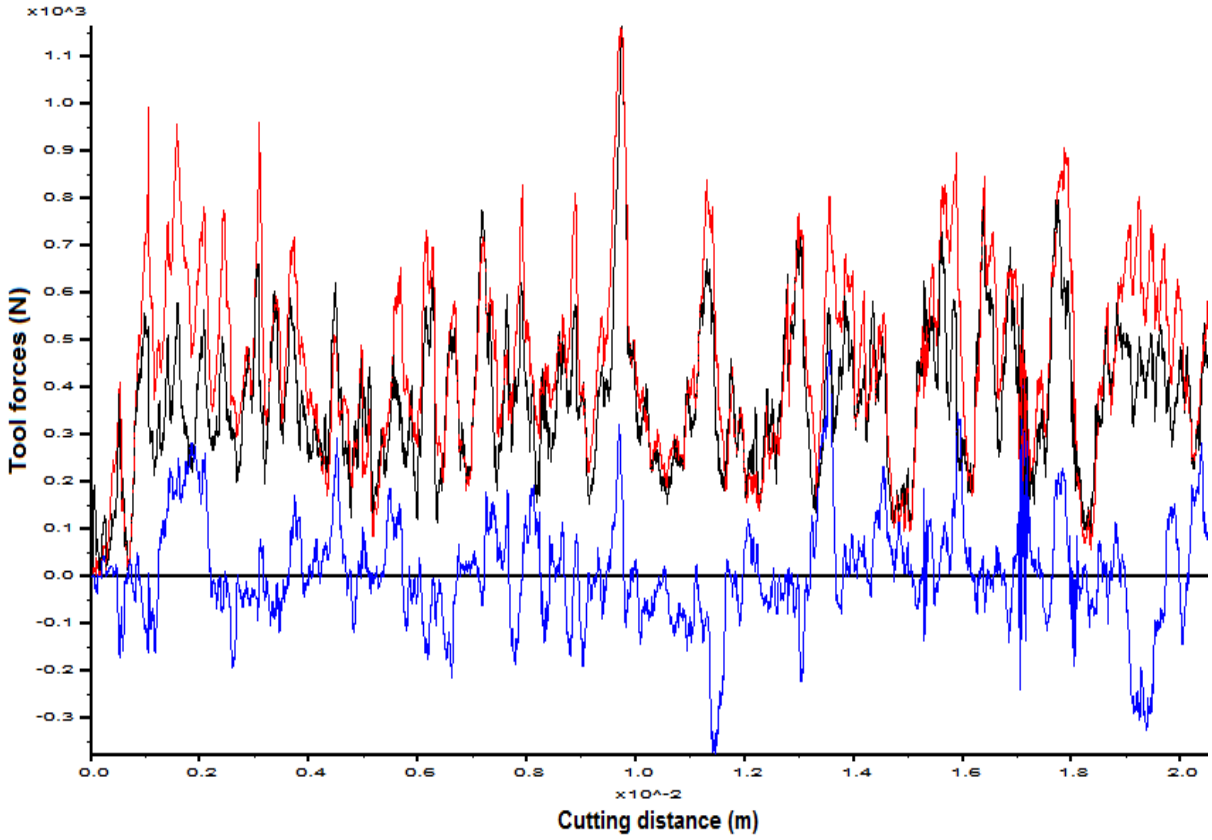

(a)

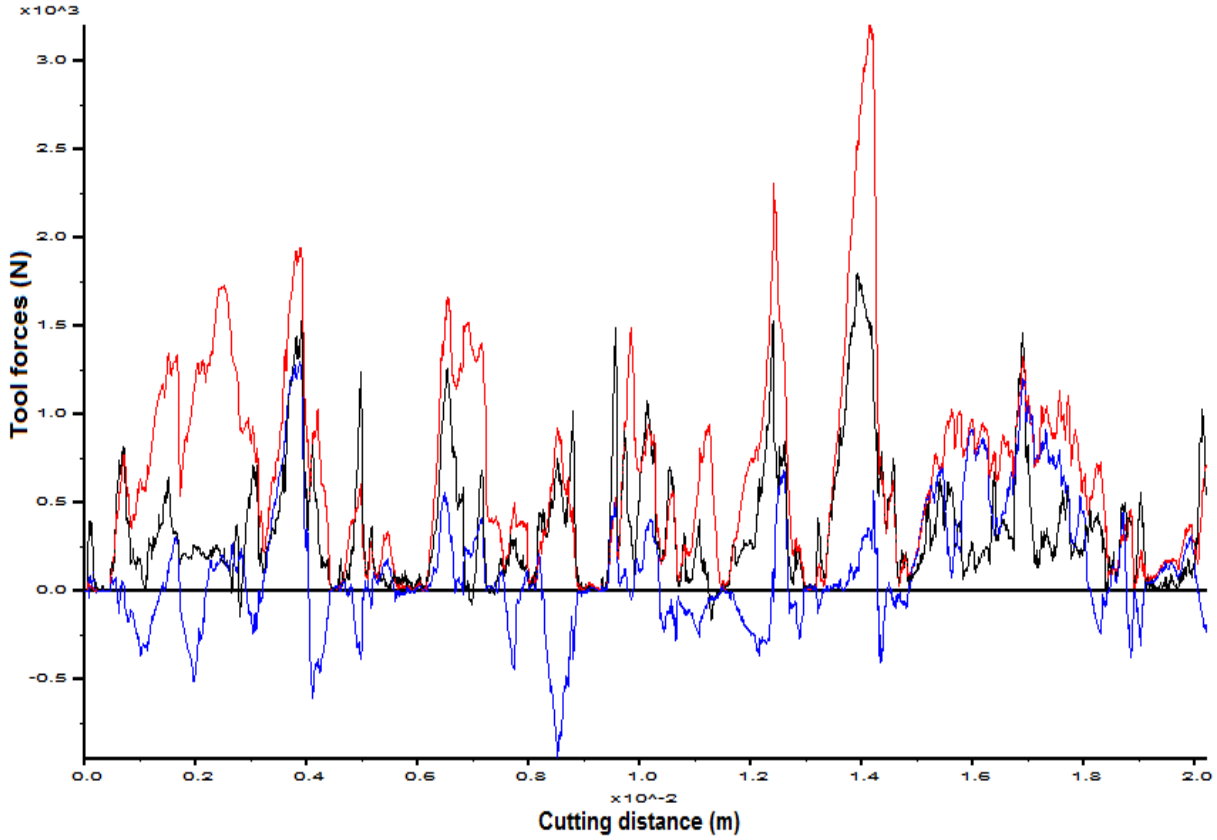

(b)

Figure 89: The variation of tool forces versus cutting distance for a blunt wide point-attack pick with 1 mm wear flat at 0.5 mm depth of cut

(a) 0.401 mm particles; (b) 0.802 mm particles

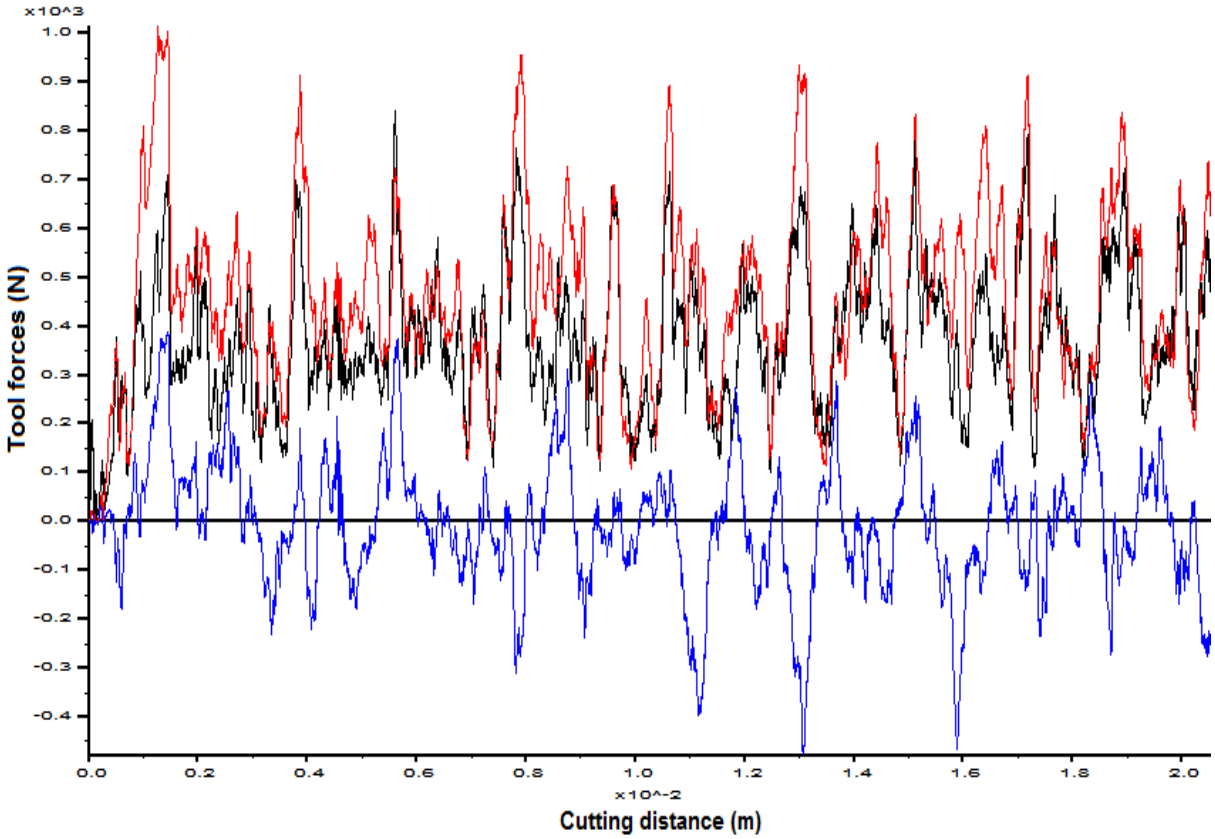

(a)

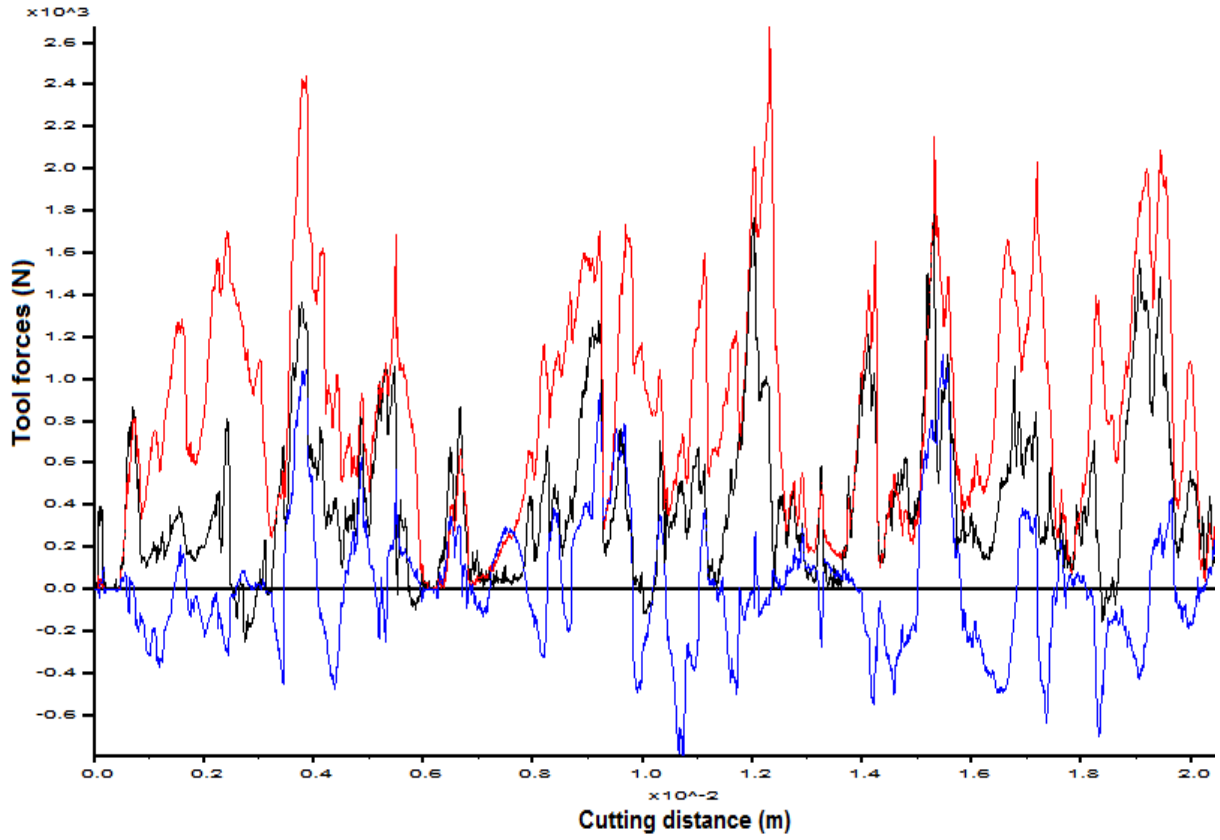

(b)

Figure 90: The variation of tool forces versus cutting distance for a blunt wide point-attack pick with 1.5 mm wear flat at 0.5 mm depth of cut

(a) 0.401 mm particles; (b) 0.802 mm particles

Figure 91 shows the shape that the micro-cracks form after 20 mm cutting distance when cutting with blunt point-attack picks with different wear flats. The shape is triangular and it becomes more trapezoidal with an increase in the wear flat. At the shallow depth of cut the micro-cracks are just around the point-attack pick.

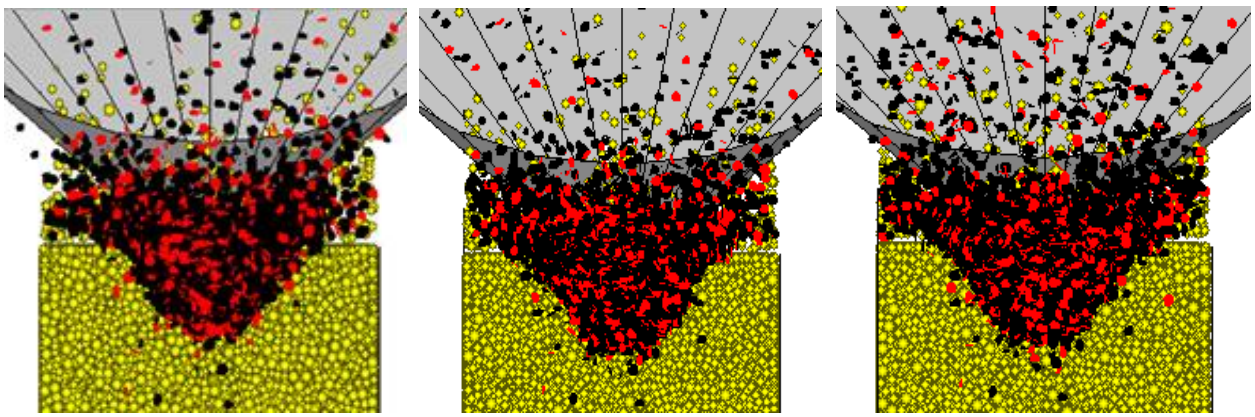

(a) (b) (c)

Figure 91: Shape of cracks in specimen when cutting with blunt wide point-attack picks at 0.5 mm depth of cut

(a) 0.5 mm wear flat; (b) 1 mm wear flat; (c) 1.5 mm wear flat

D7. Results of rock cutting at 1.5 mm depth of cut for Bilgin et al. (2006)

The simulated tool forces for the wide point-attack picks with different wear flats at 1.5 mm depth of cut are shown in Figure 92 to Figure 95. The normal and cutting forces increase over a certain distance and then it fluctuates around an average value. For the cutting of the samples with 0.401 mm particles, there is a greater difference in the normal and cutting forces than the cutting of samples with 0.802 mm particles. The sideways forces still fluctuate around zero.

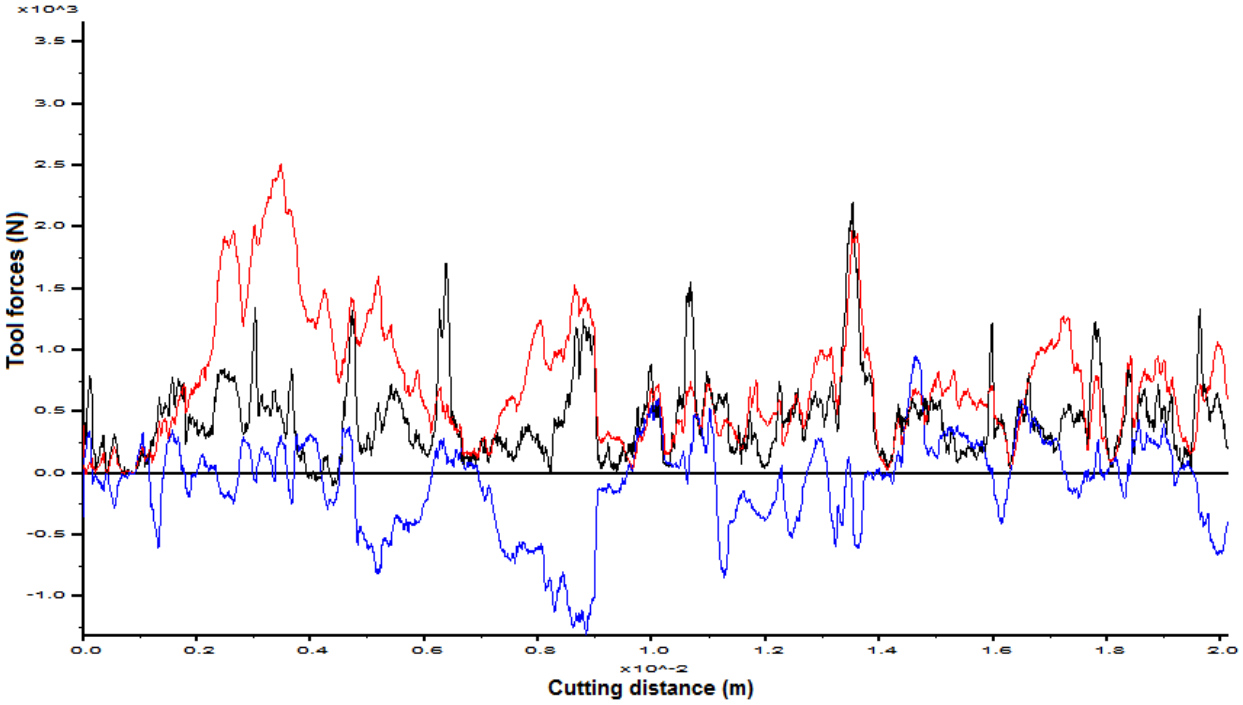

Figure 92: The variation of tool forces versus cutting distance for a wide point-attack pick cutting 0.802 mm particles at 1.5 mm depth of cut

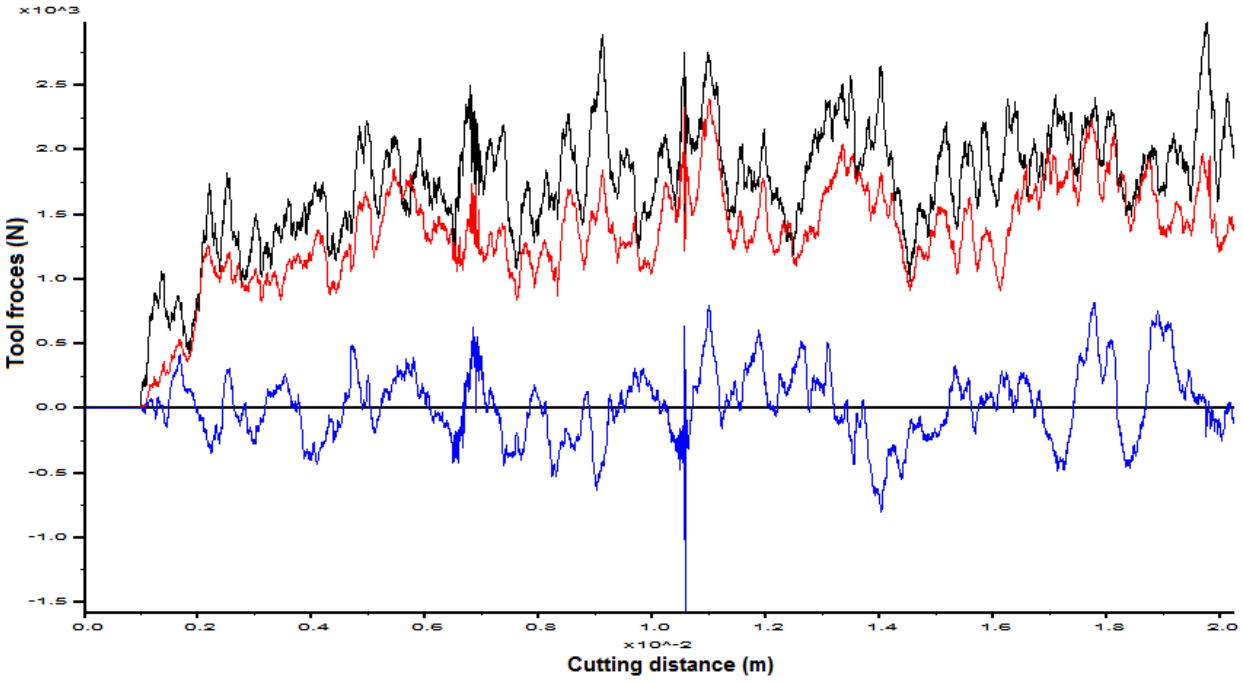

(a)

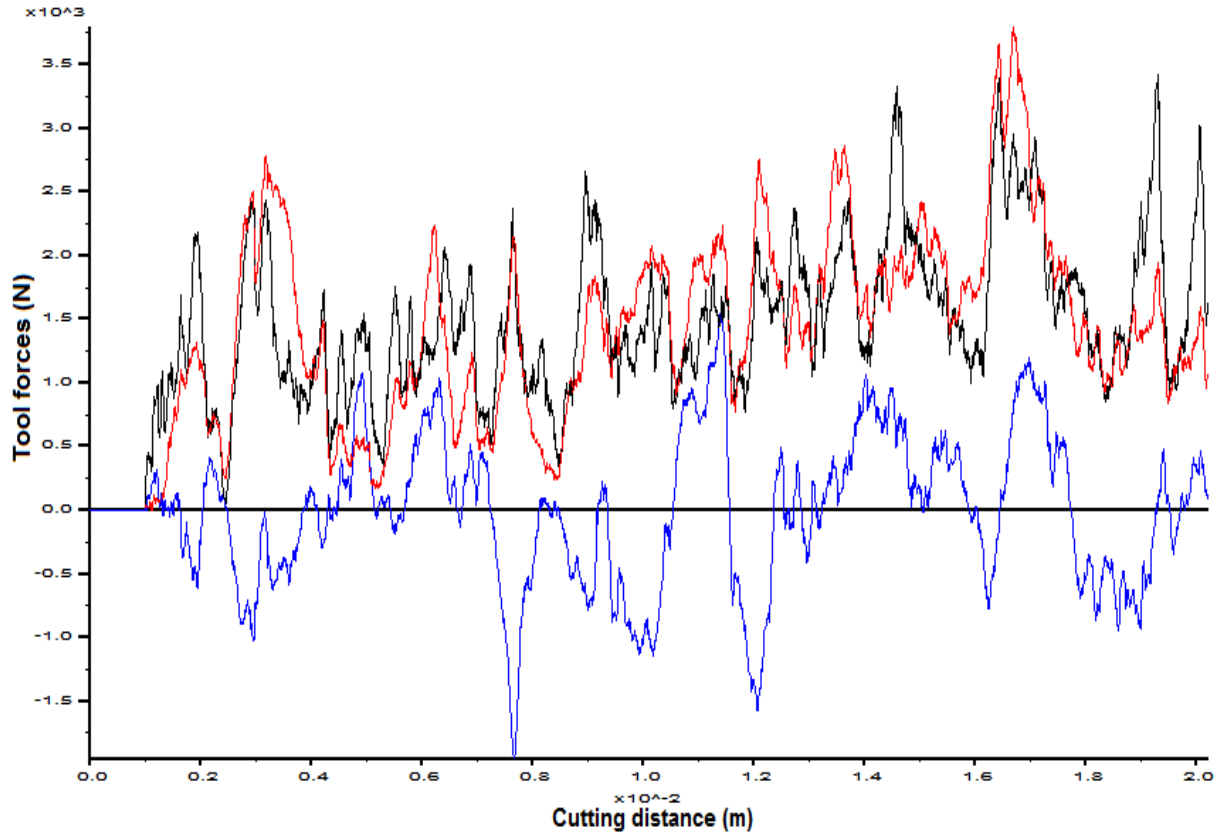

(b)

Figure 93: The variation of tool forces versus cutting distance for a blunt wide point-attack pick with 0.5 mm wear flat at 1.5 mm depth of cut

(a) 0.401 mm particles; (b) 0.802 mm particles

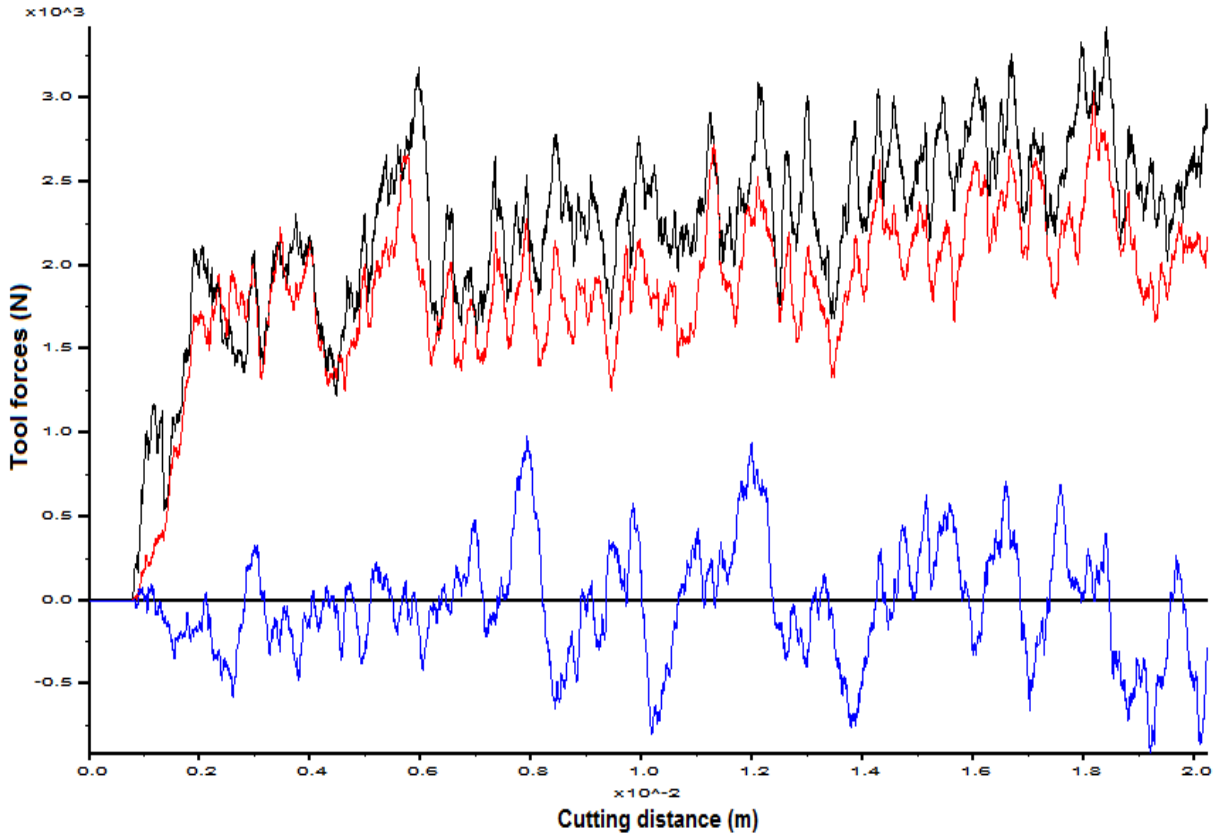

(a)

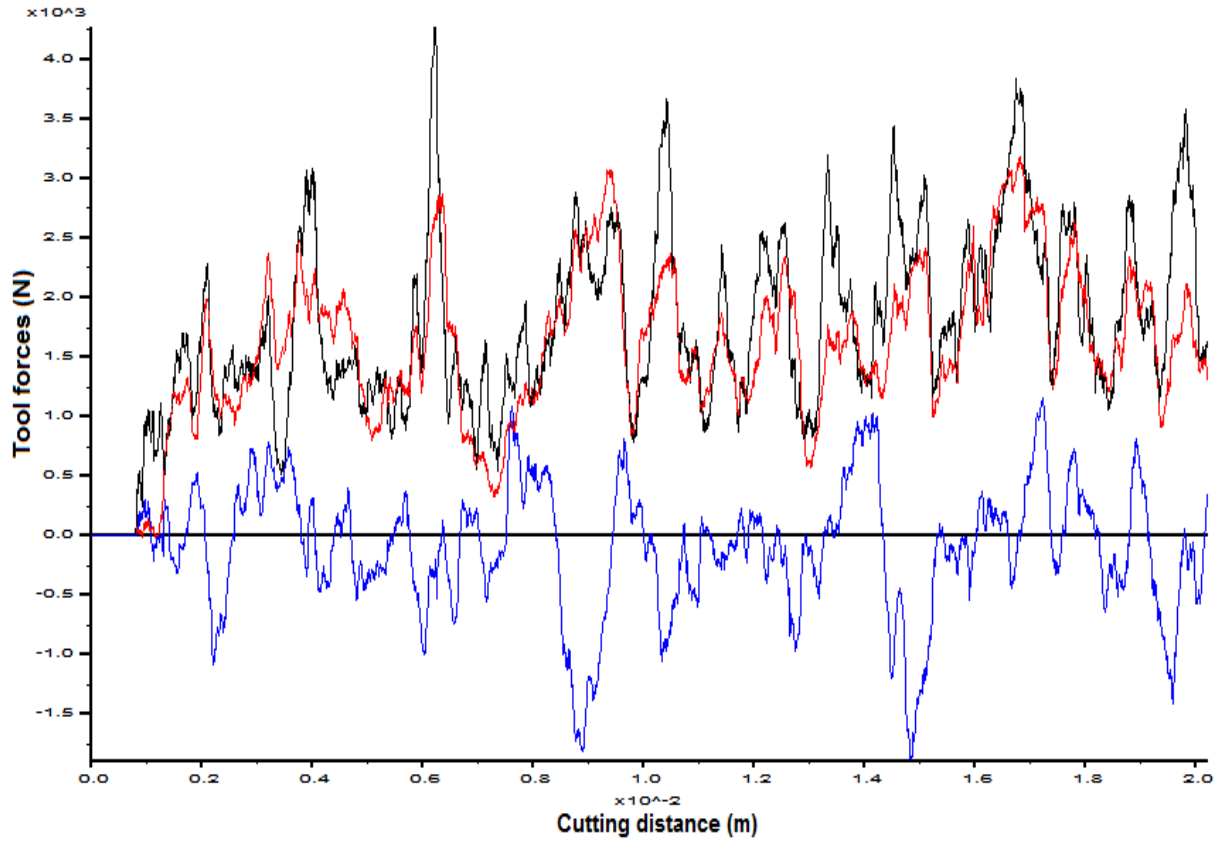

(b)

Figure 94: The variation of tool forces versus cutting distance for a blunt wide point-attack pick with 1 mm wear flat at 1.5 mm depth of cut

(a) 0.401 mm particles; (b) 0.802 mm particles

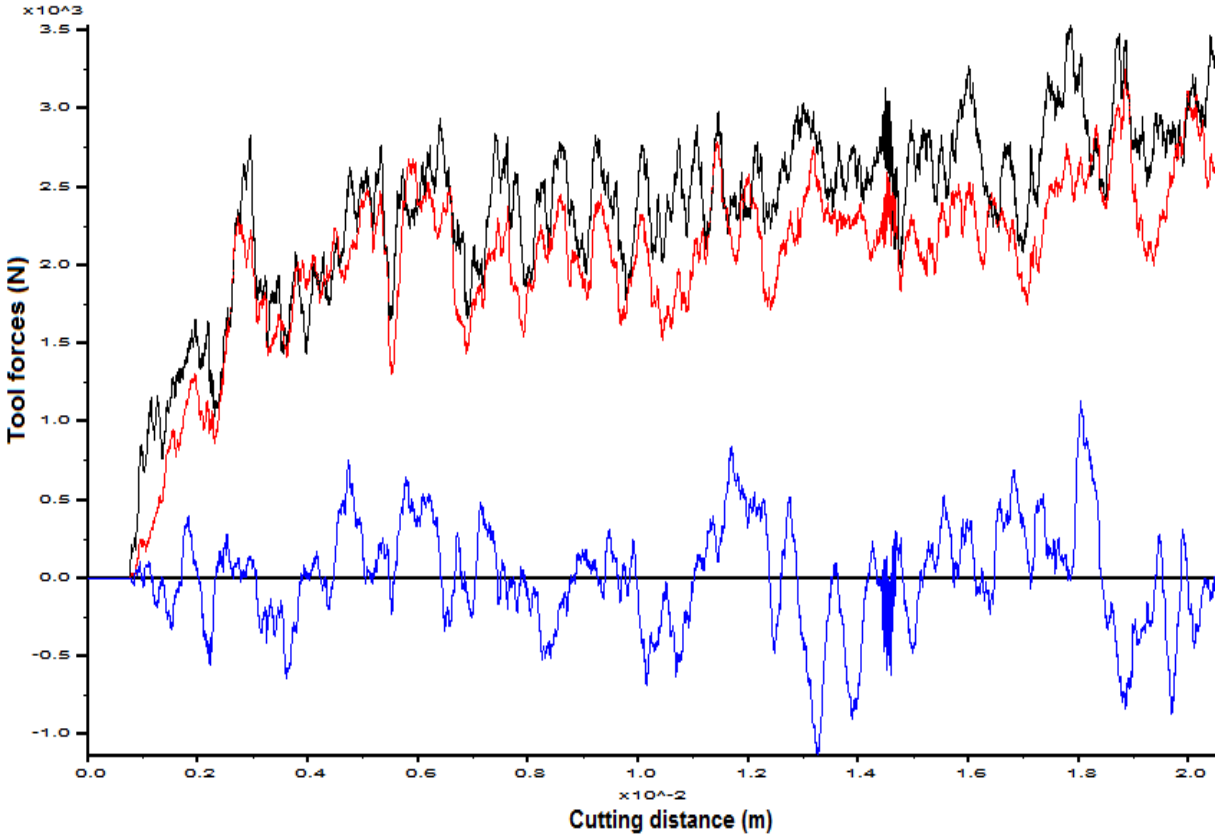

(a)

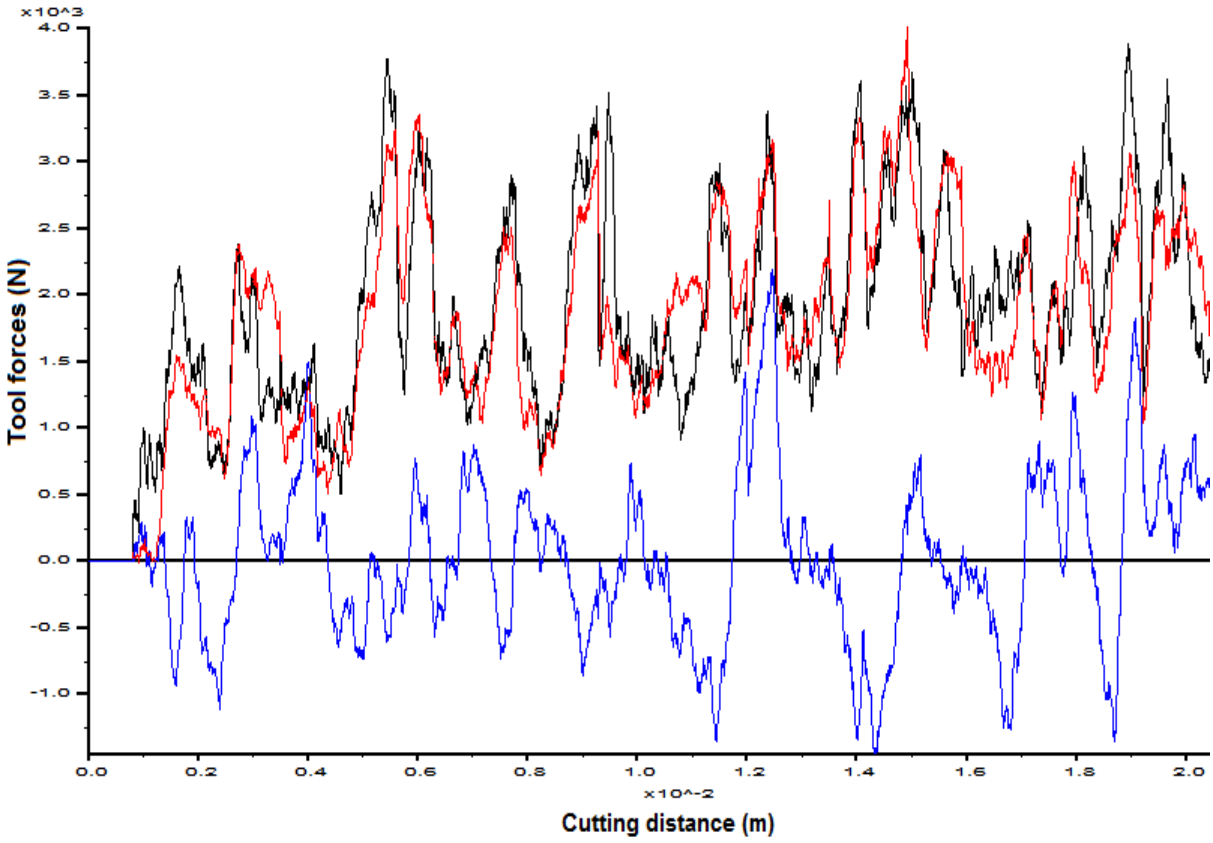

(b)

Figure 95: The variation of tool forces versus cutting distance for a blunt wide point-attack pick with 1.5 mm wear flat at 1.5 mm depth of cut

(a) 0.401 mm particles; (b) 0.802 mm particles

Figure 96 shows the shape that the micro-cracks form after 20 mm cutting distance when cutting with blunt point-attack picks with different wear flats. The shape is oval for each wear flat at 1.5 mm depth of cut.

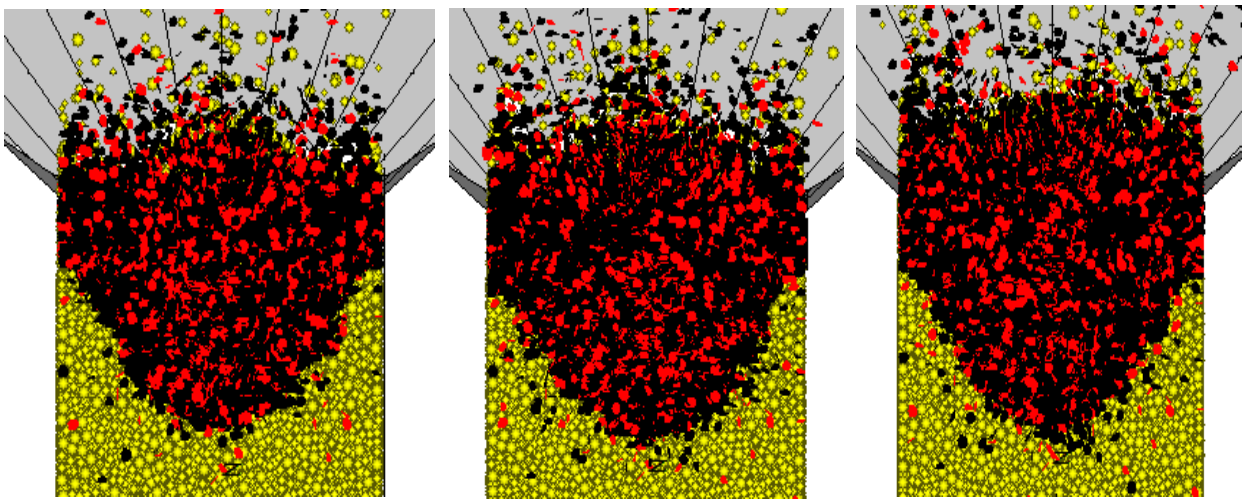

(a) (b) (c)

Figure 96: Shape of cracks in specimen when cutting with blunt wide point-attack picks at 1.5 mm depth of cut

(a) 0.5 mm wear flat; (b) 1 mm wear flat; (c) 1.5 mm wear flat

D8. Results of rock cutting at 3 mm depth of cut for Bilgin et al. (2006)

The simulated tool forces for the wide point-attack picks with different wear flats at 3 mm depth of cut are shown in Figure 97 to Figure 100. The normal and cutting forces increase over a certain distance and then it fluctuates around an average value. At this depth of cut there is also a greater difference in the normal and cutting forces when cutting samples with 0.802 mm particles. The sideways forces still fluctuate around zero, except for the blunt point-attack pick with 0.5 mm and 1.5 mm wear flat cutting a sample with 0.401 mm particles.

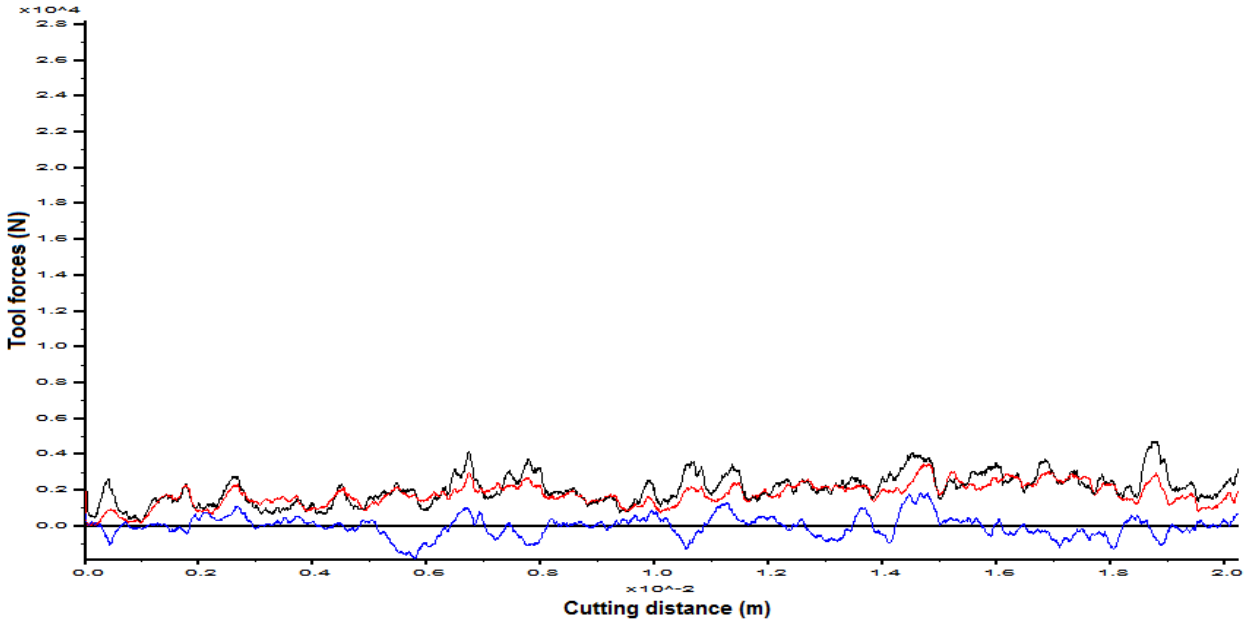

Figure 97: The variation of tool forces versus cutting distance for a wide point-attack pick cutting 0.802 mm particles at 3 mm depth of cut

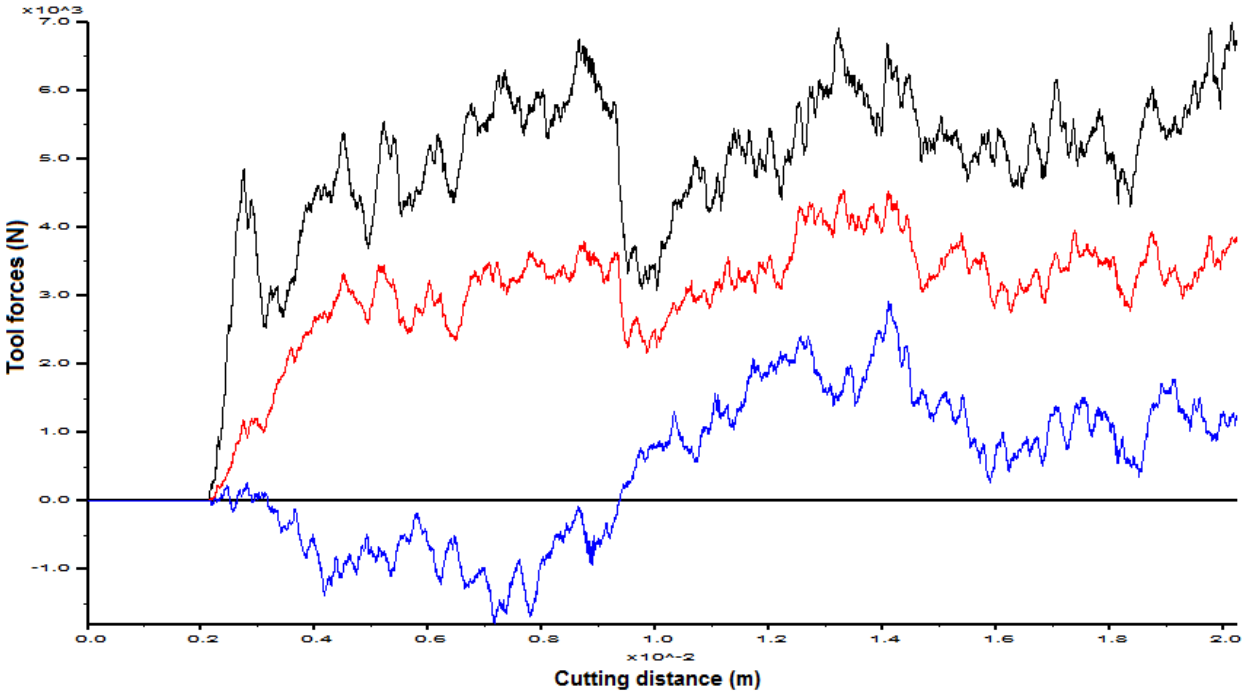

(a)

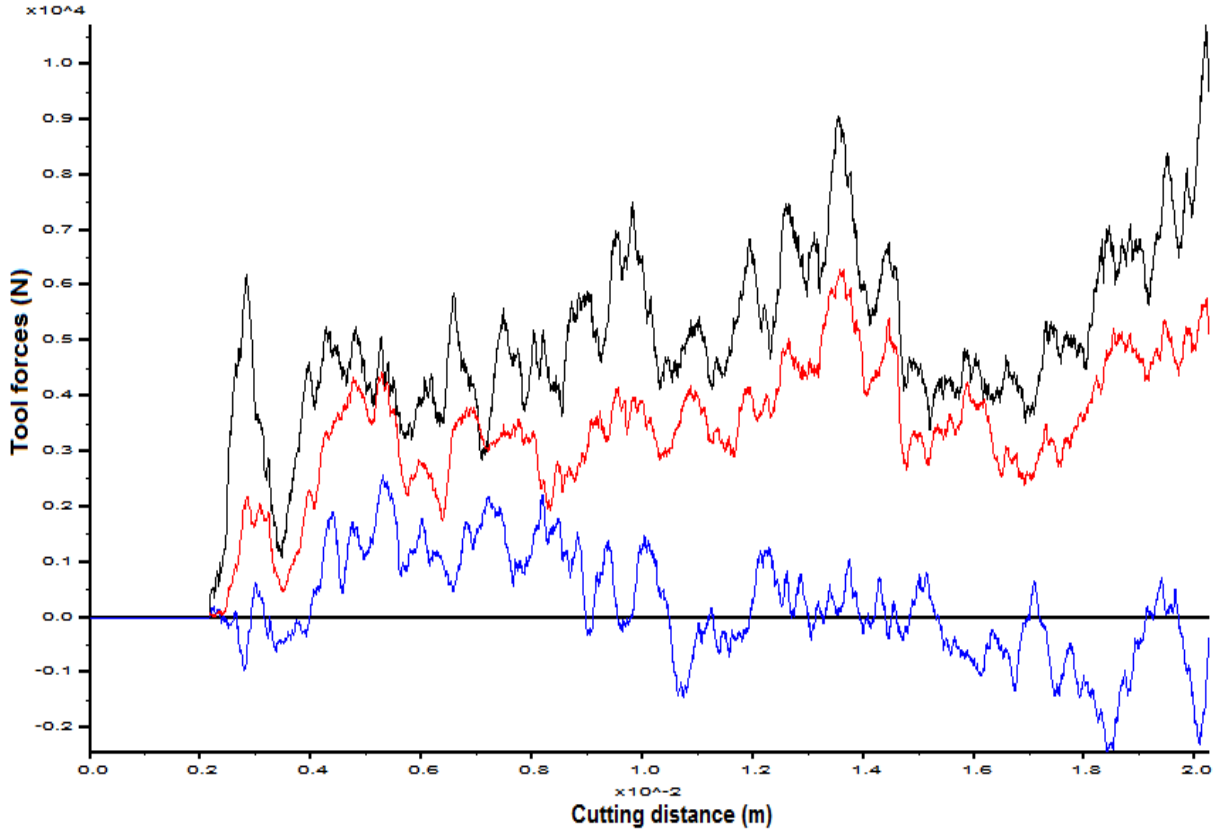

(b)

Figure 98: The variation of tool forces versus cutting distance for a blunt wide point-attack pick with 0.5 mm wear flat at 3 mm depth of cut

(a) 0.401 mm particles; (b) 0.802 mm particles

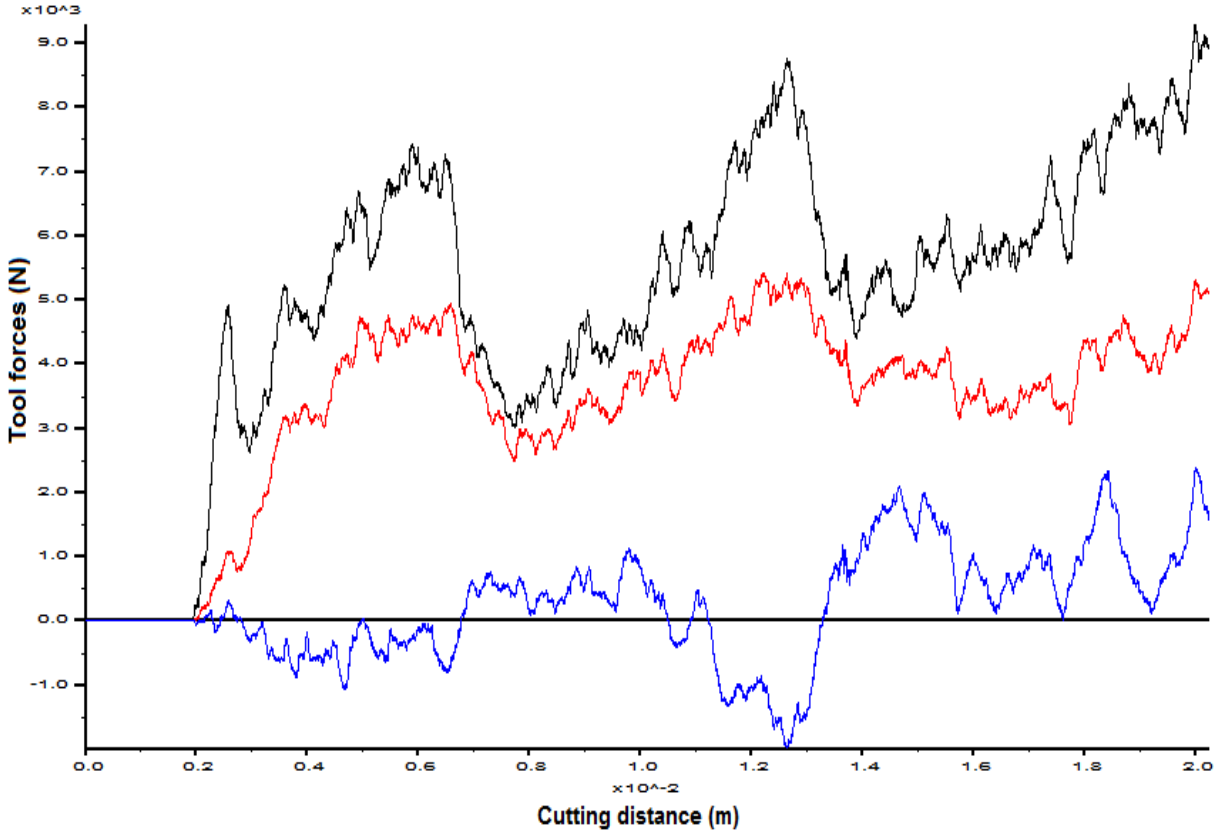

(a)

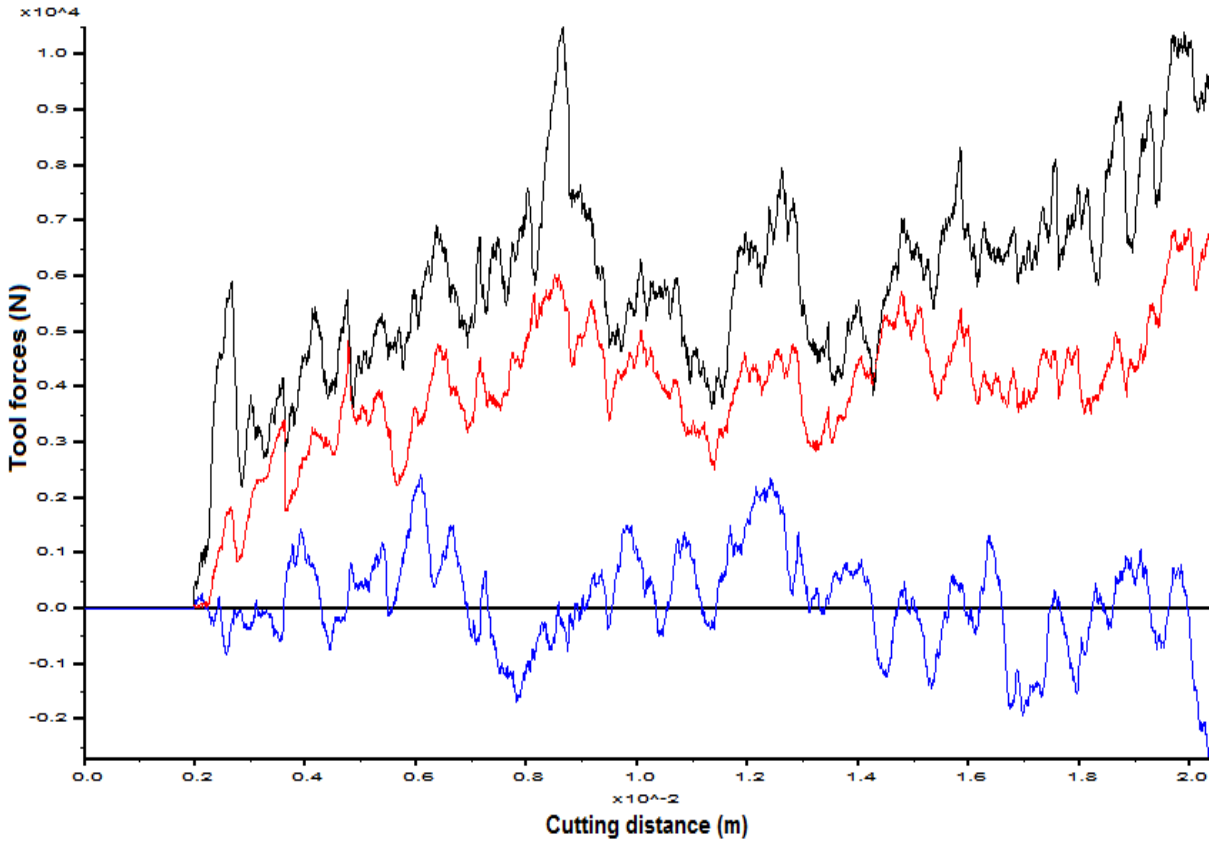

(b)

Figure 99: The variation of tool forces versus cutting distance for a blunt wide point-attack pick with 1 mm wear flat at 3 mm depth of cut

(a) 0.401 mm particles; (b) 0.802 mm particles

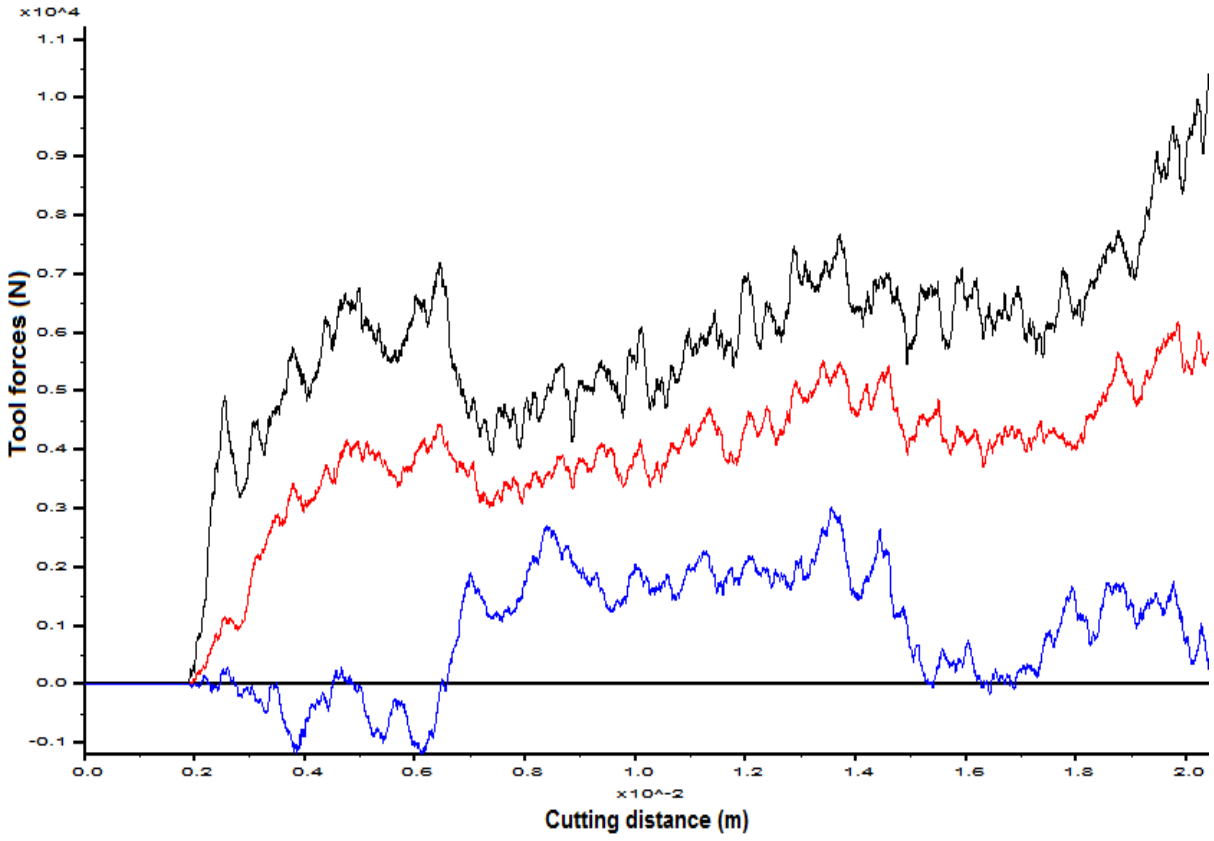

(a)

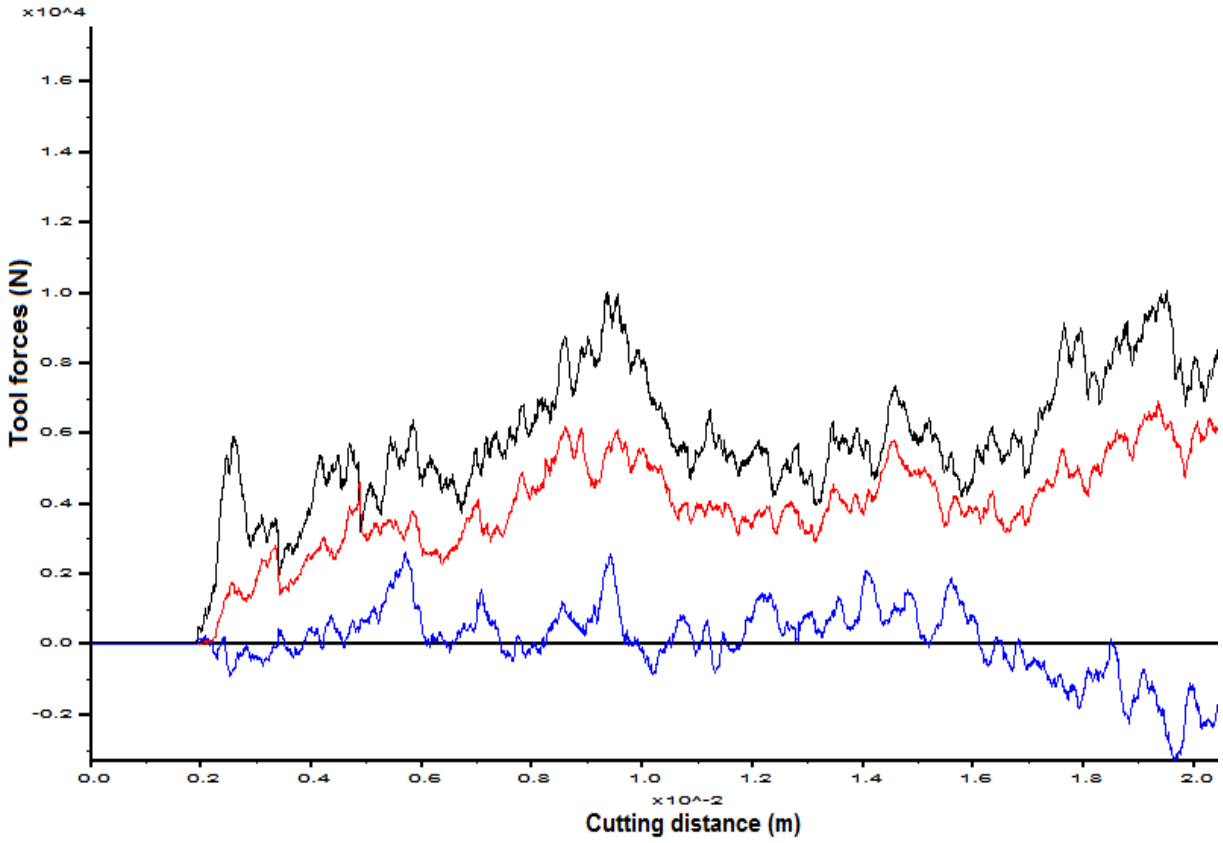

(b)

Figure 100: The variation of tool forces versus cutting distance for a blunt wide point-attack pick with 1.5 mm wear flat at 3 mm depth of cut

(a) 0.401 mm particles; (b) 0.802 mm particles

Figure 101 shows the shape that the micro-cracks forms in the specimen after 20 mm cutting distance when cutting with blunt point-attack picks with different wear flats. The shape is oval for each wear flat at 3 mm depth of cut and it becomes flatter with an increase in wear flat.

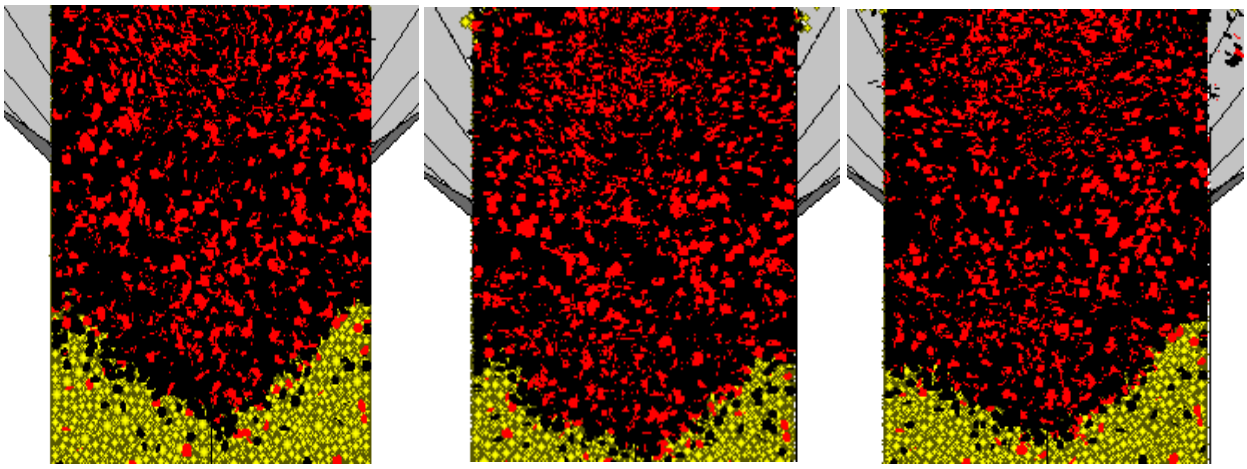

(a) (b) (c)

Figure 101: Shape of cracks in specimen when cutting with blunt wide point-attack picks at 3 mm depth of cut

(a) 0.5 mm wear flat; (b) 1 mm wear flat; (c) 1.5 mm wear flat

D9. The standard deviation of numerically simulated forces

The average values of the tool forces and their standard deviation during each numerical simulation of the rock cutting tests are summarized in the following tables.

Table 22: Standard deviation when cutting with a narrow point-attack pick at 0.5 mm depth of cut

	0.401 mm particles				0.802 mm particles			
	Cutting force (N)	SD (N)	Normal force (N)	SD (N)	Cutting force (N)	SD (N)	Normal force (N)	SD (N)
Sharp pick	44	64	45	68	63	151	39	114
0.5 mm wear flat	142	118	145	154	166	247	228	338
1 mm wear flat	281	153	357	210	334	392	526	525
1.5 mm wear flat	299	147	378	199	313	338	514	571

Table 23: Standard deviation when cutting with a narrow point-attack pick at 1.5 mm depth of cut

	0.401 mm particles				0.802 mm particles			
	Cutting force (N)	SD (N)	Normal force (N)	SD (N)	Cutting force (N)	SD (N)	Normal force (N)	SD (N)
Sharp pick	345	144	252	119	287	296	357	377
0.5 mm wear flat	1344	222	951	194	1044	630	928	626
1 mm wear flat	1689	267	1374	213	1246	593	1255	636
1.5 mm wear flat	1887	303	1642	288	1433	610	1338	618

Table 24: Standard deviation when cutting with a narrow point-attack pick at 3 mm depth of cut

	0.401 mm particles				0.802 mm particles			
	Cutting force (N)	SD (N)	Normal force (N)	SD (N)	Cutting force (N)	SD (N)	Normal force (N)	SD (N)
Sharp pick	1864	419	1253	302	1455	684	1074	627
0.5 mm wear flat	3532	1300	1775	706	2901	1067	1553	617
1 mm wear flat	4335	1065	2408	603	3766	1019	2049	716
1.5 mm wear flat	4385	949	2658	510	4031	1115	2481	909

Table 25: Standard deviation when cutting with a wide point-attack pick at 0.5 mm depth of cut

	0.401 mm particles				0.802 mm particles			
	Cutting force (N)	SD (N)	Normal force (N)	SD (N)	Cutting force (N)	SD (N)	Normal force (N)	SD (N)
Sharp pick	44	58	51	79	54	140	60	144
0.5 mm wear flat	193	139	237	155	245	295	248	301
1 mm wear flat	359	146	438	195	306	346	596	592
1.5 mm wear flat	364	141	448	193	363	356	783	567

Table 26: Standard deviation when cutting with a wide point-attack pick at 1.5 mm depth of cut

	0.401 mm particles				0.802 mm particles			
	Cutting force (N)	SD (N)	Normal force (N)	SD (N)	Cutting force (N)	SD (N)	Normal force (N)	SD (N)
Sharp pick	420	174	386	180	389	340	709	495
0.5 mm wear flat	1750	441	1356	375	1474	581	1412	743
1 mm wear flat	2255	507	1880	462	1771	714	1616	661
1.5 mm wear flat	2379	531	2079	495	1896	754	1851	776

Table 27: Standard deviation when cutting with a wide point-attack pick at 3 mm depth of cut

	0.401 mm particles				0.802 mm particles			
	Cutting force (N)	SD (N)	Normal force (N)	SD (N)	Cutting force (N)	SD (N)	Normal force (N)	SD (N)
Sharp pick	2703	432	2062	297	1913	1326	1775	655
0.5 mm wear flat	5041	1041	3137	768	4955	1432	3533	1432
1 mm wear flat	5723	1621	3727	1052	5908	1686	3958	1223
1.5 mm wear flat	5977	1316	3990	1038	5882	1751	3964	1365

Table 28: Standard deviation when cutting with a sharp chisel-shaped pick

Depth of cut	0.401 mm particles				0.802 mm particles			
	Cutting force (N)	SD (N)	Normal force (N)	SD (N)	Cutting force (N)	SD (N)	Normal force (N)	SD (N)
0.5	891	290	377	226	627	438	596	428
5.0	9789	6090	1763	758	8067	5650	1985	1040